REPORT DOCUMENTATION PAGE

AD-A232 372

2. REPORT DATE	3. REPORT TYPE AND DATES COVERED
1990	THESIS/DISSERTATION

4. TITLE AND SUBTITLE
Thermal Ion Upwelling in the High-Altitude Ionosphere

5. FUNDING NUMBERS

6. AUTHOR(S)
Richard Walter Cannata

7. PERFORMING ORGANIZATION NAME(S) AND ADDRESS(ES)
AFIT Student Attending: University of Michigan

8. PERFORMING ORGANIZATION REPORT NUMBER
AFIT/CI/CIA-90-035D

9. SPONSORING/MONITORING AGENCY NAME(S) AND ADDRESS(ES)
AFIT/CI
Wright-Patterson AFB OH 45433-6583

10. SPONSORING/MONITORING AGENCY REPORT NUMBER

11. SUPPLEMENTARY NOTES

12a. DISTRIBUTION/AVAILABILITY STATEMENT
Approved for Public Release IAW 190-1
Distributed Unlimited
ERNEST A. HAYGOOD, 1st Lt, USAF
Executive Officer

12b. DISTRIBUTION CODE

13. ABSTRACT (Maximum 200 words)

14. SUBJECT TERMS

15. NUMBER OF PAGES
221

16. PRICE CODE

17. SECURITY CLASSIFICATION OF REPORT	18. SECURITY CLASSIFICATION OF THIS PAGE	19. SECURITY CLASSIFICATION OF ABSTRACT	20. LIMITATION OF ABSTRACT

GENERAL INSTRUCTIONS FOR COMPLETING SF 298

The Report Documentation Page is used in announcing and cataloging reports. It is important that this information be consistent with the rest of the report, particularly the cover and title page. Instructions for filling in each block of the form follow. It is important to *stay within the lines* to meet *optical scanning requirements*.

Block 1. Agency Use Only (Leave blank).

Block 2. Report Date. Full publication date including day, month, and year, if available (e.g. 1 Jan 88). Must cite at least the year.

Block 3. Type of Report and Dates Covered. State whether report is interim, final, etc. If applicable, enter inclusive report dates (e.g. 10 Jan 87 - 30 Jun 88).

Block 4. Title and Subtitle. Title should be taken from the part of the report that provides the most meaningful and complete information. When a report is prepared in more than one volume, repeat the primary title, add volume number, and include subtitle for the specific volume. Classify titles in parentheses.

Block 5. Funding Numbers. To include contract and grant numbers; may include program element number(s), project number(s), task number(s), and work unit number(s). Use the following labels:

C	- Contract	PE	- Program Element
G	- Grant	TA	- Task
PR	- Project	WU	- Work Unit Accession No.

Block 6. Author(s). Name(s) of person(s) responsible for writing the report, performing the research, or credited with the content of the report. If editor or compiler, this should follow the name(s).

Block 7. Performing Organization Name(s) and Address(es). Self-explanatory.

Block 8. Performing Organization Report Number. Enter the unique alphanumeric report number(s) assigned by the organization performing the report.

Block 9. Sponsoring/Monitoring Agency Name(s) and Address(es). Self-explanatory.

Block 10. Sponsoring/Monitoring Agency Report Number. (If known)

Block 11. Supplementary Notes. Enter information not included elsewhere such as: Prepared in cooperation with ...; Trans. of ...; To be published in .... When a report is revised, include a statement whether the new report supersedes or supplements the older report.

Block 12a. Distribution/Availability Statement. Denotes public availability or limitations. Cite any availability to the public. Enter additional limitations or special markings in all capitals (e.g. NOFORN, REL, ITAR).

DOD	See DoDD 5230.24, "Distribution Statements on Technical Documents."
DOE	See authorities.
NASA	See Handbook NHB 2200.2.
NTIS	Leave blank.

Block 12b. Distribution Code.

DOD	- Leave blank.
DOE	- Enter DOE distribution categories from the Standard Distribution for Unclassified Scientific and Technical Reports.
NASA	- Leave blank.
NTIS	- Leave blank.

Block 13. Abstract. Include a brief (*Maximum 200 words*) factual summary of the most significant information contained in the report.

Block 14. Subject Terms. Key words or phrases identifying major subjects in the report.

Block 15. Number of Pages. Enter the total number of pages.

Block 16. Price Code. Enter appropriate price code (*NTIS only*).

Blocks 17. - 19. Security Classifications. Self-explanatory. Enter U.S. Security Classification in accordance with U.S. Security Regulations (i.e., UNCLASSIFIED). If form contains classified information, stamp classification on the top and bottom of the page.

Block 20. Limitation of Abstract. This block must be completed to assign a limitation to the abstract. Enter either UL (unlimited) or SAR (same as report). An entry in this block is necessary if the abstract is to be limited. If blank, the abstract is assumed to be unlimited.

THERMAL ION UPWELLING IN THE HIGH-LATITUDE IONOSPHERE

by

Richard Walter Cannata

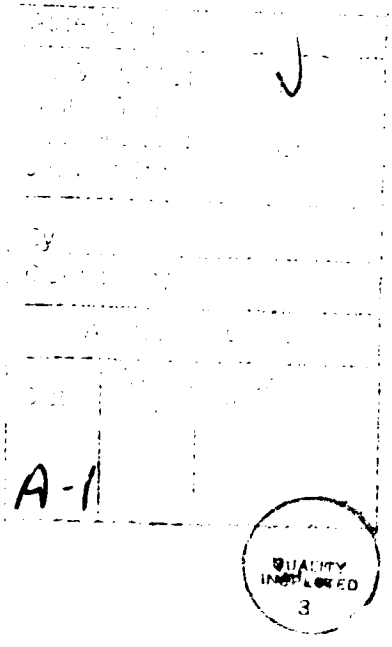

A dissertation submitted in partial fulfillment
of the requirements for the degree of
Doctor of Philosophy
(Atmospheric and Space Sciences)
in The University of Michigan
1990

Doctoral Committee:

Professor Tamas I. Gombosi, Co-Chairman
Professor Timothy L. Killeen, Co-Chairman
Associate Professor Mary L. Brake
Professor Andrew F. Nagy

ABSTRACT

THERMAL ION UPWELLING IN THE HIGH-LATITUDE IONOSPHERE

by

Richard Walter Cannata

Co-chairs: Timothy L. Killeen, Tamas I. Gombosi

High latitude observations of thermal ion outflows, traditionally known as the "polar wind", and heavy ion upwellings, consisting chiefly of heated O^+, suggest that the terrestrial ionosphere acts as an important, and at times, dominant source of ions for the magnetosphere. The topside ionospheric processes responsible for modulating both types of polar ion flows were examined to quantify the magnitudes and compositional variability of steady-state polar wind flows and to identify the role of low-altitude frictional heating in transient heavy ion (O^+) upwellings. Theoretical and experimental approaches were used to elucidate the high-latitude processes that influence ionospheric source strength and transient behavior.

A time-dependent hydrodynamic model was used to examine solar cycle and seasonal dependencies under steady-state assumptions. For solar cycle extremes, H^+ fluxes were found to be invariant with flux-limited magnitudes of 4×10^7 cm^{-2} sec^{-1}. A low speed ambipolar flow of O^+ also occurred, with upward flows increasing from 8×10^6 cm^{-2} sec^{-1} at solar minimum to 9×10^7 cm^{-2} sec^{-1} at solar maximum due to increased EUV, larger atomic oxygen concentrations and reduced molecular loss. Seasonal influences were

found with large wintertime flux variations for both ions caused by ionization source strengths. A marked shift towards O^+ enriched upwellings occurred at solar maximum and for wintertime, at certain noontime locations.

The role of low-altitude ion frictional heating was examined by coupling the National Center for Atmospheric Research -Thermosphere/Ionosphere General Circulation Model (NCAR-TIGCM) to the polar wind model to specify time-dependent frictional heating during a period of observed high-altitude O^+ outflow. Preferential O^+ heating resulted in a factor of four increase in modeled O^+ fluxes, which coincides in both space and time with the observed heavy ion outflows.

Finally, the role of frictional heating and global heating morphology was related to observations of high-altitude ion outflows using Dynamics Explorer-2 satellite data and incoherent scatter radar observations. The locations and dynamic behavior of global frictional heating patterns were found to match well with statistical locations of heavy ion outflows, further suggesting that energization by frictional heating is an important contributing process in initiating transient heavy ion outflows.

"..We turn to our modern theologians, the physical scientists, for words of comfort. They peer beyond the limits of time and space, wrestle with the inadequacies of language, and at last come forth with the answer: the mystery is even bigger than we thought."

Bruce Catton

ACKNOWLEDGMENTS

I decided to write these acknowledgements a few days after my defense, to give me time to step back and view my academic undertaking in full and unhurried perspective. As I reflect back on the experience, I realize that it has been both a deeply personal and, at the same time, a decidedly public, experience. Completing the requirements for this Ph. D. has given me intense satisfaction but in considering my accomplishment, it is clear that my success follows from the many contributions and support by others. In this respect, much of the happiness, excitement and congratulations bestowed upon me following my successful thesis defense must be shared among many. In a sense, each time a Ph. D. is awarded, faculty, staff, students, and the academic process have succeeded and are due special recognition. Therefore, by writing this acknowledgement after-the-fact, I can wax philosophical about the entire process (I've already forgotten the more painful parts) and at the same time, give special recognition to the contributions and achievements of others.

First, I would like to thank Professors Tamas Gombosi and Tim Killeen for their advice, guidance and enthusiasm. It has been inspiring and richly rewarding to work with these two gifted scientists. Professor Gombosi has been ever helpful in creating a learning environment by blending the right amounts of perspiration (mine) and inspiration (usually his). He has also taught me to never take myself to seriously; a philosophy which is quite helpful in surviving the rigors of graduate school. Professor Tim Killeen has been equally helpful by suggesting a number of potential research directions and keeping me in touch with the realities of research. His guidance and assistance has kept me on track and helped me to finish in the allotted time time. He has also taught me to split never my infinitives! Both co-chairs provided extended financial support to allow me to participate in a number of international and stateside scientific conferences. My attendance at these meetings has helped to focus my research and allowed me to interact professionally with others in the same field. At the same time, I would also like to thank my other committee members, Professors Andy Nagy and Mary Brake for their helpful comments and quick-response proofreading of the thesis manuscript. Professor Nagy has a great wealth of corporate knowledge on the subject of ionospheres, and science in general, which has helped me in preparing this thesis. Professor Brake provided me with many of the fundamentals in her

plasma physics course (the first class I took here). Her genuine concern and interest in her students was an excellent introduction into graduate studies at the University of Michigan.

Within the Space Physics Research Lab (SPRL), there were a number of individuals who contributed time and help. Dr Alan Burns, a New Zealand transplant, was extremely helpful throughout the course of my research. First, through his assistance in developing and using software routines for extracting information from the Thermosphere/Ionosphere General Circulation Model and later, for the countless discussions we had about thermospheric and ionospheric processes. Alan was always willing to put aside his work to help me when I needed assistance. Additionally, he would often act as a sounding board for many of my ideas and always had the professional courtesy to forget immediately some of my less flattering theories. Although we agreed on most things in general, I believe much of his happiness was derived from the Kiwi victories in the America's cup and the '89 Whitebread Sailing events. I could often raise a smile in him just by mentioning Dennis Conner's name. A special thanks to Dr Gerry McCormac is also necessary. Gerry provided a number of useful suggestions at the start of my research which later proved to be invaluable. I think a great deal of his enthusiasm for Aeronomy rubbed off on me at the beginning and helped me throughout my research efforts. He returned to his native Ireland in 1989 but somehow I hope he'll return - we need more scientists like him. Finally, I should mention the many helpful discussions and assistance I received from Dr. Janet Kozyra, who explained everything from SAR arcs to Speiser motion, Dr. Roberta Johnson, who guided me through the intricate field of incoherent scatter radar, and Dr. Rick Niciejewski, for several helpful discussions.

I must also thank a number of graduate students throughout this department for useful discussions, advice and opinion. First, my officemates both past and present: Dr Jeff Thayer, Bruno Nardi, Daryl Barlett and Elaine Trudell. The collective office discussions we had were useful and, at times, entertaining depending on the subject matter (those who share a large office with graduate students of diverse backgrounds and interests know exactly what I mean). Other graduate students who had a lasting impression on my experience include, Jhoon Kim (provided simple explanations on complex processes), Junxue Wang (unbounded mathematical insight), Claudia Alexander (always upbeat and able to add common-sense insight into any space plasma problem) and Steve Thomas ("someday this will all be yours"). Steve always had credibility with me until the day he told me he hated Florida (I still shrudder). Finally, I would like to pass on my appreciation to Captains Ken Reese (recently departed for Mt Home AFB in Idaho) and Steve Carr (still laboring in the vineyards of academia for his Ph. D. circa 1990 but I understand 1992 will

be a very good year) for helpful comments on my research and a number of insightful discussions into the socioeconomics and psychodynamics of the Air Force way of life.

The administrative staff here at SPRL also deserves accolades for their role in providing a smoothly running facility, a useful source of skills and resources, and a refreshing family atmosphere within the Lab. Some of those most helpful include Nelly DeMaldenado, Marti Moon, Donna Todd, Jill Belmore, Brenda Gilligan and Lori Kwiecinski. With their continual support I successfully navigated the hazardous waters of Microsoft Word, the Travel Auditors, and Graduate registration. Equally helpful were Jeff Hale (un artiste premier) and Gerry Schmitt, Jeff Hays and Dave Steinbach (although the latter two were ex-Navy, they would rapidly repair my self-inflicted computer problems without disparaging comments about "Air Force officers"). Although they are in no way associated with the SPRL, I should take a moment to thank the Dominos Corporation for their part in delivering the 400 or so pizzas which kept me going on Sunday nights to odd hours, and to James D. Buffett whose stories, melodies and lyrics provided an unending source of relaxation and relief. No matter how stressful or difficult the situation, a short dose of Jimmy Buffet ("Off to See the Lizard", "A Pirate Looks at 40", "One Farticular Harbor", "Boat Drinks" and "Havana Daydreamin'") could restore my perspective on life and strengthen my resolve.

Finally and most importantly, my success is due in large part to my family. My wife, Patricia, has had an even more challenging job than mine: that of raising three young children while managing a household in my absence. We jointly made the decision for my return to school knowing full well what lay in store but I am still amazed at the demands placed upon "family life". It will take a number of years for me to repay her vote of confidence and commitment to my success. I deeply appreciate all that she has given-up for me. My children, although they are unaware of it due to their young age, also provided me with inspiration and relief (" Dad, when you finish school will you get a job ?" and " Dad, do tomatoes have brains?"). Through their daily antics and dialogue, they provided me with continuous, positive diversion and the necessary counterbalance to the rigor of academic life. I hope that they are too young to remember all the weekends they spent without me. In the long run, I know that these short-term sacrifices will pay bigger dividends but it clear to me that without the support of my family, I would not enjoy my present success.

On a more personal level, earning my Ph. D. has allowed me to fulfil one of two lifelong ambitions. My second lifelong goal is a westbound circumnavigation under sail. Although these aspirations seem completely unrelated, they are linked, in my mind, by a common interest in science and the physical environment which connects us all. Even

more importantly, both goals represent undertakings in which the journey, and not the destination, is most important. I look forward to continued success in one and hope to begin the second, soon!

TABLE OF CONTENTS

LIST OF TABLES

LIST OF FIGURES

CHAPTER 1

INTRODUCTION

1.1 Overview

Over the last 20 years, a growing body of observational evidence has accumulated which suggests that the terrestrial ionosphere acts as an important and, at times, dominant source of ions for the magnetosphere (Chappell et al., 1987). The discovery of energetic O^+ ions in the magnetosphere by Shelley et al. (1972) provided the first direct evidence of a probable terrestrial ion source and forced a dramatic reevaluation of our knowledge about plasma sources which populate the magnetosphere. As instrument sensitivity improved, lower energy particle measurements could be made. Based on observations of large field-aligned fluxes of relatively low energy ions leaving the high-latitude ionosphere, the contributions from ionospheric sources were realized to be much greater than previously anticipated. Since 1982, in situ measurements from the Retarding Ion Mass Spectrometer (RIMS) on the Dynamics Explorer-1 (DE-1) identified ions with energies ranging from near spacecraft potential (a few eV) up to 50 eV, thus filling-in a previously unobserved ionospheric supply region of the energy spectrum. In addition to confirming the theoretically predicted polar wind component, the RIMS revealed a strong source of low energy (< few eV) heavy ions which originate from the cleft region (Waite et al., 1985). These flows consist primarily of O^+, however, N^+, N^{++} (Chappell et al., 1982) and even molecular ions (Craven et al., 1985) have also been observed. These recent observations have generated considerable interest in the ionospheric sources and processes leading to such outflows and prompted new theoretical treatments in an area previously thought to be well understood.

Estimates of source region strengths for ionospheric outflows have been made based on both direct and indirect observations leading a number of investigators to propose a major role for terrestrial ion sources. Horwitz (1987) proposed that low energy terrestrial

ions constitute a "core" population of magnetospheric plasma, while Chappell et al. (1987) suggested that the ionosphere is capable of fully populating the magnetosphere to observed densities. These theories implicate the flow of not just mass, but of momentum and energy as well and represent a dramatic reversal from the traditional belief that mass, momentum, and energy transport proceeded from the solar wind towards the Earth only. Even more importantly, the presence of a temporally-changing envelope of terrestrial ions within the magnetosphere suggests that feedback effects, beyond the usual electrodynamic type, might influence energy storage or even substorm initiation and development (Baker et al., 1982; Young 1986). It is clear then that many of the traditional views of near-Earth plasma transport continue to change in light of recent observations of the low-energy component of ion outflows.

1.2 Thesis Objectives

The current revisions in our understanding of high-latitude terrestrial ion transport place great emphasis on understanding the processes by which ionospheric ions are supplied to the near-Earth environment. The research goal of this work is to advance our understanding of polar ion flows by investigating the processes responsible for thermal ion transport in the high-latitude polar ionosphere. In particular, the objectives of this investigation are:

(1) To quantify the magnitudes and compositional variability of steady-state polar wind flows under various solar and geophysical conditions;

(2) To identify the role of low-altitude ion frictional heating in transient heavy ion (O^+) upwellings;

(3) To relate the location, magnitudes and characteristics of low altitude transient upwelling to high-altitude observations of field-aligned ion outflows;

In meeting these objectives, both model calculations and data analysis/interpretation will be used to elucidate the high-latitude processes that influence ionospheric source strength and transient behavior. Throughout this work emphasis is placed on relating each aspect of this research to observations of high-latitude ion outflows.

1.3 Thesis Methods

The central theoretical focus of this research involves the use of a time-dependent hydrodynamic model developed by Gombosi et al. (1985) which is capable of describing polar wind flows. As part of this research, the model was modified to extend its utility to a wide variety of solar and geophysical conditions. The model is then used to investigate

solar cycle, seasonal and local-time variations in composition and source strengths for steady-state polar ion upwellings. Model results in these cases are particularly useful since they are obtained self-consistently from a stationary, partially-ionized ionized gas mixture under the assumption of photochemical equilibrium at the lower model boundary. Predicted variations in flux composition and intensity for each case are related to thermospheric structural changes or solar influences thus providing insight into the fundamental processes responsible for modulating these zeroth-order (steady-state) flows. Comparisons are made between modeled and observed topside densities and fluxes where appropriate to ensure that the important physical processes underlying these upwellings are properly considered in the model and to relate the predicted ion source characteristics to those observed in the magnetosphere.

A second theoretical aspect to this work involves modeling the transient character of heavy ion flows due to ion frictional heating. A number of observational studies have linked this type of energy input to upflowing O^+ events seen by the RIMS on DE-1 (Moore et al, 1986; Waite et al, 1986) but no quantitative modeling efforts have been conducted to identify the role of frictional heating in initiating these events. In this work, a case study is considered using a coupled model approach. The National Center for Atmospheric Research-Thermosphere/Ionosphere General Circulation Model (NCAR-TIGCM) is linked to the polar wind model to specify the time-dependent thermosphere/ionosphere frictional heating and resulting transient O^+ upwellings. These results are then related to observed O^+ upwelling characteristics to identify the role of ion frictional heating. It may appear inconsistent to apply a "polar wind" model to heating locations which are primarily in the auroral zones; however the model approximations are still valid in the auroral zone (i.e., a ambipolar flow of thermal plasma directed upwards) except that additional processes are also present such as particle precipitation, parallel electric fields and field-aligned currents. These add considerable more structure and energy to the plasma but as long as a description of the background polar wind flows are sought and a reasonable electron temperature profile employed, the model can be used for auroral latitudes as well. For this study, an electron temperature profile is derived based on DE-2 measurements taken near the cusp.

In this work, modeling efforts have focused on the dayside polar regions generally described as near the cusp/cleft since this is a particularly strong source region for both light (H^+, He^+) and heavy (O^+) ions based on satellite measurements. In focusing the investigative effort in this location, it is reasonable to question whether some process(es) is actively present which locally enhances terrestrial ion fluxes in this region or whether uniform dayside conditions prevail implying some location-specific, high-altitude "demand" which draws out larger fluxes of ions in this region. This work highlights a

number of important factors which support the former hypothesis and provides quantifiable estimates of the intensity and composition of upwelling ions in this region.

Based on the theoretical behavior of ion frictional heating and transient O^+ upwellings and their relation to higher-altitude outflows, a systematic comparison into the ionospheric signature of frictional heating, ion upwellings and ion outflows is made. This approach relies on measurements from the polar orbiting Dynamics Explorer-2 (DE-2) satellite to provide quantitative information about the plasma response to frictional heating events. Additionally, thousands of measurements are binned and averaged to obtain average global heating patterns, which can be compared to ion outflow patterns obtained through DE-1 measurements. This treatment is designed to qualitatively relate the low-altitude signatures of ion heating to higher-altitude outflows.

In addition to the investigation using satellite observations, a study using ground-based radar measurements is conducted to measure and relate field-aligned ion flows to low altitude Joule heating. This approach permits one to examine the altitude-dependent ion behavior within a flux tube to very high altitudes (~1000 km) while measuring the low attitude frictional heating environment. This experiment was the first ever to attempt such high altitude measurements using the Sondrestrom Radar Facility (aided in part by solar maximum conditions, which helped improve signal strengths from normally unreachable altitudes). Many of the high-altitude observations provided unexpected results, which underscore the inherent dynamic processes that influence the topside ionosphere and remain outside the present-day capabilities of model treatments.

In short, several important processes operating in the polar ionosphere are examined from different perspectives to identify their role and influence on the intensity and character of polar ion upflows. Both the qualitative and quantitative aspects of transient heavy ion upwelling are examined and related to observations of higher-altitude outflows. The results from this investigation will help advance our understanding of the role and importance of terrestrial ions upwelling from the high-latitude ionosphere

1.4 Thesis Results

Both the theoretical and observational aspects of this work offer new insight into the processes surrounding steady-state and transient flows in the topside polar ionosphere. The modeling treatment has the clear advantage of sorting out the complex processes which occur simultaneously at high latitudes, so that the effects of individual processes can be considered.

Under the assumption of steady-state flows, modeled ion upwellings indicate a number of long term changes in composition and intensity are possible due to solar and

thermospheric variability. Over long time scales like the (11-year) solar cycle, H^+ fluxes were found to be invariant however; O^+ flows increased by one order of magnitude from their solar minimum low. These different behaviors were found to arise from structural changes in the thermospheric composition and scale heights, which occur due to increased solar EUV fluxes at solar maximum. Greater O^+ fluxes occur due to increased O^+ number densities, which result from higher photoproduction rates, reduced molecular loss and local increases in neutral oxyger number densities. Opposing changes in the H^+ density and field-aligned flow velocity for the two solar cycle extremes produced near constant fluxes. The distinctive flux behaviors for both H^+ and O^+ produced a marked shift towards an O^+-enriched upwelling at solar maximum. These results match the behavior of higher altitude ion outflows of both energetic O^+ and H^+. Similar solar cycle behavior has also been found in both the O^+ and H^+ plasma sheet densities measured near geosynchronous altitudes (6.6 R_e).

Seasonal behaviors were also considered to evaluate the role of ionization sources. For summer, the dominant and strong influence of solar EUV provides smoothly varying fluxes of H^+ and O^+ across the polar regions. For winter, only a small portion of the ionosphere receives solar illumination so the importance of impact ionization sources due to transient and spatially confined electron precipitation takes on a dominant role. Winter fluxes are found to be highly variable in magnitude and composition based on the ionization history of individual flux tubes. Winter H^+ fluxes vary slightly less than the O^+ fluxes. The latter varied by a factor of 10 for the representative extremes considered in this study.

Finally, local time variations in O^+ and H^+ fluxes were considered by comparing steady-state flux solutions at various local solar times (LST). Along a constant geomagnetic latitude, variations in LST most strongly influenced the flux magnitudes through changes in the solar zenith angle which modify the O^+ photoproduction rates. Variations in both O^+ and H^+ were smaller than in the seasonal and solar cycle cases and for all local times examined for summer solstice, O^+ fluxes remained higher than H^+ flows.

Taken together, these results indicate that O^+ production is a major influence in modulating the character and intensity of steady-state polar ion upwellings. Variations in the modeled O^+ fluxes are most effectively influenced by changes in O^+ number densities which are related, in turn, to solar activity levels, solar zenith angles or, in winter, impact ionization sources. In both summer and winter, the results of this work indicate that a quasi-permanent region of enriched O^+ upwelling is present near local noon due to these factors. This result offers some evidence that an optimum set of thermal ion flow conditions persist in the underlying thermosphere/ionosphere in the same general region where unusually large ion outflows are observed.

The theoretical treatment of transient heavy ion outflows demonstrated the role played by a distributed ion heat source in the lower ionosphere. Ion heating rates were derived from changes in the relative drift velocity of ion and neutral winds brought about by temporal variations in the convection electric field. A Lagrangian representation was adopted to prescribe time dependent ion heating, derived from the TIGCM, in the rest frame of a convecting flux tube. In examining the time-dependent plasma response to low-altitude ion frictional heating, preferential heating of the major ion (O^+) leads to large (a factor of 3-4 increase over steady-state flux) flux transients which shift upwards in the flux tube column on time scales of tens of minutes. Local perturbations in the number density and field-aligned flow velocity of O^+ were noted in response to scale height changes caused by the ion heating. The modeled minor ion, H^+ receives much less of the volumetric heating, so H^+ flows are not affected. These results demonstrate a preferential mechanism which initiates O^+ transient upwellings based not on mass per se, but on relative abundance of species with the dominant (major) ion effected most. Additionally, the model results predict that a period of ion-ion counterstreaming immediately follows the maximum heating period in which O^+ flows downward against the upflowing H^+ as the plasma cools. The coupled model approach was developed for a case study simulation on a day on which an upflowing ion event (UFI) was detected by the DE-1 RIMS. The model simulations predicted a thermal O^+ flux transient at the same altitude and approximate location as observed by RIMS based only on transient ion heating specified by the TIGCM for that day. Comparing the modeled plasma conditions with multi-instrument measurements from DE-1, it is clear that transverse frictional heating cannot provide sufficient energy to match observations. Nevertheless, the initiation of such transient heavy ion fluxes by frictional heating is clearly demonstrated on this day. Further examination of this case, and others, points to a quasi-permanent frictional heating enhancement, which prevails near the convection reversal boundary so that convecting flux tubes experience periods of elevated heating and transient upwellings as they convect first sunward then antisunward across the polar cap. This mechanism, in addition to a universal time variation in the convection electric field were both found to be important in influencing the ion heating rates during the simulation described above. In evaluating the role of frictional heating, the collisional process of frictional heat generation is found to be self-limiting for two reasons. First, very large convective velocities help maintain large relative ion-neutral velocities and produce high heating rates, but at the same time, reduce the duration of heating experienced by the flux tube as it convects across the localized heating source. This behavior suggests that localized regions with persistent directional shears may be more effective at initiating O^+ upwellings than regions experiencing speed shears since longer transit times do not

affect the directional shear. Second, once heated, the ions move upwards out of the region of strongest heating thus limiting the amount of transverse energization that might occur. Together, these factors limit the amount of energy that can be converted from bulk to thermal forms, so that additional energy sources appear necessary in the evolution of thermal ion upwellings into energetic outflows. In summary, this aspect of the study has helped identify the role of frictional heating in initiating transient upwelling of ions and further underscores the unique conditions which persist in the dayside cusp/cleft region that act to locally increase transient flows.

In the data analysis section of this work, the morphology of frictional heating was examined more closely and related to higher altitude upflowing ion events (UFI). In particular, multi-instrumented observations by DE-2 were used to derive frictional heating rates along the satellite track. The derived rates are somewhat larger than the model-derived rates due to the coarse spatial resolution of the model and exhibit considerably more spatial structure than the models can describe. Typical heating enhancements occur on horizontal scales of 10's to 100's of kilometers in latitude. Increases in heating rate magnitude by a factor of 5 to 10 are commonly seen . Two distinct types of frictional heating regions were identified, one corresponding to the dawn (and to a lesser degree, the dusk) convection channel, where speed shears persist due to entrainment of low momentum neutral particles into an area of high ion velocities. A second region occurs near the cusp/cleft area, where semi-permanent directional shears persist due to the strong spatial gradients in the ion velocity vector. Derived ion frictional heating rates were compared to the ion internal energy (3/2 kT) to quantify a heating time scale. Typically, the ions are found to experience an energy gain equal to their internal energy every 2-5 minutes (discounting cooling). However, within the regions of strong heating, this time decreases to a few seconds, suggesting that the plasma response to heating will occur almost simultaneously with the heating increase. Despite the very large rates of frictional heating sometimes seen, the bulk ion temperature remains below a few eV (<30,000 K), suggesting that most of the ions have insufficient energy to overcome gravity and escape. Very large, 100-fold enhancement in upwelling plasma are sometimes seen in these heating regions, but cannot be fully attributed to frictional heating alone, because the strongest heating generally falls at or near the auroral boundary, where particle precipitation and field-aligned currents may also contribute heating. Likewise, large, downward directed fluxes are observed and appear to be related to post-heating relaxation as the plasma cools to background temperatures.

An extensive set of ionospheric plasma measurements, taken during multiple orbits across the polar latitudes were combined to obtain patterns of average global heating for

low and moderate levels of geomagnetic activity. Heating magnitudes were found to increase significantly with larger Kp (a 3-hour global index of geomagnetic disturbance level) as the relative ion-neutral velocity difference increased. At the same time, the areas of strongest heating tended to expand and shift equatorwards. Asymmetric heating patterns along the local noon-midnight magnetic meridian were evident with the dawn side receiving greater heating. Both the magnitude and locations of ion frictional heating were examined for low and moderate levels of activity and were found to exhibit the same behavior as the UFI occurrence frequencies measured by the energetic ion mass spectrometer (EICS) on DE-1.

Simultaneous observations along the same field line using incoherent scatter radar also suggest that frictional heating in the lower F-region plays a role in evolving plasma upwellings, but the radar data were inconclusive in some respects because large transient upwellings were found at times where frictional heating was not varying significantly. The large spatial integrations necessary to compute frictional heating, taken over relatively long periods reduced the ability of the radar to resolve the time-dependent electric fields associated with transient heating enhancements. This would act to reduce correlations between heating rate increases and ion upwellings. For this study, positive correlations between heating and upwelling fluxes were strongest, but only for long-term averages of 60 minutes. Correlations ran from 0.42 to 0.85 depending on altitude, while a model simulation showed consistently higher correlation (0.75 to 0.83) at all altitudes using 15-minute or 30-minute averages. Despite these limitations, several conclusions can be made concerning these radar observations. First, it is difficult to make high-altitude radar measurements in conjunction with observations of low-altitude heating, since the long integration periods needed to boost signal strength tend to limit the temporal resolution of the low-altitude measurements. This tends to destroy the coherence between the ion heating signal and plasma response since both processes are evaluated over different time intervals. Second, given the wide variance in observed field-aligned flows, it appears that ion motion can be strongly influenced by other, unmeasured processes such as precipitation. Heating due to energy deposition by precipitating particles was not characterized in this study, but would certainly affect topside ion motions. Finally, for one day in which heating and auroral activity was at an extreme low, a steady transition from up and down ion flows to predominantly upward motion was detected as the local time of observation moved from pre-dawn to local noon, suggesting that EUV heating helps to organize a diurnal pattern with upward flows in the daytime and subsidence in the night. This same general pattern has been observed in the DE-2 vertical ion drifts by Loranc (1989).

In summary, this research identified a number of ionospheric processes which are influential in modulating the composition and intensity of polar wind flows. Additionally this work identified a quasi-permanent region of enhanced ion upwelling near the dayside cusp/cleft where both modeled ion fluxes were at a maximum, independent of any "topside demand" other than the nominal pressure gradient which exists along open flux tubes. Finally, average patterns of low-altitude frictional heating appear to match well with the occurrence frequency for upward flowing ions, suggesting that this form of heating is an important influence in the dynamics of the topside ionosphere and in initiating transient upflows of heavy ions.

1.5 Historical Perspective: Theory of the Polar Wind

The earliest suggestion that ionospheric ions might be able to escape the Earth's gravitational field can be traced to the models of the Earth's magnetosphere which developed in the early 1960's. At that time, it was recognized that the interaction of the high speed solar wind with the Earth's dipole magnetic field acted as a dynamo to drive an intense current system. These currents act to compress the sunward portion of the field and stretch it into a long comet-like tail on the antisunward side. The vast region of space dominated by these field lines was called the magnetosphere (Axford and Hines, 1961; Dungey, 1961). Conflicting theories developed about whether the magnetosphere was "closed" or "opened". In a closed system, it was suggested that field lines would not merge to the solar wind magnetic field so that plasmas of terrestrial and solar origins would not mix. The open model (Dungey, 1961) allowed for convection and plasma transport due to magnetic reconnection of fields which threaded the two plasmas. Gradually, the open model gained widest acceptance but not before a great deal of heated debate

The role of ionospheric plasmas was primarily dependent on which magnetospheric model one adopted. The Axford and Hines model of a closed magnetosphere considered an ionosphere that enveloped the Earth as a dense passive medium, absorbing solar particle precipitations and EUV, fluxes while maintaining approximate hydrostatic equilibrium. This view placed the primary direction of mass and energy flow as being Earthward with the ionosphere gaining small amounts of mass but large amounts of energy of solar origin. Dungey's (1961) proposal that geomagnetic field lines rooted in the polar ionosphere could reconnect at the magnetosphere boundary with the field embedded in the solar wind emphasized a more active ionospheric role. His theory implied that the solar wind plasma could mix with terrestrial plasma along these open field lines to prevent equilibrium from developing in the polar regions. Based on whistler data which indicated reduced densities it the outer magnetosphere, Dungey reasoned that plasma was being lost to the solar wind

along the opened field lines. This outward flow, he reasoned would populate the magnetosphere with plasma of terrestrial origin. In this sense, Dungey's view was far ahead of its time.

To account for the observed sharp drop in cold plasma density at the plasmapause, Nishida (1967) extended Dungey's hypothesis by considering the behavior of plasma circulation within the magnetosphere. Newly opened flux tubes would exhaust their contents to the solar wind as they convected antisunward across the polar cap. Refilling from below with terrestrial plasma would take place, but only after the flux tube had convected Earthward again. The plasmapause was the boundary between flux tubes which had been opened and were in various stages of refilling and flux tubes which remained closed and contained higher densities. The different populations of flux tubes were defined by whether they "corotated", and remained closed, or "convected", in which case densities were depleted when the flux tube opened. Brice (1967) proposed an alternative theory to the plasmapause location in which the corotation boundary defined hot solar plasma and cold terrestrial plasma. The former entered the magnetosphere and circulated throughout the convection regions to establish a new equilibrium in which backpressure from the overlying hot plasma confined the ionosphere to low altitudes and prevented escape. Both the convection/loss model of Nashida and the convection/hot plasma model of Brice helped to establish a separation of views on ionospheric and magnetospheric plasma as either cold (ionospheric) or hot (magnetospheric) in which sources were considered independent of their characteristic energies.

Bauer (1966) and Dessler and Michel (1966) argued that since the geomagnetic field lines, which form the magnetotail, originate in the Earth's polar regions and since the pressure is greater in the ionosphere than in the tail, a continual escape of thermal plasma would be possible along the open field lines. Motivated by the problems of thermal evaporative escape of terrestrial H and He, Axford (1968) proposed an escape mechanism for ionospheric H^+ and He^+ which operated at high latitudes, thus allowing him to reconcile underestimated losses of H and He. According to his theory, important ion species in the high latitude ionosphere included light and heavy ions. The larger scale height of the electrons compared to the heavy ions (O^+, O^{++}, NO^+) and the constraint of charge neutrality creates an upward directed electric field. Light ions (H^+, He^+) respond to this field and are accelerated upwards, where escaping photoelectrons permit these lighter ions to escape. Later, it was argued that the role of photoelectrons was unimportant and that the charge separation field was sufficient to drive out the light ions. This escape was termed the polar wind in analogy to the solar wind. A consequence of this flow is that the mean ionic mass at a given altitude would be greater than at lower latitudes due to the

escape of light ions. Detailed treatments of the polar wind soon followed by Banks and Holzer (1968, 1969). Their theory predicted supersonic bulk outflow and a significant decrease in scale heights of the light ion species which were driven by the nonequilibrium pressure gradient along the field lines at high latitudes. Along field lines where this plasma gradient was reduced, the flow could be subsonic ("polar breeze"); however, Banks and Holzer argued that estimates of the solar wind thermal pressure were low enough so that a supersonic solution, at the limiting flux predicted by Hanson and Patterson (1963), was the only correct one for the terrestrial polar wind. Since their polar wind model was based on the convection/loss model by Nishida, observational confirmation became a key test for the "open" magnetospheric model as well as terrestrial ion escape.

1.6 Historical Perspective: Observations of Polar Ion Upflows

Direct measurements of the upward flow of light ions from the Earth's polar ionosphere were first made by Hoffman (1970) using observations from the mass spectrometer on Explorer 31. Data from the spinning satellite were roll-modulated with the concentration peaks between H^+ and O^+ separated by a constant phase angle during measurements over the polar regions. This phase angle was interpreted as an upward directed H^+ flow through a stationary O^+ background. Subsequent measurements by Brinton et al. (1971) and Hoffman et al. (1974) indicated the correctness of polar wind theory in that low densities, low pressures and an upward flow of light ions was present across the polar latitudes. Direct confirmation of the supersonic nature of the polar wind flow was not made until much later however when Nagai et al. (1984) observed supersonic H^+ and He^+ ions with temperatures <5 eV flowing along polar cap field lines.

Up to about 1980, there appears to be reasonable agreement between the light ion ambipolar flow described by Axford and Banks and Holzer, and the observations cited above. There has, however, been a growing body of observational evidence indicating the presence of additional upflowing ions in the polar regions, which can be heavier than the polar wind component and appear heated, suggesting there are additional sources of terrestrial ions to populate the magnetosphere. These ion flows are distinguishable from the polar wind (classic) component by both mass and characteristic energy and are sometimes referred to as the non-classic polar ion flows. These non-classical ion flows will be briefly described next in their context of transport in the polar latitudes.

Shelley et al., (1972) was the first to report in situ measurements of energetic terrestrial ions in the magnetosphere. Their mass-to-charge measurements taken during a geomagnetic storm found ions with m/q of 16 (presumably O^+ and some N^+) precipitating in the low altitude nightside auroral region. The ratio of heavy ion density to the local H^+

number density was greater than the solar wind value so an ionospheric origin was inferred. A number of subsequent measurements indicated that the hot magnetospheric plasma contains significant quantities of O^+ (Lundin et al., 1982; Balsiger et al., 1980; Lennartsen and Shelley, 1986). Further studies by Sharp et al. (1977), Ghielmetti et al. (1978) and Gorney (1981) showed that ionospheric ions could be energized to far above thermal energies and flow upward in the auroral zones. These energetic flows are outside the perview of this research and will not be considered further. The cooler or slightly heated ion component, flowing upward while convecting horizontally across the polar cap and embedded in the polar wind flows, is more relevant however.

As the low-end energy threshold of mass analyzers and particle detectors improved with instrument sophistication, the role of ionospheric plasma in the magnetosphere has gained increased recognition. The term core plasma has been introduced (Horowitz 1987) to refer to plasma populations with energies less than 50 eV because the term reflects both a significance in number density as well as the position occupied in a velocity phase-space diagram. Shelley et al. (1982) reported observations from the EICS on DE-1 of predominantly O^+ upward fluxes in the polar cap. These ions had a temperature of about 3 eV and a bulk flow speed of 46 eV. They felt that the cold, less energetic ions comprising the polar wind could not gain entry into the detector due to the positive spacecraft potential so that these measurements represented an upward flux from an ionospheric source. Yau et al. (1984) conducted a statistical study of ion outflows across the polar cap using EICS data from DE-1 and found that the occurrence frequency of upward flowing ions, or UFI "events", across the polar cap was as large as 0.33 for O^+. Here, the term UFI connotates escaping fluxes because the lower energy range of the measurements exceeded 10 eV. Lower altitude observations of O^+ have also confirmed the importance of these flows and underscore the presence of a large ionospheric source of core plasma.

The RIMS instrument on DE-2 permitted a more detailed analysis of core plasma since it covered the energy range of 0-50 eV and performs pitch angle measurements. A wide variety of distributions were found and have been described in detail by Chappell et al. (1982) and Moore et al. (1985). On the dayside at high altitudes, Moore et al. (1985) found field-aligned flows that were sometimes dominated by O^+ and showed evidence of mass and energy dispersion as they were convected across the polar cap. These upward flowing ions had energies of < 30 eV with the majority having less than 2 eV. Those with energies less than the gravitational binding energy (about 10 eV) could be convected to the nightside and become a possible source of low energy ions for the nightside auroral regions and eventually become transported to other parts of the magnetosphere. Those with greater than 10 eV could escape directly. Waite et al. (1985) combined measurements from both

the DE-1 and DE-2 and found large outflows of 2-8 eV O^+, with a small percentage of N^+, over the polar cap during active geomagnetic conditions. These O^+ distributions were found to have temperatures of 2000-5000 K suggesting a cold thermal ionospheric source with altitude corrected fluxes of about $5\text{-}10 \times 10^7$ cm^{-2} sec^{-1}. Waite used the derived electric field from the DE-2 ion drift meter to convection map these field-aligned flows back to to a spatially-confined region centered near the dayside cusp/cleft areas. This result suggested that the low and high altitude RIMS measurements were related and that O^+ ions were flowing out of a confined dayside location and were drifting antisunward at the same time, embedded in the polar wind flows. Lockwood et al. (1985) found that the upflowing ions were chiefly O^+ although H^+, He^+ , O^{++}, and N^+ were also found. All ion species appear to participate in roughly equal ion heating with typical parallel and perpendicular temperatures of 2 and 10 eV respectively. These ions were given the name upwelling ions (UWI) since they may or may not escape. The roughly equal heating of the various ion species implies that their field-aligned flow velocities are inversely proportional to the square of their mass. The resulting mass dependent ion velocity, in combination with the horizontal convection away from the localized source region, results in a dispersion of these ions by mass and velocity as they convect across the polar cap (Figure 1.1). The effect has been called the geomagnetic mass spectrometer and results in the lowest energy and highest mass ions extending furthest towards the nightside from the cusp/cleft region so that O^+ is often observed across large regions of the polar cap.

The upwelling source region identified using DE-2 RIMS data has been termed the cleft ion fountain by Lockwood (1985) in analogy to a water fountain blowing in the wind. Statistical analysis by Lockwood (1985) indicates that the source region for this fountain could be convection mapped back to a dayside latitude band between 75° and 80° invariant. This further supports the view that the dayside cusp/cleft region is a large and persistent source of core plasma. Lockwood (1985) concludes that, based on observed densities and flow velocities, O^+ UWI fluxes are on the order of 10^8 ions cm^{-2} sec^{-1} at 2.5 Re which corresponds to about 10^9 cm^{-2} sec^{-1} at 1000 km when corrected for the change in flux tube area.

Heelis et al. (1984) has also reported large ion fluxes ($> 10^{10}$ cm^{-2} sec^{-1}) in the vicinity of dayside field-aligned currents at altitudes as low as 900 km based on DE-2 data. Charge exchange between O^+ and H supplies the escaping H^+ flux of the polar wind, so this mechanism can account for observed O^+ fluxes on the order of 10^8 cm^{-2} sec^{-1}.

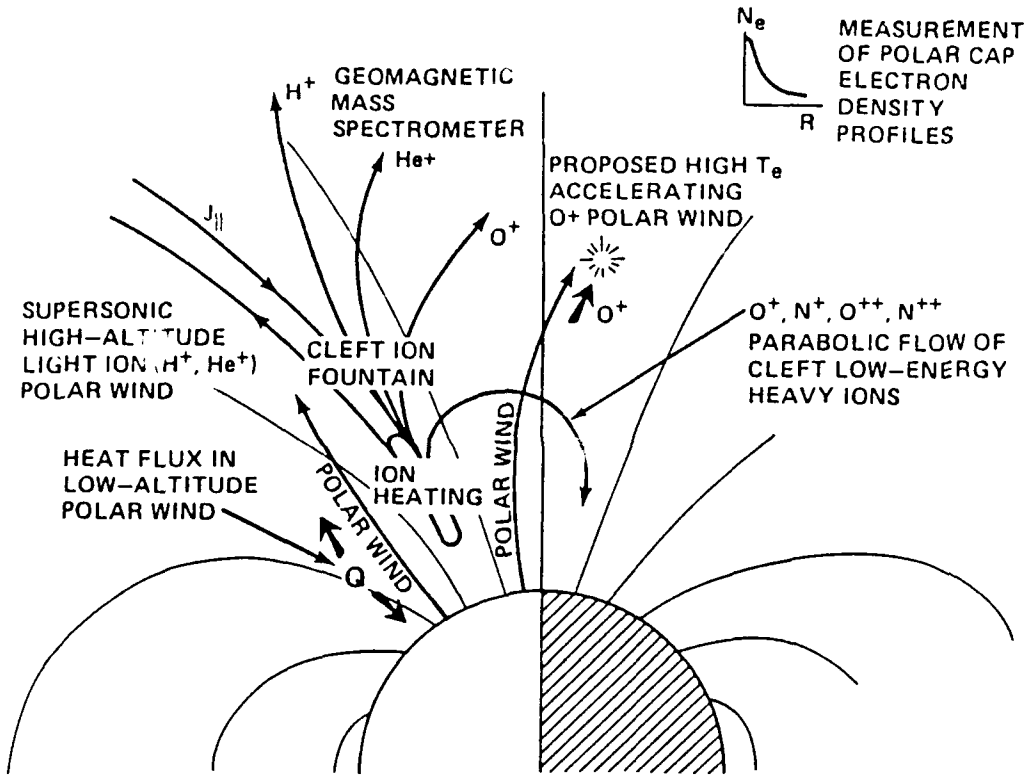

Figure 1.1 Schematic representation of the various polar ion flows and source region terminology. Both the classic polar wind, and non-classic, ion upwelling fluxes are illustrated. The superposition of these flows, due to antisunward convection of magnetic flux tubes, results in a combined flux of cold thermal ions and a heated ion component over the high-latitude ionosphere (after Horwitz, 1987).

Since the observed flux exceeded the charge exchange flux by a factor of 100, Heelis et al. (1984) reasoned that some mechanism must be operating at or above the the satellite to provide escape energy to a large part of this thermal O^+. Field-aligned currents of 100 μA m^{-2}, large gradients in the horizontal thermal drift, and enhanced fluxes of <300 eV precipitating electrons were also detected so a number of free energy sources are potentially involved. Waite et al. (1985) and Moore et al. (1986) have evaluated a number of possible energization mechanisms. Both conclude that the close correspondence between O^+ heating in UWI events and their coincident location near convection jets is highly suggestive of a collisional or Joule heating process. Lockwood et al. (1985) propose that the observed UWI signature is observed above the low altitude heating region only when the thermal ion flows are no longer collisionally bound. Most recently, Loranc (1989) showed that regions of average upward and downward ion drifts can be statistically identified in the DE-2 IDM data. The regions of upward drifts compare favorably with the statistical locations of the auroral zone, the boundary plasma sheet electron precipitation and

field-aligned current systems suggesting that topside ionospheric processes are closely tied to UWI and their higher altitude (and more energetic) UFI counterparts.

One historical difficulty in tracing the location and strengths of terrestrial ion upflows has been the difficulty in measuring the lowest energy component of the core plasma. As a result of photoelectric effect (solar radiation removes electrons from the spacecraft surface), the spacecraft charges positively and this floating potential obscures much of the ionic component below 10 eV. This problem is most acute in sunlit regions where densities are less than 50 cm^{-3} (Olsen, 1982), but can be circumvented to some degree by the application of an instrument aperture bias. By carefully stepping through a negative bias setting, a zero potential should occur near the aperture. However, this technique fails when the positive spacecraft potential exceeds the bias setting. Consequently, in situ measurements probably do not reflect some "invisible" low energy component, most likely of ionospheric origin, which may often dominate the local density and therefore plasma origin (Chappell et al., 1987). Even the simple technique of discriminating between solar or terrestrial origin can be ambiguous. It is possible, in theory at least, to infer the the origin of magnetospheric ions by considering the charge state and the ratios of local H^+ and O^+ number densities. Unfortunately, mass selective energization of ionospheric ions and charge exchange with the hydrogen geocorona tend to blur this distinction (c.f. Chappell et al., 1987). Furthermore, H^+ ions "look" the same irrespective of a solar or terrestrial source. As a result of these limitations, it has been difficult to establish fully the source strength and character of the lowest energy, thermal component of upwelling ions.

Given the sparse nature of polar wind measurements and the limitations in observing thermal upwellings described above, the role of modeling takes on added importance. Through the efforts presented here, both the thermal composition, character and behavior of polar wind flows will be examined. Furthermore, the unambiguous role of frictional heating in association with horizontal convection jets can be identified as it pertains to transient heavy ion upwelling events.

1.7 The High-Latitude Ionosphere: Working Definition

From the previous section which traces the historical development of theory and observations of polar ion flows, it is apparent that the high-latitude ionosphere is considerably more complex than other portions of the ionosphere. In the lower latitude ionosphere, magnetic contact with the plasmasphere is continually made and shielding from the convection field is nearly complete so that field line merging and convection do not occur. The high-latitude ionosphere, for the purposes of this work, is defined as that

region of invariant latitudes where, at least some of the time, the plasma may flow along flux tubes which have one foot in the ground or are so distorted and tail-like that connection in the conjugate hemisphere has little effect on the local plasma behavior. From a statistical consideration of the convection pattern, this definition includes latitudes poleward of about 50° invariant. The vertical definition of the ionosphere is somewhat more problematic since a number of definitions have been advanced, usually in context of the particular phenomenon being studied. In following this example, a vertical definition for this work is adopted which extends from the lower F-region (about 150 km) to several thousand kilometers (say 8000 km). This definition allows one to consider the polar ion flows as ionospheric in nature rather than resorting to terms like lower magnetosphere (probably more correct) or near-Earth. When considering the vertical transport of ions, ions which have escape velocities (for example, 10 eV for O^+ at 150 km) the term outflow will be used. Terms such as upwelling, upflowing and upward will be reserved for ions which exihibit field-aligned upward motion but have insufficient energy to overcome gravity. In the fluid sense, some portion of the distribution probably does, but the majority of these particles trace out parabolic or hopping trajectories (c.f., Horiwitz, 1987). Although horizontal ion drifts in the high-latitude regions are generally larger than the vertical flows, it is the field-aligned motions that are of interest to this work and will be considered next.

In placing the field-aligned ion fluxes in the polar regions in the broader context of the magnetosphere, it is useful and valid to consider the geomagnetic field line topology threading this immense volume of space. Plasma transport through out the magnetosphere-ionosphere system is governed by convection and field-aligned flows with plasma moving with the field lines due to the high conductivity of the medium. Figure 1.2 illustrates the various regions of the magnetosphere which are organized by particle types and field line geometry.

The high-latitude ionosphere communicates with a large portion of the magnetospheric volume in an electrodynamic sense through field-aligned currents and particles transport. The outermost region, known as the magnetopause, represents a boundary layer separating the solar wind plasma and magnetosphere plasma. On the dayside, distinct regions of this layer are defined by their different plasma characteristics (the low latitude boundary layer, entry layer and plasma mantle). In all cases however, the magnetopause boundary layer contains shocked solar wind particles and, depending on location, some terrestrial ions as well. Field lines threading the highest polar latitudes in the ionosphere map out to the plasma mantle, a volume containing both magnetosheath ions and electrons of solar origin, and terrestrial upflowing ions. The mantle region is less dense than the magnetosheath in number density and grows in volume as one moves

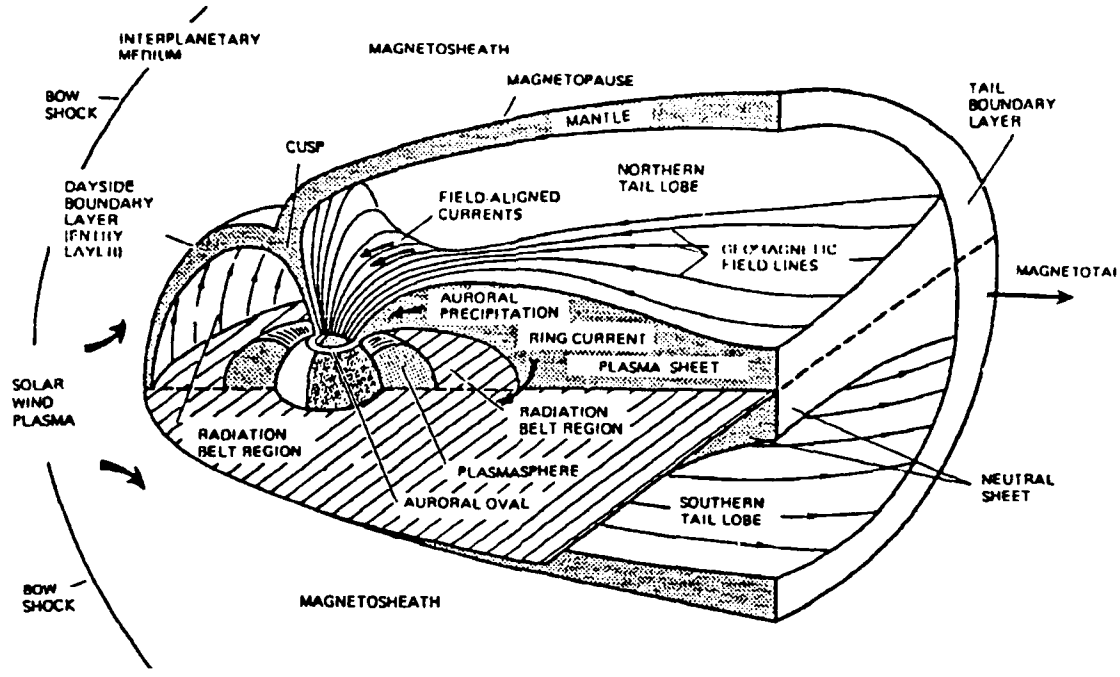

Figure 1.2 Schematic illustration of the magnetosphere (from Kelley, 1989)

down the magnetotail. At some point, the open field lines from each hemisphere of the mantle are near enough to merge magnetically resulting in a region of heated plasma known as the plasma sheet. Ions flowing out of the ionosphere on polar field lines can therefore be lost to the interplanetary medium, or, become transported inward to the inner plasma sheet following tail reconnection. At slightly lower ionospheric latitudes, a narrow region of field lines delineate the cusp footprint. This region is generally thought to extend over some 2-3 hours of magnetic local time and about 1° of latitudinal width. The equatorial edge is statistically located between 72°-78° although the exact location and size of the cusp footprint depends on the orientation of the interplanetary magnetic field which in turn, dictates the field line merging geometries at the dayside magnetopause. Cusp fieldlines map outward in funnel shape to the dayside boundary layer and the magnetosheath. The cusps are particularily interesting features in that several processes involving the ionosphere take place there. First, there is a strong and highly variable current system which flows across the magnetopause and closes down in the ionosphere through field aligned currents. Second, the entire magnetospheric boundary layer maps into this small ionospheric region so that dayside magnetosheath plasma, composed of solar wind H^+ and He^+, has direct access to the ionosphere. These processes transfer both mass and momentum from the magnetosheath to the ionosphere. Transfer into the ionosphere also implies the possibility

of the reverse process. It is not suprising then that several investigators have reported the presence of terrestrial O^+ in the exterior cusp and surrounding plasma mantle (Frank, 1977; Lundin, 1985; Peterson, 1982). The flanks of the cusp give way to a region known as the cleft although the precise location as well as the definition tends to vary. The cleft is a region of large electron fluxes of relatively low energy (<500 eV) electrons which maps around the periphery of the dayside boundary between open field lines and lines connected to the low latitude boundary layer. Again, entry of shocked solar wind particles occurs in this region as well as terrestrial outflows into the mantle and boundary layers. The connections between the ionosphere and magnetosphere are illustrated in Figure 1.3. The presence of terrestrial ions, transported along field lines to various volumes within the magnetosphere, represents an important new plasma source for the magnetosphere and suggests that the transfer of mass and momentum must work in two directions.

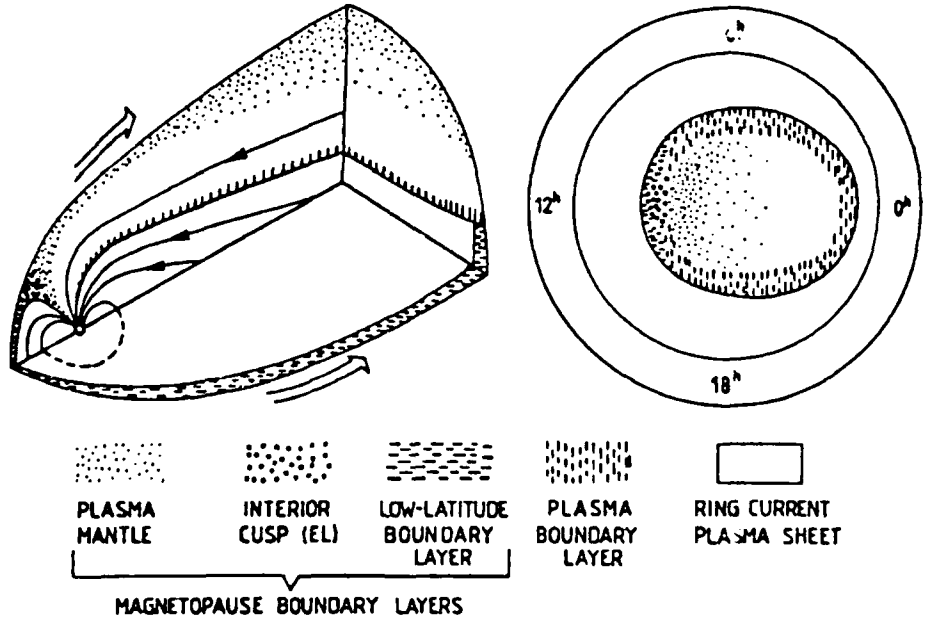

Figure 1.3 Schematic diagram of the regions occupied by the various magnetospheric boundary layers (left) and their ionospheric counterparts (right) based on mapping along geomagnetic field lines (after Vasylinas, 1979).

1.8 Polar Wind Theory

In this section, the basic physics behind polar wind flows is developed as background for understanding the theoretical aspects of this research. Additionally,

working definitions are provided in this description, which will be adopted throughout this thesis. The theory behind UWI flows is not presented beyond what was descibed above since no comprehensive theory has yet to be worked out on the energization process(es). There are a number of time-dependent modeling treatments which suggest possible mechanisms but a description of these treatments is deferred until later.

The classic polar wind is an ambipolar outflow of thermal plasma from the topside ionosphere. By definition, the flow consists of H^+ and He^+, but this definition will be broadened somewhat in this work to include the thermal O^+ component, because it also flows upwards, but at a much lower velocity. In the course of moving outward along essentially radially-divergent field lines, these ions experience four major transitions. The first occurs in the F-region where chemical dominance gives way to diffusive dominance at the F-region peak. Another transition takes place between 800 km and 2000 km when the

Polar Wind Aeronomy		
alt. (km)	**feature**	**dependence**
>2000-3000	thermal anisotropies **collisionless flows**	collisions ion densities, T_i, T_e
800-2000	**transonic flows**	mass, T_i, T_e, T_n
< 2000	collision-dominated flows coulomb collisions binary elastic collisions	 ion densities, T_i, T_e neutral densities, T_i, T_e
200-2000	**charge exchange**	neutral & ion chemistry, T_n
150-400	**chemistry/diffusion dominance**	time constants for reactions and transport
150-250	max O^+ photoproduction	solar EUV neutral density (T_n)

Table 1.1 Summary of the physical and chemical influences and their dominant locations for the major transitions (in bold) involved in polar wind flows.

light ion flows increase from subsonic to supersonic. The exact altitude differs for each ion and is influenced by both ion and neutral densities through binary and elastic collisions. A third transition occurs over a wide altitude region when charge exchange with O^+ creates a

light ion out of atomic hydrogen. Finally, the last major transition for the polar wind occurs as the ions move from collisional to collisionless regimes. Again, the exact altitude differs for each ion, but the transition region is usually defined when the time taken to travel one ion scale height is equal to the inverse of the collision frequency. In each of these cases, a number of interrelated factors can influence transition location and outcome. The major processes and their dependencies are summarized in Table 1.1.

A fundamental process in polar wind flows involves the interaction which develops between major and minor ion species under the influence of gravity and pressure gradients. Consider the simplest case of a quasi-neutral plasma consisting of a single ion species and electrons, each with different temperatures, T_e, and T_i, under the influence of gravity and a pressure gradient. The electrons tend to diffuse more rapidly than the ions due to their greater mobility and in doing so, set up a small space charge and electric field which acts to slow them down. This field also acts in the opposite direction to speed up the ions. This polarization field is known as the ambipolar electric field and plays an important role in modifying the ion number density distribution and accelerating light ions to create the classic polar wind.

To illustrate the effects of the ambipolar electric field on diffusion in the topside ionosphere, consider the following simplifying assumptions:

1) The geomagnetic field lines are vertical so that horizontal drifts are negligible.
2) Steady state conditions exist.
3) Initial flow speed is subsonic.
4) Heat flow is negligible.
5) Charge neutrality exists and no field aligned currents exist.
6) Pressure is isotropic.

With these assumptions, the ion momentum equation for motion along the magnetic field (**B**) is:

$$\frac{\partial P_i}{\partial z} + n_i m_i g - e n_i E = -n_i m_i \upsilon_{in}\left(u_n - u_i\right) \qquad (1.1)$$

when g is gravity; E, the polarization electric field; z, the vertical direction; ν_{in}, the collisional frequency between ions and neutral; e, the electronic charge; $n_i m_i$, the mass density of ion species i and u_i the vertical drift velocity. The electric field can be expressed in terms of the electron momentum equation after neglecting the collisional and gravitational terms since they involve the electron mass which is very small. Under these assumptions, the electron momentum equation reduces to:

$$en_iE = -\frac{1}{n_e}\frac{\partial P_e}{\partial z} \tag{1.2}$$

where the e subscript refers to electrons. Combining equations 1.1 and 1.2 and expressing the pressure gradient terms one obtains:

$$u_i = -D_a\left[\left(\frac{1}{n_i}\right)\frac{\partial n_i}{\partial z} + \left(\frac{1}{T_p}\right)\frac{\partial T_p}{\partial z} + \frac{1}{H_p}\right] \tag{1.3}$$

where: D_a = ambipolar diffusion coefficient = $K(T_e + T_i)/m_i\nu_{in}$

H_p = Plasma scale height = $2\,kT_p/m_ig$

T_p = plasma temperature = $(T_e + T_i)/2$

Equation 1.3 is very similar to the standard diffusion equation for a neutral gas under the influence of a pressure gradient and gravity, except that the presence of the ambipolar electric field modifies the diffusion coefficient and plasma scale height. If electrons and ions have the same temperatures, these expressions show that the ambipolar diffusion coefficient and the plasma scale height are each twice as large as the corresponding quantities in a neutral gas having the same mass. The electrons have exerted their more mobile influence through the electric field, so that the resulting velocity and scale heights are doubled. This electric field is quite small in the ionosphere and is determined by equating gravity with the electric field. One obtains $E=m_ig/2e$ which works out to about 10^{-6} V/m. Equation 1.3 can be rewritten as:

$$\left(\frac{1}{n_i}\right)\frac{\partial n_i}{\partial z} = -\frac{1}{H_p} - \left(\frac{1}{T_p}\right)\frac{\partial T_p}{\partial z} - \frac{u_i}{D_a} \tag{1.4}$$

under the assumption that diffusion dominates above the F-region peak due to a rapid increase in D_a with altitude. For an isothermal ionosphere when $T_e = T_i$ the equation reduces to:

$$\left(\frac{1}{n_i}\right)\frac{\partial n_i}{\partial z} = -\frac{1}{H_p} \tag{1.5}$$

By neglecting the variation of gravity with altitude, this expression can be integrated to:

$$n_i = n_{io}\exp\left(\frac{-(z - z_o)}{H_p}\right) \tag{1.6}$$

where the subscript "o" refers to some fiducial level. Equation 1.6 indicates that ions will tend to distribute themselves according to a plasma scale height. Physically, the ions and electrons are influenced by gravity and gradients in density and temperature. Since the electrons are much lighter, the ions tend to settle below them setting up a polarization electric field. This field acts to prevent further separation and forces the ions and electrons to move together under the influence mentioned above. With a multi-constituent ion plasma, the major ionic component acts to set up the polarization electric field which the minor species respond to. Due to the open-field line topology in the polar ionosphere, minor ions can be accelerated to high speeds in a direction parallel to the geomagnetic field to form the polar wind.

The basic features for low speed minor ion outflows can be illustrated by considering a multi-component ion plasma under ambipolar diffusion. The continuity and momentum equations are used for this purpose after the following assumptions:

1) The flow is field-aligned and vertical.
2) production and losses are not significant.
3) H^+ and He^+ are minor ions (subscript x).
4) O^+ is the major with $n_e = n_i \approx [O^+]$.
5) Collisions between with the major and minor ions only occur through the long range nature of Coulomb force. Collisions with neutrals are ignored.

Considering a steady state, subsonic flow, the minor ion continuity and momentum equations are:

$$\frac{\partial(n_x u_x)}{\partial z} = 0 \tag{1.7}$$

$$\frac{\partial P_x}{\partial z} + n_x m\, g - e_x n_x E = -n_x m_x \upsilon_{xi}(u_i - u_x) \tag{1.8}$$

where E is the electric field vector set up by the major ion (O^+) and electrons. Equation 1.7 can be integrated over altitude to show that the flux, $n_X v_X$, is a conserved quantity that is ultimately determined by chemical processes taking place at lower altitudes. Rewriting the pressure term and expressing equation 1.8 in terms of the minor ion velocity yields:

$$u_x = u_i - D_x\left[\left(\frac{1}{n_x}\right)\frac{\partial n_x}{\partial z} + \left(\frac{1}{T_x}\right)\frac{\partial T_x}{\partial z} - \frac{eE}{kT_x} + \frac{1}{H_x}\right] \tag{1.9}$$

where the minor ion diffusion coefficient and scale height are given by:

$$D_x = \frac{KT_x}{m_x \upsilon_{xi}} \qquad H_x = \frac{KT_x}{m_x g}$$

Equation 1.9 indicates how the presence of a major ion modifies the minor ion behavior in three ways. First, if the major ion is moving, it tends to carry the minor ion along with it. Secondly, the minor ions tend to diffuse, driven by temperature and density gradients, but are limited by collisions with the major ion. Finally, the polarization electric field set up by the major ions and electrons will exert an electrostatic force on the minor ions. Using equation 1.2, the electric field term can be eliminated from equation 1.9 to give:

$$u_x = u_i - D_x\left[\left(\frac{1}{n_x}\right)\frac{\partial n_x}{\partial z} + \left(\frac{1}{T_x}\right)\frac{\partial(T_e + T_x)}{\partial z} + \frac{T_e}{T_x n_e}\frac{\partial n_e}{\partial z} + \frac{1}{H_x}\right] \qquad (1.10)$$

This equation is the standard diffusion equation for a minor ion in the terrestrial ionosphere. To obtain solutions of the minor ion flow velocity with height, it is useful to assume an isothermal atmosphere with no motion of the major ions (not exactly true, but a useful approximation which simplifies the derivation). Equation 1.10 can then be written as:

$$F_x = n_x u_x = D_x\left[\frac{\partial n_x}{\partial z} + n_x\left(\frac{1}{H_x} - \frac{T_e}{T_x H_p}\right)\right] \qquad (1.11)$$

differentiating this equation with respect to height yields:

$$\frac{\partial^2 n_x}{\partial z^2} + \left[\frac{1}{H_p} + \left(\frac{1}{H_x} - \frac{T_e}{T_x H_p}\right)\right]\frac{\partial n}{\partial z} + \left(\frac{1}{H_x} - \frac{T_e}{T_x H_p}\right)\frac{n_x}{H_p} = 0 \qquad (1.12)$$

This equation has two linearly independent solutions:

$$n_x = n_{xo}\exp\left[\left(\frac{T_e}{T_x H_p} - \frac{1}{H_x}\right)(z - z_o)\right] \qquad (1.13)$$

$$n_x = n_{xo}\exp\left(\frac{-(z - z_o)}{H_p}\right) \qquad (1.14)$$

From Equation 1.13, if T_e and T_X are approximately equal and if the minor species is light, the density of the minor species will increase exponentially with altitude. This situation

corresponds to diffusive equilibrium and is valid until species x is no longer a minor constituent. Equation 1.14 indicates the minor ion's density will decrease with altitude with the same scale height as the major ions. This solution represents the maximum outflow possible with flow velocity increasing exponentially with altitude to keep the flux, F_x, constant. This condition represents a flux limited process in which the minor ion flux is limited by its number density which, in turn, is defined by the major species (O^+ in the polar wind case). With this solution, the minor ion species will always remain a minor constituent; however, at some point the minor ion flow will exceed the sound velocity so the previous assumption of subsonic flow becomes invalid.

When considering the case of supersonic flow, the non-linear inertial term must be included in the momentum equation. Assuming only one ion species, with similar assumptions as before, the sum of the ion and electron momentum equation is:

$$n_x m_x u_x \frac{\partial u}{\partial z} + k\left(T_e + T_x\right)\frac{\partial n_x}{\partial z} + n_x m_x g = -n_x m_x \upsilon_{xn} u_x \qquad (1.15)$$

where the major ion velocity has been assumed to be close to zero. Equation 1.14 can be rewritten by substitution with the continuity equation:

$$\frac{\partial n_x}{\partial z} = \left(\frac{n_x}{u_x}\right)\frac{\partial u_x}{\partial z} \qquad (1.16)$$

to obtain

$$\left(u_x^2 - v_{th}^2\right)\left(\frac{1}{u_x}\right)\frac{\partial u_x}{\partial z} + g = -\upsilon_{xn} u_x \qquad (1.17)$$

where v_{th} is defined as the thermal speed of the ion-electron gas

$$v_{th} = \sqrt{\frac{k\left(T_e + T_i\right)}{m_x}} \qquad (1.18)$$

Rewriting equation 1.16 in terms of a Mach number where $M = u_i/v_{th}$ gives:

$$\frac{\partial M}{\partial z} = -\left[\frac{g}{v_{th}^2} + \frac{\upsilon_{xn} M}{v_{th}}\right]\left(\frac{M}{M^2 - 1}\right) \qquad (1.19)$$

This first-order ordinary differential equation has a host of solutions possible, two of them contain singularities at M=1 and M=-1. The family of solutions are shown in figure 1.4 in

an ion Mach number versus altitude format. Physically real solutions corresponding to light ion outflows can be determined by matching solutions with appropriate boundary conditions. For H^+ outflows, the negative branch can be discounted immediately since these solutions correspond to inflow conditions (valid for stellar accretion!). All solutions which remain subsonic are valid (polar breeze) physical solutions. For these cases, H^+ flow velocities increase to a subsonic maximum and then decrease to a small value at high altitudes. There is one additional solution possible involving supersonic flow. This curve passes through the critical point of M=1, so a transonic velocity profile results. In this case, the H^+ flow starts as a low speed flow, accelerates to Mach 1, and continues as a supersonic flow to high altitudes. The correct solution, subsonic or supersonic, depends on the pressure difference between the ionosphere and the magnetosphere. At polar latitudes, the flux tube pressure differential is sufficient to drive H^+ into supersonic flow, while O^+ flows upward at only very low speeds.

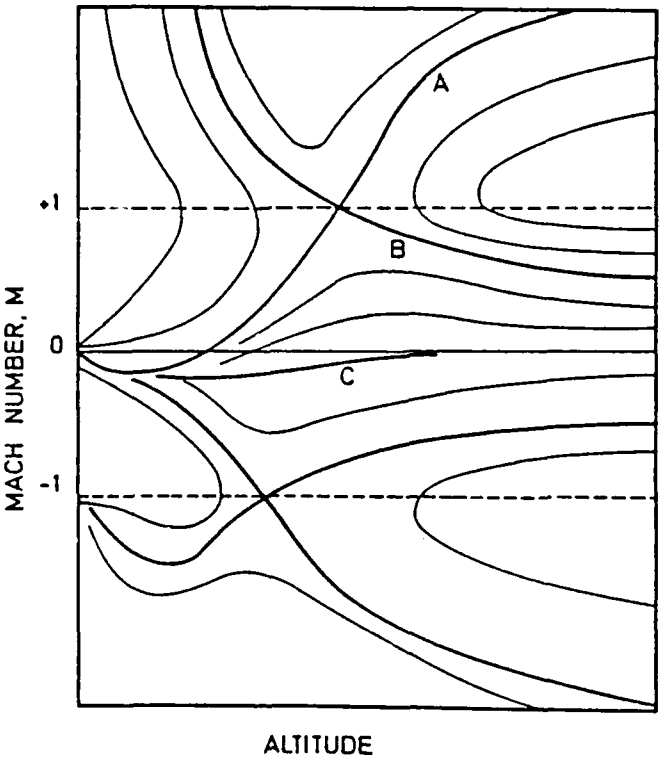

Figure 1.4 Family of solution curves for light ion outflow based on a simple hydrodynamic model (after Banks and Holzer).

The major influence in the behavior of field-aligned ion flows in the high-latitude region is the presence of a strong, upward-directed pressure gradient force so that a diffusive equilibrium cannot fully develop. At lower latitudes, the flux tubes are relatively

short so that ionospheric plasma can move into the volume allowing it to fill within a few days or so. Filling proceeds until a balance is struck between pressure gradient forces and gravity. When the balance is achieved, the bulk flow is zero and the plasma is in a state of diffusive equilibrium. A sub-equilibrium state exists in the polar latitudes for both the major ion, O^+, and the minor species, H^+ and He^+ (other species are also present but will not be discussed since H^+ and He^+ are the most abundant minors) since the pressure gradient force exceeds gravity, and friction as well. In the case of O^+, a close balance exists between gravity, pressure gradient and frictional forces (primarily with O) so that a net upward flow exists. However, this is a very low speed flow when compared to the lighter, minor ions.

In the following chapters, both the supersonic, H^+ flows and the lower-speed O^+ field-aligned flows will be considered in more detail by modeling the topside processes using a sophisticated, time-dependent hydrodynamic model. Variations to both species flux profiles will be examined and related to the chemical and frictional influences exerted by both the ionospheric and thermospheric constituents.

CHAPTER 2

RESEARCH TOOLS

2.1 Background

An investigation of the steady-state and transient behavior of high-latitude ion upwelling warrants both theoretical and experimental consideration due to the complex nature of these ion flows. Theoretical treatments, in the form of various modeling approaches, provide insight into the physical processes which govern the character and composition of ion outflow. They have the advantage of an extended range of application in either space or time, limited only by the model assumptions and numerical scheme and can therefore be designed to identify the underlying physics which change in importance from one altitude to the next. Experimental observations by both ground-based and satellite systems are also important since they quantify the spatial and temporal extent of polar wind flows and provide important benchmarks upon which to build theoretical descriptions. Together, the two techniques provide complementary perspectives into our understanding of high-latitude field-aligned ion flows and will be used in this thesis to meet the research objectives cited earlier.

A consolidated approach has been adopted here which brings together several research tools to examine both the steady-state and transient behavior of ion outflows. While the main focus of this work is centered on theoretical treatment using suitable modifications to the Gombosi polar wind model, additional modeling and experimental techniques have been employed to support (or in some cases contradict!) the theory. These additional techniques include use of the National Center for Atmospheric Research's Thermospheric/Ionospheric General Circulation Model (hereafter referred to as the NCAR-TIGCM or TIGCM) along with both satellite and incoherent radar measurements. Together, they permit further analyses and understanding into the thermosphere-ionosphere

interactions which govern upwelling processes than would be possible using a single tool alone.

The purpose of the present chapter is to describe each research tool in sufficient detail so that results, and the underlying techniques employed to obtain them, can be understood and interpreted correctly. To this end, a section is devoted to the Gombosi polar wind model which forms the central theoretical focus on steady-state as well as transient polar wind behavior. The NCAR-TIGCM is also described separately since it is used to provide a realistic specification of thermospheric-ionospheric interaction associated with frictional (Joule) heating and related transient ion outflow behavior. A third section is devoted to the Dynamics Explorer-2 satellite instrumentation used later in Chapter 4 to quantify the magnitudes and the high latitude morphology of frictional heating and in Chapter 3 to examine the altitude distribution of ion densities. Finally, incoherent radar theory is briefly described as it relates to ionospheric measurements of velocity and density since radar observations that relate frictional heating to transient ion upflows are also presented in Chapter 4 . In describing these tools, emphasis will be placed on how they relate to and support this research. In the interest of brevity, no attempt will be made to provide a full theoretical development of each model or technique if the work has been discussed in detail elsewhere. Instead, reference will be made to previous descriptions by other authors when appropriate.

2.2 Numerical Treatments

2.2.1 The Generalized Transport Equations

Any quantitative examination into the macroscopic properties of the ionosphere depends upon a knowledge of certain properties of the plasma such as concentration, bulk velocity, temperature and heat flow etc. Such physically significant information is contained in the individual species, s, phase-space distribution function, $F_S(\mathbf{r},\mathbf{v}_S,t)$. Within a gas mixture, the evolution of each species "s" can be described by a separate Boltzman equation:

$$\frac{\partial F_s}{\partial t} + \left(c_{si} + u_{si}\right)\frac{\partial F_s}{\partial x_i} + \left[G_i + \frac{e_s}{m_s}\varepsilon_{ijk}\left(c_{sj} + u_{sj}\right)B_k - \left(c_{sj} + u_{sj}\right)\frac{\partial u_{si}}{\partial x_j} \right]\frac{\partial F_s}{\partial c_{si}} = \left(\frac{\delta F_s}{\delta t}\right) \quad (2.1)$$

where $F_S(\mathbf{r},c_S,t)$ is the distribution function of species s, x_i represents spatial coordinates (i=1, 2, 3), c_{si} is the random velocity component, u_{si} is the bulk flow velocity of the species s (a function of time and space), e_s is the charge, m_s is the mass, G_i is the local acceleration due to gravity, B_i is the magnetic field component, ε_{ijk} is the permutation

tensor, $\partial / \partial t$ is the time derivative. The term on the right hand side represents the rate of change of the distribution function due to interparticle collisions. For a known distribution function, any macroscopic parameter can be obtained directly by taking the appropriate velocity moment of the phase-space distribution function. For most aeronomic applications, the species distribution is unknown since the macroscopic variables are more commonly measured. In these cases, it is useful to work with a set of transport equations which describe the temporal and spatial evolution of the macroscopic physical quantities for each component (species) in the plasma.

A generalized set of transport equations can be obtained from the Boltzman equation (equation 2.1) by multiplying it by m_s, $m_s c_s$, $^1/_2 m_s c_s^2$, etc., and then integrating the product expression over velocity space. From the zeroth order moment (m_s) of the Boltzman equation one obtains the continuity equation :

$$m_s \frac{\partial n_s}{\partial t} + m_s u_{si} \frac{\partial n_s}{\partial x_i} + m_s n_s \frac{\partial u_{si}}{\partial x_i} = m_s \dot{S}_s \tag{2.2}$$

where, $n_s = \int d^3 c_s F_s$ is the particle number density and $\dot{S}_s$ is the net production rate of species s. The first moment ($m_s c_{si}$) of the Boltzmann equation yields the momentum equation:

$$m_s n_s \frac{\partial u_{si}}{\partial t} + m_s n_s u_{sj} \frac{\partial u_{si}}{\partial x_j} + \frac{\partial P_{sij}}{\partial x_j} - n_s \left(G_i + e_s E_i + e_s \varepsilon_{ijk} u_{sj} B_k \right) = \dot{M}_{si} \tag{2.3}$$

where P_{sij} is the pressure tensor and $\dot{M}_{si}$ represents the rate of momentum exchange due to collisions between species s and all other constituents. In similar fashion, from the second moment ($m_s c_s c_{si}$) one obtains the equation governing the pressure tensor:

$$\begin{aligned} &\frac{\partial P_{sij}}{\partial t} + u_{sk} \frac{\partial P_{sij}}{\partial x_k} + P_{sij} \frac{\partial u_{sk}}{\partial x_k} + P_{sik} \left(\frac{\partial u_{sj}}{\partial x_k} + \frac{\partial u_{sk}}{\partial x_j} \right) + \frac{\partial Q_{sijk}}{\partial x_k} - \\ &\qquad - \frac{e_s}{m_s} \left(\varepsilon_{ik\gamma} P_{skj} + \varepsilon_{jk\gamma} P_{ski} \right) B_\gamma = \dot{P}_{sij} \end{aligned} \tag{2.4}$$

where $Q_{sijk} = m_s \int d^3c_s c_{si} c_{sj} c_{sk} F_s$ is the heat flow tensor and $\dot{P}_{sij}$ is the second moment of the collision term. The third moment of the Boltzmann equation describes changes in the heat flow tensor:

$$\frac{\partial Q_{sijk}}{\partial t} + u_{sl}\frac{\partial Q_{sijk}}{\partial x_l} + Q_{sijk}\frac{\partial u_{sl}}{\partial x_l} + Q_{sijl}\frac{\partial u_{sk}}{\partial x_l} + Q_{sikl}\frac{\partial u_{sj}}{\partial x_l} + Q_{sjkl}\frac{\partial u_{si}}{\partial x_l} + \frac{\partial R_{sijkl}}{\partial x_l} -$$
$$-\frac{1}{m_s n_s}\left(P_{sij}\frac{\partial P_{skl}}{\partial x_l} + P_{sik}\frac{\partial P_{sjl}}{\partial x_l} + P_{sjk}\frac{\partial P_{sil}}{\partial x_l}\right) -$$
$$-\frac{e_s}{m_s}\left(\varepsilon_{km\gamma}Q_{sijm} + \varepsilon_{jm\gamma}Q_{sikm} + \varepsilon_{im\gamma}Q_{sjkm}\right)B_\gamma = \qquad (2.5)$$
$$= \dot{Q}_{sijk} - \frac{1}{m_s n_s}\left(P_{sij}\dot{M}_{sk} + P_{sik}\dot{M}_{sj} + P_{sjk}\dot{M}_{si}\right)$$

where $R_{sijkl} = m_s \int d^3c_s c_{si} c_{sj} c_{sk} c_{sl} F_s$ is the fourth order pressure tensor, and $\dot{P}_{sijk}$ represents the third moment of the collision term.

Taking the various velocity moments in this manner can provide an unlimited number of conservation equations, each one describing the temporal and spatial behavior of some physical quantity related to species s. In every case however, a finite system of equations does not constitute a closed set since the equation describing the velocity moment of order ***r*** contains a divergence term dependent on the velocity moment ***r+1***. For instance, the continuity equation (equation 2.2) depends on the bulk flow velocity, $\mathbf{u_s}$, the momentum equation contains the pressure tensor, the pressure equation contains a heat flow tensor term. It is therefore necessary to adopt some form of closure approximation to truncate this system of dependent equations. For aeronomic purposes, this involves adopting an analytic expression for the species velocity distribution function which permits higher order moments to be expressed in terms of lower order moments (Grad, 1949). The level of closure of any system of equations follows from the degree of approximation used to describe the distribution function so that some a priori assumptions are usually made to establish the level of truncation. For ionospheric studies, the infinite series of transport equations are normally truncated at the level of the 3rd moment using a closure formula after Grad (1949):

$$R_{sijkl} = \frac{1}{m_s n_s}\left(P_{sij}P_{skl} + P_{sik}P_{sjl} + P_{sil}P_{sjk}\right) \qquad (2.6)$$

Substituting (2.6) into equation (2.5) yields an approximation to the heat flow equation which closes the set of equations since no higher order terms are present:

$$\frac{\partial Q_{sijk}}{\partial t} + u_{sl}\frac{\partial Q_{sijk}}{\partial x_l} + Q_{sijk}\frac{\partial u_{sl}}{\partial x_l} + Q_{sijl}\frac{\partial u_{sk}}{\partial x_l} + Q_{sikl}\frac{\partial u_{sj}}{\partial x_l} + Q_{sjkl}\frac{\partial u_{si}}{\partial x_l} +$$
$$+\left[P_{skl}\frac{\partial}{\partial x_l}\left(\frac{P_{sij}}{m_s n_s}\right) + P_{sjl}\frac{\partial}{\partial x_l}\left(\frac{P_{sik}}{m_s n_s}\right) + P_{sil}\frac{\partial}{\partial x_l}\left(\frac{P_{sjk}}{m_s n_s}\right)\right] -$$
$$-\frac{e_s}{m_s}\left(\varepsilon_{km\gamma}Q_{sijm} + \varepsilon_{jm\gamma}Q_{sikm} + \varepsilon_{im\gamma}Q_{sjkm}\right)B_\gamma = \qquad (2.7)$$
$$= \dot{Q}_{sijk} - \frac{1}{m_s n_s}\left(P_{sij}\dot{M}_{sk} + P_{sik}\dot{M}_{sj} + P_{sjk}\dot{M}_{si}\right)$$

2.2.2 The Five-Moment Approximation

Equations 2.2, 2.3, 2.4 and 2.7 are the most general set of transportation equations used in ionospheric studies and are referred to as the 20-moment approximation : one continuity equation + three components of the momentum equation + six equations for the individual components of the symmetric pressure tensor + ten components describing the heat flow tensor. In certain applications however, a number of simplifying assumptions can often be made to restrict the number of equations to the 16-moment approximation (separate transport of parallel and perpendicular thermal energy) or the 13-moment set (single heat flows only) or the 5-moment set (no heat flow or stress). Schunk (1975, 1977), Demars (1979), Ganguli and Mitchell (1987), and Palmadesso, Ganguli and Mitchell (1988) describe the higher order equations in more detail. Here, the focus will be on the 5-moment approximation since this is the level applied to the polar wind model used in this research.

In many applications of the transport equations to ionospheric or solar wind studies, the presence of a strong magnetic field constrains the plasma to the parallel (to **B**) and perpendicular (to **B**) dimension. If one chooses a coordinate system by making a velocity transformation that moves horizontally with the flow, the average external electric field perpendicular to the magnetic field vanishes and the transport equations can be further simplified. Two assumptions are made for this approximation. First, the magnetic field, **B**, goes to infinity so that the plasma is gyrotropic (i. e., the gyrofrequency = $e_S B/m_S$ is greater than the collision frequency) and second, that no perpendicular gradients exist in the distribution function of species. As the components of **B** approach infinity, all coefficients of the magnetic field term must go to zero to keep the equations valid. Therefore, $\mathbf{u}_S \times \mathbf{B} = 0$ which implies that the flow can only be parallel to the magnetic field. In applying this

treatment to the transport equations, one defines a unit vector pointing along the magnetic field line so that $b_i = B_i/B$. The field aligned flow can be expressed as:

$$u_{si} = u_s b_i \tag{2.8}$$

In this case the spatial derivatives involving the unit magnetic field vector become:

$$\frac{\partial b_i}{\partial x_i} = \frac{b_i}{B}\frac{\partial B}{\partial x_i} \tag{2.9}$$

and:

$$b_j \frac{\partial b_i}{\partial xj} = \frac{1}{B}\frac{\partial B}{\partial x_i} - \frac{1}{B}\frac{\partial B}{\partial xj} b_i b_j \tag{2.10}$$

This reduces the pressure tensor equation to:

$$\varepsilon_{ilk} P_{sjl} + \varepsilon_{jlk} P_{sil} = 0 \tag{2.11}$$

The following form of the pressure tensor satisfies this relation:

$$P_{sij} = \delta_{ij} p_{s\perp} + \left(p_{sll} - p_{s\perp}\right) b_i b_j \tag{2.12}$$

where δ_{ij} is the Kronecker delta. Equation 2.12 shows that in the gyrotropic limit, the pressure tensor is reduced to only two independent pressure components parallel and perpendicular to the magnetic field. In these components are assumed to be equal (isotropic pressure) and for negligible heat flow, one obtains the gyrotropic five moment (hydrodynamic) approximation from equations 2.2-2.4 :

$$m_s \frac{\partial n_s}{\partial t} + m_s B \frac{\partial}{\partial z}\left(\frac{n_s u_s}{B}\right) = m_s \dot{S}_s \tag{2.13}$$

$$m_s n_s \frac{\partial u_s}{\partial t} + m_s n_s u_s \frac{\partial u_s}{\partial z} + \frac{\partial p_s}{\partial z} - m_s n_s G - e_s n_s E = \dot{M}_s \tag{2.14}$$

$$\frac{\partial p_s}{\partial t} + B \frac{\partial}{\partial z}\left(\frac{u_s p_s}{B}\right) + 2 p_s \frac{\partial u_s}{\partial z} = \dot{p}_s \tag{2.15}$$

To obtain collision terms for equations 2.13-2.15, it becomes necessary to approximate the species velocity distribution function. Only for the simplest cases of Maxwellian and bi-Maxwellian distribution functions have general collision terms been

evaluated. These approximations are valid for most of the conditions encountered in the ionosphere so they are applicable to most polar wind flows. Under the assumption of a displaced Maxwellian distribution, and neglecting the minor contributions from mass source terms and stress and heat flow (consistent with the 5-moment approximation), the collision terms for the continuity momentum and energy equations reduce to:

$$\dot{S}_s = P_s - n_s L_s \tag{2.16}$$

$$\dot{M}_s = \sum_t n_s m_s \nu_{st} \left(u_t - u_s\right) \Phi_{st} \tag{2.17}$$

$$\dot{p}_s = \sum_t \frac{n_s m_s \nu_{st}}{\left(m_s + m_t\right)} \left[3k\left(T_t - T_s\right)\Psi_{st} + m_t \left(u_s - u_t\right)^2 \Phi_{st}\right] \tag{2.18}$$

In this case, Φ_{st} and Ψ_{st} are velocity dependent correction factors generally assumed to be 1 (hard sphere collisions) while ν_{st} is the momentum transfer collision frequency between all the other species t and a single s species particle. For higher moments which include stress and heat flow, approximations of the collision terms are only given for slow speed flows where drift velocities are smaller than thermal speeds. For these cases, Burgers' linear and semi-linear collision terms are used depending on whether temperature differences between interacting species are small or large respectively (Schunk, 1983). Equations 2.13 -2.15 along with their respective collision approximations (equations 2.16 and 2.18) constitute the gyrotropic 5-moment approximation since number density, 3 components of $\mathbf{u}_s$ and pressure are included. Before discussing the polar wind model based on this level of approximation, it is useful to compare and contrast some of the other applications of transport and kinetic theory to different treatments of polar wind models.

2.2.3 Summary of Polar Wind Modeling Treatments

The evolution of theoretical studies of polar wind flows has, in many respects, followed the same historical pattern as our basic observational understanding. Initial studies of the polar wind solved the hydrodynamic continuity and momentum equations for O^+ and H^+ assuming an isothermal ionosphere and gravitationally bound O^+ population (Banks and Holzer, 1969; Marubashi, 1970). Subsequently, it was realized that at higher altitudes, the flow became collisionless so that velocity distributions could become anisotropic. This knowledge led the way for hydromagnetic and kinetic treatments (Lemaire and Scherer, 1970, 1971, 1972, 1973; Holzer et al., 1971) consistent with the collisionless character of the flow. Observations of the thermal topside structure of the polar ionosphere and the effects of magnetospheric convection electric fields resulted in

more detailed theoretical descriptions of the thermal and dynamic properties surrounding these ion outflows (Raitt et al., 1975, 1977; Lemaire and Scherer, 1973; Holzer, 1971; Schunk et al., 1975, 1976, 1978). Model treatment using generalized transport equations were later introduced (Schunk and Watkins, 1981, 1982) in order to provide a continuous description of the transition from collisional to collisionless regimes. Up to the early 1980s, model treatments focused on steady-state solutions to identify relevant underlying physics behind the polar wind. Observations by the Dynamics Explorer spacecraft confirmed many of the polar wind model predictions (Nagai et al., 1984) but also provided much of the impetus for the development of time-dependent modeling techniques by providing evidence of transient outflows of heavy terrestrial ions (Lockwood et al., 1985). The latest generation of time-dependent polar wind models (Gombosi et al., 1985; Zinin et al., 1985; Singh and Schunk, 1985; Mitchell and Palmadesso, 1983; Schunk and Sojka, 1989) have provided an important new perspective on the transient evolution of ion flows under the more common non-equilibrium conditions prevailing in the high-latitude topside ionosphere. All of the steady-state and time-dependent treatments described above have particular strengths and limitations which dictate their suitability in studies of polar ion outflows.

A summary of the four basic types of model formulations presently in use to describe polar wind flows is provided in Table 2.1. The kinetic (and semi-kinetic) models are only applicable to the collisionless state since they are derived from the collisionless Boltzman equation (Vlasov equation). With kinetic treatments, the species distribution function can be directly obtained by integrating the Vlasov equation based on a specified boundary distribution function. This approach yields a distribution function that satisfies the full hierarchy of moments enabling any physically significant system quantity to be derived. The major disadvantage in this treatment is that a distribution must be specified at the boundary making subsequent results dependent on the initial conditions selected.

The generalized transport equations is obtained by taking velocity moments of the Boltzman equation. An infinite number of high order conservation equations are possible, closure approximations are only available for Maxwellian or bi-Maxwellian distributions so that *a priori* assumptions are implicit in their application to the ionosphere. The hydromagnetic equations are derived from the Vlasov equation and is valid only in the collisionless limit. In the collision-dominated limit, the general system of transport equations reduce to either the Euler or Navier-Stokes system of equations depending on whether the stress and heat flux tensor are retained (Navier-Stokes approximation) or considered to be negligible (Euler assumption). By comparison with either the hydromagnetic or hydrodynamic treatments, the generalized transport equations have the

advantage of providing a continuous transition between collisional and collisionless regimes.

Since kinetic treatments have been typically restricted to steady-state situations, existing time-dependent models have all developed from a common lineage of generalized transport equations. Table 2.2 provides a summary of several, time-dependent polar wind models In each case, different levels of closure are assumed which, in turn, lead to different regions of validity and ultimately, different predictive abilities. Time-dependent treatments of the polar wind were first obtained by Mitchell and Palmadesso based on a 13-moment approximation with electrons and H^+ acting as dynamic species along an upper

Polar Wind Model Formulations

Consideration	Hydrodynamic	Kinetic	Hydromagnetic	Generalized
Derivation	Boltzman Eq	Vlasov Eq	Vlasov Eq	Boltzman Eq
Basic Assumptions	Maxwellian dist isotropic	boundary conditions	CGL approx gyrotropic	bi-Maxwellian or Maxwellian dist. gyrotropic
Validity	collisional	collisionless	collisionless	collisional or collisionless
Species	single or multispecies	single or multispecies	single or multispecies	single or multispecies
Advantage	fully describes collisional regime	any order moment available from distribution	simplified for collisionless flows	valid over all altitude regimes
Disadvantage	limited altitude truncation	exobase discontinuity must specify n, u	limited altitude truncation	computationally long truncation

Table 2.1 Summary of various model treatments used to describe polar wind flows.

portion of an auroral field line. Their treatment required a lower boundary specification of number density and bulk flow properties and temperature so it was not entirely self-consistent. Time-dependent hydrodynamic models were developed almost simultaneously by Gombosi et al., 1985 and Zinin et al., 1985. Zinin et al., 1985 solved the continuity,

momentum and energy equations for O^+, H^+, and electrons along auroral field lines based on chemical equilibrium conditions at the lower model boundary of 126 km and investigated typical time scales for each plasma component.

Time-Dependent Polar Wind Models						
Condition	Michell & Palmadesso 1983	Zinin et al. 1985	Gombosi et al. 1985	Singh & Schunk 1985	Ganguli & Palmadesso 1987	Schunk & Sojka 1989
dynamic components	H^+ O^+ e	H^+ O^+ e	H^+ O^+ e	H^+ e	H^+ e	H^+ O^+ e
static components	none	O_2^+ NO^+ neutrals	neutrals N_2 O_2 O H	none	O^+	neutrals N_2 O_2 O H
transport approx.	13 moment	5 moment with heat conduction	5 moment with heat conduction	5 moment constant T	16 moment	5 moment CGL approx
time dependence	yes	yes	yes	yes	yes	yes
collisional regime	collisions not important	collision dominated	collision dominated	collision-less	collisions not important	both
altitude range	800 km - 10R_e	126 km - 10 R_e	200 km - 8000 km	9000 km - 39000 km	1500 km - 10 R_e	1500 km - 9000 km
lower boundary	n & u specified	chemical. equilib.	chemical. equilib.	n & u specified	n & u specified	n & u specified

Table2.2 Summary of time-dependent models of the polar wind. All models are developed from the generalized transport equations but specific assumptions and approximations result in different applicability. Time-dependent treatments permit greater detail into the temporal character of the polar wind due to transient perturbations.

Gombosi et al., 1985, simultaneously solved the coupled continuity, momentum and energy equations for O^+, H^+, and electrons along a radially-divergent polar field line between 200 km and 8000 km taking into account the effects of ion production, charge-exchange chemistry collisions, heat conduction, and external heat sources such as field-aligned currents. The most recent version, developed as part of this research, can account for time-dependent ion frictional heating, impact ionization from external particle precipitation sources such as polar rain and height-dependent photoionization rates for atomic oxygen. By comparison with the other treatments, the Zinin et al. (1985) and Gombosi et al. (1985) models have the added advantage of self-consistent treatments since no density or flow velocities need be assumed at the lower boundary. Singh and Schunk (1985, 1986) investigated the time-dependent plasma expansion due to density perturbations using a simple hydrodynamic treatment and parametric topside density depletions. Their work showed that all ion species experience significant acceleration behind shock fronts which developed in response to the initial plasma expansion. In comparing the 13-moment collisionless model of Schunk with the hydrodynamic model of Gombosi et al. (1985), it is interesting to note that both predict the same temporal characteristics for the polar wind densities, velocities and escape fluxes (Gombosi and Schunk, 1988). The ion temperature distributions are different however, with collisionless models yielding large temperature anisotropies at high altitudes. Additionally, the 13 and 16-moment treatments permit the specification of heat flows within the modeled system. The most recent time-dependent model by Schunk and Sojka (1989) couples a low altitude ionospheric model which solves the coupled continuity, momentum and simplified ion energy equation with a high-altitude hydrodynamic model. Three-dimensional lower boundary solutions are provided to the high-altitude, coupled continuity and momentum equations to provide a Lagrangian representation of the dynamic structure of the polar wind due to transient, storm-time effects.

2.2.4 The Gombosi Polar Wind Model

The basic theoretical treatment used in this research is the 5-moment approximation which was applied to describe polar wind flows by Gombosi et al. (1985). Their original formulation has been modified as part of this research to extend its applicability for this investigation. A description of these improvements will be left to subsequent chapters and discussed in the context of their use. Here, the original model developed by Gombosi et al. (1985) is described to provide a summary of the model assumptions and operation.

In applying the gyrotropic, 5-moment equation set to describe the polar wind, several features of the high-latitude polar ionosphere help to simplify the formulation.

First, the high-latitude geomagnetic field lines are essentially radial so that $\mathbf{B} = B\mathbf{b}_r$ and the Earth's radial field can be expressed as:

$$\mathbf{B} = B_e\left(\frac{R_e}{R_e + z}\right)^3 \mathbf{b}_r \tag{2.19}$$

where B_e is the surface geomagnetic field strength, R_e is the Earth's polar radius (6.3785×10^8 cm), z is the altitude, and $\mathbf{b}_r$ the unit magnetic field field vector which is oriented radially outward. Secondly, since the flow is field-aligned and the field is only radial, the gradient and divergence terms reduce to:

$$\nabla f(z,t) = \frac{\partial f}{\partial t}\mathbf{b}_r \tag{2.20}$$

$$\nabla \cdot \left(f\,\mathbf{b}_r\right) = \frac{\partial f}{\partial z} + f\left(\nabla \cdot \mathbf{b}_r\right) \tag{2.21}$$

where f represents some dependent variable, but also,

$$\left(\nabla \cdot \mathbf{b}_r\right) = \frac{\partial B}{\partial z} = -\frac{3B_e R_e^3}{\left(R_e + z\right)^4} = \frac{3B}{R_e + z} \tag{2.22}$$

Substituting equation 2.22 into 2.21 gives:

$$\nabla \cdot \left(f\,\mathbf{b}_r\right) = \frac{\partial f}{\partial z} + \frac{3f}{R_e + z} = \frac{1}{A}\frac{\partial}{z}(Af) \tag{2.23}$$

where A represents the cross sectional area function for a radially-divergent flux tube and is defined as:

$$A = \left(\frac{R_e + z}{R_e}\right)^3 \tag{2.24}$$

When equations 2.20 and 2.23 are substituted into the 5-moment gyrotropic equations the continuity, momentum, and energy equations become:

$$\frac{\partial}{\partial t}\left(A\rho_s\right) + \frac{\partial}{\partial z}\left(A\rho_s u_s\right) = A\dot{\rho}_s \tag{2.25}$$

$$\frac{\partial}{\partial t}\left(A\rho_s u_s\right) + \frac{\partial}{\partial z}\left(A\rho_s u_s^2\right) + A\frac{\partial p_s}{\partial z} = A\rho_s\left(\frac{e_s}{m_s}E_{\parallel} - g\right) + A\left(\dot{M}_{s\parallel} + u_s\dot{\rho}_s\right) \tag{2.26}$$

$$\frac{\partial}{\partial t}\left(\frac{1}{2}A\rho_s u_s^2+\frac{1}{\gamma_s-1}Ap_s\right)+\frac{\partial}{\partial z}\left(\frac{1}{2}A\rho_s u_s^3+\frac{1}{\gamma_s-1}Au_s p_s\right)=$$
$$A\rho_s u_s\left(\frac{e_s}{m_s}E_{\|}-g\right)+\frac{\partial}{\partial z}\left(A\kappa_s\frac{\partial T_s}{\partial z}\right)+A\left(\dot{p}_s+\dot{Q}_s+u_s\dot{M}_{s\|}+\frac{1}{2}u_s^2\dot{\rho}_s\right) \quad (2.27)$$

where ρ_s is the gas mass density, p is the pressure, T is the temperature, γ is the specific heat ratio, k is the heat conductivity, g is the local gravitational acceleration, $\dot{\rho}$ is the mass production rate, $E_{\|}$ is the magnetic field-aligned electric field, $\dot{M}_{\|}$ is the momentum exchange rate, while $\dot{Q}$ and $\dot{p}$ represent external ion heating rates and energy exchange rates, respectively. Since the model considers two ion species, the 's' subscript refers to either oxygen or hydrogen ions. The plasma is assumed to be quasineutral everywhere so that the electron continuity equation is couched in terms of the ion species:

$$n_e = n(O^+)+n(H^+) \quad (2.28)$$

In a similar fashion, the electron flow velocity is prescribed based on the ion velocities and some specified current density:

$$u_e=\frac{1}{n_e}\left(n(O^+)u(O^+)+n(H^+)u(H^+)-\frac{j_{\|}}{e}\right) \quad (2.29)$$

where $j_{\|}$ is the field-aligned electric current density The total flux tube current is assumed to be conserved along the flux tube so that:

$$j_{\|}=j_{0\|}\frac{A_0}{A} \quad (2.30)$$

where the 0 subscript refers to some feducial altitude (in this case, 200 km). In the present set of calculations, $j_{0\|}$ was assumed to be zero. In this approximation the electron momentum equation determines the electric field component parallel to the magnetic field:

$$E_{\|}=-\frac{1}{en_e}\frac{\partial}{\partial z}\left(p_e+\rho_e u_e^2-\sum_{s=ions}\frac{m_e}{m_s}(p_s+\rho_s u_s^2)\right)-\dot{M}_{e\|}-$$
$$+\sum_{s=ions}\frac{m_e}{m_s}\left(\dot{M}_{s\|}-(u_e-u_s)\dot{\rho}_s\right)-\frac{A'}{A}\frac{1}{en_e}\left(\rho_e u_e^2-\sum_{s=ions}\frac{m_e}{m_s}\rho_s u_s^2\right) \quad (2.31)$$

where A' represents the vertical derivative of the flux tube cross sectional area function, A. Finally, the electron energy equation is given as:

$$\rho_e \frac{\partial T_e}{\partial t} = (\gamma_e - 1)\frac{m_e}{kA}\frac{\partial}{\partial z}\left(A\kappa_e \frac{\partial T_e}{\partial z}\right) - \rho_e u_e \frac{\partial T_e}{\partial z} - \\ -T_e\left(\dot{\rho}_e + \frac{\gamma_e - 1}{A}\rho_e \frac{\partial (Au_e)}{\partial z}\right) + (\gamma_e - 1)\frac{m_e}{k}(\dot{p}_e + \dot{Q}_e) \tag{2.32}$$

Burgers' fully linear approximation (Burgers, 1969) is used to calculate the collision terms appearing in equations 2.25 through 2.27. These expressions are similar to those given by equations 2.16-2.18:

$$\dot{\rho}_s = P_s - \rho_s L_s \tag{2.33}$$

$$\dot{M}_{sll} = \sum_t \rho_s \nu_{st}(u_t - u_s) \tag{2.34}$$

$$\dot{p}_s = \sum_t \frac{\rho_s \nu_{st}}{m_s + m_t}\left[3k(T_t - T_s) + m_t(u_t - u_s)^2\right] \tag{2.35}$$

except that hard-sphere interaction potentials have been assumed and $n_s m_s$ has been replaced by the species mass density ρ_s. Momentum transfer collision frequencies and the heat conductivities for the various charged species are taken from Schunk (1980) and Raitt (1975, 1978) respectively. With these collision terms, the model is capable of describing all significant ion-ion, ion-neutral and ion-electron interactions.

The model interacts both chemically and frictionally with the major thermospheric constituents (N_2, O_2, O and H) which are specified for a given time, location and geophysical condition based on the MSIS-86 neutral atmosphere model (Hedin, 1987). Oxygen ions are produced by photoionization and by the accidentally resonant charge exchange reaction with H^+:

$$H^+ + O \rightarrow H + O^+$$

This latest version of the polar wind model also includes a revised method for calculating photoionization frequencies as a function of altitude for atomic oxygen. Details of this new revision are discussed in Chapter 3. O^+ is chemically removed by ion atom interchange reactions with neutral molecular species:

$$O^+ + N_2 \rightarrow NO^+ + N$$
$$O^+ + O_2 \rightarrow O_2^+ + O$$

followed by fast dissociative recombinations of the NO^+ and O_2^+ molecular ions. O^+ is also removed by the reverse charge exchange reaction with H:

$$O^+ + H \rightarrow O + H^+$$

H^+ ions are created by this same charge exchange process. The H^+ is removed by charge transfer reaction with neutral atomic oxygen as discussed above. Temperature-dependent reaction rate constants have been adopted for the charge exchange reaction based on Barakat (1987), and for all other reactions, rate constants are adopted from Schunk (1980).

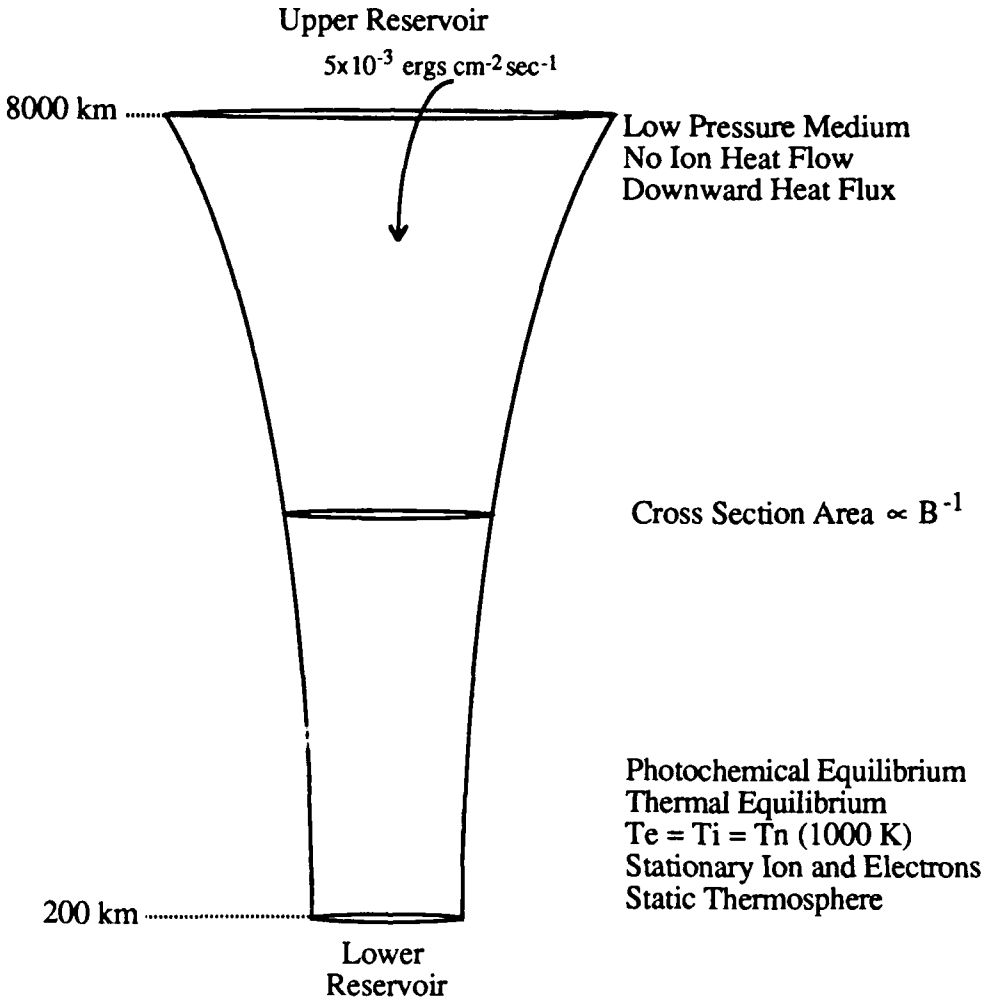

Figure 2.1 Cartoon representation of the Gombosi polar wind model identifying the major boundary conditions and their relation to the topside polar ionosphere.

The modeled flux tube connects two infinite external reservoirs located at the model boundaries of 200 km and 8000 km (see Figure 2.1). Both ion species (H^+ and O^+) in the stationary lower reservoir (located at an altitude of 200 km) are assumed to be in chemical and thermal equilibrium with the neutral atmosphere, while the electron temperature in this

lower reservoir is fixed at 1000 K. The upper reservoir (at 8000 km) represents a stationary, low pressure external medium into which the upward flowing ions may enter without reflecting back. This condition, referred to by Gombosi et al. (1985) as a topside "vacuum-cleaner ", simulates the pressure gradient along an open flux tube at high latitudes.The model represents this gradient by a order of magnitude decrease in pressure at the upper boundary. The choice in pressure gradient across the upper model boundary does not alter results since model solutions are insensitive to the assumed magnitude of this decrease as long as sufficient pressure gradient exists to drive H^+ upward. Once flowing, the ions are limited in escape by friction and the magnitude of the polarization electric field.

A topside, downward electron heat flux is a free parameter used to simulate energy deposition from the magnetosphere. Since the high-latitude ionosphere communicates with the hot tenuous magnetosphere along field lines threading both mediums, a downward flow of heat, carried by magnetospheric electrons is expected. Furthermore, this heat flux is expected to vary spatially and temporally in response to solar and geomagnetic conditions (Schunk et al., 1986). Unfortunately, little is known about the magnitude of this heat flux although its effects have been parametrically modeled (Schunk et al., 1986 and Schunk, 1987). For all studies performed in this work, the electron heat flux is set to 5×10^{-3} ergs $cm^{-2}\ s^{-1}$ so that modeled electron temperature profiles lie in the middle ranges of observed electron temperatures from DE-2 for a dayside polar location. It is also assumed that there is no ion heat flow between the upper reservoir and the ionospheric flux tube.

The numerical model simultaneously solves the time-dependent, coupled, continuity, momentum and energy equations for oxygen and hydrogen ions and the electron continuity, momentum and energy equations along radially-divergent open magnetic field lines Together, these seven equations (equations 2.25 through 2.29 and 2.31, 2.32) represent a fully-coupled, set of hydrodynamic equations based on the gyration dominated five-moment approximation. The method of solution will be briefly described before considering steady-state solutions.

The set of seven coupled equations used to describe polar wind flows is solved using a combined Crank-Nicolson and Godunov numerical scheme using time dimension splitting. This combined scheme is used to minimize error in the finite differencing schemes and at the same time, permit the time-dependent description of gases having discontinuities and propagating shocks. The equation set approximates an unsteady single-dimension system since both time and altitudinal derivatives are retained. The continuity and momentum equations can be treated with the Godunov scheme directly since only first-order derivatives are present. Solutions to the ion energy equations cannot be obtained with the Godunov scheme since the energy equation contains a term of second-order. In

this case, the heat conductivity term in the energy equation gives it a form of a parabolic partial differential equation:

$$\frac{\partial T}{\partial t} = C\frac{\partial}{\partial z}\left(K\frac{\partial T}{\partial z}\right) \tag{2.36}$$

Solutions for this type of expression can be obtained using finite differencing approximations such as the Crank-Nicolson scheme. This implicit method has the advantage of accuracy over explicit methods and can be combined effectively with the method of Godunov to conserve all modeled quantities and provide quantitatively correct results which reflect the realistic behavior of interacting gases with embedded propagating discontinuities.

The Godunov method (Goodunov, 1959) is an explicit, first-order numerical scheme developed in the early 1960's based on the behavior of real gases at discontinuities. The treatment allows for time-dependent transients generated by external sources and interactions among multicomponent gases and is therefore very useful in application to polar wind modeling. The method begins with the gas column, defined in the direction of gas flow (in this case vertical), which is divided into a number of equally spaced segments. Each cell boundary separates gases in neighboring cells. Initial gas parameters such as p, u and r are known everywhere throughout the column. All values are constant throughout each cell but may vary across cell boundaries in staircase fashion so that discontinuities exist only at the boundaries of cells. At $t = 0$, the hypothetical membrane between each cell is allowed to break and expressions for p, u and ρ in each cell are determined at some later time, $t+\tau$, assuming that the values in each cell and on the cell boundaries are constant during the time increment τ. At subsequent times, the location of the new cell boundary is determined based on the movement of the discontinuity away from the original cell boundary location. This propagation velocity can be directly determined since it is a function of the initial gas variables. Gas parameters at the discontinuities are then derived and related to the new cell parameters at $t+\tau$ using Godunov's breakdown formulae or, by a simpler acoustic approximation if the change in dependent variables is small across each cell boundary (Dr. T. Gombosi, unpublished manuscript, 1987). The advantage of the Godunov method is that solutions are obtained within each cell so that all quantities are conserved, i. e., if there is a net mass flux out of one cell, the neighboring cell experiences a similar mass influx. The Godunov scheme thus provides solutions of p, u and ρ which may then be used in the Crank-Nicolson scheme to obtain solutions to the ion energy equations by successive application of each method.

Numerical solutions to the ion energy equations are obtained by using the Crank-Nicolson method. Explicit methods can also be used to approximate parabolic differential equations but they yield a mixed order of error ($O(\Delta T) + O(\Delta x)^2$) because a forward difference was used to replace the time derivative while a centered difference was used on the spatial derivative. In the Crank-Nicolson treatment, approximations to second order expressions similar to equation 2.36 take the form:

$$\frac{CK}{2}\left(\frac{T_{i+1}^{j}-2T_{i}^{j}+T_{i-1}^{j}}{(\Delta x)^2}+\frac{T_{i+1}^{j+1}-2T_{i}^{j+1}+T_{i-1}^{j+1}}{(\Delta x)^2}\right)=\left(\frac{T_{i}^{j+1}-T_{i}^{j}}{\Delta t}\right) \qquad (2.37)$$

where CK represent constants, superscripts j refer to time and subscripts i refer to position. In this approximation, the first term on the left hand side represents a central difference at time t_j and the second term on the left hand side represents a central difference at time t_{j+1}. The time derivative is approximated with a central difference at $t_{j+\frac{1}{2}}$ which is midpoint in the time interval. This method is implicit since the temperature at t_{j+1} is not directly given but is a function of unknown temperatures at adjacent positions as well. The advantage to this method however, is that it provides second-order accuracy in both space and time. The disadvantage is that it requires more work than explicit methods since additional sets of simultaneous equations must be solved for each time step.

To minimize error, or more correctly, to match accuracy between the second order accuracy Crank-Nicolson method and the first order accuracy Godunov scheme, the time dimension is divided in half so that 2 time steps are required for a full solution. In the first time step, the gas dynamic equations are solved using the Godunov scheme. In the second time step, the heat conduction part of the ion (electron also) energy equation is solved for assuming that only heat conduction terms affect the thermal structure. This method is applied again, but in reversed order, so that the heat conduction equation is solved next followed by the gas dynamic solutions. Reversing the order of solution generates higher order terms with opposing signs which then cancel and improve the accuracy in the Godunov scheme to second order by the end of the second step. Schematically, the solution sequence is:

$$F_i^{j+2}=\begin{Bmatrix}L_{gd}(H^+)\\L_{gd}(O^+)\end{Bmatrix}\begin{Bmatrix}L_{hc}(H^+)\\L_{hc}(O^+)\\L_{energy}(e)\end{Bmatrix}\begin{Bmatrix}L_{hc}(H^+)\\L_{hc}(O^+)\\L_{energy}(e)\end{Bmatrix}\begin{Bmatrix}L_{gd}(H^+)\\L_{gd}(O^+)\end{Bmatrix}\{F_i^j\} \qquad (2.38)$$

In this expression, $L_{gd}(H^+)$ and $L_{gd}(O^+)$ represent the linear (first order) partial derivative operators which are applied in first half of a time step to the continuity, momentum and in parts of the ion energy equation. These terms are approximated with the Godunov scheme. The $L_{hc}(H^+)$, $L_{hc}(O^+)$ and $L_{energy}(e)$ denote second order operators which are applied in the other half time step to the heat conduction part of the ion energy equation and the entire electron energy equation respectively. The method is repeated, as shown above, in the second time step with the sequence reversed so that new ion and electron temperatures are obtained and used in the subsequent iteration for the gas dynamic solution. Using this technique results in second order accuracy for multicomponent state variables in the complete set of expressions in the continuity, momentum and energy equations. The model is typically run on a Cray-XMP class computer with 0.1 sec time steps. Model output solutions can be specified at any time step however, for time-independent modeling, usually only the current, or steady-state condition is shown. To reach steady-state, the model must be run for several model hours although the actual time is highly dependent on season and solar cycle with summer, solar maximum conditions having the quickest solution due to the relatively large O^+ production rates and scale heights. A typical steady-state solution is illustrated in Figure 2.2.

The steady-state profiles depicted in Figure 2.2 represent solutions from the polar wind model near solar maximum and illustrate the relative differences in behavior for H^+, O^+ and electrons. A model thermosphere, generated from MSIS-86, was used based on an averaged 10.7 cm solar radio flux of 185 Solar Flux Units (1 SFU= 10^{-22} Watts m^{-2} Hz^{-1}) assuming geomagnetically quiet conditions (Ap=4). These adopted values permit realistic specification of the neutral background gas so that the polar wind model can account for the major collisional and chemical processes for any specified location. An atomic oxygen photoionization frequency of 1.9×10^{-7} sec^{-1} at 200 km was calculated within the model based on F10.7 and date, time (19 UT) and location (73° invariant latitude). In Figure 2.2a, ions execute upward ambipolar flows due to the polarization electric field which develops between the major ion (O^+) and the more mobile electrons in response to the downward directed pressure gradient. The imposed pressure differential permits the more mobile electrons to move upward resulting in a charge separation and the creation of an ambipolar field between the major ion and the electrons. This effects both ions since the O^+ mass is effectively reduced by one-half while the lighter responds to this electric field by accelerating upwards. The major ion, O^+ has a slight upward field-aligned flow of 10's of cm/sec based on a near

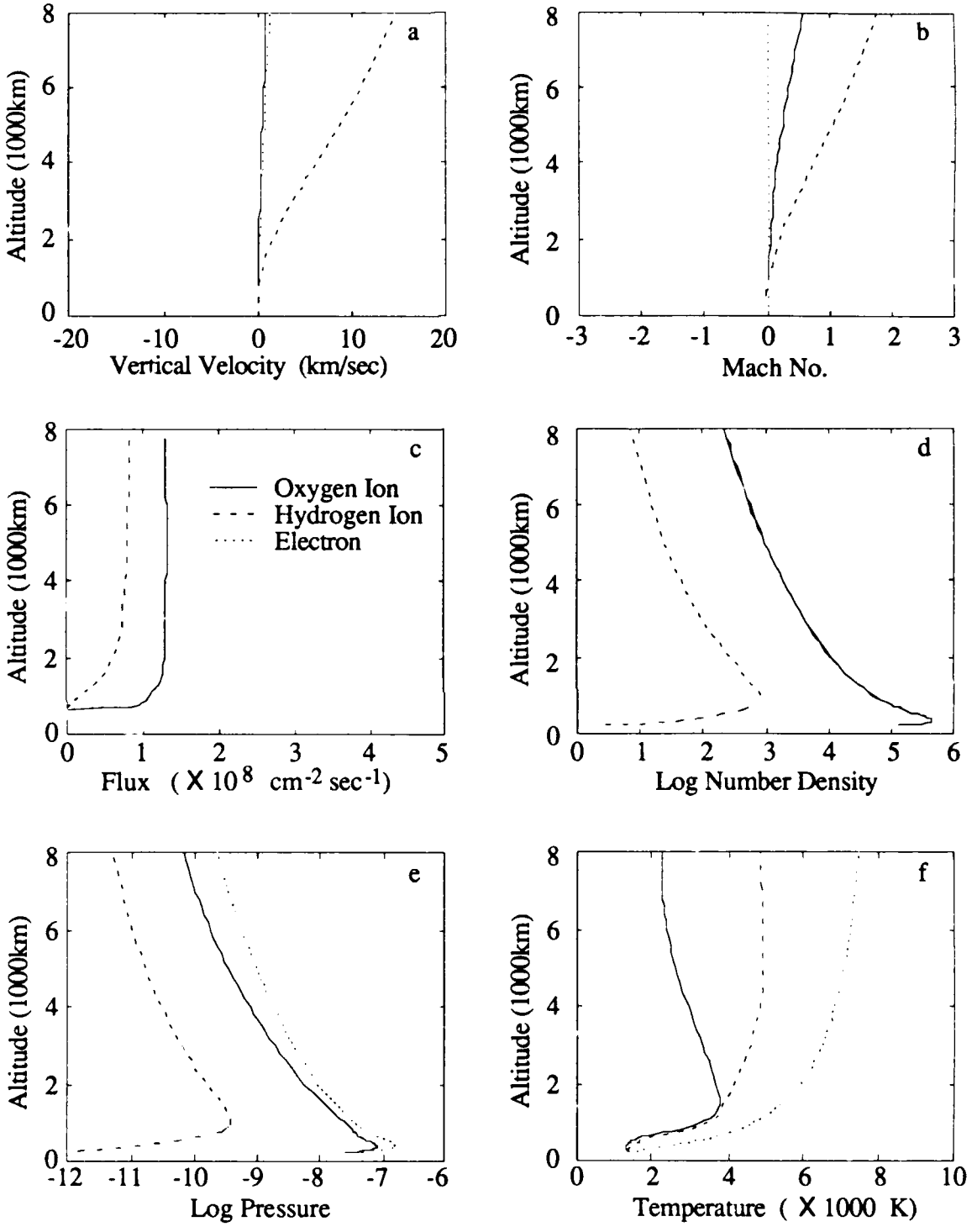

Figure 2.2 Altitude profiles of field aligned ion and electron velocities (a), Mach number (b), flux (c), number density (d), pressure (e) and temperature (f). All profiles represent steady-state solutions for 18:00 UT (06 MLT) on 12 March 1982 for a location near 73° N 278° E geomagnetic.

balance between the upward pressure gradient force (note that there are temperature and number density gradients present) and downward directed gravitational and frictional forces. The lighter H^+ is more effectively accelerated upward by the induced polarization electric field and reaches supersonic velocity near 4000 km. Direct measurements of thermal H^+ field-aligned flows by DE-1 have confirmed the supersonic nature of the these modeled H^+ flows (Nagai et al., 1984). Unfortunately, thermal O^+ flows are difficult to directly measure due to a positive spacecraft floating potential which develops and acts to repel thermal O^+ away from the sensor aperture. Radar measurements at altitudes to 1200 km indicate much higher O^+ flow velocities are possible than these model predictions but this subject will be deferred for now and discussed in more detail in Chapter 5. Density distributions (Figure 2.2d) for each ion reflect local production and loss processes with the O^+ peak located below the H^+ peak due to the smaller atomic oxygen scale height. In Figure 2.2c, the number densities and flow velocities for each species are combined as altitude-dependent fluxes. All flux profiles have been normalized to the 1000 km value to account for the radially-divergent flux tube geometry assumed in the model. The H^+ flux profile reaches an asymptotic value near 5×10^8 cm^{-2} sec^{-1} at 3000 km while O^+ flux magnitudes are somewhat larger (due to larger number densities). This solution represents only one of many possible sets of plasma conditions in the high-latitude ionosphere under steady-state polar wind outflows. In subsequent chapters, the conditions surrounding both steady-state and transient outflows will be examined in more detail to gain insight into the character of the polar wind.

2.3 The Thermosphere-Ionosphere General Circulation Model

While the Gombosi polar wind model can self-consistently derive steady-state solutions of the polar wind outflows, the model assumes a static, non-flowing neutral atmosphere which acts primarily as a net ion source and a net ion momentum sink. This is a valid treatment to first approximation, however, in modeling transient behavior initiated by ionosphere-thermosphere dynamic interactions, it is useful to consider additional influences in the lower portion of the model and treat them as an additional boundary condition. This requires some form of time-dependent information, which must be provided in the form of parameterizations, modeled inputs or observed conditions.

In Chapter 4, the role of low-altitude ion frictional heating in initiating heavy ion upwellings is examined in a time-dependent manner. This requires specification of the horizontal interactions between ionospheric and thermospheric constituents in the low altitude regions where frictional heating is most influential (roughly, below 500 km). Since horizontal velocities are generally larger than the vertical drifts of both ion and neutral

particles, some methodical approach is needed to specify the time-dependent processes which affect each species horizontal motions and ultimately, the frictional heating. The NCAR-TIGCM is particularly useful in meeting these requirements since both the ionosphere and thermosphere dynamic motions are represented in a three-dimensional time-dependent fashion. In this section, a brief description of the TIGCM is provided with emphasis on how the model can be coupled numerically to the polar wind model in studying the effects of time-dependent ionosphere-thermosphere interactions on ion upwelling properties.

The present version of the TIGCM has evolved from simple one dimensional models which were first used to study the density and temperature properties of the thermosphere assuming a static, diffusive neutral gas (Harris and Preister, 1965). These simple one-dimensional treatments met with only limited success since a full chemical description and horizontal transport effects were not included. As computing power expanded, a more robust aeronomic description of the thermosphere was possible and two-dimensional thermospheric models emerged (Richmond and Matsushita, 1975; Dickinson et al., 1975; Maeda, 1976, 1977; Mikkelsen et al., 1981).These models were capable of describing horizontal motion of the thermosphere but were not self-consistent since they relied on empirical models for pressure and temperature values and did not consider any high-latitude momentum or energy sources. Creekmore et al. (1975) developed a three-dimensional model but this treatment still depended on an empirical description of temperature and pressure. Straus et al. (1975a,b) later improved upon the model of Creekmore et al. (1975) by solving the energy equation self-consistently without empirical temperature specifications. Later, advanced three-dimensional models included the effects of magnetospheric electric fields on the thermospheric circulation but neglected the nonlinear terms (e.g., Harris and Mayr, 1975; Mayr and Harris, 1978; Straus and Schultz, 1976) and thus limited the model's ability to match observations. It became obvious that in order to adequately predict the behavior of the neutral thermosphere, fully self-consistent, three-dimensional, time-dependent models which solved the coupled continuity, momentum and energy equations simultaneously including the nonlinear terms were necessary. More recently, Dickinson et al. (1981) introduced the National Center for Atmospheric Research - thermospheric general circulation model or the NCAR-TGCM while Fuller-Rowell and Rees (1980) at the University College at London introduced their own version of a thermospheric general circulation model (UCL-TGCM). Both models solve the fully-coupled three-dimensional, time-dependent momentum, continuity, and energy equations however the UCL model uses a Lagrangian reference frame while the NCAR-TGCM uses a Eulerian grid system. Both models have been validated in their

solutions of general thermospheric densities, winds and temperatures by satellite and ground-based observations and have provided significant insight into the physics and chemistry which influence the neutral thermosphere.

More recently, the NCAR-TGCM has been extended to include a self-consistent aeronomic scheme of the thermosphere and ionosphere. The model now calculates global distributions of O^+, O_2^+, N_2^+, NO^+, electron densities and ion temperatures in addition to both major and minor neutral species. This advanced model, now called the NCAR-TIGCM (Roble et al., 1988), represents a major improvement over previous models which treat the ionosphere and thermosphere separately since mutual couplings between the ions and neutrals can occur at each time step and model grid point leading to improved specification of both temperature and number densities.

The transport equations used in the TIGCM were adapted by Dickinson et al. (1981) from the primitive equations used in tropospheric dynamic meteorology and modified for thermospheric applications. Since the thermospheric and ionospheric gases are collision-dominated over the model range of 90 km to 500 km, the equations used are based on the 5-moment approximation using simplified expressions for the stress tensor and heat flux. Solutions are derived and expressed in a geocentric reference frame (fixed with respect to the rotating earth) based on a spherical coordinate system of latitude (ϕ), longitude (λ) and pressure. Pressure is used as the independent variable making geometric height or geopotential the dependent variable. It is more common to use geopotential because surfaces of constant Φ are perpendicular to the local gravitational force (composed of Newtonian and centrifugal forces). The quantity $\Phi(h)$ represents the potential energy of a unit mass when it is lifted from sea level to some height, h. In this coordinate system, a parcel will have the same potential energy at any point along a constant surface of $\Phi(h)$. The altitude h is related differentially to Φ by:

$$dh = \frac{d\Phi}{g(h)} \tag{2.39}$$

where g(h) is the latitudinal-dependent value of gravity. The vertical coordinate in the NCAR-TGCM is expressed as:

$$Z = \ln\left(\frac{P_0}{P}\right) \tag{2.40}$$

where P_0 is a reference pressure level (5×10^{-4} mb or 50 mPa) at Z = 0. The independent variables of the NCAR-TGCM are therefore, t = time, λ = longitude, ϕ = latitude, and Z = $\ln(P_0 / P)$. A full description of the model equations used by the NCAR-TGCM along with

recent revisions which have advanced the model to its present sophistication are given by Dickinson et al. (1981) and Roble et al. (1988).

The model ionosphere is based on the ion chemistry scheme and rate coefficients, discussed by Roble et al. (1987) and Roble and Ridley (1987). The ion densities are based on the O^+ distribution which is determined first by solving the continuity equation on the TGCM grid at each time step considering production and loss mechanisms as well as transport due to **E×B** drift and magnetic field aligned diffusion. The O^+ transport equation is given by:

$$\frac{\partial n}{\partial t} - Q + Ln = -\nabla \cdot n\mathbf{v} \tag{2.41}$$

where n is the O^+ density, Q is the production of O^+ by ionization of oxygen atoms and dissociative ionization of O_2, L is the loss of O^+ by chemical interactions with O_2 and N_2, and the right hand side represents the transport term accounting for **E×B** drift and magnetic field-aligned diffusion which are derived from the following equations:

$$\mathbf{v} = \mathbf{v}_\perp + \mathbf{v}_{||} \tag{2.42}$$

$$\mathbf{v}_{||} = \left\{ \mathbf{b} \cdot \frac{1}{\nu} \left[\mathbf{g} - \frac{1}{\rho_i} \nabla \left(P_i + P_e \right) \right] + \mathbf{b} \cdot \mathbf{u}_i \right\} \mathbf{b} \tag{2.43}$$

$$\mathbf{v}_\perp = \frac{1}{|B|} \mathbf{E} \times \mathbf{b} \tag{2.44}$$

where $\mathbf{v}_{||}$ and $\mathbf{v}_\perp$ are the parallel and perpendicular velocities with respect to the magnetic field line, **b** is a unit vector along the magnetic field, ν is the O^+ ion-neutral collision frequency with a 1.5 correction factor used in the O^+-O collision frequency, g is gravity, ρ_i and P_i are the ion mass density and pressure respectively, **U** is the neutral wind vector, |B| is the magnetic field strength, and **E** is the electric field vector. The upper boundary condition is diffusive equilibrium while the lower boundary assumes photochemical equilibrium. For low and mid latitude locations, the upper boundary assumption is valid since flux tube in these regions are closed. At polar latitudes however, then flux tubes are open permitting a continual escape of thermal ions which reduces the local densities at all altitudes. Therefore, the density profiles derived from the diffusive (u_i=0) condition result in an overestimation in the topside ionosphere density distribution. This condition will be considered in more detail in Chapter 3

The output fields calculated by the NCAR-TIGCM include neutral temperature, 3-component neutral wind vector (u = eastward velocity, v = northward velocity, w or "vertical velocity" = dZ / dt), $[O^+]$, $[O_2^+]$, $[NO^+]$, $[N^+]$, $[N_2^+]$, electron densities and ion temperature as well as the mass mixing ratios for O_2, O, N_2, $N(^2D)$, $N(^4S)$, and NO. These quantities are determined for 24 pressure surfaces ranging from Z = -7.0 to Z = +5.0 which covers an approximate altitude range from about 90 km to 550 km. For each time step and pressure level, the variables are evaluated at every 5° in latitude and longitude starting at -87.5°S,-180°E and ending at 87.5° N, 180° E, although the output file containing these variables is normally written at 20, 30 or 60 minute intervals of UT. Both the ion and neutral wind pattern are important in determining the global morphology of derived frictional heating and since the high latitude neutral wind pattern is dependent to a large degree on the ion momentum source, the input parameterizations of the high latitude environment which affect the ionosphere will be briefly considered next.

2.3.1 TIGCM Input Parameterizations

Since the model is, for the most part, fully consistent, only a few external parameterizations must be provided. These include (1) solar EUV and UV fluxes, (2) auroral particle precipitation, (3) high-latitude ionospheric convection patterns, and (4) amplitudes and phases of tides from the lower atmosphere. The first three are important influences for the derived horizontal ion and neutral wind field required for this study and will be discussed further.

The solar EUV and UV fluxes represent the main energy source for the neutral thermosphere, the primary ionization source, and a major catalyst for many subsequent chemical reactions initiated by the photoabsorption. Accurate specification of the solar EUV and UV fluxes are therefore a major concern. Spectral characteristics from 50 Å to 1750 Å have been developed from solar EUV flux measurements made by the Atmospheric Explorer satellites during solar minimum and maximum, as discussed by Hinteregger (1981), Hinteregger et al. (1981), M. R. Torr et al. (1979), M. R. Torr and D. G. Torr (1985) and scaled according to the method of Hinteregger et al. (1981) based on the 10.7 cm solar radio flux. Nighttime ionizations from dark sky and backscattered radiation at several wavelengths are also considered. Absorption and ionization cross sections are based on Hinteregger et al. (1981), however, modifications to some of the absorption and ionization cross sections have recently been made and are given by Roble et al. (1987) and references therein.

NCAR-TGCM AURORAL OVAL

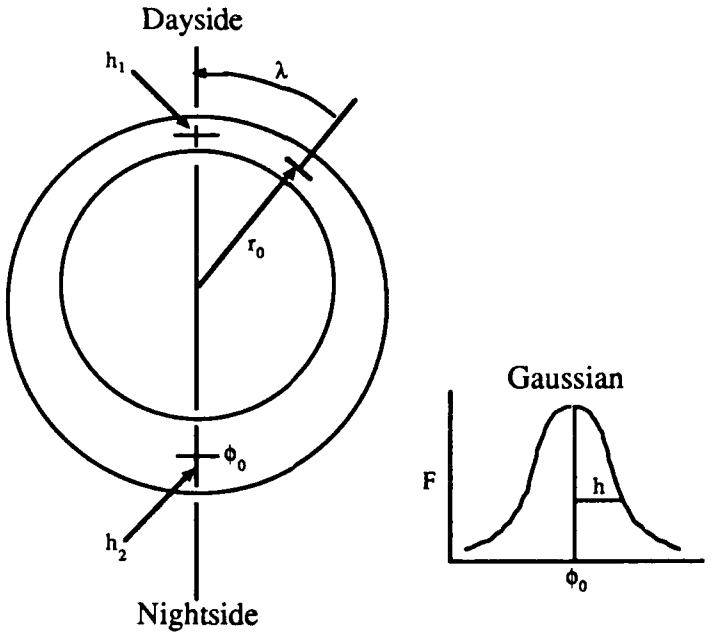

Figure 2.3 Illustration of the auroral oval model parameterized in the NCAR-TIGCM simulation (from Roble and Ridley, 1987). Subscripts represent different parameters corresponding to daytime and nighttime conditions

TIGCM AURORAL OVAL		
Parameters	**Description**	**Specifics**
f_0	angle from center of gaussian oval	degrees
r_0	radius of oval	degrees
l	angle from throat	degrees
h	half-width of gaussian oval in latitude	degrees
2a	mean electron energy	keV
E	energy flux	ergs /cm^2 sec
F	number flux = f (E / 2a)	$cm^{-2}sec^{-1}$
H_p	hemispheric power = f (F, h, a, r)	gigawatts

Table2.3 A summary of the parameters used in describing the auroral oval in the NCAR-TIGCM.

High latitude particle precipitation in the auroral oval, cusp, and polar cap are important sources of heating and ionization which can directly affect the ion and neutral density and momentum budgets. These influences and their parameterizations have been discussed in detail by Roble and Ridley (1987). The characteristics of the auroral oval used in the NCAR-TIGCM are shown in Figure 2.3 and a description of the parameters which define the oval given in Table 2.3. The auroral oval is described as a gaussian in latitude with the daytime and nighttime parameters defining the latitudinal extent of the oval and a cosine function defining its variation in λ. Once the shape has been defined, various forms of particle precipitation can be applied based on these boundary locations. Particle precipitation is based on information contained within several empirical models (Whalen, 1983; Reiff, 1984; Hardy et al., 1985; and Fuller-Rowell and Evans, 1987) as well as information taken from auroral images by DE-1 satellite images (Frank et al, 1982; Craven et al., 1984). Particle distributions are assumed to be Maxwellian with an isotropic pitch angle distribution, a total energy flux E, and a characteristic energy (one half the average energy) α. The characteristic energy of the precipitating particles is defined differently for daytime and nighttime conditions with a cosine function in λ linking the two regions. The energy flux within the oval is modeled as a gaussian in latitude and also relative differences between day and night conditions. The entire oval is offset relative to the geomagnetic pole towards magnetic midnight with the radius of the oval placed slightly equatorward of the ion convection boundary. Precipitating particle fluxes in the cusp region are treated separately from the auroral component. They are described by two gaussians in magnetic latitude and magnetic longitude located at the throat region of the ion convection and move in latitude and local time in response to changing interplanetary or geomagnetic conditions. The cusp soft particle precipitation covers an area of about 5° in latitude and 2 hours of magnetic local time.

The polar rain or drizzle within the polar cap is simulated by a uniform flux of low energy particle precipitation which falls off abruptly near the poleward edge of the auroral oval. The hemispheric power is a function of some of these parameters and acts as a single index for defining the auroral particle precipitation for a particular run. For any given flux and characteristic energy, the ionization rate as a function of height is derived from the analytic relationship of Lazarev (1967) which has been modified for an isotropic distribution. This same analytic expression has also been adopted in the polar wind model to improve topside density distributions of O^+ and H^+ in the winter polar ionosphere.

The high-latitude pattern of ion drift is an important TIGCM parameterization for determining additional momentum and energy sources for the neutral gas caused by the ion-drag and Joule heating respectively. The ion drifts are not calculated self-consistently

within the model but are, instead, specified at low and middle latitudes from the empirical model of Richmond et al. (1980) and at high latitudes from the empirical model of Heelis et al. (1982). Since the ion drifts are prescribed based on empirical input, no feedback effects occur on ion drifts due to neutral motions, although ion-neutral collisions are included to modify the E and lower F region ion drifts. For high latitude ion convection patterns, the empirical model of Heelis et al. (1982) requires 13 parameters to describe properly all relevant convection features. The input parameters are given in Table 2.4. and a typical potential distribution illustrated in Figure 2.4.

Heelis Ion Convection Model		
Parameters	**Description**	**Specifics**
Θ_0	radius of convection reversal boundary	degrees
Θ_c	phase angle of auroral oval	degrees
ϕ_d	angle of zero potential line on day side	degrees
ϕ_n	angle of zero potential line on night side	degrees
ϕ_d^+	angular dimensions of day side entrance region off of ϕ_d towards evening	degrees
ϕ_d^-	angular dimensions of day side entrance region off of ϕ_d towards morning	degrees
ϕ_n^+	angular dimensions of night side exit region off of ϕ_n towards morning	degrees
ϕ_n^-	angular dimensions of night side exit region off of ϕ_n towards evening	degrees
Ψ_m	maximum potential in morning cell	kV
Ψ_e	minimum potential in evening cell	kV
R_1	electric field variation inside polar cap	exponential factor
R_2	electric field variation outside polar cap	exponential factor
Offset	pattern displacement toward midnight	degrees
Dusk Offset	pattern displacement toward dusk	degrees

Table 2.4 A description of the parameters used in the Heelis model to describe the ion convection pattern used in the NCAR-TIGCM.

The Heelis model has been incorporated into the NCAR-TIGCM formulation and simplified somewhat so that only three variables need to be specified. Convection patterns are now derived based on a parameterized input of the total cross-cap potential, the hemispheric power, and the magnitude of the IMF B_y component. The hemispheric power is determined from TIROS/NOAA satellite measurements (NOAA, 1984) while the IMF components are obtained from satellite measurements such as those available from IMP-8.

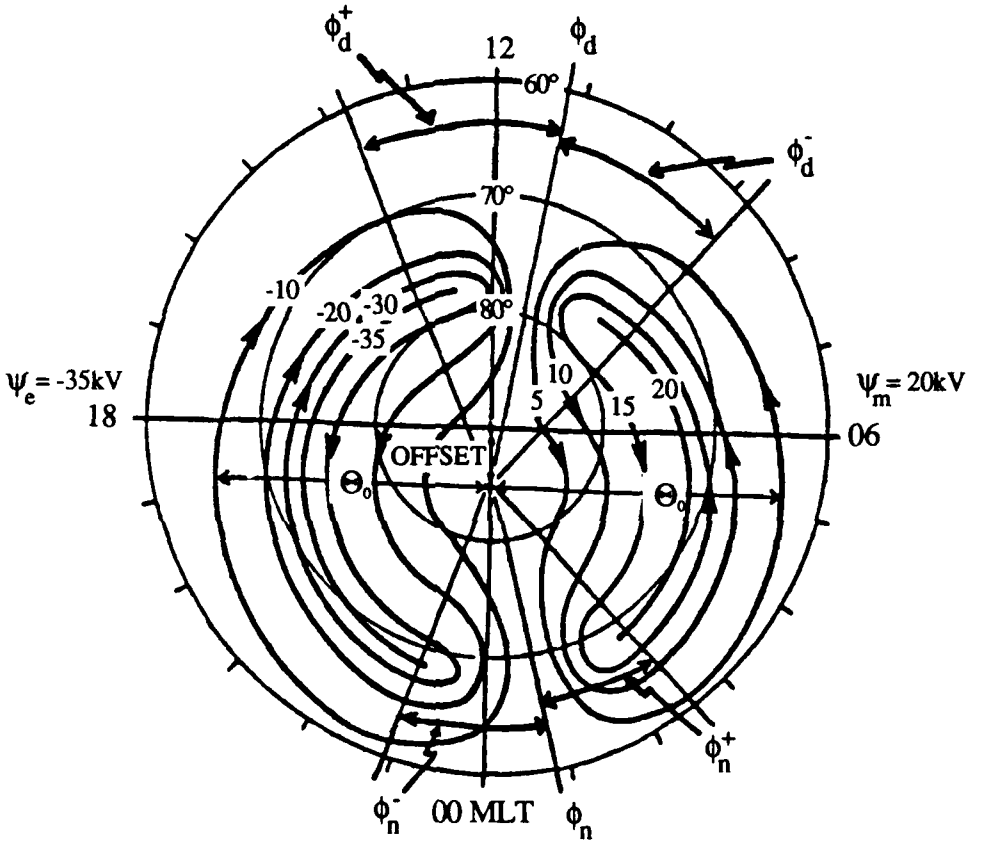

Figure2.4 Illustration of the ion convection model parameterized in the NCAR-TIGCM simulation. A total cross cap potential drop of 55 kV is distributed unequally between the dusk and dawn convection cells (after Thayer, 1990).

The total cross-cap potential is based on one of the formulae in Reiff and Luhman (1986) as:

$$\Phi(\mathrm{kV}) = 12.7 + 0.041\, v_{sw}\, \min(B_t, 9)\, \sin^3\left(\cos^{-1}\left(\cos\left(\frac{B_z}{B_t}\right)/2\right)\right) \qquad (2.45)$$

where v_{sw} is the velocity of the solar wind in km/sec, B_z and B_t the the north-south and total interplanetary magnetic field in nanotesla. The total potential is divided between the

morning and evening cells described by the Ψ_m and Ψ_e parameters, where the percentage of partitioning is dependent on the value of the IMF B_y component. The dusk sector is given a negative potential which is typically 60% of the total cross-cap potential when B_y = 0, with the remainder distributed across the dawn sector. The IMF B_y input also modifies the parameters which determine the configuration of the entrance and exit regions of the ion convection (i.e., ϕ_d, ϕ_n, ϕ_d^+, ϕ_d^-, ϕ_n^+, ϕ_n^-) so that the dynamic shape of the convection throat and the convection reversal boundaries are properly accounted for. This influence is important for this study since quasi-permanent regions of enhanced frictional heating are often found in these locations due to the presence of large relative ion-neutral drift velocities.The hemispheric power, determined from TIROS/NOAA satellite measurements (NOAA, 1984) along with the total cross-cap potential, based on satellite measurements such as IMP-8, determine the radius of the boundary for reversals in the ion convection given by the parameter Q_0. The remaining parameters, R_1, R_2, Offset, Dusk Offset are set as constant values. Once the convection pattern is is obtained, it is vectorized and incorporated into the model run to obtain ion drag and Joule heating terms at each model time step and grid location.

2.3.2 TIGCM Simulations

Due to the unlimited range of input parameterizations possible, the TIGCM can be used to simulate a wide variety of solar and geophysical conditions. Solar cycle conditions can be characterized by choosing the appropriate F10.7 solar radio flux while various levels of geomagnetic activity are simulated by adjusting the ion convection pattern and/or precipitating particle spectra. For each TIGCM simulation, the input parameterizations can be held constant throughout the model period (normally 24 hours) or, time varying input parameters can be used. In the first case of fixed inputs, solar EUV/UV fluxes, ion convection and particle precipitation are time-invariant resulting in solutions which are "diurnally reproducible". Since the geographic pole is offset from the rotational axis, the sun-aligned, geomagnetically-controlled ion convection pattern exhibits a strong UT dependence when viewed in geographic space. The related ion drag terms and related forces introduce their UT dependencies on the neutral wind so that some local accelerations are a function of universal time and are non-zero even though parametric inputs are constant. Diurnally reproducible means that the model has reached a state where solutions for a given UT will be reproduced again if the model is permitted to run for another 24 model hours (1 UT day later). This condition is an unnatural state considering the high degree of variability inherent in the solar wind / magnetosphere interaction, however it does provide a baseline solution which is useful for relative comparisons (i e winter vs. summer

or solar maximum vs solar minimum). The other option, which depends on time-varying input parameterizations, is useful for simulating storm-time variability or for reproducing conditions on a particular day or period. In the course of this research, both types of simulations have been used in studying frictional heating. Diurnally reproducible simulations are easier to generate but lead to unnaturally low ion frictional heating (in one case, by two orders of magnitude). This underestimation occurs since, with time, the neutral wind pattern assumes the character of the ion winds due to the near-constant ion drag forcing. As the neutral flow increases speed, the relative ion-neutral drift velocity (proportional to the frictional heating rate) decreases so that actual heating may be different from that given in the diurnally reproducible case. For this reason, accurate specification of frictional heating rates for a given day or period are best represented by time varying (cross cap potential) conditions. In Chapter 4, a time-dependent TIGCM simulation is employed to simulate the frictional heating history of a convecting flux tube. For this case, realistic variations to the cross cap potential resulted in order of magnitude variations in the derived ion frictional heating rates.

The three-dimensional global solution set of neutral and ionospheric parameters produced by the TIGCM is contained within a large number of arrays. Access and analysis of this information has been greatly improved by the development of the NCAR-TIGCM post-processor package by Killeen and Roble (1984) with further updates and modifications developed by Dr Allan Burns. This original software permitted a term-by-term analysis of the momentum and energy equations by interpolating the solutions in three-dimensional space for any modeled location. The utility of this diagnostic package was further enhanced by follow-on modifications that now permit forward and backward trajectories to be computed in either geographic or geomagnetic space (Killeen and Roble; 1985). When the two capabilities are coupled together, ionospheric and neutral gas parameters are readily available along any neutral parcel or flux tube trajectory. This capability is an important complement to this research since all variables needed to calculate ion frictional heating (the second term in equation 2.18) are readily available from this post-processor package. By coupling TIGCM solutions of time-dependent frictional heating rates, obtained in Lagrangian form along the trajectory of a flux tube, one can extend the usefulness of the one-dimensional (Eularian) polar wind model to a wider variety of high latitude processes.

2.4 Incoherent Scatter Radar

The theoretical tools described above can provide extensive insight into the steady-state and transient processes effecting polar wind flows. Observations of these phenomena

are equally useful since they provide a complimentary perspective of the modeled phenomena in addition to validating the model predictions. One of the most powerful observational techniques for this purpose involves the use of incoherent scatter radar (ISR) to remotely sound the F-region ionosphere and derive a number of important plasma variables. The utility of the ISR technique is exploited in Chapter 5 to obtain simultaneous observations of low altitude frictional heating and the related transient field-aligned flows. As a prelude to these observations, a brief description of radar theory and radar application is presented here.

2.4.1 Incoherent Scatter Radar Theory

In applying the classic Appleton-Hartree equation to the propagation of radio waves in the ionosphere, the medium is considered, to first approximation, to be a continuous dielectic so that radio wave frequencies (f) greater than the local plasma frequency (f_p) cannot be reflected back. These types of waves are almost unattenuated as they pass into space. However, as pointed out by Thomson (1906), electrons are capable of scattering electromagnetic waves at all frequencies so a very small amount of energy can be scattered back towards the transmitter. Later, Fabry pointed out that the random thermal motions of the electrons would produce Doppler-broadening of the returned signal causing the intensity of the scattered power to fluctuate about some mean value determined by the sum of the reflected powers. This gives rise to the term incoherent since all electrons do not share a common thermal velocity. Since the radar cross section of an electron is extremely small, original predictions were that incoherent scattering could not be detected without an exceptionally large reflector antenna. Bowles (1958) was the first to report detection of incoherent scattering in the ionosphere and made the important discovery that the Doppler width of the returned spectrum was not:

$$\frac{\delta f}{f} \cong \frac{\langle v_e \rangle}{c} \tag{2.46}$$

where c is the speed of light and $\langle v_e \rangle$ the average thermal velocity ($\langle v_e \rangle = \sqrt{2k\,T_e / m_e}$ where k is Boltzmann's constant, T_e the electron temperature and m_e the electron mass) but was proportional to $\langle v_i \rangle / c$ instead. He later correctly deduced that the limited frequency range of the returned signal was caused by coulomb attractions with the ions which limited the electron motion. Subsequent theoretical treatment indicated that the returned reflections are from density irregularities in the electrons due to the presence of ions and that the Doppler broadening is governed by the random thermal ion motion and not that of just electrons.

The scattering of radar signals by density irregularities can be simply understood by examining the ratios of two characteristic scale lengths in the extremes. From the Bragg scattering formula, signals will be returned by the presence of irregularities having a spacing of λ_p. The spacing, λ_p, is defined along the perpendicular bisector of the angle between incident and scattered wave directions. For backscattered returns, $\lambda_p = \lambda/2$ where λ is the radar wavelength and this represents one of the fundamental scale lengths. The other scale length depends on the plasma characteristics of temperature and density. As described by Fejer (1960) and Hagfors (1961), ions organize the electron density fluctuations in the plasma over a distance greater than the electron Debye length (D_e) where:

$$D_e = \sqrt{\frac{kT}{4\pi n_e e^2}} \tag{2.47}$$

and all the usual variable definitions apply. Therefore, ions play an important role in scattering processes whenever $\lambda_p >> D_e$. For backscatter experiments, a parameter α is defined as $4\pi De/\lambda$. In the case where $\alpha > 1$, the scattering comes from individual electrons as described by Gordon. In the ionosphere below about 2000 km, De is usually less than 1-2 cm (Evans, 1974) and for most HF thru UHF radars, $\alpha < 1$ so the scattering is best thought of as arising from transient local increases in the electron density surrounding each ion. For these cases, the Doppler width, W_i of the returned spectrum is proportional to the ion thermal speed:

$$W_i \approx 2\frac{\langle v_i \rangle}{\lambda} \tag{2.48}$$

A schematic diagram of the Doppler spread due to scattering from the thermal fluctuations of ions (the so called "ion line") is presented in Figure 2.5. The spectrum profile can be described by the presence of two ion-accoustic waves, one moving away and the other towards the radar at the mean thermal speed of the ions. Although the scattering is from electrons, the scattered reflections really represent the ability of the ions to organize the density variations among the electrons through coulomb interactions. Coupling between ions and electrons depends on their thermal velocities so that the spectrum profile changes shape whenever $T_e > T_i$. If the ion temperature is held constant and the electron temperature increases,the ion acoustic velocity increases thereby spreading the spectrum. Additionally, there will be more electrons moving faster than the wave at higher T_e so there will be less damping. Both effects modify the profile shape producing a broader spectrum with more pronounced wings. One additional factor which affects the spectral width is the

ion mass. Since the ion acoustic velocity is inversely proportional to the ion mass, the Doppler width will vary as a function of composition (or mass). In the simplest case, if a O^+ plasma was replaced by a He^+ plasma having the same temperature, the spectral width of the return profile would double; similarly, the H^+ spectra would be twice as wide again.

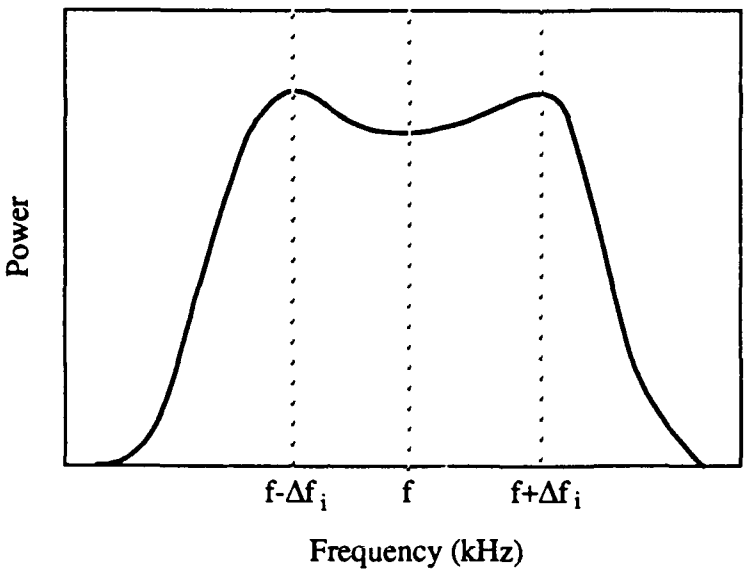

Figure 2.5 Sketch of the hypothetical frequency power spectrum of incoherent scatter signals in the limit of large radar wavelength compared to the plasma Debye length and for $T_e = T_i$. Backscatter from the transmitted radar frequency (f) is Doppler shifted based on the ion acoustic velocity.

Finally, the area under the power spectrum curve represents the total power returned. For a vertically-directed radar, the total reflected power is also defined by:

$$P_s = P_t n_e \sigma c \tau \lambda^2 L / r^2 \qquad (2.49)$$

where Ps is the backscattered power, P_t is the transmitted power, ne is the electron density, σ is the effective cross section for scattering, c is the velocity of light, τ is the radar pulse length, L is the system loss factor and r is the range of the illuminated volume element. This relationship allows direct reduction of the returned power into electron density since the range is related to the time delay on the returned signal. By allowing for this r^2 dependence, it is possible to obtain a profile in electron density ("power profiles") however, an implicit assumption about horizontal stratification must be made but is not necessarily always true. Additionally, σ is related to the ion-electron temperature profile (as is α) so that corrections are required to improve accuracy for derived densities in the F-region. The power profiles thus provide initial but directly measurable information about

the plasma under illumination by the radar. All other plasma quantities, including refined electron density values can be obtained from the power spectrum.

By now it should be clear that the return signal power spectrum represents a rich source of information about the plasma medium. There are actually two return signal components to the power spectrum. One component, the "electron line" dominates the return spectrum when $\alpha >> 1$ or stated another way, when the radar wavelength gets so small that only individual electrons can respond to the changing electric field associated with the wave. This line provides useful information but will not be considered further since it occupies a broad frequency range which is difficult to measure at once given the limited bandpass of the radar receiver. The ion line is easier to measure since it is much narrower in frequency range and has been traditionally fitted to determine characteristics about the plasma. The ion line dominates the power spectrum whenever α is less than unity or whenever λ is smaller than the Debye length. In terms of absolute size, the ion line comprises a very narrow band and is typically about 100 times narrower than the electron line when $\alpha < 1$. For an ion acoustic velocity of 1000 m/s, the width of the ion line return at Sondrestrom (1290 MHz operating frequency or 20 cm wavelength) is $(4\pi/0.20 \times 1000)$ or about 1×10^4 Hz which is very small considering all the information stored within its shape Since knowledge of incoherent scatter theory is well advanced, a number of techniques have been developed which allow one to extract key plasma parameters such as ion and electron density, drift velocities and ion and electron temperatures from the power spectrum. It is impossible of course to derive all these variables simultaneously however, with suitable models and a methodical approach, the returned signal can provide considerable information about the nature and dynamics of the medium under investigation.

To obtain physical properties of the plasma, the power spectral density function must be analyzed in either the frequency or time domain. In the frequency domain, the signal voltage is passed to a series of bandpass filters centered on different frequencies. The average power output from each of these filter bins gives an estimate of the power spectral density of the signal at the various filter frequencies. In the time domain, the scattered signal is sampled as a function of time and the average correlation as a function of time lag is computed to obtain an autocorrelation function (ACF). The power spectral density function and the ACF contain equivalent information since they form a Fourier transform pair. The ACF method is used at most ISR facilities since one can take advantage of digital signal processing techniques that are somewhat cleaner than frequency analysis. Once the signal has been digitized, no systematic drifts occur and the averaging of lagged products can be handled by computer.

The electron density power profile is the only parameter which can be directly determined from total power versus height. All other parameters require measurements of the signal spectra (or equivalently, the ACF). By measuring the returned spectrum (or the ACF of the signals) as a function of height, it is possible to measure (corrected) n_e, T_e and T_i simultaneously however as α approaches unity (a function of n_e) the spectrum shape changes making it difficult to recover T_e/T_i. Through an iterative process involving the assumed temperature ratio and $\alpha = 0$, successive approximations of the scattering cross section can be made, then the power profile can be corrected for the T_e/T_i and α dependence to deduce a corrected n_e, then α, and finally, the ion and electron temperatures. T_i accuracies on the order of 5% can be obtained in this manner (Evans, 1974). Ion drifts result in the entire spectrum having a small Doppler shift as shown in Figure 2.6.

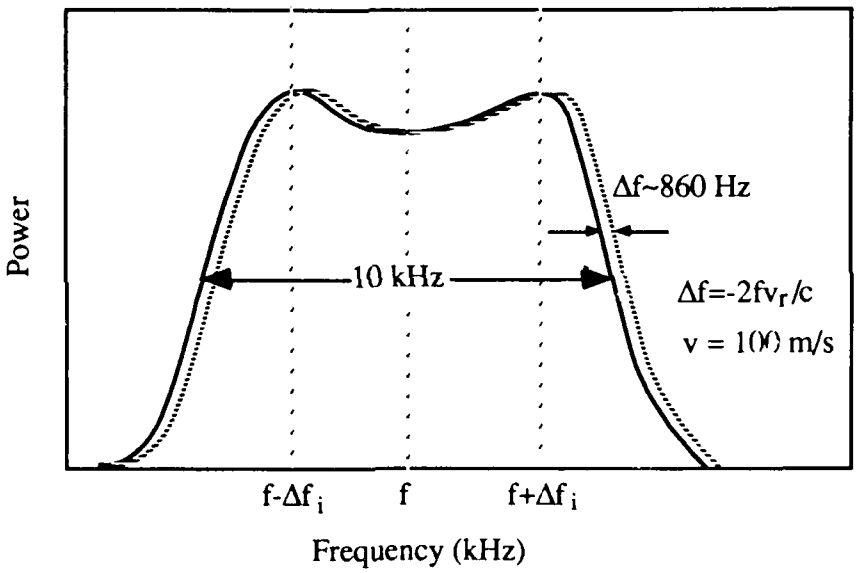

Figure 2.6 Hypothetical power spectral density profile (ion line) indicating the effects of a net drift in the line of sight velocity component of the ions.

From the offset in frequency, Δf, the line of sight ion velocity can be determined from the relation:

$$\Delta f = \frac{(\mathbf{k} \cdot \mathbf{v})}{2\pi} \tag{2.50}$$

where $\mathbf{k}$ is the ion wave number and $\mathbf{v}$ the ion drift velocity vector. Orienting the radar receiver in mutually orthagonal directions in successive fashion allows one to obtain a full vector representation of the ion drift vector in spatial and temporal homogeneity are

assumed during the scan sequence. Additionally, with application of a geomagnetic field model in the F-region, the ion flow velocity yields the perpendicular electric field components from the relationship $\mathbf{E} = \mathbf{B} \times \mathbf{V_i}$. Once the thermal properties are derived, a modeled neutral atmosphere together with n_e measurements can be used to derive Hall and Peterson conductivities. These conductivities, when combined with perpendicular electric field and ion drifts measurements permit the height-integrated Joule heating rate to be calculated. Further descriptions of this procedure will be deferred until Chapter 5. Table 2.5 provides a summary of the wide variety of ionospheric parameters available, either directly or indirectly, using the ISR technique.

Derived Geophysical Parameters			
Ionospheric Variable	Symbol	Ionospheric Variable	Symbol
raw electron density	n_e'	electron energy flux	Q_e
corrected electron density	n_e	line of sight velocity	v
ion temperature	T_i	perpendicular current	**J**
electron temperature	T_e	field-aligned current	$j_{\|\|}$
electric field	**E**	collision frequency	ν_i
Hall conductivity	σ_H	ion composition	n_i
Pedersen conductivity	σ_P	energy spectrum of precipitated electrons	f(E)

Table 2.5 Summary of ionospheric quantities which are available from incoherent scatter radar measurements.

The Sondrestrom radar has a number of different operating modes which are used to make two basic measurements: power versus range and the autocorrelation function versus range. A number of pulse schemes can be used to obtain these measurements including a short pulse (60 μs), long pulse (320 μs) and two multipulse modes. The short pule provides the total power measurement from which the power profile of electron density is obtained. Multipulse modes are optimized for improved range resolution in the lower F and E regions and will not be considered here. The long pulse is best suited for F-region and topside plasma measurements since it provides better signal to noise ratio at the expense of less resolution in range.

In the long pulse mode used in this research, the Sondrestrom radar transmits a 320 μs signal followed by a brief (13.2 ms) listening period during which all backscattered

radiation is collected (see Figure 2.7). The listening duration is long enough to maintain coherence with the backscattered signal from the preceding pulse so that no ambiguity occurs in identifying the source pulse for each receive period. The interpulse period (IPP) consists of the time between successive signal transmission starts. During this period, the entire pulse is transmitted, received and initially processed. Once transmitted, a pulse of length τ illuminates a volume of space of range $\Delta r = \tau \times c$. By adjusting the receiving or listening period, a specific altitude or range gate is determined for the signal returns. Successive pulses (at the same pulse widths) enhances signal returns and improves overall signal accuracy later when longer signal integrations are performed

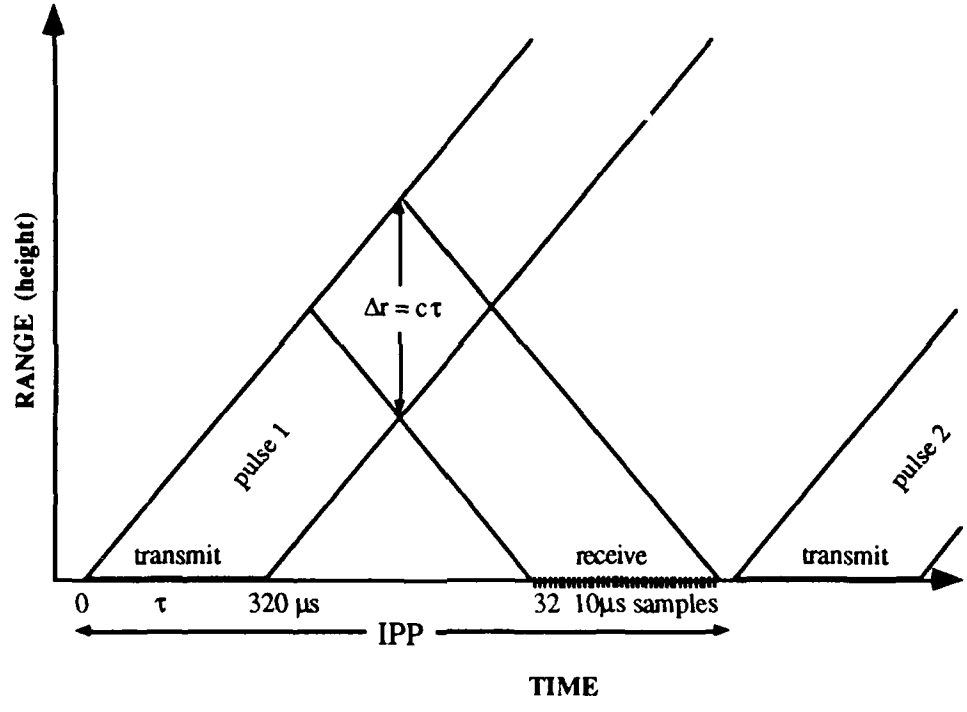

Figure2.7 Range-time diagram indicating the relationships between range and size of al illuminated plasma volume and the corresponding time intervals for transmitting pulses and collecting the backscattered return.

The long pulse correlator is used to compute autocorrelation coefficients whenever single long pulses are transmitted. This digital processing technique accumulates 32 samples of 10 μs duration and then forms 32 lagged products for each time interval. This involves computing the mean product of pairs among 32 samples for 0 to 31 time lags: 32 products for 0 lag, 31 products for 1 lag (10 μs), etc., and finally, one product for 31 lags (310 μs). The zeroth lag is the product of each 10 μs sample with itself; the first lag is the product of

each sample with its neighbor and so forth. The mean correlation as a function of lag is computed from these values to obtain the ACF. Due to the method used to sum the lags, the range resolution is not directly related to $\tau \times c$ (pulse duration and speed of light). Weighting factors enter into the measurements that improve the range resolution to $\tau \times c/2$ (de la Beaujardiere, 1984) or about 50 km for the long pulse. Nine correlation functions may be formed with 8 signal gates used for data accumulation and the ninth gate is set at a range distant enough that no signal is available so that a system noise level can be determined. The accuracy of both the density and spectral measurements depends on a number of factors. Range resolution depends on the pulse width which was 320 μs for the field-aligned ion velocity measurements. Greater range resolution is possible with shorter pulse widths but since the study sought to maximize range (altitude) at the expense of resolution, 320 μs pulses were used. This pulse width also had the advantage of improving signal to noise ratio which limiting accuracy in the uppermost gates due to very low ion densities. The measured SNR also depends on bandwith and range but both of these are fixed based on experiment design.

The above description assumed successive 320 μs pulses were always used when in fact, the 60 μs pulse modes was also employed to derive the power profile and obtain horizontal electric field measurements for the Joule heating calculations. The full dwell sequence used by the radar to obtain heating and vertical velocity data will be discussed more extensively in Chapter 5 however, it is apparent from the above discussion that the ISR hardware and software systems are both flexible and versatile when used to probe the high-latitude F-region.

2.5 Dynamics Explorer Satellite Observations

In-situ measurements of the ionosphere/thermosphere environment by the Dynamics Explorer-2 spacecraft (DE-2) provide a wealth of information regarding the dynamic processes associated with frictional heating and thermal ion upwelling. Data collected along single orbit passes through the high latitudes can be analyzed individually, to gain insight into the magnitudes of heating and the ionospheric response, or collectively, to derive the global morphology of frictional heating. Used in either manner, the satellite data provide a greater coverage than is possible from the ground-based observations provided by incoherent scatter radar. The locations, magnitudes and behavior of low-altitude frictional heating using both these methods are considered in Chapter 5 and related to in situ and higher altitude ion upwelling characteristics. In the following subsections, a brief description of the the DE-2 satellite, onboard sensors and data used in this research

are provided to highlight the utility and uniqueness of the data set for describing thermosphere/ionosphere energy coupling.

2.5.1 Dynamics Explorer Mission

The Dynamics Explorer mission was developed to investigate the energetic and dynamic coupling processes between the magnetosphere, ionosphere and the thermosphere. The mission design called for polar orbiting satellites operating at different altitudes with an instruments capable of measuring relevant plasma and neutral gas components in addition to electric and magnetic fields. The two satellites, known as Dynamics Explorer-1 (DE-1) and Dynamics Explorer-2 (DE-2) were placed into high and low orbits respectively in August 1981 to meet these requirements. Both satellites were inserted in coplanar orbits with inclinations near 90° so that high and low altitude measurements could be made along the same or neighboring flux tubes. Table 2.6 summarizes the initial orbital configurations of both spacecraft. With high inclination orbits, the satellite pair do not precess however the Earth's changing position with respect to the inertial orbit planes permits all local times to be sampled by north and southbound passes after approximately six months.

Satellite Orbital Parameters		
Characteristic	**DE-1**	**DE-2**
Apogee (km)	24,875	1300
Perigee (km)	675	305
Inclination (deg)	90	90
Orbital period (min)	440	101
Change of latitude of perigee (deg/day)	-0.298	-3.34
Nominal lifetime (months)	>36	25.7

Table 2.6 Summary of initial orbital characteristics for the high (DE-1) and low (DE-2) Dynamics Explorer spacecraft.

Unfortunately, DE-2 did not reach it's expected apogee which decreased it's lifetime and introduced an altitude bias in the local time sampling. The local time bias effects coverage above 600 km where the majority of orbits occur in the 9-12 MLT and 21-24 MLT sectors. This does not affect heating rate calculations in Chapter 5 since only data below 600 km are used but it does limit modeled density comparisons in Chapter 3 to either

of these two time periods. The DE-1 satellite is still operating and providing useful data. In fact, it was the Energetic Ion Mass Spectrometer (EICS) on DE-1 which first identified the presence of predominantly O^+ upward fluxes across the polar cap (Shelley et al., 1982) generating interest in the both the sources as well as the sinks for these flows. The DE-2 spacecraft reentered the atmosphere in February 1983 but not before amassing an extensive multi-instrument data set that is particularly useful in quantifying high-latitude ion energetics.

Telemetry from the DE satellites were received at the NASA ground tracking and data acquisition stations and transmitted to the Science Data Processing System (SDPS) at Goddard Space Flight Center. The SDPS is a Xerox Sigma-9 linked remotely to the principle investigators' supporting institutions and acts as a central repository for telemetry data while providing the ability to process the DE data into Mission Analysis Files and data summary plots. Satellite data in these forms can then be shared with other investigators to study a wide variety of coupling processes. As part of the cross flow and exchange of data from the DE-2 satellite, a Dynamics Explorer-2 satellite database has evolved locally at the Space Physics Research Laboratory under the guidance of Professor T. L. Killeen. Originally containing only Fabry-Perot Interferometer data for the Winter '81-'82 and Winter '82-'83 periods, the database has expanded significantly (to cover both Fall and Spring periods) as more FPI data was processed through the Sigma-9 and as more shared data from other experiments became available. At present, the database contains 16 different data types measured from 6 separate experiments onboard DE-2 in addition to 12 geophysical indices for each of the corresponding measurements. The satellite data is available on-line and in 8-second resolution thus permitting a wide range of uses. Due to satellite instrument duty cycles and onboard power limitations, not all of these data are available at the same time however, over 200 northern and southern hemisphere polar passes are currently on-line containing periods when a full complement of data types are available.

In this work, the data from six separate experiments are combined to derive ion frictional heating rates and then related to upwelling ion characteristics in both the low and high altitude regimes. The instruments and the data types used are summarized in Table 2.7. Each of these instruments has a earlier counterpart which flew on the Atmospheric Explorer series satellites so they represent proven capability. A special issue of Space Sciences Instrumentation (Hoffman, et al., 1981), and references cited within, trace the technical evolution and provide a full description of each experiment. Here, a brief summary of each instrument and data type, used later in Chapters 3 and 5, are provided.

2.5.2 Dynamics Explorer-2 Data Set

The DE-2 data set is unique in that it represents the first time satellite observations were made simultaneously with measurements of neutral and ion wind vector components. When combined with the other plasma and neutral gas measurements, the data provide a significant improvement in the experimental description of ionosphere/thermosphere interactions. Since the ion frictional heating rate (described by the second term in equation 2.18) is dependent on neutral and ion winds, temperatures (through the collision terms) and densities, the full DE-2 instrument compliment can be used to obtain ion frictional heating rates. In the following paragraphs, a brief description of each instrument is provided.

The Retarding Potential Analyzer (RPA) provided thermal plasma diagnostics from two separate sensors mounted approximately normal to the spacecraft velocity vector. Sensor heads measure the thermal ion energy spectrum in the satellite frame. A least squares fit to the ion collector current verses retarding potential curves from the RPA sensor provides information on the thermal ion density, temperature and bulk plasma flow in the direction of the satellite velocity. This technique involves finding the mean energy

DE-2 Data Set			
Experiment		**Measurement**	**Accuracy**
Retarding potential analyzer	RPA	T_i meridional ion wind	2% ± 50 m/s
Ion drift meter	IDM	zonal, vertical ion wind	± 10 m/s
Langmuir Probe	LANG	T_e electron density	5% 5%
Neutral mass spectrometer	NACS	zonal, vertical neutral wind	15%
Wind and temperature spectrometer	WATS	Tn zonal neutral wind	5 K 10 m/s
Fabry -Perot Interferometer	FPI	meridional neutral wind	25 m/s

Table 2.7 Experiments and data types from the Dynamics Explorer-2 satellite that are used in for model density comparison (Chapter 3) and frictional heating rate calculations (Chapter 5).

separation between arriving ions of different mass and comparing the results to what might be expected if the ions were immobile. The derived bulk plasma flow parallel to the satellite vector is taken as the meridional (or north-south) ion drift component. As might be expected, a precise knowledge of the spacecraft velocity and attitude is required. Thus, the

accuracy of the meridional wind measurements are typically not better than 50 m/s (St. Maurice and Hanson, 1984). RPA temperature measurements have errors of less than 2% based on the performance of other RPA devices (Hanson et al.,1973). Both the meridional wind and ion temperature data are stored in the local database as 8-second averages.

The Ion Drift Meter (IDM) sensors on DE-2 measured the bulk thermal ion drift velocity components transverse to the satellite velocity vector (X direction). The two ion drift components are measured along the spacecraft Y (vertical) and Z (horizontal or "zonal" direction) axes. An electrically segmented sensor with 4 sections is used to discriminate in the arrival angle, α, of incoming ions. The ratio of collector currents on opposing sections, corresponding to the Z or Y directions, can be used to derive the incident arrival direction once the X component of the ion drift has been specified. The RPA provides the X component and by switching between collector segments, both vertical and horizontal (to the spacecraft) drifts can be derived. The uncertainty in the IDM measurements are $\pm$ 10 m/s since the spacecraft attitude is known to about 0.1° (Heelis et al., 1981). In combination with the RPA measurements, orthagonal drift components from the IDM enable a full vector representation of the ion drift velocity. For the frictional heating calculations in this research, the horizontal ion wind vector is used based on the RPA X component and the IDM Z component.

The DE-2 Langmuir probe (LANG) provided electron densities and electron temperatures (Krehbiel et al., 1981). This instrument operated by measuring the probe current as an applied voltage is stepped from negative to positive potential. An electron retardation region occurs over a range of potentials (mostly negative) where the potential is not strongly negative enough to attract fast moving ions and yet not strongly positive enough to attract thermal electrons. The logarithm of the probe output over this region is a straight line with a slope proportional to the electron temperature for Maxwellian distributions. As the probe voltage becomes more negative (positive), ion (electron) saturation occurs due to coulomb attraction. Either of these extremes on the current-potential diagram can be used to derive the total ion concentration or electron concentration respectively. Errors of less than 5% for either temperature or density are likely for ambient $T_e > 1000$ K and $n_e > 10^3$ cm^{-3} (Brace et al. (1973).

The Neutral Atmosphere Composition Spectrometer (NACS) was used to obtain neutral density measurements of molecular nitrogen and atomic oxygen and other trace neutral constituents such as helium and argon. The instrument operated based on the principles of an ion mass spectrometer in that a neutral gas sample was partially ionized with the ionic component passing along charged grids. Charged particles which were not deflected from the straight-line path to a sensing device could be identified by mass and

number based on potential applied to the grid and sensor count rate. This sensor was limited to altitudes where the gas composition is primarily atomic oxygen or helium and the neutral densities were less than 10^9 cm^{-3} which is above about 300 km. Absolute accuracy of this instrument is approximately ± 15% with a relative uncertainty between species of ± 5% (Carrigan et al., 1981). These data were used to derive the ion-neutral collision frequencies for the ion frictional heat calculations.

The Wind and Temperature Spectrometer (WATS) provided measurements of the zonal (cross track) and vertical components of the neutral wind. The neutral wind components were measured by determining the arrival angle of neutral particles which entered the aperture of a mass spectrometer using an oscillating baffle (Spencer et al., 1981). Neutral temperatures were also derived from the same measurements. Statistical errors of less than 10 m/s are likely once accurate spacecraft attitude information was made available (Killeen et al., 1982). Neutral temperatures were known to within 5 K (Spencer et al., 1981).

The Fabry-Perot Interferometer onboard DE-2 provided a mean meridional (along-track) neutral wind component by measuring the Doppler shift of the 6300 Å emission from the metastable oxygen atom (O^1D). The instrument was oriented in the ram direction but pointed 15° down (towards Earth) so that limb scans could be performed ahead and approximately 225 km below the spacecraft altitude. Since these naturally occurring emissions exist over a range of altitudes, each sampled volume was assigned a latitude and altitude when the line of sight tangent point altitude exceeded the altitude of peak emission. After completing a number of limb scans (scanning mirror cycles limit the spatial resolution of the measurements to about 100 km), an altitude profile of meridional winds can be assembled for a given latitude. The altitude profiles of these winds are thus weighted by the LOS distribution of O^1D emissions. For the altitude interval sampled (250-400 km), these winds were shown to vary by only a small amount (Killeen et al., 1982) so averages were computed to represent the mean meridional wind. Statistical uncertainties in these measurements are about 25 m/s.

The WATS and FPI experiments provided component values of the zonal and meridional winds allowing the recovery of a full horizontal neutral wind vector. Before this can be accomplished however, allowances must be made since the WATS measurements are in situ, and the limb-scanning FPI measurements are made "ahead" of the spacecraft. This has been accomplished in the data base by shifting the FPI measurements in time (forward slightly) to match the times of data collected in situ (Killeen et al., 1982). Treated in this manner, representative, horizontal neutral winds are available for frictional heating calculations.

In summary, the DE-2 data set described above provides an extensive description of the thermospheric and ionospheric environment that can be used to derive ion frictional heating over large portions of the high latitude environment. The measurements are particularly useful when averaged over long periods since they provide extended spatial coverage across many local time planes and therefore permit the evaluation of global patterns in average ion heating rates which can then be related to patterns of upflowing ions.

CHAPTER 3

MODELING THE STEADY-STATE POLAR WIND

3.1 Background

Unlike the low and mid-latitude ionosphere, the high-latitude ionosphere is considerably more complex in structure and behavior due to a variety of unique physical processes. A number of theoretical and observational studies have examined such processes as solar EUV radiation, energetic particle precipitation, magnetospheric heat flux, and variations in the neutral gas composition in order to assess their relative importance in the high latitude environment A common theme that emerges from these works is the lack of a single dominant process that can adequately account for the range of spatial and temporal variability in the ionospheric observations. For instance, in the summer polar regions, ionization by solar EUV is the dominant production mechanism for O^+ but in winter, EUV ionization is limited due to low solar elevation angles so that ion production due to particle precipitation can dominate. Furthermore, precipitation varies considerably from one point to the next so that even within a localized area of a few hundred square kilometers, order of magnitude differences may exists in ionization rates based on differences in the energy spectra of ionizing particle fluxes. Such ionization processes are further modified by energy-dependent chemical reactions and transport making it difficult to order the relative importance of these elements on the basis of observations alone.

In the present chapter several processes responsible for modifying the upwelling fluxes of thermal ions are examined within the broader context of thermosphere-ionosphere interactions by employing suitable assumptions to the polar wind model described in Chapter Two. The use of a model in this context allows one to isolate and examine the basic physical mechanisms which alter the density, velocity and vertical fluxes of upflowing ions. Throughout this treatment, the assumption of steady-state is frequently used which implies a constant nature to the solution obtained. In fact, the condition of

steady-state is almost never reached since ambient conditions are continually changing in the drifting frame of the convecting flux tube as the plasma moves into different regions due to convective drifts. More appropriately, the solution obtained is an "average" in the sense that it is representative of a long-term tendency in observed conditions. Even with this limitation, the model provides a useful means for examining the importance of the underlying physics which contribute to the structured and variable outward flows of plasma in the topside polar ionosphere.

In the following sections, modifications to the basic polar wind model are described which permit more accurate specification of the ionization sources. With these improvements, a full range of solar cycle, seasonal effects and local time effects can be accurately represented. Following this, the effects of thermospheric composition and the influence of downward magnetospheric heat flux are separately considered. Through these studies, the basic character of the polar wind can be identified for a wide range of geophysical conditions.

3.2 Model Ionization Source Modifications

In the original version of the polar wind code (Gombosi et al., 1985), an optically thin F-region was assumed and an altitude-independent photoionization frequency was used based on those given by Banks and Kockarts (1973) for various solar conditions. Under the assumption of an unattenuated EUV flux down to the lower model boundary of 200 km, the photoionization rate, P_i (ions cm^{-3} sec^{-1}) was defined as:

$$P_i(z) = n(z)\int_{\lambda}^{\infty} d\lambda\, I_{\infty}(\lambda)\,\sigma^i(\lambda) \qquad (3.1)$$

In equation 3.1, the integral represents the altitude-independent photoionization frequency (ions sec^{-1})based on $I_{\infty}(\lambda)$, the wavelength-dependent differential flux of the unattenuated solar radiation and $\sigma^i(\lambda)$, the total ionization cross section for atomic oxygen. For this approximation, the altitude dependence of the photoionization rate is due only to the density profile of the neutral atomic oxygen. This condition is valid for a wide range of summertime conditions when the sun is high overhead and the level of maximum ionization is well below the model boundary. However, at larger zenith angles, the increased optical path results in a shift upwards in the peak ionization altitude. To show how this effects the ionizing flux above or below the peak ionization region it is useful to apply Chapman theory to an ion production layer and examine how the solar flux varies as a function of altitude. Assuming an exponential atmosphere with one ionizable constituent with constant

scale height and monochromatic radiation which enters a stratified atmosphere at a zenith angle χ, the intensity of the radiation changes with distance according to Beer's law as:

$$\frac{dI(\lambda,s)}{ds} = -I(\lambda)\sigma^a(\lambda)n(s) \tag{3.2}$$

where σ represents the absorption cross section; I, the intensity of incident radiation (photons cm^{-2} sec^{-1}) and n, the number density of absorbing atoms which varies along the slant path, s. This expression can be integrated to obtain:

$$I(\lambda,s) = I_\infty(\lambda)\exp\left(-\int_s ds\, \sigma^a(\lambda)n(s)\right) \tag{3.3}$$

where the expression in parentheses represents the optical thickness, ds. Rewriting this as a function of altitude and scale height using the relations ds = dz secχ and $n(z) = n_0 \exp\left(-\frac{z}{H}\right)$ one obtains:

$$I(\lambda,z) = I_\infty \exp\left(-\sec\chi\, \sigma^a H n(z)\right) = I_\infty \exp\left(-\sec\chi\, \sigma^a H n_0 \exp\left(-\frac{z}{H}\right)\right) \tag{3.4}$$

where n_0 is taken at some feducial altitude. The altitude of maximum rate of energy deposition (z_{max}) can be determined by solving for the relation:

$$\frac{d^2I(z)}{d^2z}\cos\chi = 0 \tag{3.5}$$

When equation 3.4 is substituted for I(λ,z), the solution can be expressed as:

$$z_{max} = H \ln\left(\sigma^a n_0 H \sec\chi\right) \tag{3.6}$$

This equation provides the altitude of maximum rate of energy deposition for a given zenith angle condition but can also be rewritten in terms of a departure from a fixed, reference altitude corresponding to an overhead sun (χ= 0° so sec χ =1):

$$z_{max} = z_0 + H \ln(\sec\chi) \tag{3.7}$$

where $z_0 = H \ln\left(\sigma^a n_0 H\right)$. Equation 3.7 shows that the altitude of maximum energy deposition shifts upward as the zenith angle increases from an initial position overhead. As the level of maximum energy deposition changes, so will the ion production. Energy deposition and ion production (volume rate) are linked through the following expression:

$$P_i(z) = n(z)\sigma^a \eta\, I(z) \tag{3.8}$$

where η is the probability that absorbed radiation at a given wavelength will ionize the atom and σ^a is the total absorption cross section. Maximum ionization will therefore occur at the level of maximum energy rate deposition. For this condition:

$$\frac{dP_i}{dz}\cos\chi = 0 \tag{3.9}$$

must be satisfied. Using equations 3.4 and 3.8 and the definition of scale height, H, the solution to equation 3.9 indicates that maximum ionization results where:

$$\left(\sigma^a n H \sec\chi\right)_m = 1 \tag{3.10}$$

By definition of the optical depth,

$$\frac{I}{I_\infty} = \exp\left(-\sigma^a n H \sec\chi\right) = \exp(-\tau) \tag{3.11}$$

Therefore at the level of maximum ionization, τ is unity. Above this altitude, τ decreases rapidly so the left-hand side of equation 3.8 approaches unity with $I(z) \approx I_\infty$. Below the altitude of maximum ionization, τ exceeds unity and the medium is no longer optically-thin. In this case, I(z) is strongly dependent on altitude and should be considered as altitude dependent.

For many cases in the polar regions, low zenith situations arise in which unity optical depth will occur above 200 km, resulting in significant attenuation of the incident flux throughout the lower portion of the modeled flux tube. To account for attenuation of the ionizing EUV fluxes for model calculations involving large zenith angles or optical depths >1, the polar wind code was modified to include the effects of an altitude-dependent photoionization frequency. The revised formulation for O^+ production rate is:

$$P_i(z) = n(z)\int_\lambda^\infty d\lambda\; I(\lambda,z)\,\sigma^i(\lambda) \tag{3.12}$$

where σ^i, represents the total ionization cross section and I represents the attenuated flux at a given altitude. The total ionization frequency for O^+ is obtained by summing over all ionization states ($O^+(^4S)$, $O^+(^2D)$ and $O^+(^2P)$). The local flux intensity is defined as:

$$I(\lambda,z) = I_\infty \exp\left(-\sigma^a n H\, Ch(R,\chi)\right) \tag{3.13}$$

where $R = (R_e + z)/H$. Here, R_e is the Earth's radius, z the altitude and H, the local gas scale height. Equation 3.13 relates the intensity of solar flux at some location and altitude to the incident, unattenuated flux. The last term in parentheses represents a Chapman function and is used here to account for spherical effects due to the earths curvature by considering both χ and the altitude where absorption occurs.

The formulation for calculating O^+ production rates using equations 3.12 and 3.13 was adopted in the polar wind model by including portions of a solar flux model developed by Dr Stan Soloman (private communication, 1988). The revised polar wind model now calculates height-dependent photoionization rates for O^+ for any given location and altitude by combining the attenuated EUV flux at each model altitude with known cross sections for O^+ across various wavelength intervals. The unattenuated solar irradiance is first determined by scaling a reference EUV spectrum based on the solar radio flux at 2800 MHz (10.7 cm). This reference spectrum (SC#21REFW) was consolidated by Hinteregger based on measurements from the Atmospheric Explorer satellites C, D, and E and is applicable for solar minimum only. However, Hinteregger (1981) developed a method of scaling the reference spectra based on using the daily and 81 day average solar radio flux to determine enhancement ratios for two key EUV emissions at 102.6 nm and 33.5 nm (the H Lyman B an Fe XVI lines, respectively). The following relation, developed by Hinteregger (1981), relates the flux intensity for a given day (for which the day and averaged F10.7 flux is known) to the key emission intensities of the reference spectrum:

$$\frac{I(\lambda)}{I_{ref}(\lambda)} = B_o + B_1\left(\langle F_{10.7}\rangle_{81d} - 71.5\right) + B_2\left(F_{10.7} - \langle F_{10.7}\rangle_{81d} + 3.9\right) \qquad (3.14)$$

where F10.7 is the daily 10.7 cm solar radio flux expressed in Solar Flux Units (one SFU $= 1 \times 10^{-22}$ Watts m^{-2} Hz^{-1}) and $\langle F_{10.7}\rangle_{81d}$ is the 81-day centered average value of the 10.7 cm flux. Hinteregger (1981) also provided best estimates for two sets of B parameters (B_0, B_1, B_2) at two wavelengths by fitting using observations available in the data base. The algorithm used here employs only one set in which B_0 was set to unity (Table 3.1). In this case, the calculated flux reduces to the solar minimum reference (SC#21REFW) when F10.7 = 71.5 and $\langle F_{10.7}\rangle_{81d}$ = 75.4 are used. Once the flux intensity at both key wavelengths is known, the remaining portions of the spectrum below the ionization threshold for atomic oxygen (911 Å) are scaled according to these emissions using the Hinteregger method (1981). To simplify calculations, the EUV spectrum capable of ionizing O^+ is averaged into 50 Å bins with 15 prominent emission features below 911 Å handled separately. Ionization cross sections and branching ratios for each of three

ionization states corresponding to $O^+(^2P)$, $O^+(^2D)$ and $O^+(^4S)$ are considered in determining attenuation of the incident flux and the total photoionization rate. These values were taken from Samson and Pareek (1985) and Kirby et al. (1979) and a weighted average was calculated corresponding to each of the spectral bins and emission features described above.

λ (nm)	B_0	B_1	B_2
102.6	1.0	0.01380	0.00500
33.5	1.0	0.59425	0.38110

Table 3.1 The B parameters defined by Hinteregger and used in equation 3.14 to adjust the solar EUV reference spectra according to the F10.7 solar radio flux.

A horizontally-uniform, vertically-stratified thermosphere based on MSIS-86 is used when calculating column densities above each specified height for a given solar zenith angle. In all cases, a Chapman function is used to account for spherical geometry when determining the local flux intensity by using an analytic function developed by Smith and Smith (1972) and adopted by Dr. S. Solomon to the solar flux code. Additionally, for very large zenith angle cases where the grazing height extends below 90 km, column density calculations include logarithmically-interpolated densities from the appropriate levels of the US standard atmosphere. The photoionization rates obtained in this manner allow for variations in the peak production altitude throughout the low altitude portions of the modeled flux tube under any zenith angle condition. This treatment must be modified for large zenith angle cases to include the important contributions from photoelectrons since their contributions become important at large optical depths.

A secondary process which leads to additional O^+ production involves inelastic collisions between neutral atomic oxygen and energetic photoelectrons. Absorption of EUV can lead to the creation of energetic electrons. The energy of the primary photoelectron is proportional to the wavelength of the absorbed photon minus the energy expended in removing the electron from its orbit. Not all of the locally-produced photoelectrons participate in this ionization since some escape upwards along the field lines and become lost in the magnetosphere. Transport into the high-latitude region from the conjugate (sunlit) hemisphere is unlikely due to the unfavorable field line topology at high geomagnetic latitudes so only topside losses may occur. The photoelectrons that are not lost will act locally as an additional, embedded ionization source.

Chemically, the collision between an energetic (fast) photoelectron and an oxygen atom can be expressed as :

$$O + e_p \rightarrow O^+ + e_p + e_s \tag{3.15}$$

where e_p represents the original, primary photoelectron and e_s, the ejected secondary electron. The scattered primaries are indistinguishable from the secondaries except that they usually are more energetic and have an angular distribution peaked in the forward direction. Secondaries can be ejected from more or less any point in their orbit and so are distributed isotropically. Additionally, secondary electrons may leave with enough kinetic energy to cause additional impact ionization and the production of tertiary electrons. This process continues until the primary, secondary or tertiary electron energy drops below the ionization potentials of the neutral gas. At this point, energy loss to the ambient electron gas occurs as the photoelectron "thermalizes". The production rate for O^+ due to impact ionization can be expressed in a form similar to Equation 3.12:

$$P_i(z) = \sum_{\ell} n(z) \int_{E_{\ell}(\ell)}^{E_{max}} dE\, I(E,z)\, \eta(E,\ell)\, \sigma^{\ell}(E) \tag{3.16}$$

In this case, the integration is taken from the ionization threshold for a given state to the maximum electron energy in a given spectral distribution. The electron impact ionization states for O^+ and branching ratios $\eta(E,\ell)$ are given in Table 3.2. The differential electron density, $I(E,z)$ is defined as follows:

$$I(E,z) = 2\pi \int_0^{\pi} d\mu\, I(\mu,z,E) \sin\mu \tag{3.17}$$

where $\mu = \cos\theta$ and θ is the pitch angle of the electron. Calculations of the impact ionization rate thus requires a full knowledge of the differential photoelectron flux spectrum which can be both difficult to determine and computationally intensive to model. As a result, impact ionization rates are often estimated as a fixed fraction of the photoionization rate without full consideration of changes in the EUV spectral profile with altitude.

Early estimates of the ion production rates due to fast photoelectrons were based on the calculations of G. A. Victor (Oppenheimer et al., 1976; Torr and Torr, 1979). The most common simplification of this type currently in use (Roble et al., 1987; Sojka and Schunk, 1985) assumes that impact ionization of neutral atomic oxygen is about 30% of the primary photoionization rate based on the results of D. G. Torr et al., 1979. This assumption is valid for cases involving optically-thin regimes. However, for application in the polar regions where large zenith angles result in an optically-thick ($\tau > 2$) medium, the

results of Richards and Torr (1988) suggest that this ratio is not constant with altitude. Calculations by Richards and Torr (1988) indicate that the ratio of photoelectron ionization to EUV ionization rates are not simply constant but vary greatly with altitude. In fact, they found that below the altitude of peak production, the photoelectron ionization rate can exceed the EUV ionization rate for atomic oxygen.

Ionization State	Branching Ratio	Threshold energy (eV)
$O^+(^4S)$	0.4	13.61
$O^+(^2D)$	0.4	16.92
$O^+(^2P)$	0.2	18.61

Table 3.2 The fraction of oxygen ions produced in various states by electron impact ionization and the corresponding threshold (minimum) ionization energies.

The changing importance in photoelectron ionization with altitude (actually optical depth) comes about due to selective absorption of certain wavelength intervals with optical depth. Only solar fluxes below about 310 Å are important for photoelectron flux (Richards and Torr, 1985). Therefore, O^+ produced by impact ionization is restricted to the 0-310 Å portion of the EUV spectrum. Photoionization however occurs over most of the EUV spectrum with maximum cross sections near 500-700 Å. Since the longer wavelengths are attenuated more effectively than those below 310 Å, the relative importance of ionization type shifts in favor of impact ionization with increasing optical depth. Based on their calculations, Richards and Torr (1988) developed a convenient analytical expression for quantifying the relative importance of impact ionization when transport effects from the conjugate hemisphere are absent. The ratio of impact to EUV ionization rate is given by:

$$R = \frac{2.4\, e^{-\tau}}{e^{-\tau} + 2\left(e^{-1.3\tau} + e^{-2\tau} + e^{-2.5\tau}\right)} \qquad (3.18)$$

The exponential term in the numerator represents the attenuation of short wavelength fluxes responsible for photoelectron impact ionization while the terms in the denominator represent photoionization at four separate EUV wavelengths corresponding to approximately 225, 300, 400, 500 Å. To save computational time, the optical depth at other wavelengths is expressed by multiples of the 225 Å optical depth. At high altitudes

where τ is small and the ratio, R, is about 0.36. For low altitudes or large zenith angles, τ becomes large and R approaches 2.4. Parameterization beyond this point was not reliable due to uncertainties in the short EUV spectrum and truncation of the photoelectron calculation at 100 eV. This restriction limits the use of Equation 3.18 to conditions where $\tau < 9$ however for application to the polar wind model, this limit does not affect the results since optical depths do not normally exceed 9 above the lower model boundary of 200 km.

The effects of photoelectron impact ionization were added to the polar wind model by including ionization rates derived from Equation 3.18. To account for loss of photoelectrons due to transport, the ratio values obtained above 250 km were linearly reduced so that values in the optically-thin region near 450 km were reduced by a factor of two. This reduction follows the behavior reported by Richards and Torr (1988) when comparing winter (with conjugate photoelectrons) and summer (no conjugate effects). In this study, it is assumed that no conjugate photoelectron enhancement is possible but that some loss is inevitable as a fraction of the photoelectron population will have field-aligned velocities which carry them into the magnetosphere. In any case, the effects of transport are not important at lower altitudes where photoelectron ionization rates are comparable to the photoionization rate. With the addition of this analytic approximation into the polar wind model, significant increases to the total ionization rate due to impact ionization can be accounted for throughout the lower volume of the modeled flux tube.

To illustrate the importance of primary and secondary ionization sources in determining the altitude-dependent production rate for O^+, seasonal ionization scenarios at a fixed location were considered. Assuming a position near 70°N 00° W (geomagnetic) at solar maximum (daily and average F10.7=180) under quiet (Ap=4) geomagnetic conditions, ionization rate profiles for atomic oxygen were calculated for summer and winter solstice (day 172 and 355 respectively). Under these assumptions, differences in the profiles result only from different zenith and neutral atmosphere conditions for summer and winter solstice. Both profiles assume a universal time (UT) of 17:00 hours which aligns the geomagnetic pole along the local noon meridian where solar photoproduction is at a diurnal maximum. This geometry for the summer case (Northern Hemisphere) is illustrated in Figure 3.1. The combined displacement of the geomagnetic pole from geographic pole of 11° and the flux tube location 20° off the geomagnetic pole (at 70° invariant) results in an angular displacement of 31° from the geographic pole at 12 MLT.

For summer solstice, the subsolar point is at about 67° N (colatitude) along the local noon meridian which results in a zenith angle of 67°-31° or about 35°. At winter solstice, the subsolar point is 113° from the geomagnetic north pole resulting in a much greater zenith angle near 82°.

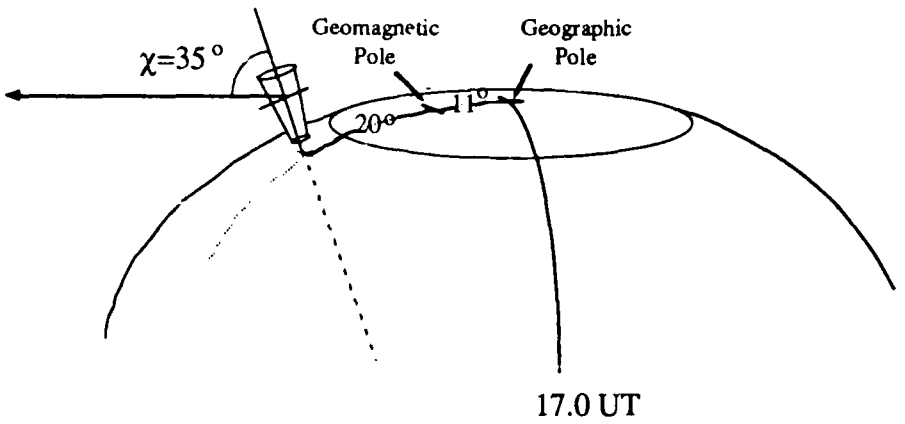

Figure 3.1 A flux tube located near 70° N 00°W geomagnetic experiences the greatest amount of EUV flux near 17 UT (12 MLT) at summer solstice due to the relative positions of the geographic and geomagnetic poles.

Figure 3.2a illustrates the relative importance of photoelectron ionization and the enhancement provided to the total ionization rate for the two different zenith conditions. A low zenith angle of 35° for the summer case corresponds to a relatively short optical path permitting most of the EUV spectrum to penetrate evenly to low altitudes. As a result, the contribution of photoelectron ionization is almost constant so the ratio of electron impact ionization to photoionization does not change much between 200-300 km. Photoelectrons still contribute a non-negligible component however accounting for 36% of the total ionization at the lower model boundary of 200 km. For the winter case, a larger zenith angle of 82° results in a longer optical path and a reduction of the middle EUV wavelengths (500-700 Å) by oxygen absorption so that photoelectrons produced by wavelengths shortwards of 310 Å play a larger role in O^+ production. This is most apparent in the lower altitudes due to the decreasing importance of middle EUV wavelengths. For this winter solstice case, photoelectrons account for about 62% of the total ionization rate at 200 km. The effects on the summer and winter ionization rate profiles can be seen in Figure 3.2b where the total ionization rates (solid) and photoionization rates (dashed) are plotted. The low zenith, summer case corresponds to an optically-thin atmosphere so that the maximum O^+ production region is lower in altitude (unity optical depth near 168 km). For winter, a larger zenith angle shifts the maximum production to higher altitudes (unity optical depth near 235 km). In both cases, the contributions of photoelectrons can be seen by comparing the dashed and solid line profiles under each zenith condition.

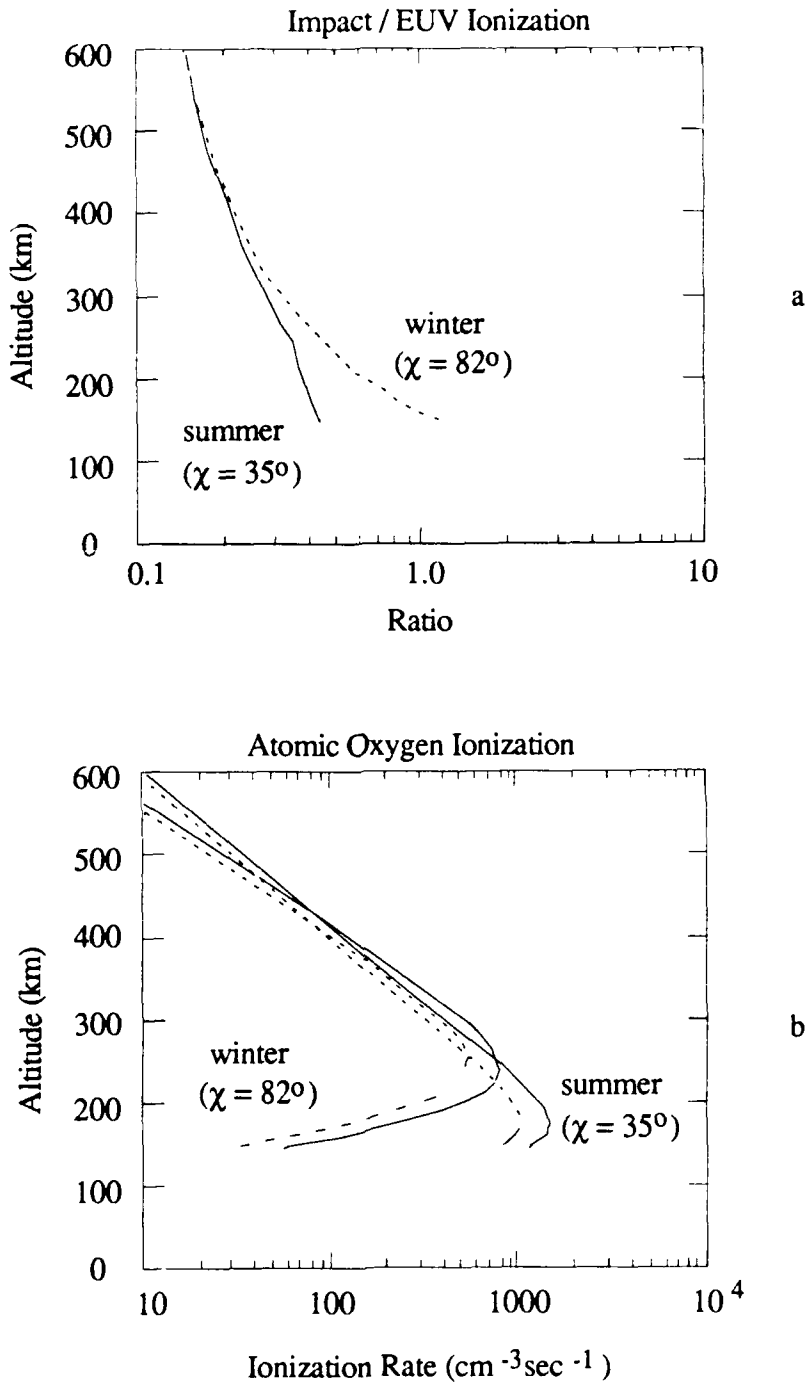

Figure 3.2 The relative importance of secondary ionizations caused by photoelectrons is illustrated in (a) where the ratios of impact ionization rate to EUV ionization rate are compared for a low and a high zenith angle case. The enhancement in total ionization rate is depicted in (b) where primary ionization rates (dashed) are compared to total (solid) ionization rates for the two zenith conditions. Greater contributions from impact ionization are present for the low zenith case with enhancements of 62% apparent near 200 km.

For larger zenith angles during winter solstice, the contributions to ionization by photoelectrons take on additional importance by about 50% .

Although the cases chosen here represent the greatest differences for the location and UT specified, they serve to illustrate the importance in considering primary and secondary photoproduction sources in addition to altitude variations in the ionization rate for the full range of zenith conditions to be modeled. When these processes are included in the polar wind model, a self-consistent treatment of photoionization throughout the modeled flux tube can be applied that extends the utility of the model to any local time, season, or solar cycle period where EUV fluxes are present.

3.3 Solar Cycle Variations in the Polar Wind

With the ability to derive the O^+ photoproduction rates as a function of altitude, the revised polar wind model can be used to examine the composition and outflow properties of the the polar wind for a number of solar-geophysical conditions in the polar regions where solar ionization is important. The model modifications described above add a new dimension to the self-consistent model calculations since the same static, neutral atmosphere which acts through collisions to impede the flow is also used to determine the source strength of the major ion, O^+. Since the polar wind is linked both chemically and frictionally to the thermosphere, the effects of EUV variability on the thermosphere can be directly related to changes in the polar wind character.

A number of modelling efforts have been directed towards a description of the solar cycle dependence of polar ion outflows which are statistically identified and well documented in observational literature (c.f. Chandler et al., 1990; Grebowski et al., 1990; Yau et al., 1985a, 1985b). Agreement between model and observational findings are important since it would imply that the relevant physics behind the outflow process are accounted for. For example, Barakat and Schunk (1987) performed extensive parametric simulations of H^+ and O^+ outflows to identify and understand how topside plasma conditions, associated with various solar-geophysical conditions, could effect the nature of ionospheric flows. Their work pointed to a number of neutral gas and topside F-region plasma conditions which could influence the limiting values and composition of escape fluxes. In this thesis however, the consequences of thermospheric variability on H^+ and O^+ outflow character between 200 km and 8000 km are examined directly. These effects were briefly suggested by Moore (1980) and parametrically examined by Barakat and Schunk (1987). The major difference between this study and that of Barakat and Schunk is that no ionospheric demand is imposed to simulate the removal of H^+ and O^+ by unspecified, energetic plasma process(es). Instead, the fully-coupled transport equations

are solved based on a self-consistent treatment of the significant chemical, collisional and transport processes which depend, to large degree, on the thermospheric temperature and density. In this section, only the variability as a function of changes to EUV/UV fluxes associated with solar cycle minimum/maximum is considered.

To determine the extent and influence of thermospheric variability on ion flux character, modeled upflow properties are compared based on a solar minimum and solar maximum thermosphere. These periods were selected because solar EUV fluxes are at their extrema resulting in the greatest amount of change in the long-term thermospheric state. This choice simplifies comparisons so that relevant differences can be easily identified. In each case, thermospheric densities and temperatures were derived from the Mass Spectrometer/Incoherent Scatter (MSIS-86) model (Hedin, 1987) and used to calculate neutral-ion sources, sinks, and collision frequencies for a flux tube location at 80° N 00° W geomagnetic coordinates and a local magnetic time of 1200 hours (1700 UT). Separate model thermospheres were obtained using a daily and 81-day average 10.7 cm solar radio flux of 60 SFUs for solar minimum and 180 SFUs for solar maximum. For the specified time, location, and solar radio flux the polar wind model scales the local EUV flux then computes the height-dependent photoionization rate (primary and secondary) for atomic oxygen using MSIS-generated neutral density and temperature profiles. To limit this comparison to only solar cycle (EUV) influences, geomagnetically quiet conditions (Ap=4) during summer (day 182) were considered in both cases. With these adopted differences the model can account for the major collisional and chemical processes associated with a solar cycle-dependent thermosphere.

As Moore (1980) pointed out, accidentally-resonant charge exchange chemistry closely couples H^+ and O^+ flows to the neutral density profiles of atomic hydrogen and oxygen. Therefore, before considering the effects of long-term changes in solar EUV flux on the high latitude polar wind, it is useful to examine the differences between the solar minimum/maximum thermosphere. Molecular as well as atomic thermospheric species are considered in the background gas through which H^+ and O^+ flow and therefore, changes to all neutral species used in the polar wind model runs should be considered. Molecular nitrogen and molecular oxygen (Figure 3.3b), increases in local number density are readily apparent from solar minimum to solar maximum due to larger scale heights at solar maximum associated with higher exospheric temperatures (Figure 3.3a). Although the MSIS-generated thermosphere profiles extend in altitude to match model calculations up to 8000 km, only profiles up to 4000 km are shown to highlight key structural differences.

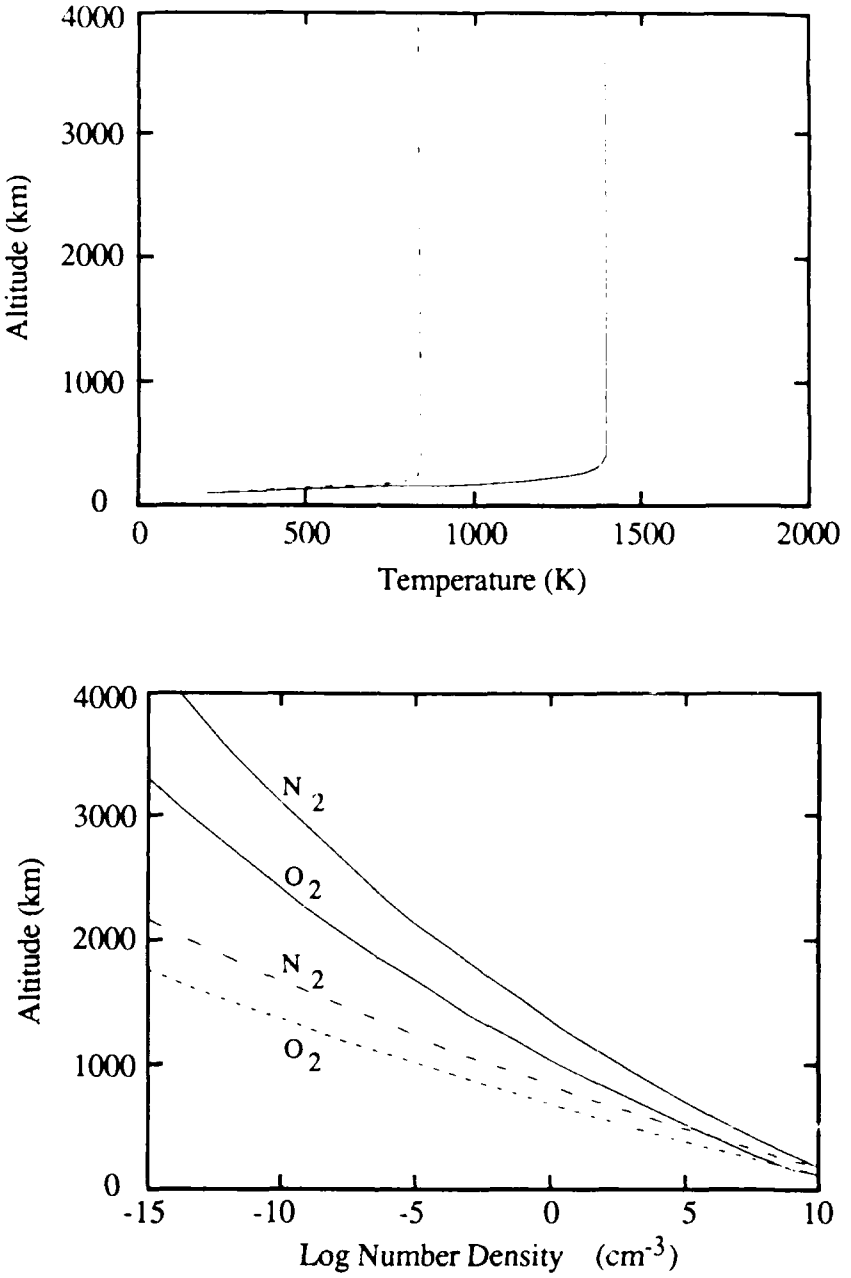

Figure 3.3 Number density profiles of molecular nitrogen and oxygen (b) derived from MSIS-86 for 80° N 00° W geomagnetic at 12 MLT for solar minimum (dashed) and maximum (solid). Number density enhancements for both species occur for the solar maximum case due to higher Thermospheric temperatures(a).

The higher temperatures (for this case, a 60% increase) are the direct result of the stronger EUV flux during solar maximum which increases ionospheric heating and ultimately through collisions, the neutral gas.

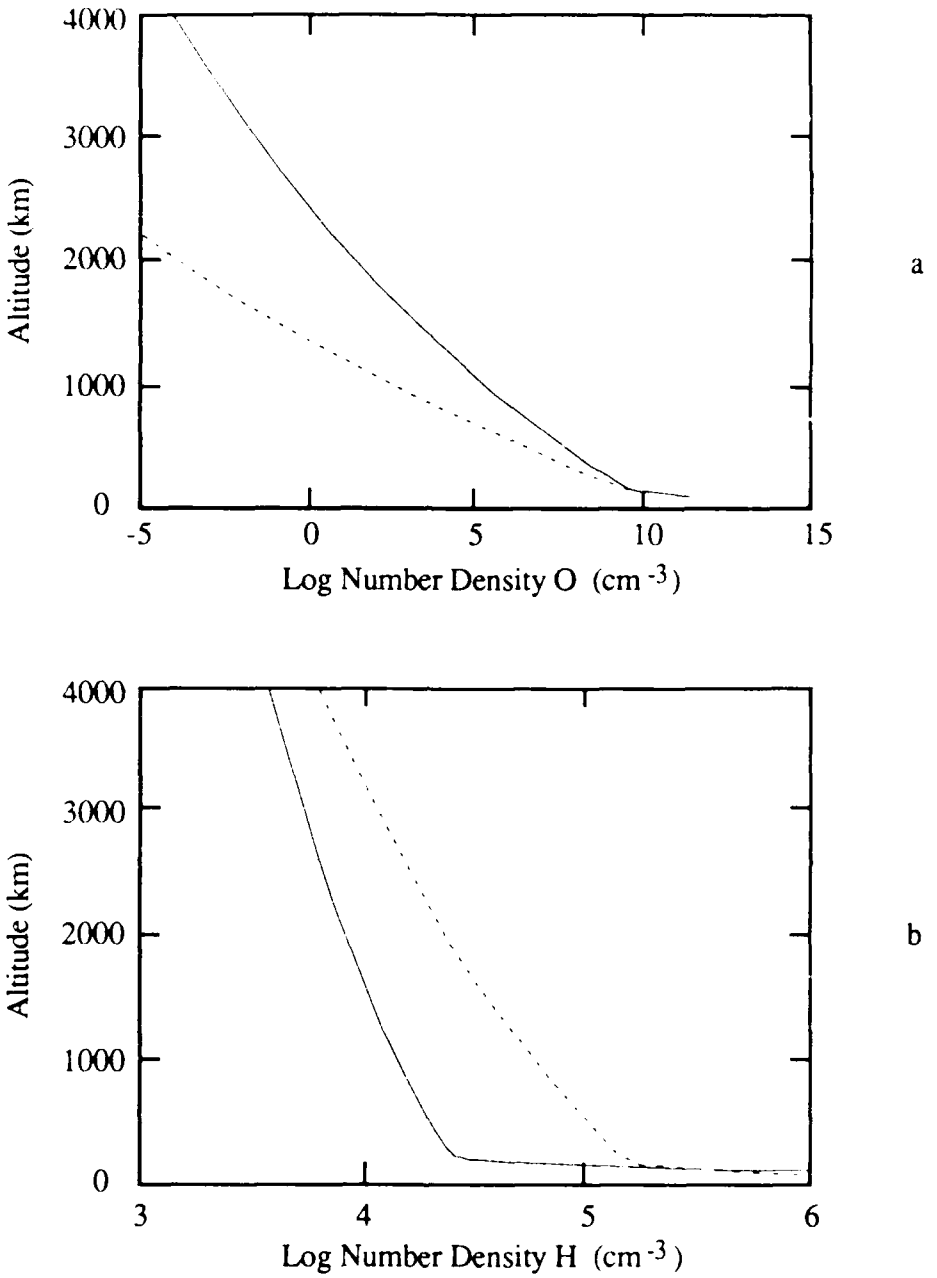

Figure 3.4 Number density profiles of atomic oxygen and hydrogen derived from MSIS-86 for 80° N 00° W geomagnetic at 12 MLT. Oppositely directed responses in number density for each species between solar minimum(dashed) and solar maximum (solid) conditions significantly modify F-region ion composition and the character of the polar wind.

The lighter atomic species included in the polar wind model reacted somewhat differently than the molecular constituents. In Figure 3.4, neutral hydrogen and oxygen number density profiles are shown for the two cases corresponding to solar minimum and solar maximum. The significantly greater exospheric temperature associated with enhanced

EUV/UV flux during solar maximum results in distinct changes to the number density profiles of both major atomic species. In addition to the expected scale height increase for H and O at solar maximum, both constituents are subject to transport which further modifies their local concentrations. In the case of the heavier, atomic oxygen (Figure 3.4a), local decreases due to transport are small so the scale height change dominates resulting in an overall local density enhancement at all altitudes at solar maximum. A decrease in H number densities at solar maximum (Figure 3.4b) results from enhanced evaporative escape associated with higher thermal velocities. This different behavior of H and O at solar minimum/maximum leads to substantial differences for H^+ and O^+ upwelling intensities. In fact, it is the oppositely-directed responses to solar cycle EUV/UV flux of hydrogen and atomic oxygen which constitute the most effective thermospheric change in altering the high latitude ion outflow character for the summer conditions examined in this work.

The two different thermospheric states corresponding to solar cycle minimum and maximum were used in the model calculations to achieve steady-state conditions. The condition of steady-state was based on a variation in number density and velocity of less than 1% at 2000 and at 4000 km. Once this criterion was met, the different velocity and density fields could be compared. Figure 3.5 summarizes the equilibr um profiles of hydrogen and oxygen ion densities (Figures 3.5a and 3.5b) and fiel -aligned flows (Figures 3.5c and 3.5d) for the solar minimum /maximum summer case. T ese plots have also been limited to the 200 km-4000 km interval to highlight important diff rences. In the case of the major ion O^+, enhanced number densities are apparent at all altit des for solar maximum. The 'nose' on the solar maximum density profile corresponds to the peak in O^+ production level which has moved upward (compared to solar minimum) in response to the change in neutral oxygen scale height mentioned earlier. For solar minimum, the peak production level is is not entirely visible since it is located near the lower boundary (200 km) of the model. More importantly, enhanced number densities are apparent at all altitudes for solar maximum. This order of magnitude increase in O^+ results from a combination of two factors. First, higher neutral oxygen scale heights at solar maximum shifts the maximum production level of O^+ to higher altitudes where loss by reaction with O_2 or N_2 is less frequent. Secondly, enhanced photoionization rates at solar maximum result in greater O^+ production. For the season, location and time used in this study, the photoionization frequency increased from 2.0×10^{-7} sec^{-1} to 4.2×10^{-7} sec^{-1} based on the specified increase in F10.7 solar radio flux from 60 SFUs to 180 SFUs. Together, the reduced loss and enhanced production of O^+ during high solar activity substantially increases the O^+ number density at all altitudes. In contrast to the number density

behavior, the field-aligned flow velocities of O^+ shown in Figure 3.5d exhibit almost no solar cycle variation. For this heavier ion, the diffusive flow which develops from the imposed pressure differential along the model flux tube is constrained to approximately constant velocity by the near balance between gravity, friction and the induced polarization electric field.

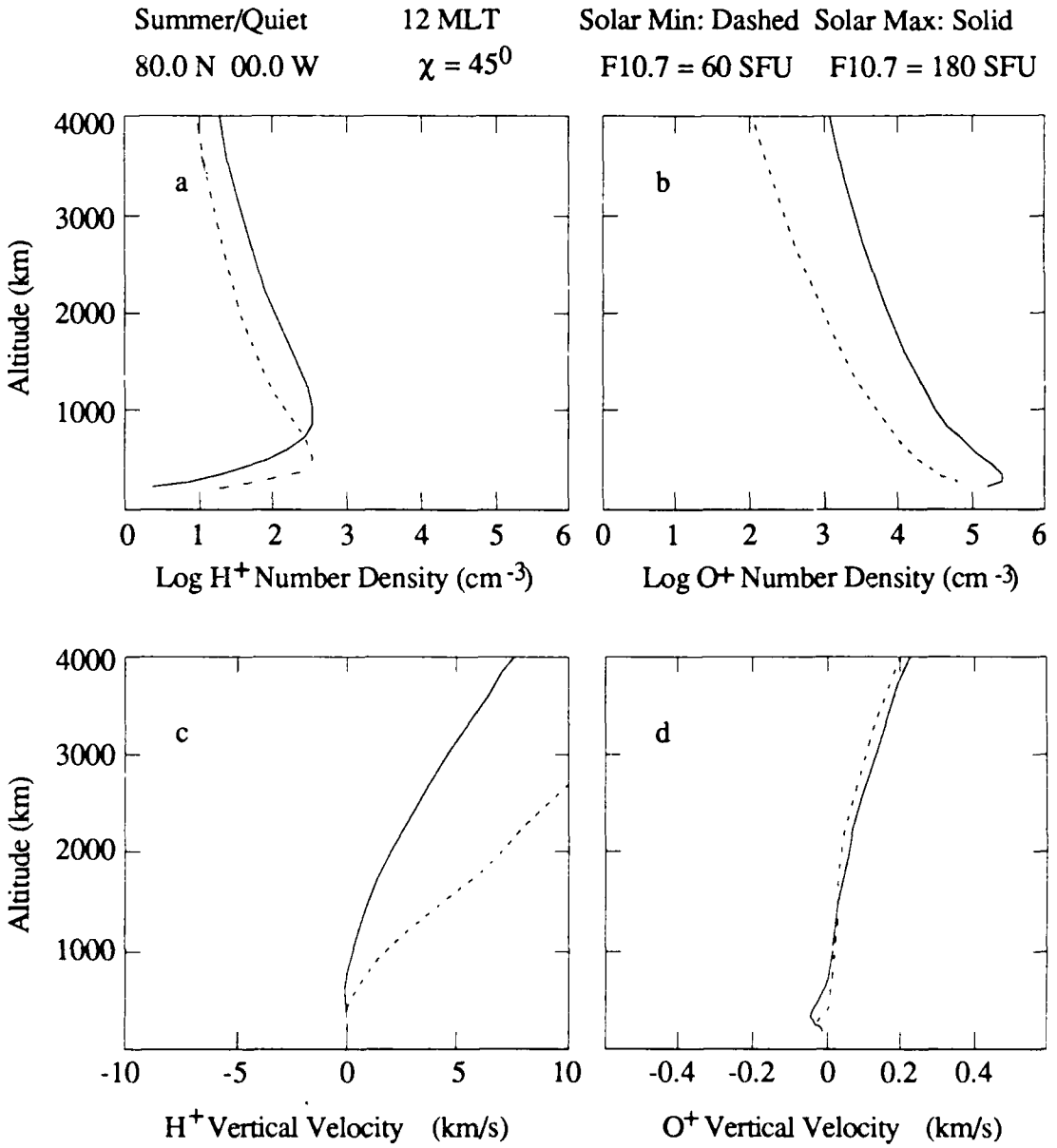

Figure 3.5 Steady-state profile of vertical velocity and number density for hydrogen and oxygen ions at solar minimum (dashed) and maximum (solid). Characteristic changes for each ion result from differences in EUV fluxes which effect production and momentum processes.

For H^+, the density and flow velocity profiles shown in Figures 3.5a and 3.5c exhibit a more complex behavior. Production of H^+ in the high latitude F-region occurs via accidentally-resonant charge exchange:

$$O^+ + H \leftrightarrow O + H^+ \tag{3.19}$$

Since generation of H^+ through the forward charge exchange reaction is most important near the altitude where n(O) equals n(H) (hereafter referred to as the O/H crossover altitude), the peak in H^+ number density shifts upwards as the crossover altitude in the adopted MSIS thermosphere moved from 690 km (solar minimum) to 1290 km (solar maximum). This change in crossover altitude has important consequences for the H^+ outflow velocities shown in Figure 3.5c. Once created, hydrogen ions move primarily in response to the ambipolar electric field established by the major ion (O^+). A lower crossover altitude corresponding to solar minimum, implies a greater vertical distance over which the hydrogen ion can be accelerated by the electric field free from collisions with atomic oxygen. Additionally, since collisions are less frequent above the crossover altitude, hydrogen ions experience less drag and therefore less momentum loss compared to the solar maximum case. As a result, hydrogen outflow velocities are greater at solar minimum (by a factor of 3 at 1000 km). In effect, the upward shift in the collision-dominated regime for the solar maximum thermosphere tends to reduce the effectiveness of H^+ acceleration leading to lower H^+ outflow velocities at solar maximum.

The distinct variations in density and field-aligned velocities described above for each ion species leads to substantial differences in equilibrium fluxes for both solar cycle cases. Figure 3.6. compares equilibrium flux profiles of hydrogen and oxygen ions for solar minimum and solar maximum summertime conditions. Here, flux profiles have been normalized to the 1000 km value to account for the radially-divergent flux tube geometry assumed in the model. The H^+ flux profile shows little variation with solar cycle conditions reaching an asymptotic value near 4×10^7 cm^{-2} sec^{-1} at 4000 km for both solar minimum and solar maximum. This near constant H^+ flux profile can be explained in terms of the opposing responses in H^+ number density and outflow velocities for solar minimum/maximum periods. Above 4000 km, variations are small and in opposite senses. As discussed in Chapter 1, the minor ion H^+ is limited in escaping by the major constituent, O^+. It therefore assumes the same density scale height as the major ion and and is limited in flux by it's number density distribution. To conserve flux, the variations in density and velocity must therefore oppose one another. At lower altitudes, slower field-aligned velocities at solar maximum reduce the H^+ flux between 4000 km and the H/O crossover altitude. Below about 1000 km, both number density and flow velocity are

slightly reduced (compared to solar minimum values) and thus act together to reduce H^+ fluxes during high solar activity. The O^+ flux also responds to thermospheric changes but in an entirely different manner. In the lowest altitude region, the peak in O^+ production shifts upward during solar maximum so that a small downward directed motion of the oxygen ion away from the source tends to hide the flux profile 'nose' which is visible in the solar minimum case. Just above the peak production region, substantial fluxes of O^+ move upward and contribute to the generation of H^+ flux via the forward charge exchange reaction with neutral hydrogen. In contrast to the hydrogen ion, the O^+ flux profile shows an order of magnitude variation for solar cycle extremes with fluxes increasing from near 0.78×10^7 cm^{-2} sec^{-1} at solar minimum to approximately 9.3×10^7 cm^{-2} sec^{-1} at solar maximum.

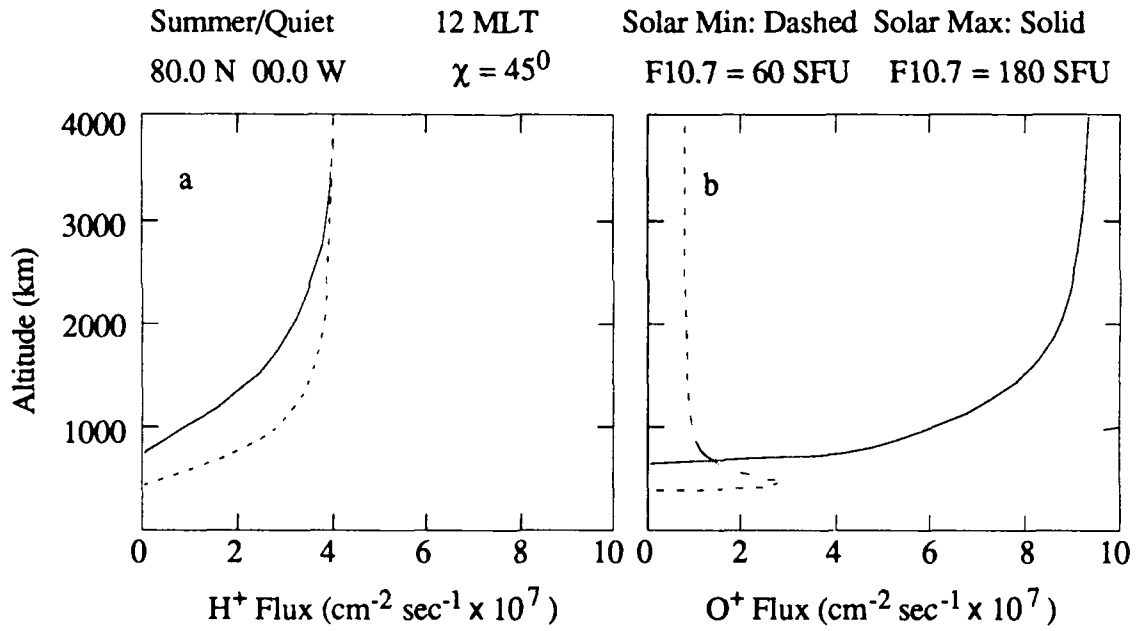

Figure 3.6 Flux profiles for H^+(a) and O^+(b) for solar minimum and solar maximum conditions. Flux values have been normalized to an altitude of 1000 km.

By comparison with Figures 3.5b and 3.5d, this behavior can be directly attributed to the approximate 10-fold increase in O^+ number density associated with thermospheric compositional changes and solar EUV/UV variations. Additionally, the magnitude of the O^+ flux at solar maximum exceeds that of H^+ by a factor of two. Based on the invariant behavior of the H^+ flux with solar cycle and the large relative increase in O^+ fluxes at solar maximum, it appears that the polar wind character changes in favor of oxygen ion dominance during solar maximum for the case studied here. Variations in position and

UTs modified the magnitudes of the fluxes slightly due to different ionization rates (zenith angle effects) or changes in loss rates (composition effects) but do not alter the solar cycle behavior of the two ion fluxes described above.

In conclusion, steady-state solutions to the coupled, time-dependent continuity, momentum and energy equations were examined for a two-ion quasi-neutral plasma along an open flux tube at high geomagnetic latitude. Unique solutions were obtained for different MSIS-derived thermospheric states corresponding to summer solar cycle minimum and solar cycle maximum. Equilibrium fluxes in both ion species profiles were compared and analyzed to determine the influence of solar cycle dependent thermospheric variability. The following relationships were found:

1. O^+ fluxes exhibit a strong EUV/UV dependence resulting in a 10-fold increase in O^+ upflow at solar maximum over solar minimum. Fluxes of O^+ with magnitudes of 10^8 cm^{-2} sec^{-1} are likely at solar maximum and exceed H^+ fluxes .

2. The H^+ flux exhibits essentially no upflow variations above 4000 km under similar conditions. Small, factor of 2-3 changes with solar cycle were noted in H^+ fluxes but only below about 4000 km.

3. Increases in the O^+ upflow during solar maximum can be explained by EUV-related thermospheric increases in neutral atomic oxygen density and, to a lesser degree, increases in the photoionization frequency.

4. Roughly equal and oppositely-directed responses to EUV variations for H^+ number density and field-aligned velocities account for the steady upflow of H^+ above 4000 km since H^+ is essentially flux-limited in both cases examined. Below this altitude, reduced H^+ field-aligned velocity and lower densities act to reduce H^+ fluxes at solar maximum.

3.3.1 Comparison of Solar Maximum Results to Earlier Polar Wind Predictions by Banks and Holzer

Compared with the previous predictions of Banks and Holzer (1968), the field-aligned H^+ and O^+ fluxes obtained in this study are significantly different. For solar maximum, the O^+ flux magnitudes are near 9.3×10^7 cm^{-2} sec^{-1} which are about 100 times greater than that predicted by Banks and Holzer (1968; hereafter referred to as BH). Additionally, the H^+ fluxes in this study are near 4×10^7 cm^{-2} sec^{-1} which are substantially lower than the $2\text{-}7 \times 10^8$ cm^{-2} sec^{-1} obtained by BH. Since these predicted fluxes are so different, the model assumptions for both studies were examined to identify the source of the discrepancy.

In their formulation, BH employed a hydrodynamic treatment to solve the steady-state continuity and momentum equations for the individual ions H^+, He^+ and O^+. They considered daytime conditions but did not specify solar cycle conditions or self-consistently solve for any ion energy equations so in all cases $T_e=T_i$. Instead, they choose three model neutral atmospheres (T_n=750 K, T_n=1000 K, T_n = 1500 K) of Nicolet et al.,1969 to approximate different thermospheric states and assumed an ion temperature profile for all solutions. Their choice of an O^+ photoionization frequency of 5×10^{-7} sec^{-1} is appropriate to solar maximum, low zenith conditions so a comparison with polar wind model solutions for solar maximum conditions is appropriate. In addition to the simplifying assumptions in the BH model, two major differences exist which could explain the difference in modeled fluxes:

(1) thermospheric H densities for the three different neutral atmosphere cases assumed by BH were larger by a factor of 2 to 10 compared to MSIS-86 cases for corresponding exospheric temperatures (their adopted thermosphere was based on mid-latitude observations).

(2) the 3000 K electron temperature (T_e) assumed by BH was significantly lower than the 7500 K temperature calculated here based on a specified downward heat flux.

A comparison of the Nicolet model atmosphere and MSIS-86 model atmosphere for the three exospheric temperatures used by BH is shown in Figure 3.7. For all cases, the neutral hydrogen density profiles are substantially lower than the corresponding Nicolet profiles for the same exospheric temperatures. This also effects the O/H crossover altitude resulting in a higher peak production altitude and greater dominance of collisions on the hydrogen ion's upward momentum

The calculated, low altitude profile of T_e used for this study is consistent with DE 2 observations of low altitude, cusp region electron temperatures reported by Curtis et al.(1985). Since the hydrogen-rich atmosphere and lower T_e assumed by BH could act to impede O^+ flows through friction and a reduced ambipolar electric field, a test was conducted to examine the effects of the BH assumptions on the polar wind model solutions.

The effects of high neutral H densities and low T_e were tested through suitable modifications to the polar wind model for three cases. In the first case, the neutral H density was artificially enhanced by a factor of 10. For the second case, the downward electron flux was lowered by one order of magnitude to from 5×10^{-3} erg cm^{-2} sec^{-1} to 5×10^{-4} erg cm^{-2} sec^{-1} . This change reduced the electron temperature at 4000 km to 3800 K. In the third case, both modifications were combined to match the BH assumptions. Results

for each case are summarized in Table 3.3. For the case of enhanced neutral H density (column labeled "enhanced H"), H^+ upflows increased by a factor of 8 with only

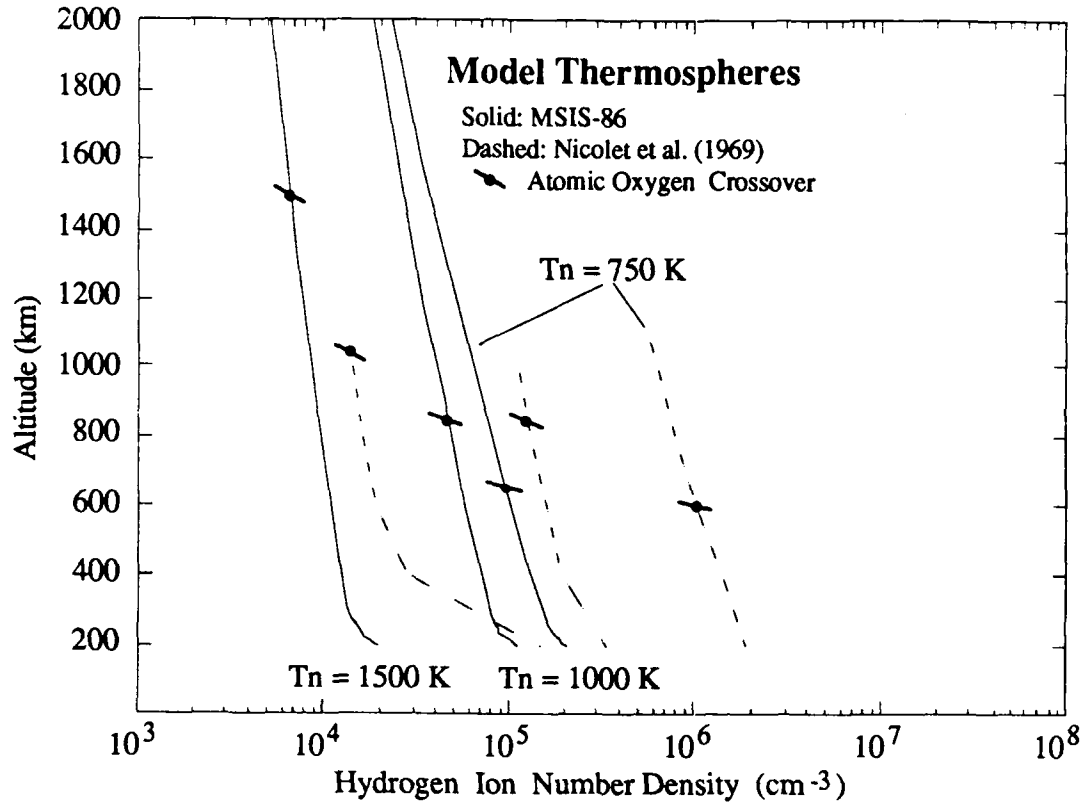

Figure 3.7 Comparison of thermospheric models used by Banks and Holzer (1968) and Cannata and Gombosi (1989). The hydrogen-rich thermosphere used by Banks and Holzer (dashed) results in greater H^+ fluxes than those obtained with MSIS-86 (solid).

negligible effect on O^+ flows. For the second case, decreases in T_e (column labeled "T_e=3800 K") reduced the O^+ flux by almost 3 orders of magnitude with only a small (factor of 3) decrease in the H^+ flux. The decrease in O^+ flux with lowered T_e is qualitatively similar to results obtained by Barakat and Schunk (1983). In their study, T_e was found to be the most important parameter with regard to O^+ polar wind solutions. When both effects were considered (column labeled "Combined Effects"), O^+ fluxes decreased by a factor of 200 while H^+ flows increased by a factor of three. For this latter case, the same flux magnitudes were obtained for both ion species as in the BH study. In conclusion, adopting the BH assumptions of a cooler thermal population, results in almost a 1000-fold decrease for O^+ upwelling fluxes. Adopting their enriched hydrogen thermosphere results in H^+ fluxes which are also similar to their original study. Based on these findings, the differences between this study and earlier model results by BH can be

explained by a more realistic specification with the polar wind model of the electron temperature profile (based on DE-2 satellite observations) and thermospheric hydrogen densities (based on MSIS-86) appropriate for high-latitudes.

Ion	Unmodified Model Flux	Enhanced H	Te=3800 K	Combined Effects
H^+	$4.1 \times 10^{+7}$	$3.4 \times 10^{+8}$	$1.4 \times 10^{+7}$	$1.3 \times 10^{+8}$
O^+	$9.3 \times 10^{+7}$	$1.5 \times 10^{+8}$	$1.4 \times 10^{+5}$	$4.4 \times 10^{+5}$

Table 3.3 Steady-state fluxes (ions cm^{-2} sec^{-1}) for summertime solar maximum conditions at 80° 00° invariant at 12 MLT for cases using the polar wind model. Unmodified model results are shown in comparison to results for a hydrogen-rich thermosphere and a cooler, thermal electron population. Fluxes listed under the "Combined Effects" column assume both conditions exist together and are similar in magnitude to results presented by Banks and Holzer (1968).

3.3.2 Comparison of Solar Cycle Variations With Ion Outflow Observations

A quantitative comparison between the flux magnitudes of the thermal (< 1eV) plasma flows described by the polar wind model and in-situ, outflow measurements is difficult to make directly since most satellite data are measured over an integral energy range above the spacecraft potential which normally is above +10 eV. Furthermore, these modeled fluxes do not necessarily represent the total ion outflow measured at higher satellite altitudes since further energization processes can occur which will alter the phase-space distributions of particles. In fact, Moore et al. (1986) found upwelling fluxes on the order of 10^9 cm^{-2} sec^{-1} and, at times, 10^{10} cm^{-2} sec^{-1} (C. J. Pollock, private communication, 1989) in the same region modeled here suggesting that further energization of the plasma is likely. With these limitations in mind, a qualitative comparison can be made which indicates the solar cycle trends in the modeled fluxes of H^+ and O^+ are remarkably similar in character to those seen in direct and indirect outflow measurements. In the latter case, in-situ compositional variations in the near-earth plasma sheet can yield information in the form of ion outflows necessary to populate this region assuming steady state conditions. Young et al. (1982) for example, examined 48 months of ion composition data collected by the ESA/GEOS 1 and 2 satellites at geosynchronous orbits and found a strong correlation (R=0.94) between monthly averaged O^+ densities (0.9-15.9 keV) and the F10.7 solar radio flux (80-220 $\times$ 10^{-22} Watts m^{-2} Hz^{-1} range) during quiet geomagnetic conditions. For the same period, the H^+ densities showed only a weak F10.7 dependence

(although some ambiguity exists in the H^+ densities as the authors point out since solar as well as terrestrial sources contribute to the H^+ plasma sheet density) implying that O^+ outflows are much more sensitive to F10.7 (and therefore EUV/UV) variations. The modeled flux behavior also agrees with the statistical studies using satellite observations. Yau et al. (1985, 1985a) used direct measurements of ion outflows from the Energetic Ion Composition Spectrometer on the Dynamics Explorer I satellite to determine the statistical occurrence of O^+ and H^+ outflows as a function of solar activity. They found the occurrence frequency of upflowing O^+ increased markedly with solar activity with average fluxes 2-3 times greater at solar maximum (F10.7 > 200 SFUs) than during a period of reduced activity (F10.7 < 90 SFUs). For the corresponding period, H^+ outflows exhibited no statistically significant change in outflow rate. These findings, along with the indirect evidence presented by Young et al. (1982) suggest an outflow modulation in O^+ and H^+ fluxes closely tied to solar cycle EUV/UV variations and qualitatively similar to model results presented in the previous section.

3.3.3 Comparison of Solar Cycle Topside Density Profiles: Model Versus Observations

In the ideal case, it would be useful to verify the modeled polar wind fluxes with observations. Unfortunately, observations of the polar wind are very limited (Hoffman and Dodson, 1980; Nagai et al., 1984) so that synoptic or even ensemble averages of the thermal ion outflows are not available. The lack of flux observations stems in large part on the difficulty of accurately and completely measuring the vertical velocity component of the thermal ions since the satellite orbital velocities and/or spacecraft charging effects introduce large uncertainties in the measurements. Without the vertical velocity measurements necessary for flux calculations, an alternative means of comparison is to consider average topside number density profiles for the major and minor polar wind ions since these observations should reflect the general physical and dynamical processes associated with outflow properties. The ability of the model to represent these averaged density profiles will give some indication of the accuracy in the predicted flux magnitudes and help establish the model's ability to represent outflow/equilibrium conditions in the topside polar F-region.

Recently, Grebowski et al. (1990) examined the solar cycle variations in O^+ and H^+ number densities using a combined dataset of ion composition observations from the OGO-6 and AE-C, -D satellites. They combined a large number of individual satellite data points for different solar cycle periods and then derived ensemble averages for solar minimum and solar maximum conditions near local magnetic noon (± 3 hours) and

poleward of 70° invariant latitude. The average F10.7 for their solar minimum and solar maximum data bases was 80 and 141 SFUs respectively so steady-state modeled profiles were produced based on these values for comparison. Their results, shown in Figures 3.8 and 3.9, are compared with the predicted ion distributions for solar minimum and solar maximum for 80° invariant at 12 MLT.

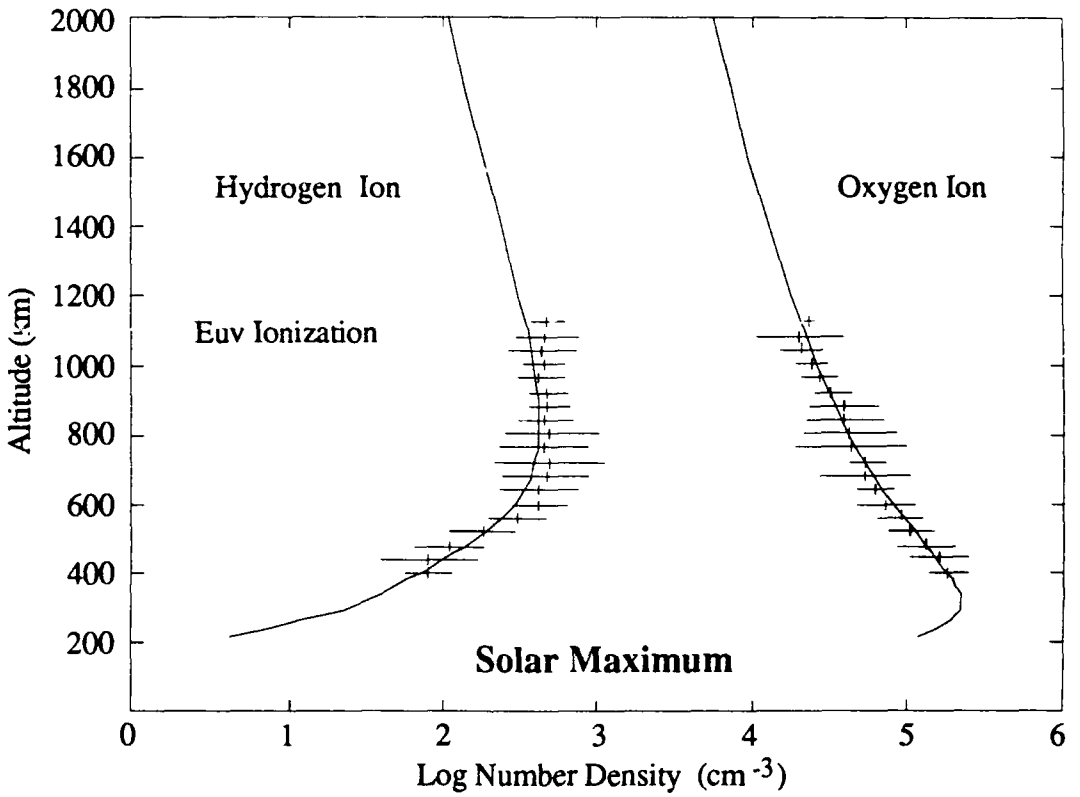

Figure 3.8 A comparison of observed averages and modeled density profiles for the topside polar F-region for solar solar maximum. Data and model results are for summer, magnetic local noon conditions. Modeled distributions of H^+ and O^+ are in close agreement when the model uses EUV ionization based on F10.7 averages for the data collection interval

The predicted density profiles for solar maximum case shown in Figure 3.8 are remarkably similar to the observed averages if one considers the rather extended window over which the observations were collected (6 hours MLT, poleward of 70° invariant). The slightly lower model predictions for H^+ could appear from model ion temperatures being warmer than the observed averages resulting in a shift in the charge exchange equilibrium in favor of lower modeled H^+ densities or may result from uneven sampling of the polar regions in favor of cooler (more dense), evening or dusk/dawn sectors where observed neutral temperatures and atomic hydrogen concentrations would be higher.

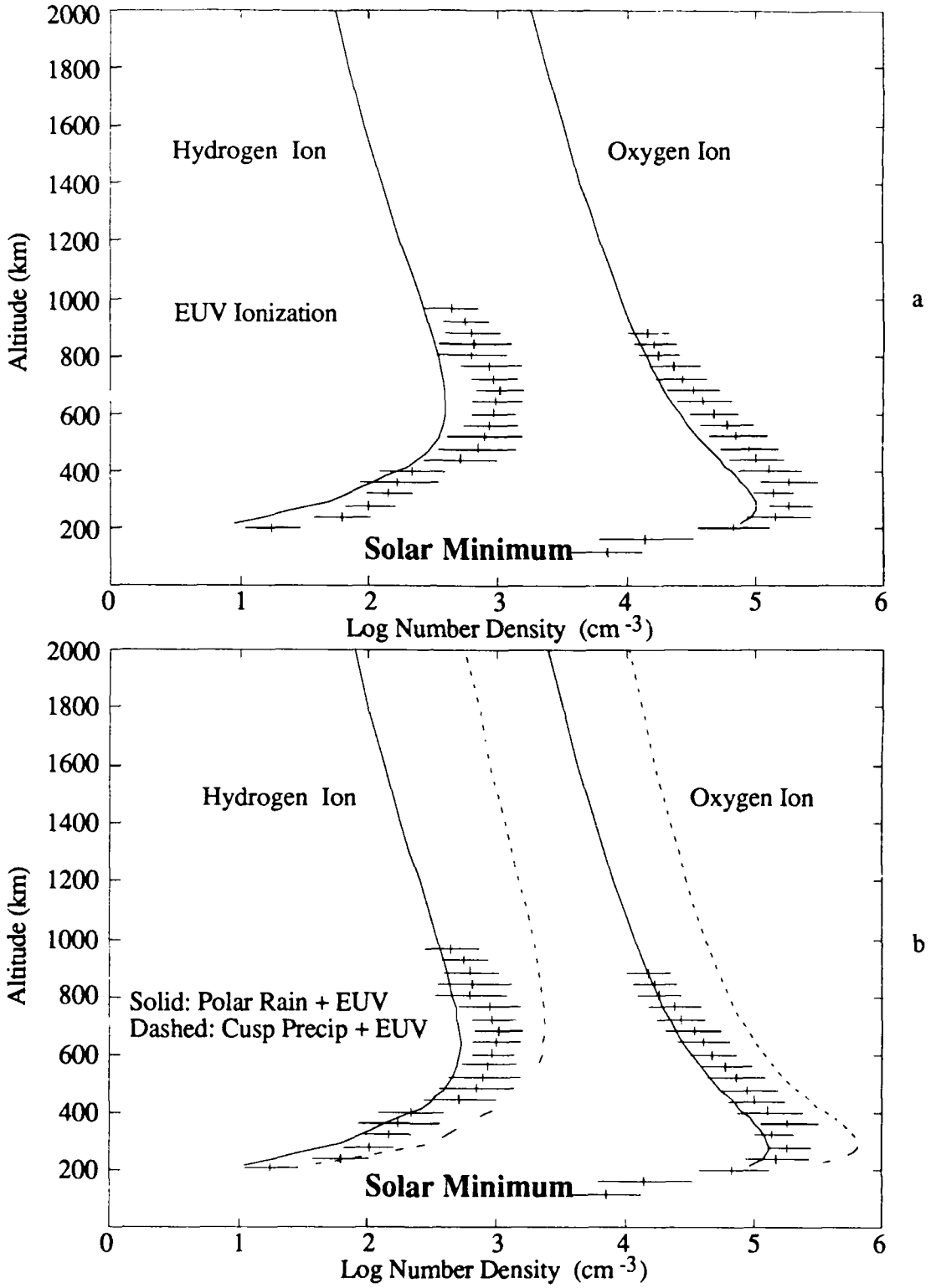

Figure 3.9 Modeled and observed average density distributions of O^+ and H^+ for summer, solar maximum conditions. Modeled profiles underestimate observations when only EUV ionization is considered (a). Agreement is better when ionization from cusp-like particle precipitation is included (dashed curve in b).

These data offer evidence that the polar wind calculations by Cannata and Gombosi (1989), for the slightly higher F10.7, are good representations of the summer noontime distribution of O^+ and H^+ during solar maximum.

For solar minimum (Figure 3.9a-b), the agreement is not as strong since predicted densities for both O^+ and H^+ are consistently low at all altitudes. Large 25%-50% increases in F10.7 could increase both modeled distributions but would noticeably alter the density peaks to higher altitudes. Assuming the data are correct then, there appears to be an additional O^+ production source which is unaccounted for in the model treatment.

The polar wind model was revised to include ionization from precipitating electrons (described in an earlier section) using an analytical energy deposition function and the solar minimum case was reconsidered with additional ionization enhancements typical of polar rain and polar cusp precipitating electrons. The modeled density profiles shown as solid lines in Figure 3.9b reflect EUV and ionization from low energy (0.4 keV) precipitating electrons typically observed across the polar cap (Gussenhaven et al., 1985). Densities for both ions increase with this additional ionization source but still appear slightly lower than the data averages. When ionization from cusp particles are considered with EUV, an overestimate in modeled distributions occur due to large O^+ production increases due to the greater fluxes of precipitating particles which occur in the cusp region (Gussenhaven et al., 1985). In all likelihood, these observations represent an average of additional ionization sources which is difficult to model precisely without further knowledge on their geographic distribution. The modeled profiles effectively bracket the data and suggest that additional ionization contributions, possibly from electron precipitation take on additional importance during solar minimum. This makes physical sense as well since the relative role of impact ionization should increase as solar EUV fluxes diminish. For solar maximum, ionization contributions by precipitating electrons are sill present but are far less important in O^+ production than the high levels of EUV flux and are therefore less important in modeling solar maximum distributions. With additional consideration for wintertime particle ionization, the modeled and observed densities show closer agreement suggesting that both chemical and dynamical processes responsible for each profile are properly accounted for.

3.4 Local Time Variations in the Polar Wind

To highlight further the dominance of solar EUV on summer polar wind fluxes and to identify the relative changes in flux magnitudes due to local time effects, steady-state fluxes were derived for a flux tube near 80° invariant latitude at local magnetic noon during quiet geomagnetic conditions for 4.5 UT, 10.5 UT and 16.5 UT. These times correspond to 00 LST, 06 LST and 12 LST thus permitting a comparison of diurnal outflow

magnitudes for a flux tube at the same geomagnetic location but for different local solar times under summer, sunlit conditions. For the location chosen, sunlight is always present (for any local time), but ionization rates vary considerably due to the large range in zenith angle. Thermospheric conditions for each of the representative UT locations were considered by adopting MSIS-86 neutral densities and assuming quiet geomagnetic conditions with an Ap value of 4. For each of the three cases, steady-state flux solutions were obtained using the polar wind model. Changes in the UT for each case result in different boundary conditions for each modeled location since both neutral composition and solar zenith angles are uniquely determined for a specified universal time and longitude.

Steady-state model solutions of density, vertical velocity and flux for both O^+ and H^+ are shown in Figures 3.10 and 3.11. For clarity, only the 00 LST and 12 LST solutions are depicted in Figure 3.10. Solution profiles for the 06 LST case (18 UT also) fall within the 00-12 LST range in all cases. Diurnal changes in O^+ and H^+ vertical velocity and density profiles are qualitatively similar to the solar cycle variations in the sense that the noontime (solar maximum) case shows higher density and velocity values for both ions compared to the midnight (solar minimum) case. These diurnal variations are smaller than those produced by solar cycle effects but result in significant changes in both the O^+ and H^+ outflow magnitudes as illustrated in Figure 3.11. For O^+ fluxes, a 50% increase near 4000 km is apparent in Figure 3.11 between midnight and noon due to a corresponding increase in number density. H^+ outflows show a smaller diurnal sensitivity with highest values near local noon. Unlike the solar cycle case, H^+ fluxes exhibit a 28% variation between midnight and noon at 4000 km. For the times considered here, the small increase in H^+ outflow velocity does not balance the decrease in densities near midnight so the flux decreases at all altitudes. The small increase in H^+ velocity at midnight results from a decrease in collisions and momentum transfer to the slower moving major ion due to lower O^+ concentrations. The much larger decrease in H^+ densities can be explained by charge exchange equilibrium conditions which prevail below about 1000 km. In cases where the vertical flows are slow enough (less than the smallest scale height per charge exchange period), charge exchange equilibrium is maintained so that equation 3.19 can be expressed as (Banks and Kockarts, 1973):

$$n(H^+) \cong \frac{9\, n(H)}{8\, n(O)} n(O^+) \left(\frac{T_n}{T_i} \right)^{\frac{1}{2}} \qquad (3.20)$$

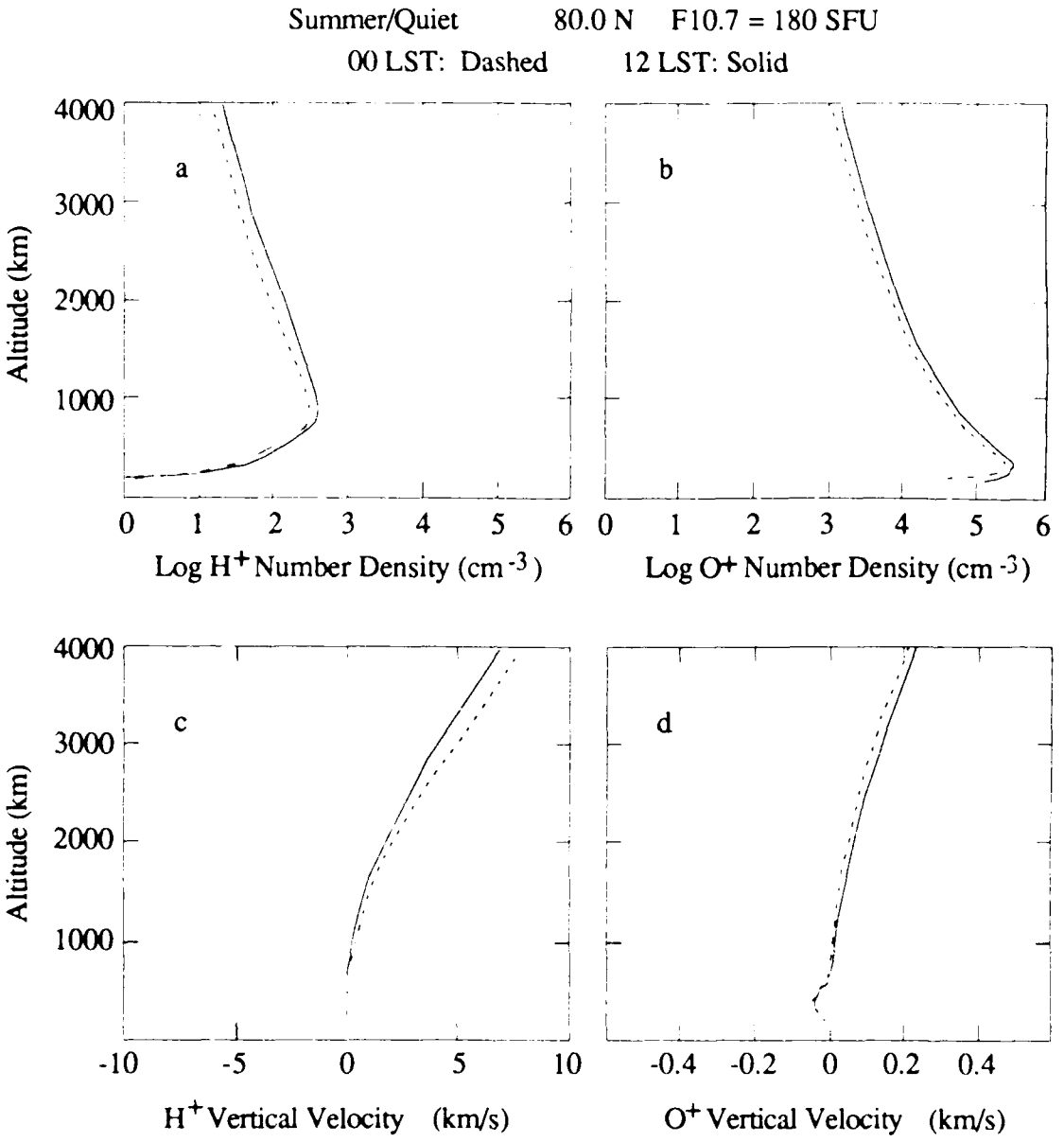

Figure 3.10 Number density profiles of atomic oxygen and hydrogen derived from MSIS-86 for 80° N 00° W geomagnetic at 00 and 12 LST. Decreases in number density for each species between noon (solid) and midnight (dashed) are related to O^+ photoproduction causing diurnal variations in both O^+ and H^+ fluxes.

For this case, decreases of O^+ and to a lesser extent, increased atomic oxygen and decreased hydrogen near midnight act to limit H^+ concentrations throughout the flux tube. In comparing Figures 3.10 and 3.11, changes in the velocity and flux profiles are found to be closely related to density variations in both ion species. To determine the relative importance of model boundary conditions in determining these distributions, the effects of neutral chemistry and photoionization must be separately considered.

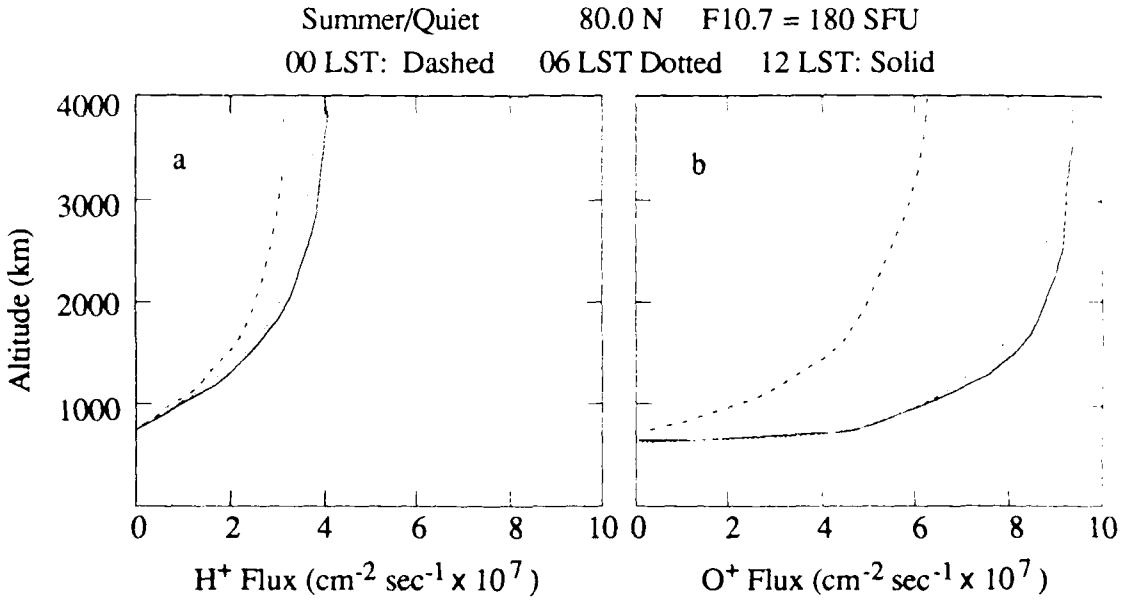

Figure 3.11 Diurnal variations in the H^+ and O^+ densities due to changes in the solar zenith angle modify the ion fluxes significantly between noon and midnight. In this case, O^+ and H^+ fluxes increase by 50% and 28% respectively between 00 LST and 12 LST.

Model variables and flux magnitudes for O^+ and H^+ for the three times considered are summarized in Table 3.4 to help order the relative contributions from thermospheric composition and zenith conditions (or a combination of both factors) on modeled source strengths. The first three rows indicate relatively large changes in O^+ photoproduction brought about by a decreasing zenith angle between midnight and noon. Changes in the photoionization frequency at 200 km ($P_{O^+}(200)$) and photoionization rate ($J_{O^+}(200)$) reflect exponential increases in magnitude as the zenith angle changes. The next three rows relate relative thermospheric composition changes (obtained from the MSIS model) for the same diurnal interval. Ratios of the molecular to atomic species represent relative loss to production ratios in this case, and for the times examined, exhibit very little variation. In fact, the molecular species were constant for each LST case so that ratio changes are due only to a small increase in atomic oxygen between 00 LST and 12 LST. This increase, along with the small increase in hydrogen for the same interval, leads to greater source strengths for O^+ and H^+ respectively but are of secondary importance compared to photoproduction. Based on the percent changes in photoproduction terms and thermospheric compositional changes, it appears that diurnal variations in the O^+ and H^+ flux magnitudes for the quiet, summertime case are most influenced by solar zenith conditions. Lower latitude conditions were also considered but even at 70° invariant, the

compositional variations derived from MSIS for the three local solar times were small by comparison with the variations in ionization due to LST zenith changes. In fact, a wider range in diurnal zenith conditions at the lower latitude location resulted in an even greater variation in flux magnitudes. Based on these results, it appears that in the sunlit polar regions, the magnitudes of upward thermal fluxes for both O^+ and H^+ are closely tied to the diurnal variations in solar zenith angle. In the moving frame of a convecting flux tube, true steady-state fluxes such as those determined here are modified due to horizontal convective transport which introduces additional universal as well as magnetic local time dependencies. The ability to attain steady-state thus depends on the initial flux tube location, convection velocities and vertical transport and chemical processes within the flux tube.

Parameter	00 LST	06 LST	12 LST	Percent Change 00 to 12 LST
Zenith Angle	88°	68°	45°	-49%
P_{O^+} (200) sec^{-1}	48	626	1011	2694%
J_{O^+} (200) cm^{-3} sec^{-1}	1.7×10^{-8}	2.2×10^{-7}	3.6×10^{-7}	2018%
N_2/O (200)	1.65	1.65	1.72	4%
O_2/O (200)	0.107	0.107	0.112	5%
H(200) cm^{-3}	3.3×10^4	3.3×10^4	3.4×10^4	3%
F_{O^+}(4000)cm^{-2} sec^{-1}	6.2×10^7	8.97×10^7	9.3×10^7	50%
F_{H^+}(4000)cm^{-2} sec^{-1}	3.2×10^7	3.8×10^7	4.1×10^7	28%

Table 3.4 Model solutions for three cases representing local time variations for a flux tube at 80° invariant latitude. Changes in geographic space due to the specified UT times result in different thermospheric conditions and zenith angles. Both effect modeled sources and losses however, photoproduction enhancement due to the zenith angle change is the dominating influence in the diurnal flux variations.

3.5 Seasonal Variations in the Polar Wind

Since thermospheric composition and photoproduction rates modulate summertime fluxes, significant differences are expected under wintertime conditions due to alteration of chemical and ionization processes by the reduction and absence of solar EUV. Under summer conditions, solar EUV dominates as an ion source resulting in relatively smooth variations in ion production. Summertime plasma content within convecting flux tubes is

dependent on slowly varying zenith conditions resulting in relatively small variations in ion outflow magnitudes across the polar cap. In winter however, the influence of precipitating particles takes on a more important role since solar EUV ionizations are substantially reduced or entirely absent. A greater degree of spatial and temporal variability in ion content, composition and outflow character is also introduced due to differences in the types of precipitation and to the individual trajectories of convecting flux tubes. These wintertime processes may result in momentarily neighboring flux tubes containing different ion content due to their unique ionization histories. The effects of transport and ion production in the wintertime high latitude region has been parametrically examined by Sojka and Schunk (1986) for various precipitating particle scenarios and will not be considered further. Instead, the goal here is to modify the polar wind model to account for wintertime ionization sources, to identify the importance or lack of importance of transport in relation to wintertime ionization regions and, for cases where transport effects are minimal, to examine the limiting wintertime extremes of production sources and their influence on polar wind fluxes.

3.5.1 Background

Although solar EUV ionization dominates over particle precipitation in the high latitude summer, the relative importance of these processes reverses during winter, with precipitation across the high-latitude regions providing much of the atomic oxygen ionization in the F-region. In terms of total ion production, precipitating electrons are far more important than precipitating ions based on energy considerations. For high latitude regions, the integrated hemispheric energy input for ions is only 11%-17% that of electrons (Hardy et al., 1989). Electron precipitation is highly variable in spectral features, horizontal extent and temporal character so that considerable spatial and time-dependent plasma structure is introduced which alters both the character and composition of polar outflows. Since three basic precipitating particle fluxes can be identified in the high-latitude region (see Table 3.6), a full treatment of the modulating influences on polar ion upwellings would require detailed specification of at least three time-dependent ionization sources along the convection trajectory of a flux tube. This amount of mesoscale information is clearly not available. Instead, the limiting wintertime extremes are examined using available observations in order to establish a range of possible outflow characteristics for representative "winter season" conditions.

3.5.2 Ionization Source Modifications to the Polar Wind Model

To model ionization from any type of precipitating particle source, an analytical expression must be adopted that accounts for various particle fluxes as a function of energy

(particle spectrum) and the altitude-dependent ionizations which result from collisions with the neutral atmosphere. Primary precipitating electrons ionize the neutral gas components producing secondary electrons which are equivalent to photoelectrons produced by photoionization. The analogy ends at this point however because the primary electrons are not absorbed as photons are. Instead, they produce secondary and tertiary particles and gradually loose energy until they become indistinguishable from the ambient thermal electrons. Collisional interactions between the energetic primaries (secondaries, tertiaries, etc) and neutral particles involve elastic and inelastic scattering. In the former, linear momenta may change but no energy exchange between collision partners occurs. In the latter, a change in the internal energy of the atmospheric particle can occur which results in an electronic, vibrational or rotational transition accompanied by a discrete energy loss or ionization, accompanied by a continuous energy loss above some threshold for the precipitating electron. In either case energy is conserved so that the total energy lost by the primary particle is equal to the sum of the ionization potential and the energy carried off by the secondary electron.

A height profile of ion production rates can be determined directly by calculating electron fluxes (Banks et al., 1977) or by using an energy deposition function to calculate energy deposition height profiles together with the assumption that each ion pair produced removes a fixed amount of energy. For the latter case, assuming an extended source of monoenergetic electrons of energy E_p, the ionization rate at some altitude, z, can be expressed as:

$$P_i^e(z) = \frac{\varepsilon\left(z, E_p\right)}{\Delta\varepsilon_{ion}} = F\, E_p \Lambda\left(\frac{s}{R}\right) \frac{\rho(z)}{R\left(E_p\right)\Delta\varepsilon_{ion}} \qquad (3.21)$$

where $\varepsilon\left(z, E_p\right)$ represents the average energy deposition rate at a given altitude for a given particle energy and $\Delta\varepsilon_{ion}$, the average energy loss per ion-elecrons pair formation which has been experimentally derived and set to 35 eV for all interacting neutrals (O, O_2, N_2). The energy deposition rate depends on the degradation of energy flux along the incident path and is therefore a function of the incident flux and the total scattering cross section (the sum of all interacting neutral's cross sections) and the local concentration of the scattering neutrals. This relationship is expressed by the last term in equation 3.21 as the product of the incident flux, F, the primary particle energy, E_p, the energy dissipation function $\Lambda\left(\frac{s}{R}\right)$ the neutral mass density, $\rho(z)$ and the effective range $R\left(E_p\right)$. The effective range is an experimentally derived parameter that describes the indirect distance travelled by an electron before it is stopped. The energy dissipation distribution accounts for the fact that the

electron energy is not dissipated uniformly along the collision path but reaches a maximum at some distance from the source. In the atmosphere, this quantity is proportional to the fractional range, s/R where s represents the scattering depth in gm cm^{-2}. Equation 3.21 represents the total ionization rate for a given energy flux of electrons at a particular altitude. The ion production rate for any species can be determined from this total based on a knowledge of the parent species relative abundance and their ionization cross sections.

A number of analytic expressions have been developed that approximate solutions to equation 3.21 and greatly simplify model computations. For application to the polar wind model described in Chapter 2, an expression derived by Lazarev (1967) and used by Roble et al., 1987 has been adopted. Originally derived for a monodirectional electron beam penetrating the Earth's atmosphere, the expression has since been modified by Roble et al. (unpublished manuscript, 1988) to account for isotropic distributions of precipitating electrons which is a more accurate description of electron precipitation in the high latitude environment. The expression for total ionization rate is:

$$P_i^e(z) = \frac{F\,\alpha\,d(x)}{\Delta\varepsilon_{ion}\,H} \tag{3.22}$$

In this case, α represents the characteristic (defined as one half the average energy) electron energy in keV and F, the electron number flux, such that the *average* energy flux in ergs $cm^{-2}\ s^{-1}$ is $E = \left(1.602 \times 10^{-9}\right) 2\alpha F$. The dimensionless energy dissipation function, d(x), for an isotropic distribution is:

$$d(x) = C_1 X^{C_2} \exp\left(-C_3\ X^{C_4}\right) + C_5 X^{C_6} \exp\left(-C_7\ X^{C_8}\right) \tag{3.23}$$

Coefficients for this expression are listed in Table 3.5. The quantity X is defined as:

$$X(z) = (\alpha)^{-1} \left(\frac{\rho(z)\,H(z)}{4 \times 10^{-6}} \right)^{0.606} \tag{3.24}$$

where $\rho(z)$ and H(z) represent the mass density (gm cm^{-3}) and scale height (cm) respectively for the neutral atmosphere.

Once the total ionization rate as a function of altitude is determined, the production rate of O^+ can be derived based on the local relative abundances and ionization cross sections of parent neutral species. For application to the polar wind model, the two relevant reaction schemes are direct ionization of atomic oxygen and a smaller contribution

C_1	C_2	C_3	C_4
3.233	2.56588	2.2541	0.7297198
C_5	C_6	C_7	C_8
1.106907	1.71349	1.8835444	0.86472135

Table3.5 Coefficients used in the energy dissipation function (equation 3.23) to derive the total ionization rate for an isotropic monoenergetic flux of precipitating electrons.

from dissociative ionization of O_2. The total O^+ production rate can be expressed as:

$$\eta(O^+) = \frac{(0.56\ n(O) + 0.5\ n(O_2))\ P_i}{0.92\ n(N_2) + 1.5\ n(O_2) + 0.56\ n(O)} \qquad (3.25)$$

The numerical constants in this expression follow from the relationships given by Jones and Rees (1973) and represent the peak ionization cross sections (normalized to the O_2 cross section) for the three major neutral species. Adopting equations 3.22-3.25 into the polar wind model permits calculations of height-dependent ionization rates for O^+ production for any specified characteristic particle energy and electron number flux.

Ionization Type	Average Energy (keV)	Characteristic Energy (keV)	Energy Flux (ergs cm^{-3} sec^{-1})
polar rain	0.4	0.2	0.03
cusp	0.2	0.1	0.3
dayside auroral	4.0	2.0	1.5

Table 3.6 Characteristic energy and average energy fluxes of electrons precipitating into the auroral/polar cap region for low levels of geomagnetic activity (after Hardy et al., 1985 and Gussenhaven et al., 1985). These values were used to construct the O^+ production profiles in Figure 3.12.

Several ionization frequency and rate profiles for O^+ production are illustrated in Figure 3.12 using equations 3.22-3.25 with different types of precipitating electron spectra. For comparison, a wintertime solar EUV ionization profile is also included. Three types of electron precipitation (summarized in Table 3.6) were considered separately in Figure 3.12.

Characteristic energy and energy fluxes for polar cap precipitation, in the form of polar rain (Winningham and Heikkila, 1974) were adopted from statistical averages of measurements from the Defense Meterological Satellite Program (DMSP) satellite F2 as reported by Gussenhaven et al., 1985. Cusp spectra were based on Gussenhaven et al., 1985. but included additional satellite measurements from DMSP-F4 and the Satellite Test Program P78-1 satellite. Auroral precipitation fluxes and energy were taken from the same measurements as reported by Hardy et al. 1985. Dayside locations appropriate for each precipitation location were selected for calculating ionization rates based on MSIS-86 atomic oxygen and low Kp conditions were considered for these profiles. By assuming dayside conditions, the auroral energy flux for precipitating electrons is limited to about about half the nightside magnitude yet its contribution to the total ionization rate dominates below about 250 km. Cusp ionization is less intense with a peak ionization rate at higher altitudes. Polar rain ionization rates are about one order of magnitude lower than the EUV profile for the conditions selected here. In general, higher characteristic energies result in deeper penetration of the incident flux resulting in an ionization enhancement at lower altitudes for a constant number flux. Increases in number flux for a given energy results in greater ionization rates throughout the column. Since auroral and cusp precipitation have strong horizontal gradients, residual effects in the magnitude and altitude of maximum O^+ density occur and persist after transport outside these ionization sources. Transients in the height of maximum density dissipate on time scale of less than one half hour (Sojka and Schunk, 1986) but maximum peak densities persist until the flux tube enters a strong, uniform region of ion production that for winter, may not be present. For these cases, a steady-state treatment that ignores transport and time dependencies is not appropriate.

3.5.3 Wintertime Ionization Extremes and Related Ion Flux Characteristics

Of the several types of ionization found in the winter polar regions, a uniform, structureless and nearly isotropic electron flux called "polar rain" or "polar drizzle" (Winningham and Heikkila, 1974) results in a zeroth-order plasma source. Other forms of precipitating particle sources are more important, but to the convecting flux tube, polar rain provides a nearly constant background ionization source across the entire polar cap.

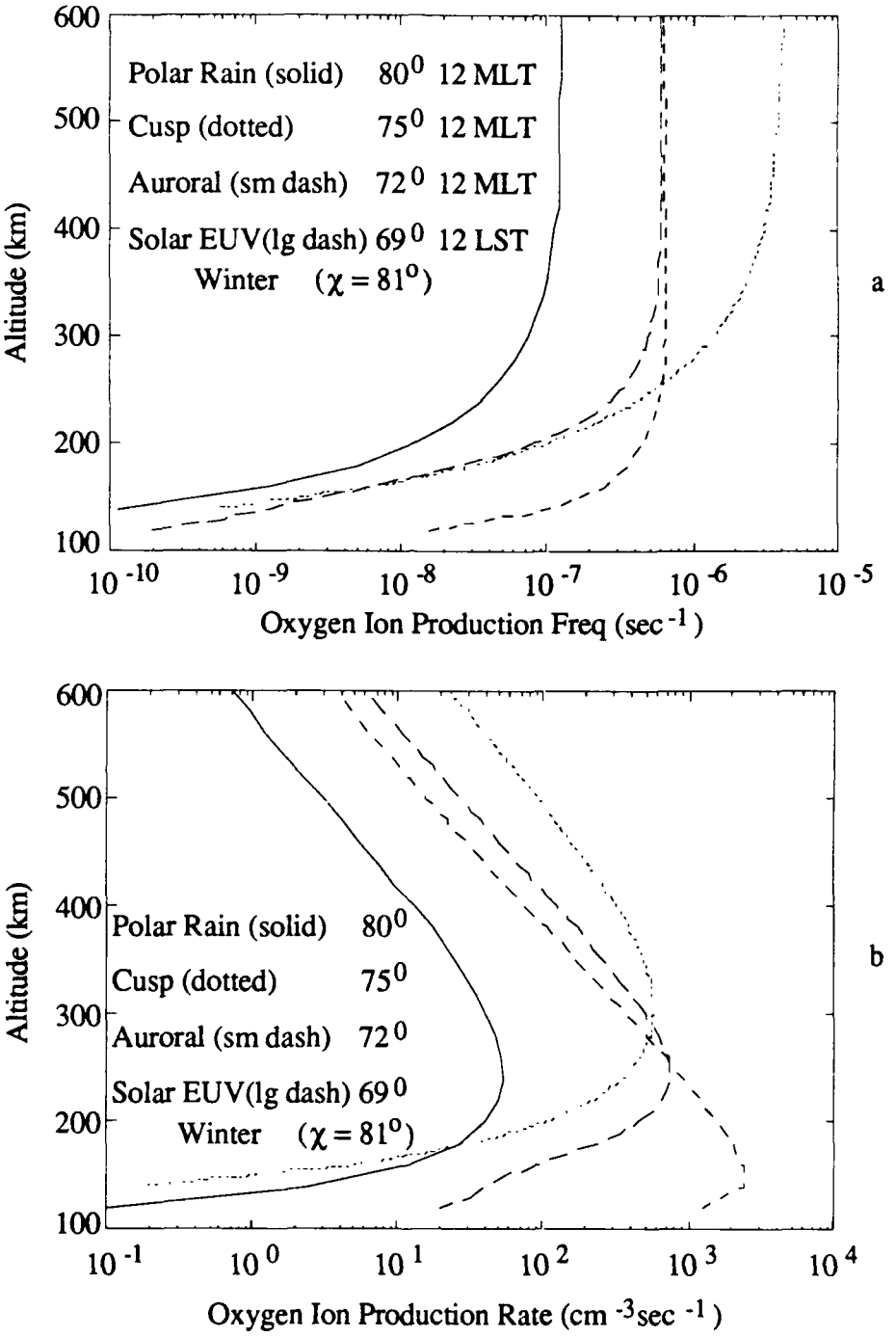

Figure 3.12 O^+ production frequencies (a) and rates (b) for representative wintertime ionization sources. In convecting about the high latitude regions, a flux tube encounters a variety of precipitating particle ionization sources in addition to brief periods of solar EUV ionization. At times, ionization due to dayside auroral particles can exceed EUV, cusp or polar rain sources. However, localized regions can be defined in which each ionization type may dominate.

In the extreme case, polar rain may represent the *major* ionization source for a wintertime flux tube. This situation can occur for flux tubes convecting in the high latitude polar cap at high geomagnetic latitudes in the absence of solar EUV.

To illustrate conditions for which polar rain is the major ionization source and to identify the relative importance of wintertime solar EUV, convection trajectories in both the geographic and geomagnetic reference frames must be considered. The geographic reference frame is used to determine the duration and magnitude of EUV ionization while the magnetic inertial frame must be adopted in determining precipitating particle ionization sources since precipitating particle fluxes are ordered about the geomagnetic pole. These effects are shown in Figure 3.13 where flux tube trajectories from a steady-state TIGCM model run are displayed in both geographic and geomagnetic reference frames for a wintertime case of 50 kV cross cap potential (30 kV across the dusk convection cell and 20 kV across the dawn cell). Due to the displacement in geographic and geomagnetic poles (about 11.5° in the Northern Hemisphere), the motion of high latitude flux tubes are influenced by the combined effects of magnetospheric convection and corotation. Since corotation occurs with respect to the geographic axes and convection with respect to the geomagnetic poles, the same trajectory looks different when transformed between coordinate systems. In the magnetic reference frame (Figure 3.13a), a flux tube located near 68° invariant latitude at 13 UT is strongly influenced by corotation effects and in the subsequent 12 hours, moves along the equatorward boundary of the auroral zone. In geographic space (Figure 3.13b), this same trajectory is subject to several hours of solar illumination and possibly to more temporally and spatially varying ionizations from precipitating auroral electrons. Considering only the less variable EUV ionization component, this trajectory (the "EUV trajectory") forms the upper boundary of the average wintertime ionization cases. Enhancements above this "limit" are possible from transient fluxes but for the case of time-invariant steady-state modeling, have not been included.

Flux tubes located at higher geomagnetic latitudes for the same universal time (13 UT) will trace out different trajectories due to the relative differences in corotation and convection effects. Figure 3.13c illustrates this point. Here, a flux tube initially at 79° invariant latitude completes about two complete circles as it convects around the dawn convection cell during a 12 hour period. The same trajectory viewed in geographic coordinates (Figure 3.13d) has a more complex form due to the relative displacement of the geomagnetic coordinate system around the geographic axis with universal time. The high invariant latitude starting location for this flux tube reduces the influence of corotation and keeps the trajectory in a region where EUV ionization is negligible compared to particle

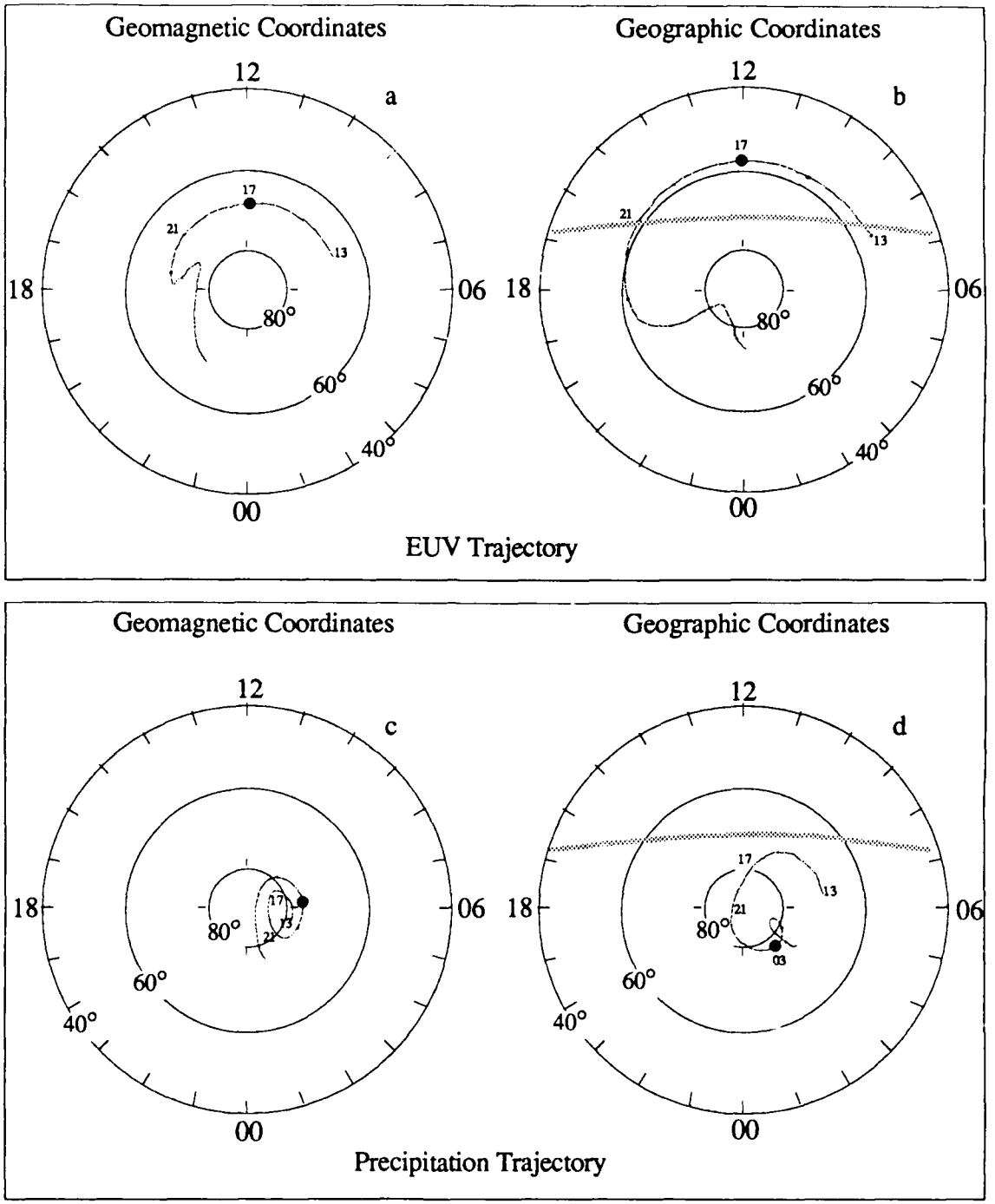

Figure 3.13 Trajectories for two different flux tubes starting at the same universal time but different invariant latitude locations. As a result of different corotation and convection influences based on initial position, each flux tube may experience totally different ionization histories. Here, two wintertime limiting cases are depicted corresponding to the dominating influence of EUV (compare a and c) and polar rain ionization (compare b and d).

precipitation (polar rain in this case). This type of trajectory represents the other limiting wintertime case, i e, a flux tube in the high latitude regions which convects about the geomagnetic pole subject to only ionization from polar rain. Based on these examples, three types of "ionization" trajectories occur in the wintertime high latitude regions:

1. Trajectories where corotation dominates over convection in such a way that the flux tube spends several hours in the sunlit portions of the winter polar regions. In this case, particle ionization may be negligible or small in comparison to EUV ionization depending on trajectory starting location and UT and geomagnetic activity levels.

2. Trajectories in which corotation and convection play important roles. In this case, the flux tubes experience several consecutive types of time-dependent ionization processes as they rotate in and out of EUV and particle precipitation regions. For this type of trajectory, O^+ densities and flux composition will vary markedly as the flux tube moves through various source ionization strengths. Most of the wintertime flux tubes fall in this category giving considerable density structure to the winter polar F-region.

3. Trajectories where convection dominates such that some flux tubes circulate in a confined region of geomagnetic space (either the dawn or dusk cell for instance) so that the dominant ionization source is polar rain.

For low Kp, the trajectory in Figure 3.13a-b represents the upper limit for EUV wintertime ionization used in this study. Auroral precipitation has been ignored assuming a path just equatorwards of the dayside oval and since the EUV ionization source changes slowly due to the incremental adjustments in the zenith angle, the flux tube plasma remains near equilibrium. Time dependencies are not important (this is an a priori assumption now but will be justified later) so a steady-state treatment is justified. Similarly, the trajectory in Figure 3.13c-d is confined to a region where nearly uniform ionization in the form of polar rain is present so that transport effects can also be ignored. Therefore, considering these two limiting cases as the "EUV" and "precipitation" trajectories respectively, a steady-state approach can be adopted in each case to obtain steady-state polar wind fluxes. Solutions obtained in this manner are only zeroth-order representations however since the effects of auroral particle precipitation and transport (both factors not considered here) could modify these fluxes within and downstream of auroral regions. For this study, the effects of winter EUV and polar rain ionization sources are used only as limiting representations of the greatest and least ionization experienced by wintertime flux tubes.

Steady-state solutions of density, velocity and flux for both H^+ and O^+ were obtained for specific locations based on the trajectories depicted in Figure 3.13. Two solution sets were obtained corresponding to O^+ production for the maximum wintertime EUV and minimum precipitating particle ionization. In the case of O^+ photoproduction, a

flux tube near 80° invariant at 12 MLT (17 UT) under quiet (Ap=4), solar maximum (day 80001; F10.7=180) conditions was assumed. This location corresponds to the point marked "17" in Figure 3.13b. For this location and time, the magnetic pole is along the noon meridian so that a flux tube near 69° invariant experiences maximum wintertime EUV flux (solar zenith angle of 81°). For the case where the only source of ionization was precipitating electrons, a flux tube position near 76° invariant and 03 MLT was selected based on a position along the trajectory illustrated in Figure 3.13c. At this location under quiet conditions, polar rain is assumed as the only O^+ production mechanism with no direct EUV ionization possible since the zenith angle was 122°. Under the assumptions described above, steady-state solutions were obtained for both types of O^+ production cases.

Model solutions of density and vertical flows for the two cases described above are plotted in Figure 3.14 and show distinctive characteristics for each ion. For the EUV case, two factors combine to produce high number densities throughout the flux tube. First, large photoproduction rates above 200 km (unity optical depth occurs near 235 km) and a small molecular loss rate combine to produce a net O^+ source which is almost 10 times greater than in the precipitation case. Second, contributions from secondary photoelectron ionization are significant for this high zenith location. In this instance, photoelectron ionization amounts to 60% of the primary ionization at the lower model boundary (200 km). These factors result in large O^+ densities throughout the flux tube column even for wintertime conditions. In fact, the density distribution for this case is slightly larger than the summer solar maximum profile examined earlier for a flux tube near 80° invariant. A small increase in upward flow velocity for O^+ is also present. (Figure 3.14d) and can be explained by a slightly higher density gradient and enhanced temperature gradient (not shown) for the EUV case. A stronger temperature gradient above 1000 km results from more effective collisional coupling with the electron population due to the greater ion densities. For H^+, densities at all altitudes are higher for the EUV case and relate directly to greater O^+ distributions through charge exchange chemistry (equation 3.20). Similarities in the topside density scale heights between both ions suggest that H^+ is near its limiting flux value. The biggest difference in H^+ behavior between the two cases occurs in the vertical velocity profile. For the EUV trajectory, clearly slower upward velocities are present due to increased O^+ density. Collisions and momentum transfer to the slower moving O^+ ion act in the same manner as during solar maximum to effectively impede acceleration of the lighter H^+ ion . For the EUV case, this retardation delays the sonic transition until 4700 km whereas in the precipitation case, the transition occurs much lower, near 2300 km. Even without the influence of a larger and more variable auroral ionization source, significant changes in in the mass and momentum budgets appear for

both ions in the wintertime ionosphere between sunlit and polar rain cases. These changes lead to large variations in upwelling fluxes so that uniform or even slowly varying outflows across the winter polar regions appear unlikely.

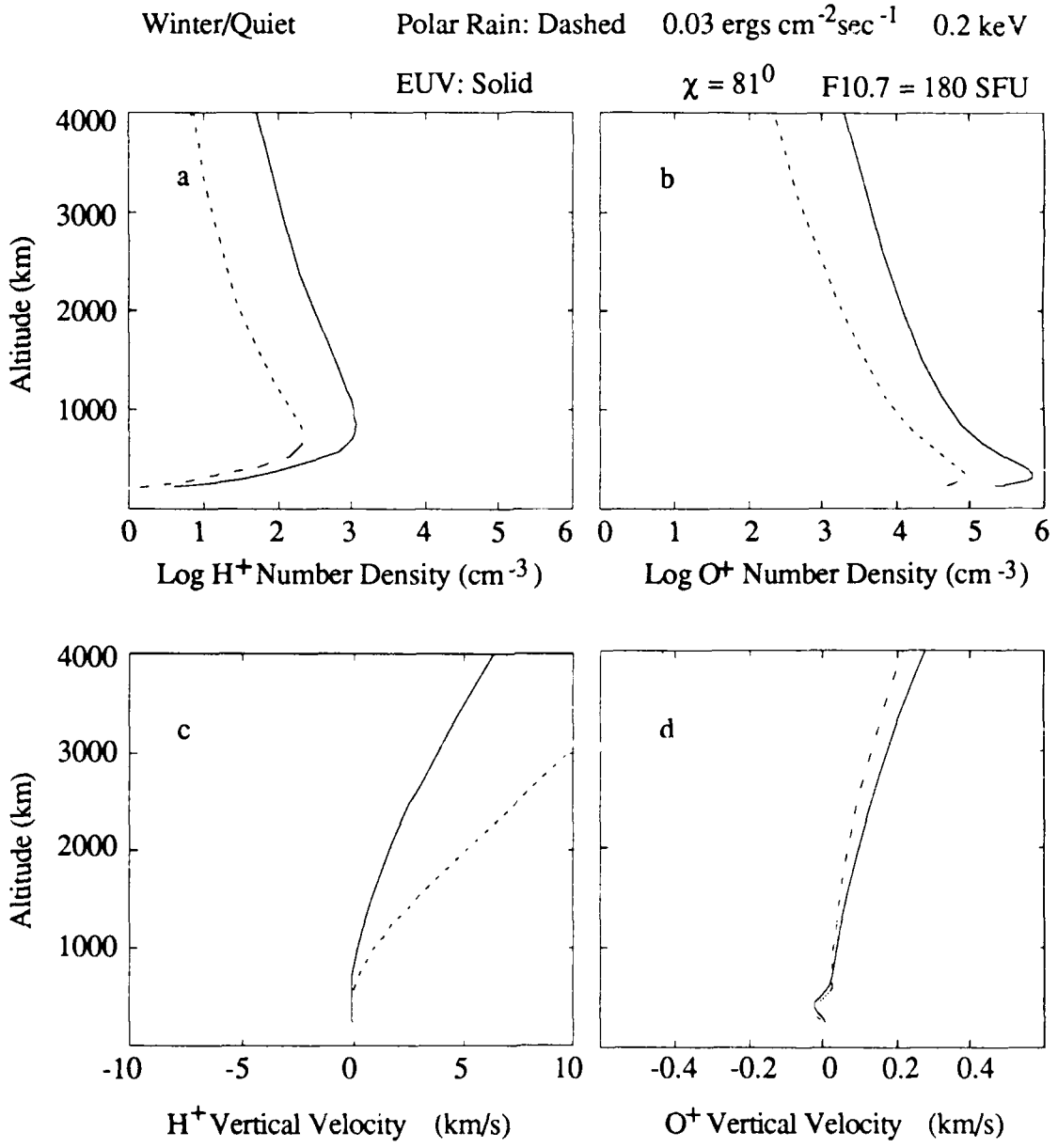

Figure 3.14 Modeled profiles of H^+ and O^+ density and vertical velocities for two wintertime cases. Solid lines are for a location where solar EUV is the dominant ion production source. Dashed lines correspond to a location experiencing ionization from precipitating electrons in the form of polar rain. Each ionization source creates unique changes within the flux tube.

The distinct variations in density and flow velocity described above are combined in the form of upwelling fluxes and presented in Figure 3.15. Flux magnitudes have been

normalized to 1000 km to account for the diverging flux tube cross sectional area. A factor of three increase in the steady state H^+ flux for the EUV case is evident in Figure 3.15a, and by comparison with Figure 3.14, can be explained by the enhanced number densities associated with O^+ photoproduction. Even though upward velocities are significantly lower than for the precipitation case, the H^+ flux remains larger. Oppositely directed responses in both density and velocity profiles occur for H^+ throughout the column but the relative changes in number density are the controlling influence in dictating flux variations between cases. For O^+, the large variation in flux between cases illustrates the importance

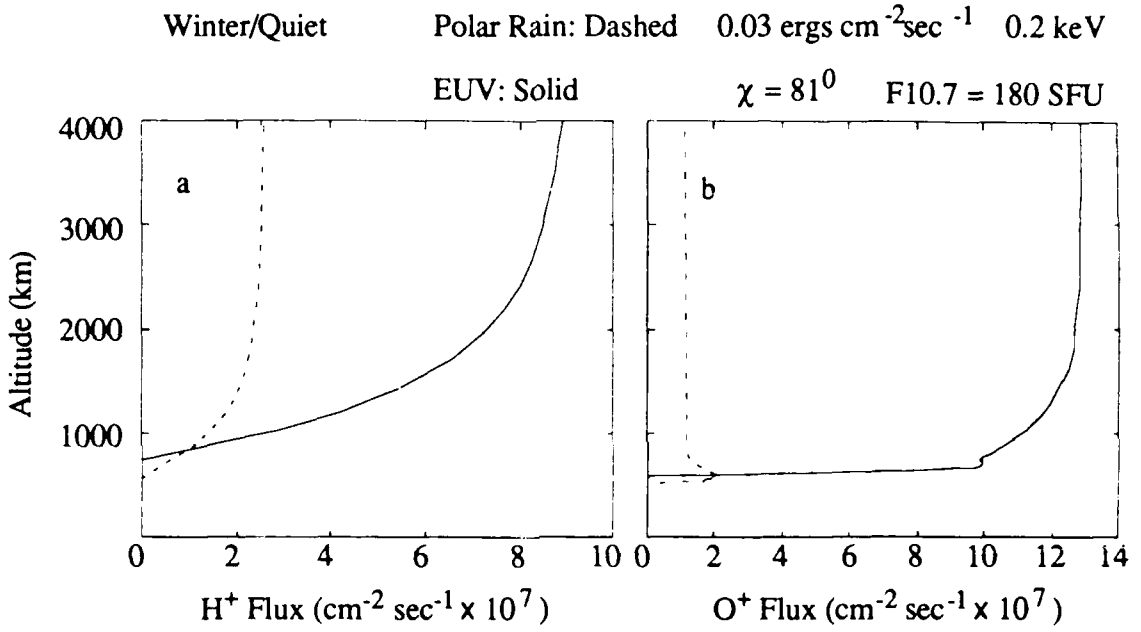

Figure 3.15 O^+ and H^+ flux profiles for the wintertime EUV and polar rain ionization sources. Distinct changes in magnitude for each species occur primarily as a result of ion density variations caused by different ion production strengths.

of ionization sources during wintertime conditions. For the limiting cases examined here, a large, order of magnitude difference in O^+ flux exists between the polar rain and EUV trajectory. This behavior is similar to the solar minimum/maximum variations since the O^+ upwelling velocity remains relatively constant with large number density variations supporting the flux enhancement. The large differences in flux magnitudes between these cases suggests that highly patterned and structured outflows prevail across the winter polar regions.

A comparison of flux composition and magnitude for both wintertime cases and a summertime solar maximum case illustrates the modulating effect of ionization sources and

chemistry during wintertime. Figure 3.16 contrasts the H^+ and O^+ fluxes for the two wintertime cases described above along with the summer solar maximum case considered earlier.

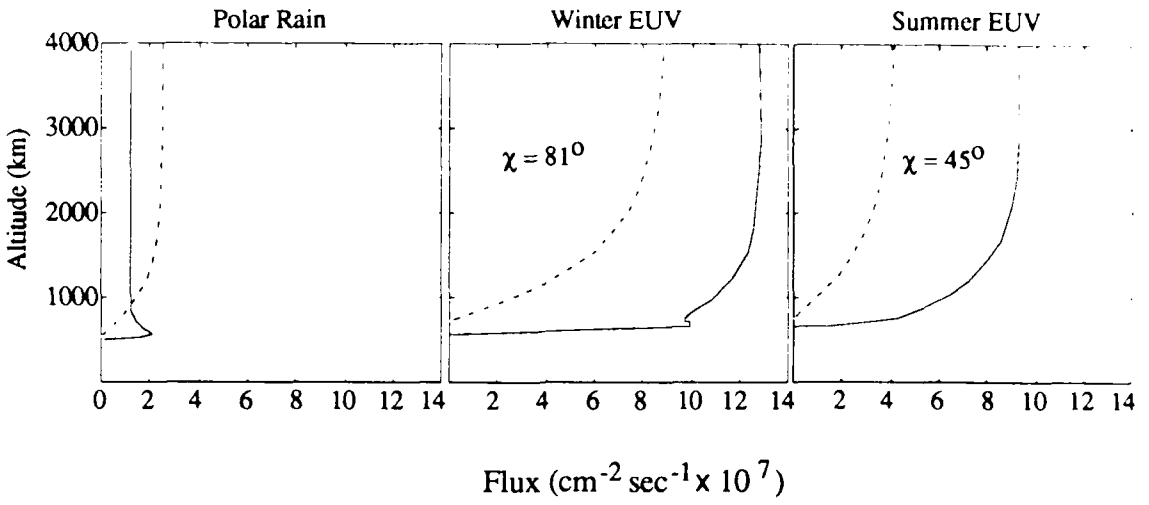

Figure 3.16 O^+ and H^+ flux profiles for the two wintertime cases compared to summer solar maximum. Flux magnitudes and total outflow composition vary due to differences between ionization sources. For the winter EUV case, O^+ fluxes exceed summer values due to an increase in the net source strength for O^+. Increases in source strength result from a shift upward in the altitude of peak ion production for winter EUV illumination.

A comparison of the three cases illustrates two important points. First, for the wintertime high latitude environment, the intensity and the composition of the polar wind will vary considerably from one flux tube to the next. Do to differences in wintertime flux variations, the H^+/O^+ flux ratio changes from 0.69 for the winter EUV case to 2.3 for the polar rain case. This behavior suggests that the composition of outflows varies a great deal due to ionization source type but also due to ionization history. For certain regions, such as the inner vortex of convection cells, enriched H^+ flows will prevail when only polar rain precipitation is present. Likewise, along the dayside where EUV and possibly auroral ionization is present, highly enriched O^+ thermal upflows will dominate based on high O^+ production rates. H^+ fluxes will also increase for this latter case to maintain charge exchange equilibrium (compare the H^+ flux behavior in Figures 3.16a and b) however, frictional interaction limits the number density scale height to that of the major ion so that H^+ is at or near its limiting flux value. If the effects of transport are included, these features should still appear but may be shifted in location away from the major ionization regions in a manner similar to that reported by Sojka and Schunk (1986). A second important feature illustrated here involves the importance of chemistry in "controlling"

outflow magnitudes. In comparing the summer and winter O^+ flux magnitudes, one finds the winter flux is about 39% greater than the summer flux even though the photoionization frequency for the summer case is greater (zenith angles for summer and winter cases considered are 45° and 81° respectively). This behavior arises due to the shift upwards in the altitude of peak production during wintertime. The slightly lower ionization frequencies during winter are offset by the reduced loss rate for the O^+ produced at higher altitudes. The combined effect in this case is a slightly higher net source of O^+ (and therefore density) throughout the column under greater zenith conditions. This effect can be seen easily by examining photochemical lifetimes for O^+ at 200 km and 400 km. Assuming loss by ion atom interchange with N_2 or O_2 and charge exchange with atomic hydrogen photochemical lifetime for O^+ can be defined as:

$$\tau_{O^+} = \frac{1}{k_1[O_2] + k_2[N_2] + k_3[H]} \tag{3.26}$$

where k represents the reaction rate coefficients for the various loss processes. O^+ lifetimes were calculated using MSIS-86 neutral densities and temperatures for summer and winter solar maximum conditions and are summarized in Table 3.7.

Chemical Lifetime	Summer 200 km	Summer 400 km	Winter 200 km	Winter 400 km
τ_{O^+}	163 seconds	3.43 hours	176 seconds	3.45 hours

Table 3.7 Chemical lifetimes for O^+ at 200 km and 400 km are similar for both summer and winter polar regions due to opposing changes in seasonal concentrations for molecular nitrogen and oxygen and atomic hydrogen. If created at higher altitudes, O^+ is more likely to experience diffusive rather than chemical control.

Photochemical lifetimes are surprisingly similar when winter and summer lifetimes are compared due to relative changes in abundance for molecular species (reduced in winter due to lower thermospheric temperatures) and competing changes to atomic hydrogen (concentrations almost double in winter due to interhemispheric transport) at both altitudes. Production processes which create O^+ at higher altitudes such as winter EUV or even large fluxes of low energy electrons (cusp electrons for instance) will act to increase the major ion column density and ultimately, the major ion flux magnitudes. This behavior effects both summer and winter locations to various degrees but appears more pronounced in the winter case examined here since reduced molecular losses and enhanced photoelectron

ionization both contributed to the larger net source of wintertime O^+. Extending this process to all forms of ionization sources, wintertime dayside fluxes should have an increasingly dominant O^+ composition as the flux tubes move away from sunlit areas and into regions of cusp precipitation. Moving out of these ionization source regions, the effects of increased ion production would be displaced downstream by a distance proportional to the horizontal convection velocity. For the lifetimes considered above, the effects of winter EUV or cusp ionization can be transported over the polar cap along many flux tube trajectories. Considering the complex trajectories traced out by the time-dependent motion of flux tubes and the inherent spatial and temporal variability in particle precipitation across the high latitude region, there appears to be a wide range in magnitudes and composition of wintertime polar wind flows.

3.5.4 Comparison of Seasonal Cycle Topside Density Profiles: Model Verses Observations

As before, direct comparisons between observations and the "average" fluxes predicted above are difficult since no statistical data on polar wind outflow conditions are available. Indirect comparisons can be made however by examining the consequence of these outflows on the topside density distributions of the major ion. Under steady-state conditions, the major ion density distribution should reflect the sum total of production, loss and transport processes. Since the observed density distribution includes the low altitude region where photochemistry dominates and a topside regime where transport effects dominate, a comparison between observations and predictions will provide insight into the model's ability to represent accurately both the low-altitude photochemical processes as well as the higher altitude dynamics of polar wind flows. Accuracy in one regime does not necessarily imply accuracy in the other however, in achieving the correct balance between production, loss and upward flux, model representations of the density profiles should reflect the observed distribution in terms of the magnitude and altitude of peak density and the topside scale height.

In this seasonal comparison, electron density measurements from the DE-2 Langmuir probe are used to represent the O^+ ion density under the assumption of charge neutrality and negligible H^+ concentrations. To obtain adequate altitude coverage, 150-day windows centered on summer solstice for one year was selected to represent the summer season. For the winter period, this window was reduced to 60 days (centered on winter solstice) to reduce the effects seasonal solar EUV variability. Observations were further restricted to 75°-85° invariant between 11 and 13 MLT and for Kp <3 to maintain

correspondence with the model results described above. For the summer observations, only Northern Hemisphere data from 1982 were used to restrict the UT dependence to a 6 hour range centered about the model results valid at 06:00 UT. A similar treatment was used with the wintertime observations but included data from two winter seasons instead of one (1981-1982 and 1982-1983) For the seasonal intervals selected, the average F10.7 was 186 SFUs and 188 SFUs for the winter and summer periods respectively. Data from these two periods were plotted as a function of altitude to provide a seasonal range of density distributions for comparison with model estimates of average O^+ density.

A comparison between modeled O^+ density profiles and seasonal observations is shown in Figure 3.17. The observed densities have not been averaged into a single profile to permit a range over which model results may be interpreted. This treatment is particularly important for two reasons. First, extended altitude coverage depends on a number of measurements taken at different altitudes/times and therefore, geophysical conditions. The modeled profiles, however, represent average O^+ densities at one time and for one set of conditions. Secondly, each observation retains some degree of time-dependent chemical or dynamic influence which cannot be resolved by a single in situ measurement or fully represented through steady state modeling treatments. This is especially true for the wintertime period where only two limiting cases for ionizations were made without additional consideration of prior forcing along individual trajectories. For these reasons, it is better to interpret the goodness of the model profile in terms of the range of observed conditions. Model results based on "mean" conditions should fall near the midpoint of the data while predictions based on extremes should lie near the limits of observed conditions.

In Figure 3.17a, modeled density distributions (for the EUV and polar rain cases) are compared with the range of observed density measurements for the wintertime period. Two density distribution solutions were obtained using the polar wind model for the extremes in ionization determined by the earlier trajectory analysis. The position of the two model profiles on either side of the range of observations suggests that the assumed trajectory positions and ionization sources for each case do in fact represent limiting wintertime conditions. Observed densities within these limits probably occur as a result of time-dependent processes associated with trajectories threading both types of ionization source regions. Both the altitude of peak density and overall profile of the modeled distributions follow the observations suggesting that the major chemical and vertical transport processes have been properly modeled. The close fit between observational range

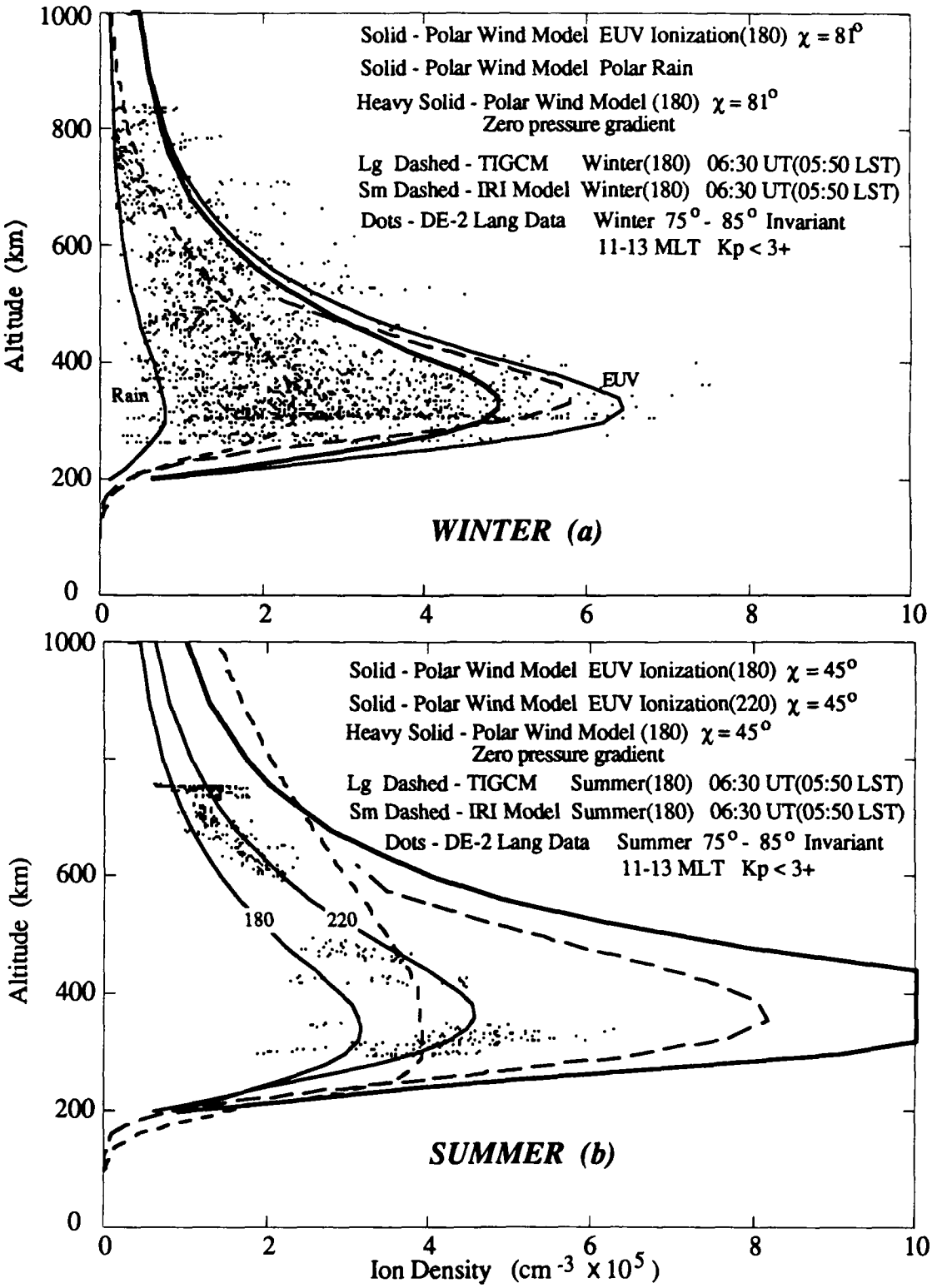

Figure 3.17 Observed and modeled O^+ density distributions for winter (a) and summer (b) solar maximum conditions. Data based on Langmuir probe observations from the Dynamics Explorer-2 satellite are for 75°-85° invariant, 11-13 MLT (3.5-9.5 UT). Modeled profiles are steady-state solutions at similar locations and times.

and modeled extremes points to the range of variability in density and therefore fluxes which should occur in the wintertime polar region and highlights the importance that precipitation plays as a ionization source in the absence of EUV.

In contrast to the wintertime period, the summer distributions illustrated in Figure 3.17b exhibit far less variability due to the dominating influence of EUV. While some precipitation, particularly at low altitudes in the auroral region, may result in momentary ionization enhancements, the more uniform and slowly varying EUV flux dominates the ion production and results in far less structure and variability in the observed summertime densities. For comparison, a number of modeled ion density profiles are also shown. The IRI model profile was based on a single location, F10.7 and universal time and appears to represent the average density peak reasonably well although the topside scale height seems too large based on the overestimated densities above 450 km. The TIGCM profile was obtained from a diurnally-reproducable summer solstice run under quiet geomagnetic conditions at solar maximum. Although the density peak lies at about the right altitude, densities are greater than the observations by 30-50% for this case. This overestimation results from a zero flux condition which is assumed at the TIGCM upper boundary (private communication, Dr R. Roble, 1989). Under this assumption of diffusive equilibrium, no net loss of ions occurs due to upward transport across the model boundary so that for steady-state, local densities are defined by a balance between production and chemical loss and are therefore higher. The same assumption exists for the wintertime case but is less apparent due to the greater range of observed densities and a wintertime reduction in the modeled ion production rate. In both instances, diffusive equilibrium assumptions result in much larger O^+ concentrations at all altitudes since loss due to upward transport has been set to zero.

To further examine the sensitivity of modeled densities to imposed upper boundary conditions, the polar wind model was modified by reducing the pressure gradient to zero across the upper model boundary . This has the effect of turning off the topside "vacuum cleaner" but still permits a non-zero flux across the boundary due to pressure variations within the modeled flux tube volume. Similar conditions might be expected in a flux tube which has recently closed off due to magnetic recofiguration or merging. A steady-state summer distribution is illustrated in Figure 3.17b. For this case, the same location, time and F10.7 (180) as used previously was assumed; only the pressure gradient at the top boundary of the model (8000 km) was changed. The O^+ distribution under these conditions differs significantly from the non-zero pressure gradient case with ion densities far in excess of the observed summertime densities at all altitudes. This ion density enhancement develops due to a reduction in O^+ field-aligned flow in the absence of a

topside pressure gradient. For instance, at 1000 km, the O^+ field-aligned flow was reduced from 14 m/s to 2 m/s when the pressure gradient was set to zero. With decreased loss due to upward transport, the densities increase everywhere so that the topside ionospheric scale heights are unnaturally reduced over the altitude range of observations considered here. The large departure between observed and modeled distributions under the zero pressure gradient boundary assumption suggests that a strong pressure gradient exists along open flux tubes which supports a low-speed upwelling of O^+. For comparison, a similar assumption was made for the wintertime case (also plotted in Figure 3.17a). For this case however, a non-physical solution is obtained. The assumption of an unlimited topside resovoir, into which upwelling ions normally enter, works in reverse by supporting an unlimited downward flux of O^+ once the pressure gradient is removed. The slow, downward flux develops in response to low altitude losses due to recombination. This wintertime density distribution is nonphysical however, since it is based on a steady-state condition which depends on an unlimited upper resevoir of plasma at the model boundary. While downward low-speed plasma flows are a common feature in maintaining an F-region in the absence of EUV, such fluxes are limited by the volume of plasma within the flux tube aso that an infinite supply of plasma is not available as in the model. The wintertime density profile appears to fit the observed distribution but for the wrong reason. The summertime case however, clearly indicates that pressure gradients along the flux tube and low-speed upward flows of O^+ are important in establishing the topside density distribution of O^+.

The best fit for the range of summertime observations resulted with two steady-state dynamic solutions from the polar wind model. For these cases, only the F10.7 values were varied. The low density profile was obtained using an F10.7 of 180 SFU and coincides well with the lower range of observations. The higher density profile was obtained using an F10.7 of 220 SFU and lies at the upper range of the summertime data. The close correspondence with data in both cases suggests two points. First, most of the observed variability in the summertime period can be adequately accounted for by F10.7 variations, or more correctly, solar EUV variations. Other factors such as transient particle precipitation may account for some of the low-altitude spread in observed density values. However most of the data for this period falls within the two profiles corresponding to high and very high solar activity. Secondly, the close fit in profile shape for both cases with the observed distributions suggests that topside dynamic equilibrium conditions are modeled properly. The clear departure of these profiles from the diffusive equilibrium profile (also shown in Figure 3.17b) indicates that O^+ has a net upward flux which acts to reduce the scale height for the flowing ion. Additionally, agreement between observations and

profiles, suggests that the major chemical and dynamical processes within the collision-dominated interval have been adequately addressed by the polar wind model.

The generally good agreement between observed and modeled density distributions provides additional, indirect evidence that the predicted behavior in seasonal O^+ fluxes is valid. Since modeled O^+ velocities examined in this study were found to be invariant to seasonal influences, differences in O^+ flux magnitudes between seasons are simply the result of variations in the available O^+ density. Accuracy in the predicted fluxes therefore is directly linked to the accurate specification of O^+ densities by way of the seasonal ionization source strength. The ionization source strength depends, in turn, on the accurate specification of ionization frequency as well as the altitude distributions of neutral constituents. With agreement demonstrated between model and observations for both seasonal (and solar cycle) conditions, realistic O^+ flux predictions for the summer period can be obtained once an accurate specification of the ionization production rate is obtained thru the F10.7 solar radio flux proxy. Winter flux magnitudes, apart from the limiting cases considered here, are considerably more difficult since prior ionization history along the flux tube trajectory must be included to approximate better the density profile and flux magnitudes. For this latter case, time dependent treatments are more appropriate for modeling specific locations where transport becomes important.

3.6 Summary

In this chapter, the composition and character of high-latitude ion upwelling was examined and related to the various state changes which occur within the thermosphere and ionosphere for a variety of solar and geophysical conditions. Under the assumption of steady-state, solutions to the fully-coupled continuity, momentum, and energy equations for a three species, quasi-neutral plasma were obtained for various solar cycle, local time and seasonal extremes to obtain a range of thermal ion fluxes occurring across the polar cap. In addition to providing quantifiable estimates of flux composition and intensities, this work also identified key underlying processes which act to enhance and modulate thermal ion flows under varying environmental conditions.

Accurate specification of the O^+ production rate is a prime consideration in modeling polar ion outflow properties since the mass, momentum and energy budgets of both the major and minor ion (H^+) are interrelated through chemical and frictional processes below 1000 km. Towards this goal, several improvements to the original version of the polar wind model developed by Gombosi et al. (1985) have been made. An algorithm was developed and installed in the code which derives an altitude-dependent photoionization frequency for atomic oxygen for a given location, time and solar activity

level (F10.7). Local enhancements to the ionization frequency by photoelectrons were also included. These improvements are the first of their kind to be considered in polar wind modeling and were shown to have significant effects on derived flux magnitudes, especially for high solar zenith angle conditions The model's utility was extended further by including an algorithm that models ion production based on an energy deposition function for any given spectrum of precipitating electrons. In addition to the wintertime EUV ionizations, the polar wind model can now account for other ionization sources including polar rain, cusp and auroral precipitating electrons. With this new capability, seasonal behavior in ion upwellings can be modeled to highlight differences in summer and winter outflow composition and intensity. These modifications resulted in improved accuracy of topside plasma conditions and extended the model's utility over a broader range of geophysical conditions.

Variations to ion outflow properties during the solar cycle were first considered using the improved polar wind model. Changes in thermospheric conditions at solar minimum and solar maximum, based of representative F10.7 fluxes, were found to alter substantially the character of ion outflows. For a position near 80° geomagnetic latitude and at 12 LST (12 MLT), H^+ fluxes remained invariant due to opposing changes in the density and vertical flow distributions however, an order of magnitude increase in O^+ fluxes occurred for solar maximum due to a 10-fold increase in the O^+ density profile. This behavior increased the intensity of the total ion flow at solar maximum and produced a marked shift towards O^+-enriched upwellings at solar maximum. Local time effects were next examined by considering steady-state solutions during solar maximum for the same location but at different local times. This treatment highlights the effects of diurnal solar zenith angle variations under geomagnetically quiet, summer conditions. In this case, H^+ and O^+ fluxes varied by 28% and 50% respectively due to changes in the O^+ photoproduction rate for zenith conditions between 00 LST and 12 LST. This behavior indicates that upwelling fluxes become enriched as the solar zenith angle decreases along a given flux tube trajectory, i.e., towards the local noon sector. Finally, seasonal fluxes were investigated by comparing the summer solar maximum case with two wintertime cases which were selected to represent the wintertime extremes in ion production. Wintertime photoproduction of O^+ can dominate ionization processes for up to several hours along certain flux tube trajectories and produce large total fluxes of oxygen and hydrogen ions. As before, changing zenith angles result in enriched O^+ flows near 12 LST (and 12 MLT). At the other wintertime extreme, electron precipitation in the form of polar rain may be the only source of locally produced O^+. For this extreme, O^+ fluxes, and to a lesser degree H^+ fluxes, decrease so that the composition of total ion flux shifts in favor of

an H^+-dominated flow. Within this range of wintertime extremes, a highly variable and structured composition and outflow intensity can be expected as flux tubes convect through various ionization source regions.

Condition	O^+ flux (cm^{-2} sec^{-1})	H^+ flux (cm^{-2} sec^{-1})	Total Flux (cm^{-2} sec^{-1})	Ratio H^+ to O^+
Solar Maximum Summer	9.3×10^7	4.1×10^7	13.4×10^7	0.44
Solar Minimum Summer	7.8×10^6	4.1×10^7	9.3×10^7	5.26
Solar Maximum 00 LST	6.2×10^7	3.2×10^7	9.4×10^7	0.52
Solar Maximum 06 LST	9.0×10^7	3.8×10^7	12.8×10^7	0.42
Solar Maximum 12 LST	9.3×10^7	4.1×10^7	13.4×10^7	0.44
Winter (EUV)	12.9×10^7	8.9×10^7	21.8×10^7	0.69
Winter (polar rain)	1.1×10^7	2.5×10^7	3.6×10^7	2.35
Summer (EUV)	9.3×10^7	4.1×10^7	13.4×10^7	0.44

Table 3.8 Summary of upwelling flux magnitudes and composition for a variety of solar-geophysical conditions. All values reflect steady-state solutions taken at 4000 km for quiet (Ap=4) geomagnetic conditions. Solar cycle solutions are valid at 80° invariant, 17 UT, 12 MLT, with F10.7 of 180 (solar max.)and 60 SFUs (solar min.). Summer cases are for day 172. Winter cases are for day 355. Local time study locations were taken at 80° invariant for summer, solar maximum. Wintertime cases are for 69° invariant (EUV) and 76° invariant (polar rain), for approximately 17 UT (12 MLT) and 03 UT (06 MLT).

By comparison to similar summertime conditions (but at different locations and zenith conditions), wintertime H^+ and O^+ fluxes can be very large and, at times, can exceed summertime fluxes due to a shift to higher altitudes of maximum O^+ production. This lowers the O^+ loss rate to molecular species and with local ionization enhancements due to

photoelectrons, results in a small increase in net O^+ production even with the greater wintertime zenith angle.

Table 3.8 summarizes the range of O^+ and H^+ fluxes and total flow composition under the conditions described in the previous sections. It is important to recognize that these values correspond to steady-state solutions and are representative of a long-term average for the conditions and location specified. With these limitations in mind, results provided here give some quantifiable expectations of upwelling ion characteristics for typical solar geophysical conditions.

The results provided here are unique and provide new insight into thermal ion upwelling in the polar regions for several reasons. First, in each case, predicted fluxes are derived for specified geophysical conditions and are not influenced by any imposed boundary specifications such as drift velocities or number densities. This treatment makes no a priori assumptions about plasma state variables but calculates them self-consistently so that each result depends on solar and geophysical assumptions. Second, the results obtained here represent average values as opposed to some upper or lower bound in flux. This provides additional insight into relative source region magnitudes which is important in understanding resupply processes for higher altitude UFI events. For instance, for the cases examined here, model results suggest a quasi-permanent region of O^+-enriched outflow near local noon for summer as well as winter conditions based on enhanced O^+ production. This condition has been expected to support higher altitude UFIs but has never been theoretically demonstrated without specifying some initial plasma flow or density condition Finally, single-valued solutions such as those provided in Table 3.8 do not necessarily imply improved accuracy, but they do provide a benchmark for verification and further model refinements. Indirect evidence in the topside density distributions presented earlier suggests that the model predictions are generally good, however, in situ flux measurements are clearly needed for model verification and refinement. Future comparisons, in the form of synoptic observations of polar wind fluxes, will hopefully confirm these predictions in a more direct manner.

The steady-state approach is much easier to apply to the summertime cases where flux tubes experience large and relatively continuous solar EUV ionization. Wintertime extremes can also be considered in this manner. To consider the full range of wintertime cases however, one must include the effects of horizontal transport by considering horizontal as well as vertical transport. In the next chapter, a technique is developed and used to model the time-dependent plasma response to multi-dimensional ion frictional heating.

CHAPTER 4

MODELING TRANSIENT ION OUTFLOWS

4.1 Background

In the previous chapter, time-dependent processes were largely ignored in order to isolate the underlying physical processes which alter steady state polar outflow characteristics. This treatment is particularly useful in providing insight into the zeroth-order development and behavior of the "classic" polar wind and are in general agreement with the limited polar wind measurements of supersonic light ion flow observed by the Dynamics Explorer-1 spacecraft (Nagai et al, 1984; Olsen et al., 1986). Ironically, instrumentation from the same satellite identified outflows of other terrestrial ions and has led to a profound revision in the earlier steady-state assumption that O^+ was gravatationally bound with negligible outflux.

It is now well established observationally that large fluxes of heavy, terrestrial ions are flowing out of the topside ionosphere. The retarding ion mass spectrometer (RIMS, Chappell et al., 1981) onboard the polar orbiting Dynamics Explorer 1 (DE 1) satellite has identified large fluxes (10^7-10^9 particles cm^{-2} sec^{-1}) of heavy ions moving upward along open geomagnetic field lines (Shelly et al., 1982; Waite et al., 1985; Lockwood et al., 1985a). This previously unexpected component of ion outflow consists mostly of cool (10 eV-100 eV) O^+ ions although N^+, N_2^+,O_2^+ and other molecular ions were also detected (Chappell et al., 1981; Craven et al., 1985). Convection mapping calculations and observational evidence presented by Waite et al. (1985, 1986) and Lockwood et al. (1985a, 1985b,) indicate a low altitude, dayside cleft or cusp source region for these outflows. These ions flow outwards along geomagnetic field lines from the high latitude source region and antisunward convection carries them across the polar regions where they become dispersed based on convection and corotation processes throughout the magnetosphere. A number of satellite measurements (Shelly et al., 1972; Young et al.,

1982) have confirmed the presence of large and even dominant populations of suprathermal or energetic O^+ in different parts of the magnetosphere. The energization process(es) responsible for the outfluxes has received considerable attention over the last several years but has not yet been definitively established although various modelling treatments have identified a number of possible mechanisms. Apart from the precise details which energize thermal heavy ions, such as O^+, into suprathermal populations capable of escape, these transient outflows must be supported from below with equally large fluxes of thermal ions to conserve number flux.

The purpose of the present chapter is to examine the evolution of transient upwellings of heavy ions such as O^+. In particular, the role of frictional heating is examined as it relates to the higher altitude observations of suprathermal ion fluxes in order to address the following issues:

1. What is the ionospheric response to low-altitude (<600 km) frictional heating ?

2. Can frictional heating events initiate transient ion upwellings and what is their relationship to higher altitude ion outflows ?

3. What roles do the major and minor ion play during the initiation and evolutionary phases of heating ?

4. To what degree does the time and spatial location of frictional heating relate to an observed ion outflow event ?

The theoretical and observational aspects of these questions are addressed in this chapter by developing a coupled model approach which permits specification of time-dependent frictional heating within a flux tube preceding and during a period for which a moderately strong upflowing ion event (UFI) was observed by the DE-1 RIMS instrument. The heating history and outflow conditions for a flux tube transiting the observed event location are modeled using a coupled TIGCM-polar wind model. With this method, the transient nature of the plasma response to frictional heating can be examined and a comparison made between modeled and observed upwelling properties at various intervals.

4.2 Polar Wind Dynamics in a 3-D Reference Frame

The observed morphology and behavior of topside plasma conditions are considerably more complex than steady-state treatments might imply due to the effects of horizontal convection. Even during quiet times, the ionosphere is subjected to large variations in external conditions, both at the top and bottom of the flux tube, as it $\mathbf{E}\times\mathbf{B}$ drifts about the high-latitude region. For example, a flux tube convecting through the cleft region may first experience low altitude frictional heating associated with the spatially-

confined convection reversal in the ion drifts, then, a sudden opening of the flux tube associated with dayside merging may induce pressure transients and finally, entry of boundary layer particles could further enhance low altitude heating. Subsequent convection out of cleft and into the polar cap results in a loss of these heat sources and the plasma begins to adjust to new conditions. In essence, an ionospheric response develops as the plasma convects through localized regions of heating or acceleration. This response is spatially two dimensional in the Earth frame, or time-dependent in the plasma reference frame.

In a flux tube subject to **E×B** convection, a number of external influences appear as time-dependent processes which prevent attainment of full equilibrium within the flux tube. Therefore at any high-latitude location, one may find various states of non-equilibrium or transient behavior depending on the convection path of the flux tube and the UT-varying geophysical conditions for the same period. In the simplest case of a day to night closed path under quiet conditions, the presence of solar EUV heating results in a field-aligned flow up the flux tube during the day due to higher plasma temperatures and downward drifts at night when the plasma cools. When the two separate horizontal and vertical motions are combined, the resulting ion trajectory forms a three-dimensional surface. For this simple case, the plasma exhibits a 24-hour periodicity in vertical velocity. This quiescent ionospheric "breathing mode" is further modified either mechanically, such as when day to night neutral winds move plasma up and down the field lines, or through additional heating such as by particle precipitation or frictional heating. These additional influences normally occur over periods ranging from minutes to hours and can substantially modify the quiescent motion described above. Therefore, the vertical velocity and density characteristics of the plasma at any given time are best explained only after considering a number of processes that occur with different time scales and possibly, different locations. Time-dependent treatments gain additional importance in these cases since the prior forcing history along the flux tube trajectory often dictates present conditions. It is in this context that time-dependent modeling treatments, discussed in the introduction, provide much greater insight. In effect, time-dependent models force us to view any given modeled ionospheric state as a momentary phenomenon rather than an end result.

In adopting a time-dependent treatment, one takes advantage of the fact that at F-region heights, the convecting plasma moves together as a cohesive volume taken symbolically as a flux tube. At altitudes above about 160 km, the ion and electron collision frequencies are much smaller than the corresponding cyclotron frequencies so the plasma is constrained to move along but not across geomagnetic field lines except where electric fields cause the entire ionosphere to convect horizontally. An important feature of this

plasma motion is that this flow is essentially incompressible (Rishbeth and Hanson, 1974). It may deform, but the plasma and the imbedded geomagnetic field (lines of force) can be considered as moving together. Most descriptions of the high latitude convection pattern assume that the electric field is curl free and so may be expressed as an electrostatic potential. Contours of equipotential thus describe plasma flow paths as the plasma **E×B** drifts. Therefore, if the global convection electric field (and its temporal variations) is known, one can follow the same individual "plasma parcel" or flux tube as it convects horizontally about the polar region and identify a variety of local external forcings. If these influences can be quantified and ordered temporally, the time history of flux tube forcing can then be modeled by simply applying each condition in the right sequence as they occurred along the convection path. This treatment is Lagrangian in nature since a transformation has been made implicitly into the frame of reference of the moving plasma by specifying time-dependent boundary conditions. This technique is very useful since it provides a simple and valid means for examining effects which are transient in nature due to horizontal, convection motions.

4.3 Time-Dependent Modeling of Frictional Heating

A number of studies have suggested that low altitude frictional heating may play a role in the transient generation of heavy ion outflows observed at DE-1 altitudes. Moore (1984) examined several outflow cases and found clear evidence that ion acceleration below 1000 km may play an important role in generating suprathermal (energy ranges intermediate between polar wind and keV auroral ion beams) ion outflows. Later, in identifying mechanisms responsible for ion heating in upwelling O^+ source regions, Moore et al., 1986, examined an upwelling ion event measured by DE-1 on day 82071 and cited the close correspondence between transverse O^+ heating, random thermal energy and proximity of horizontal convection jets as being highly suggestive of a collisional or Joule heating mechanism. In a related study, Waite et al. (1986) reached similar conclusions. Although other forms of low altitude heating are also possible such as current-driven ion cyclotron waves (Ashour-Abdalla and Okuda, 1984) and lower-hybrid waves (Roth and Hudson, 1985), the role of ion frictional heating in ion outflows has not been explicitly addressed.

In contrast to the more numerous observations implicating low-altitude frictional heating to O^+ outflows, relatively few published theoretical studies have been made which identify the role of ion frictional heating magnitude, or heating rate, in initiating transient upflows of O^+. To examine the transient ionospheric response to variable heating rates experienced by the convecting plasma, Gombosi and Killeen (1987) introduced a

parametric heat source, normalized to DE 2 observations, into the time-dependent hydrodynamic polar wind model developed by Gombosi et al. (1985). The shape of the altitude profile of their heat source was parameterized based on high-altitude, observed profiles from Chatanika radar observations of Banks (1977) but was normalized to heating rates derived by DE-2 thermosphere and ionosphere measurements at the cusp where they found significant horizontal frictional heating present between 300 and 350 km. Their simulated horizontal frictional heating episode was based on that which might be expected when a flux tube transits the cusp region. The O^+ upwelling they obtained was in agreement with upward directed fluxes observed by the EISCAT radar suggesting that low altitude horizontal frictional heating may trigger upflowing O^+ ions at high geomagnetic latitudes. More recently, Cannata et al., (1988) extended their work by delineating more realistic time-varying frictional heating rates using the Thermospheric General Circulation Model (TGCM) of the National Center for Atmospheric Research. Their use of a steady-state, diurnally-reproducible TGCM run provided a lower limit to the frictional heating rates however since ion-neutral coupling acts to reduce the relative velocity differences so important to frictional heating magnitudes. Most recently, Yeh and Foster (1990) report similarities between their observations of high ion temperatures associated with a measured O^+ flux of 3×10^9 cm^{-2} sec^{-1} and ion temperatures derived from a parametric heating event using a time-dependent topside diffusion model developed by St.-Maurice (unpublished). In each of these cases, time dependencies in frictional heating rates are considered parametrically or with less formalism than is presently available based on recent developments of the NCAR Thermosphere-Ionosphere General Circulation Model and improvements to the polar wind model of Gombosi (1985).

Recently, Roble et al. (1987, 1988) revised the TGCM to include a self-consistent aeronomic scheme which solves for total neutral temperature, ion density and ion winds as well as the usual neutral winds, temperature and composition. These latest revisions have enhanced the model formulation since ion drag terms and ionospheric state variables can now be determined self-consistently and from first principles without depending on external empirical inputs. The new model, referred to as the TIGCM (Thermosphere/Ionosphere General Circulation Model), provides a useful means of specifying the dynamic variability between the thermosphere and ionosphere since mutual coupling between the neutral and ion gases can occur at each geographic grid point and model time step. The model provides self-consistent solutions to the fully coupled hydrodynamic, continuity, momentum and energy equations for the neutral thermosphere using a 5 degree horizontal grid spacing and 25 constant pressure surfaces between approximately 97 and 550 km. For the high-latitude portion of the model, the Heelis et al.

(1982) convection pattern is used to order the ionospheric horizontal motion. Since the modeled solutions reflect ion as well as neutral dynamics and composition, all parameters needed to compute frictional heating (proportional to the product of the square of the ion-neutral velocity difference and the ion density) are available in the history output fields and can be calculated self-consistently along the modelled trajectory of a convecting flux tube.

In this section, previous studies of Gombosi and Killeen (1987) and Cannata et al. (1988) are extended using output from the Thermosphere-Ionosphere General Circulation Model (TIGCM) of the National Center for Atmospheric Research (NCAR) to specify more realistically the time-dependent thermosphere/ionosphere environment as input to the Gombosi polar wind code. Time and altitude-dependent frictional heating rates are derived from the TIGCM solution fields as a function of universal time along the locus of convecting flux tubes. These ion heating profiles are used as boundary conditions in the polar wind model to represent thermosphere-ionosphere interaction and resultant frictional heating for a period of time preceding and during an observed upflowing ion event. The evolving transient perturbations introduced by the simulated convection through a region of enhanced frictional heating are compared to observations of the higher altitude upflowing ions to determine the role transverse energization might play in initiating O^+ field-aligned flows such as those seen at higher altitudes.

To calculate ion frictional heating rates, a post-processor package developed by Killeen et al. (1986) is used to extract information from the TIGCM output fields. This diagnostic program allows one to track an individual flux tube in both space and time as it moves through the TIGCM output fields that contain wind, density and temperatures for selected universal times (UT). Using a simple, weighted interpolation scheme on the ion winds to step forward in UT, neutral and ion wind vectors, densities and ion temperatures are extracted at 24 pressure levels for points along the trajectory path . An ion heating rate profile is calculated from these parameters using an expression for frictional heating based on simplifying assumptions to the ion energy equation (Killeen et al., 1984) for the high-latitude F-region (described in detail in Chapter 4). The frictional heating rate in this case is given as:

$$Q = \frac{m_i \nu_{in}}{2}\left(V_i - V_n\right)^2 \qquad (4.1)$$

Where m_i represents the major ion mass, ν_{in} the ion neutral momentum transfer collision frequency and V_i and V_n, the ion and neutral wind vectors respectively. In this treatment, O^+ is considered as the major ion, colliding with atomic oxygen, O_2 and N_2. Collision frequencies are based on those given by Schunk and Nagy (1980). Equation 4.1

represents the ion frictional heating rate, expressed on a per particle basis, due to collisions between two gas particles which have a net relative drift. Per particle heating rates were explicitly selected for this study since TIGCM ion densities in the polar latitudes were derived under diffusive equilibrium conditions (Roble et al., 1988) whereas densities in the polar ionosphere appear lower due to dynamic equilibrium associated with ion outflow. Altitude profiles of frictional heating rate (ergs sec^{-1}) for specific UTs were combined with ion densities in the polar wind model to obtain volumetric heating rates (ergs cm^{-3} sec^{-1}).

TIGCM solutions provide a useful means of specifying the thermosphere-ionosphere interaction for any given modeled day however there is a limitation to this technique. Calculations of frictional heating in this case are dependent on the TIGCM Eulerian grid spacing which is effectively 5° in latitude and longitude. The derived heating rates from the diagnostic package thus represent values which have been sampled at 5° intervals so that the total ion heating becomes averaged over a rather large horizontal area. This treatment tends to smooth out the very spikey nature of frictional heating (discussed in detail in the Chapter 4) In this sense, the heating rates underestimate actual heating rates to a degree which depends on the horizontal extent of modeled velocity shear areas and their location relative to the model gridpoints. This limitation has some effect on the UT variations in the heating rates (depending on flux tube position in relation to a grid point) as well as their magnitudes. The former effect is negligible considering the rather coarse time resolution of 20 minutes in modeled solutions considered here while the latter effect results in consistent underestimations in heating magnitudes. Since the interest here is in temporal characteristics in plasma response and not absolute magnitudes, the time dependent treatment employed here still yields important and useful insight into transient plasma behavior.

For comparison purposes, an ion upwelling event occurring on day 82071 was selected. This choice was not based on any particular or unique features associated with the event but rather on the extensive particle and field analyses which have been conducted and published in the literature (Moore et al., 1986; Waite et al., 1986). The 82071 event is "typical" in many respects based on outflow magnitude (10^8 cm^{-2} sec^{-1} for O^+), composition (O^+ but with lesser amounts of H^+ and He^+) and location so it useful for model comparison. In this respect, the large amount of observational information available for this case can serve as an important benchmark for interpreting modeled transient features.

Figure 4.1 summarizes the location, times and field-aligned fluxes (values shown have not been normalized to 1000 km) for the day 82071 event. The trajectory shown on

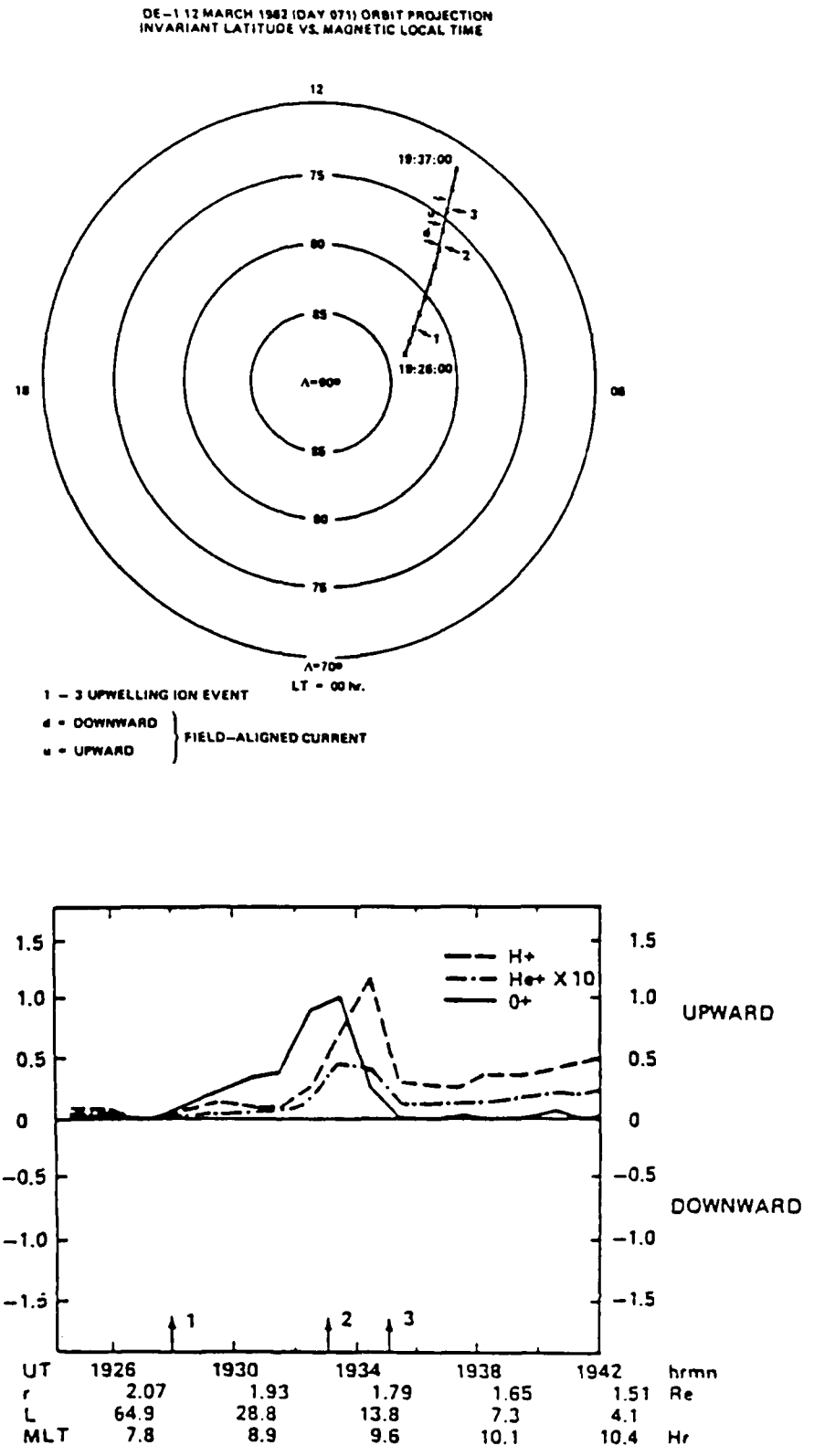

Figure 4.1 Orbit projection and RIMS flux measurements from the DE-1 satellite on 12 March 1982 (day 82071). An upwelling ion event, with O^+ fluxes near 10^8 particles cm^{-2} sec^{-1} was first detected at 19:28 UT.

the polar dial plot indicates the location in invariant latitude and magnetic local time of upward field-aligned fluxes of energized ions. O^+ fluxes were observed between about 19:28 UT and 19:35 UT reaching a maximum near 19:33 UT of approximately 10^8 cm^{-2} sec^{-1} (normalized to 1000 km). The upwelling event was spread across a broad invariant latitude and MLT sector with a rather sharp equatorward cutoff near 74°. The broad horizontal extent of these UWI features actually aided the modeling treatment since a modeled flux tube trajectory must be selected which passes through this region at about the same UT as the observations if comparison of the same volume space is to be made.

4.3.1 TIGCM Solutions for Day 82071

The fully-coupled continuity, momentum and energy equations for the thermospheric/ionospheric environment on day 82071 were solved using time-varying inputs to the TIGCM. This process involved generating a diurnally reproducible run to obtain background solution fields followed by a more comprehensive run in which time-varying solar geophysical inputs were used to produce solutions sets at 20 minute resolution. These results were interpreted in space and time using the post processor package described earlier to obtain information along the trajectory of a convecting flux tube. A number of trajectories were examined during this day, but only one which passes through the observed UWI event location at approximately 19:30 UT, is followed backwards in time to derive the history of ion frictional heating along its path.

For this study, the interval between 15 and 20 UT was influenced by significant variations in geophysical conditions. The IMF Bz component used to derive the TIGCM cross tail potential and related ion convection velocity is presented in Figure 4.2. Shortly after 15 UT, the Bz component (Figure 4.2a) turned sharply southward, then briefly nothward just prior to 18 UT before returning southward again through 20 UT. Corresponding changes in the modelled cross tail potential (Figure 4.2b) from 30 kV to 93 kV between 15 and 19 UT resulted in rapid accelerations to the ions causing large ion-neutral velocity differences and therefore ion frictional heating rates.

The time history of ion frictional heating near 200 km and the flux tube trajectory selected for this study is illustrated in Figure 4.3. All quantities were derived using the post processor package described earlier. The flux tube trajectory, plotted as a function of magnetic local time and latitude, was calculated using the Heelis (1982) convection pattern with time steps of 20 minutes under varying cross cap potential based on the observed IMF Bz component. The plot of cusp heating (parametrically modeled as a soft particle precipitation heat source in the TIGCM) to the neutral thermosphere as a function of UT is shown directly below. This heating is not used in the polar wind model simulation but is

plotted here to help identify the UT periods corresponding to cusp transits for the selected flux tube trajectory. The time series on the left of Figure 4.3 show derived ion temperatures, frictional heating rates, ion densities and the square of the difference between ion and neutral winds at approximately 200 km. The latter quantity is used to compute ion

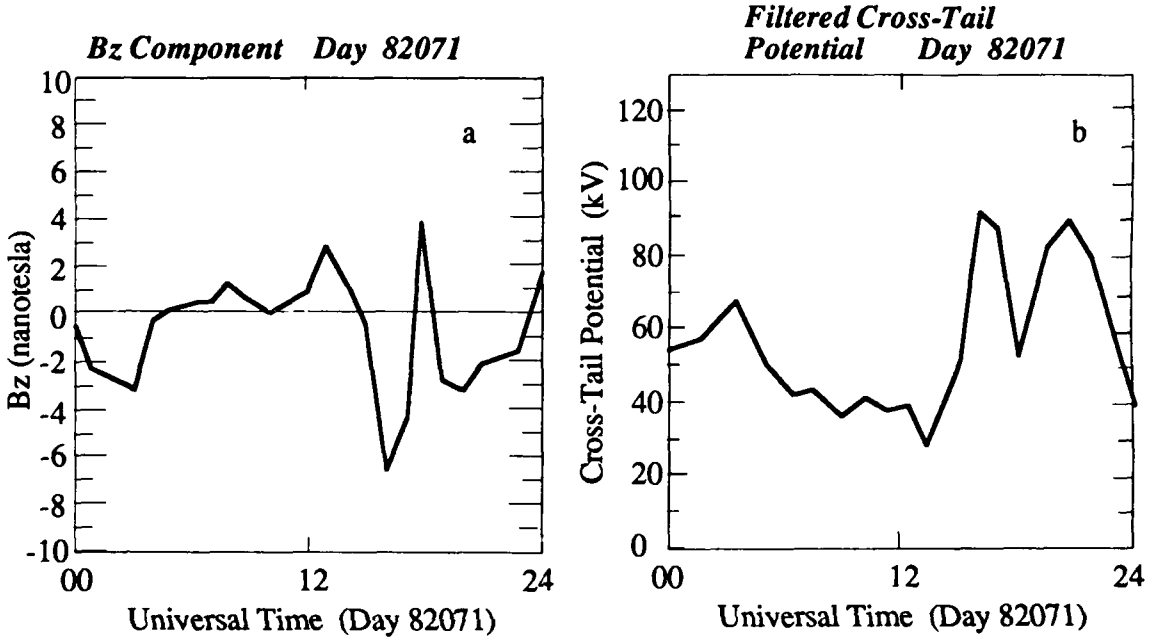

Figure 4.2 Interplanetary magnetic field Bz component (a) for day 82071 and related cross tail potential (b) used as time-dependent boundary conditions in the TIGCM run to obtain a history of frictional heating along the path of a convecting flux tube. Strong southward (negative values) excursions of the Bz component enhanced ion convection velocities resulting in increases to ion frictional heating rates.

frictional heating as previously described. An order of magnitude increase in frictional heating can be seen beginning near 16 UT along with increases in ion temperature at the same period. This behavior is related to the initial southward turning of Bz and related increase in convection indicated by Figure 4.2 A secondary enhancement in heating occurred just after 17:30 UT as the Bz component returned southward once again This latter interval of heating, between about 18:00 UT and 20:00 UT will be used in the polar wind model simulation since it spans the UWI event observed by DE-1. The modeled heating rates for the period illustrated in Figure 4.3 were extracted from the TIGCM solution fields for one of 24 possible altitudes. By obtaining the heating rates at all other altitudes, a time-dependent heating rate profile can be constructed for inclusion in the polar wind model simulations.

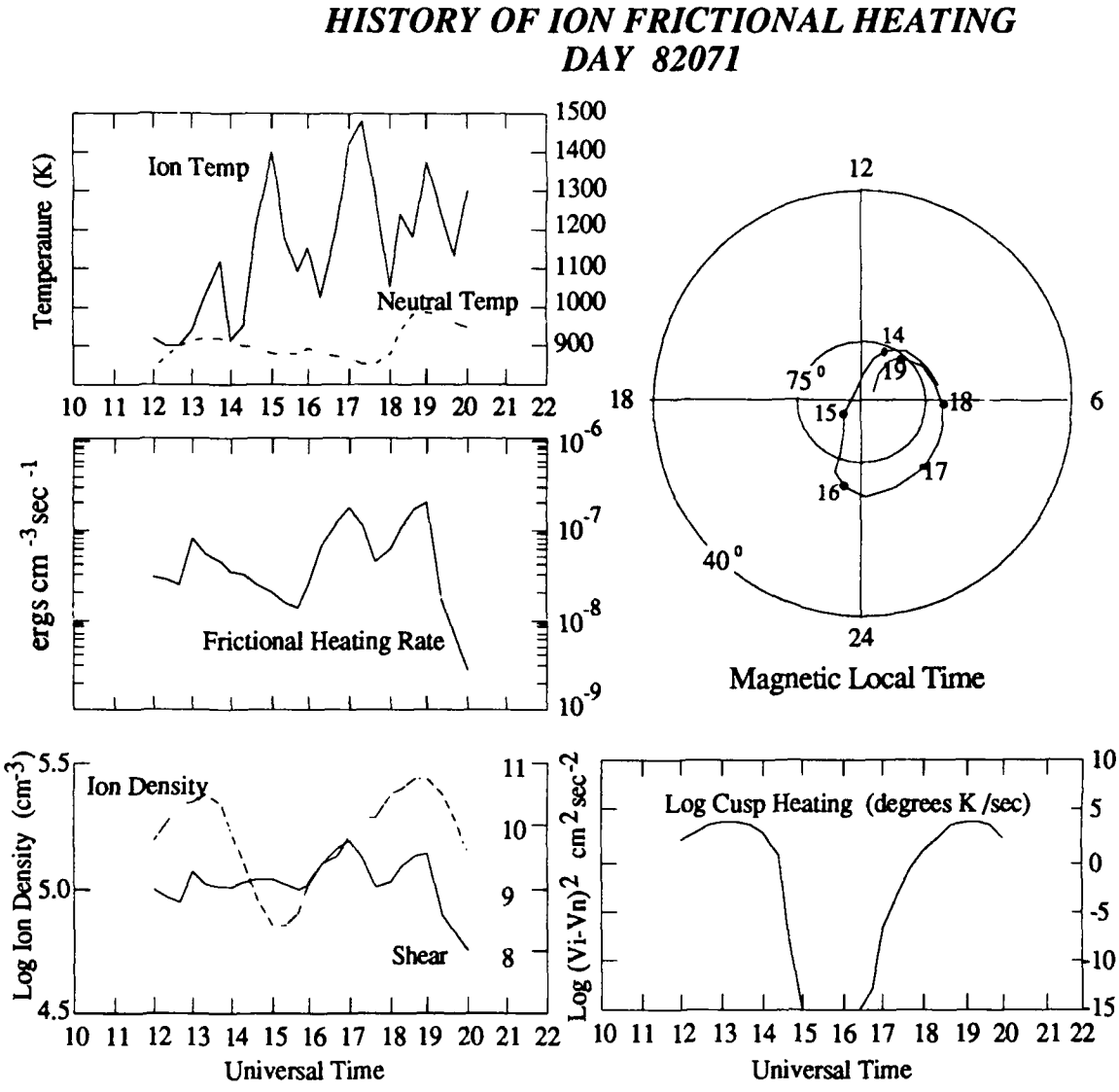

Figure 4.3 Summary plot of a flux tube convection path and frictional heating history taken from the TIGCM solution fields near 200 km. A flux tube trajectory is selected which is at or near the location of the upwelling ion event (UWI) observed by DE-1. The three-dimensional heating history of this flux tube is consolidated from the TIGCM solutions and is used as a time-dependent input to the polar wind model. Strong low altitude ion heating near 19 UT generated a transient upwelling of O^+.

Figure 4.4 illustrates volumetric heating rate profiles obtained from the time-dependent TIGCM solution along the selected trajectory illustrated in Figure 4.3. For comparison, a heating rate profile based on Chatanika radar observations for a different day is also illustrated. The characteristic inflection in both modeled and observed heating

profiles is related to ion and neutral densitty profiles. The upper portion (above about 200 km) of the profile follows the ion density profile. Moving downwards below the F-region peak, the ion density values decrease while the relative importance of the collision term increases. At lower altitudes, the profile takes on the character of the major neutral density profile (through the ion-neutral collision frequency term). This behavior introduces a local-time dependence into the shape of the profiles with much stronger "knees" appearing whenever ion densities are high, i.e., near local noon. This effect is present in Figure 4.4 but is somewhat modified by the time-dependent cross tail potentials which affect the ion velocity and hence the ion-neutral velocity difference.

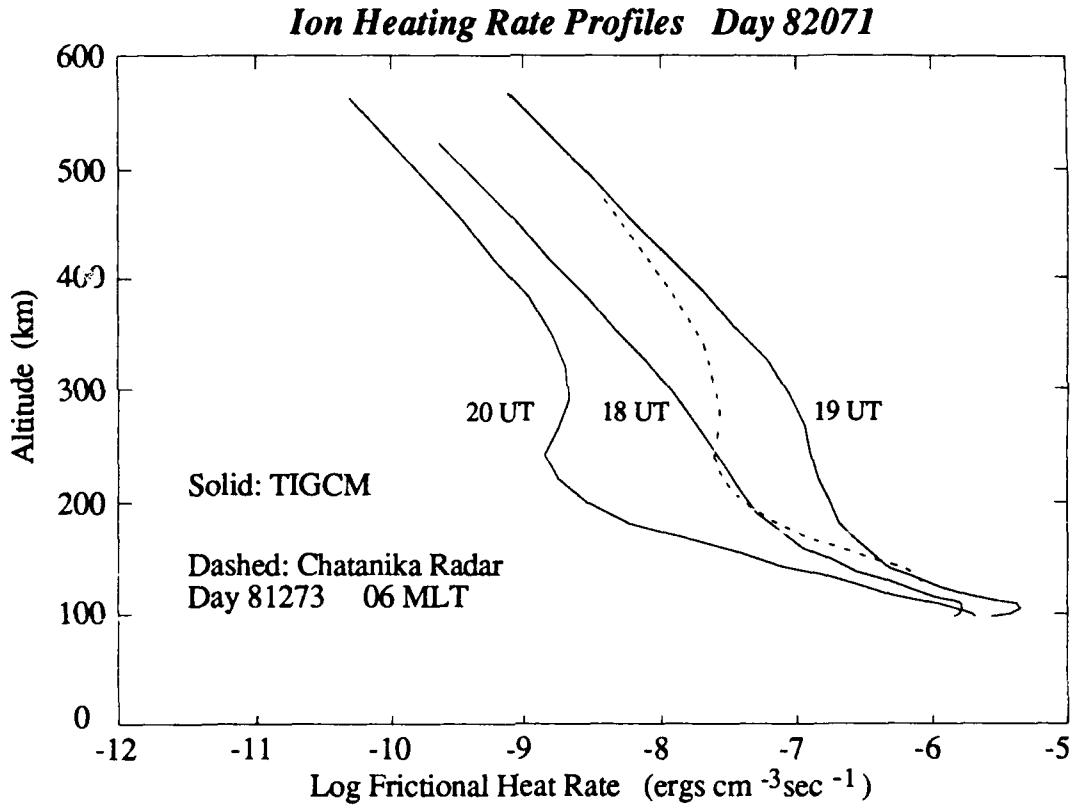

Figure 4.4 Time-dependent ion frictional heating rates derived from TIGCM solutions of the thermosphere-ionosphere environment for day 82071. A heating rate profile derived from incoherent scatter radar observations on a different day is shown for comparison.

Between 18 UT and 19 UT there is a marked increase in heating throughout the column associated with the increase in ion velocities during the same period mentioned earlier. It is interesting to note that most of the increase in this case occurs above 200 km where ion densities are locally increasing from enhanced O^+ photoproduction. By 19 UT

frictional heating has reached a maximum due to a peak in the relative ion-neutral drift velocities. The maximum in relative drift occurs due to the combined effects of large speed differences (a function of the enhanced cross-cap potential) and large directional shears which occur as the ions begin to sharply veer antisunward during cusp transit (see Figure 4.3).

4.3.2 Polar Wind Model Solutions for Day 82071

Time-dependent heating rate profiles from the TIGCM are applied to the polar wind model to simulate the distributed heating experienced within the flux tube as it moves through quasi-stationary heat sources on the modeled day. In adapting the derived ion frictional heating rates to the polar wind code, per particle heating rates are calculated for the 200 to 540 km interval as a function of UT based on the TIGCM output. Extrapolated heating rates to 800 km are also included based on the heating rate and profile slope near 540 km. For application to the polar wind code, profiles are reduced to a set of coefficients that are used in the model to reproduce the ion heating rate as a function of universal time. In this study, a steady-state solution was first obtained using a 17:40 UT heating rate to prevent artificial transients when heating was applied. The simulation begins at 18 UT (t=0) as heating rates, consistent with the movement of the flux tube, are applied at each 20 km interval up to 800 km and updated every 10 minutes between 18 and 20 UT.

Initial plasma conditions within the flux tube are shown in Figure 4.5. The plasma is near photochemical equilibrium at the lower boundary while the ion temperature is slightly elevated above the neutral temperature due to the steady heating corresponding to the 18 UT frictional heating rate. The minor ion, H^+, undergoes steady upward acceleration along open field lines due to the combined effects of the downward-directed pressure gradient along the modeled flux tube and the related, upward directed ambipolar electric field which develops between the electrons and major ion in response to this gradient. The field-aligned H^+ flow attains supersonic velocity and a constant flux profile near 3000 km.

The major ion, O^+, flows slowly upward since gravity, pressure gradient and frictional forces are in near balance. Both upward and downward fluxes are present at F-region altitudes due to diffusion away from the source region. Upward directed ion fluxes reach asymtotic values near 3000 km of 11.5×10^7 cm^{-2} sec^{-1} and 8.0×10^7 cm^{-2} sec^{-1} for O^+ and H^+ respectively. Starting at 18:00 UT, variable ion frictional heating is applied to the lower 800 km of the flux tube which substantially modifies these plasma conditions.

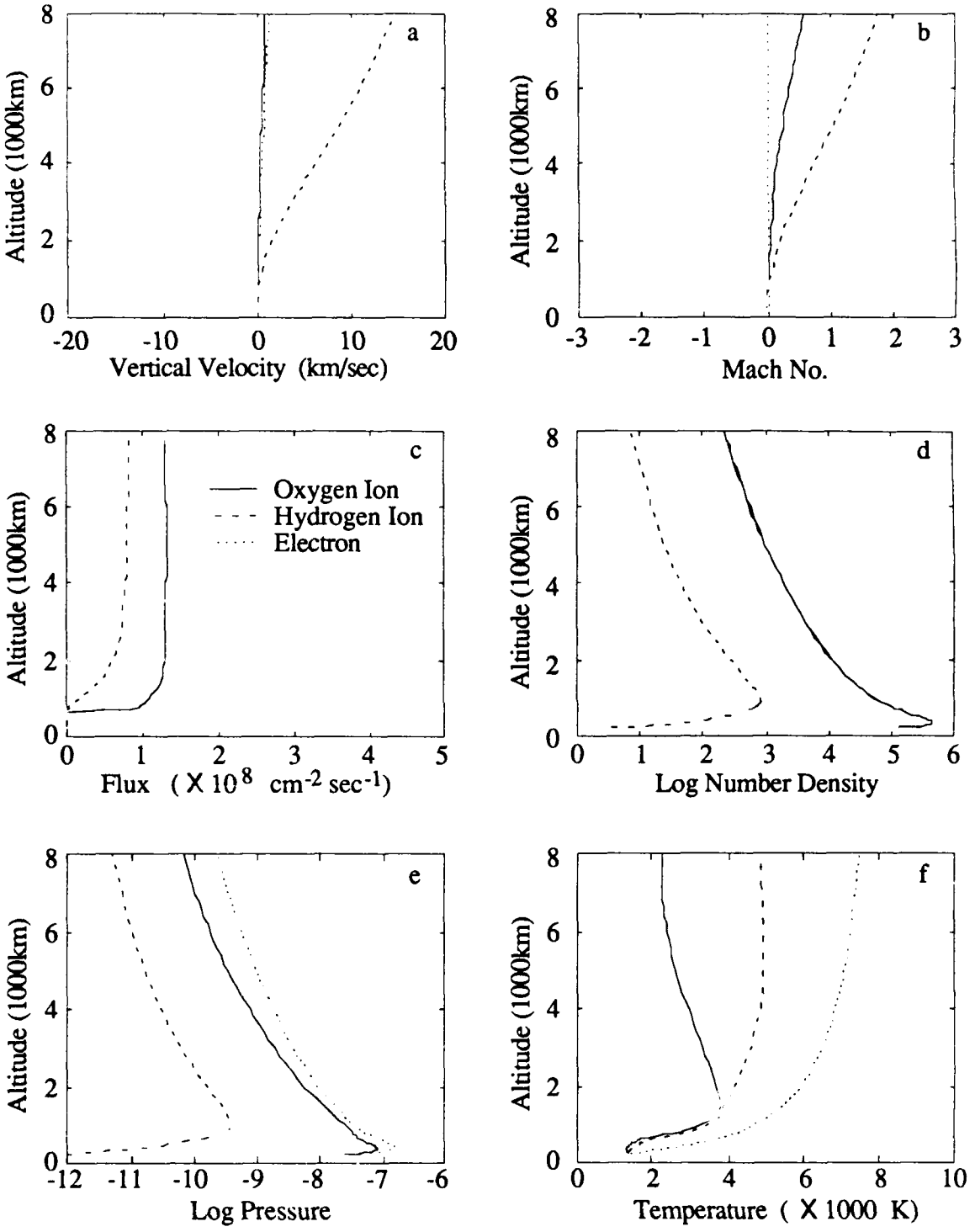

Figure 4.5 Quasi-equilibrium plasma conditions for day 82071 based on steady frictional heating near 18 UT. Profiles of field-aligned velocity (a) and Mach (b) show H^+ in supersonic outflow while O^+ flows upward much more slowly due to the imposed pressure differential between the model boundaries of 200 km and 8000 km. O^+ fluxes (c) are only slightly greater than H^+ due to greater number densities at all levels.

Ion heating rates are updated starting at 18:00 UT and every 10 minutes thereafter to be consistent with the new trajectory location and continue through 20 UT. During this interval, the flux tube moved from the morning convection channel through the cusp and into the polar region (see Figure 4.3). In the plasma frame, the flux tube first convected into a region of strong, quasi-permanent region of directional shear associated with the ion convection reversal boundary near the cusp. At the same time, ion convection velocities were increasing everywhere due to the strong increase in cross cap potential (Figure 4.2), associated with changing IMF conditions. Both effects lead to an increase in ion-neutral relative drift velocities and therefore, ion frictional heating. As the flux tube moves out of the modeled cusp area, directional shears and relative drift velocities decreased sharply and the plasma begins to cool. In describing this heating event, it is convenient to divide the interval into a heating period (18:00-19:00 UT) corresponding to cusp transit and increase convection velocities, and a recovery period (19:00-19:50 UT) corresponding to anti-sunward transport away from the heating source and into the polar cap. Time series of flux profiles for these two intervals are illustrated separately in Figures 4.6 and 4.7 to show the evolution of transient increases in O^+ fluxes.

Within minutes after the time-dependent heating rates were applied, a perturbation in the O^+ field-aligned velocity and number density appeared just above the heated region in response to a change in the pre-heating scale height of O^+. This behavior can be seen in Figure 4 6 as a flux perturbation developing below 2000 km. Perturbations to the 18:10 UT flux profile are clearly visible and indicate that the plasma has responded to the heating disturbance within 10 minutes By 18:20 UT a strong, low altitude transient is clearly present in the O^+ flux profile. The transient growth rate is not even, but tends to follow the rate at which heating rates change; slowly between 18:00 and 18:20 UT and more rapidly between 18:20 and 18:40 UT. The transient flux perturbation continues to grow until 19:00 UT when frictional heating reaches a maximum along this trajectory.

As the transient flux perturbation grows in the lowest altitudes, the heated oxygen ions move upwards causing an increase in local ion densities. In this manner, the flux perturbation appears to shift to higher altitudes as densities and therefore fluxes increase within the heated plasma column. The tendency for the perturbation to move upward with time is opposed by ion cooling which acts to reduce the local scale height of the major ion and reduce its local density. Heat can be "lost" by the ions in two ways. At lower altitudes, the ions cool through collisions with neutrals. At higher altitudes where collisions are less frequent and upward velocities greater, adiabatic cooling dominates as

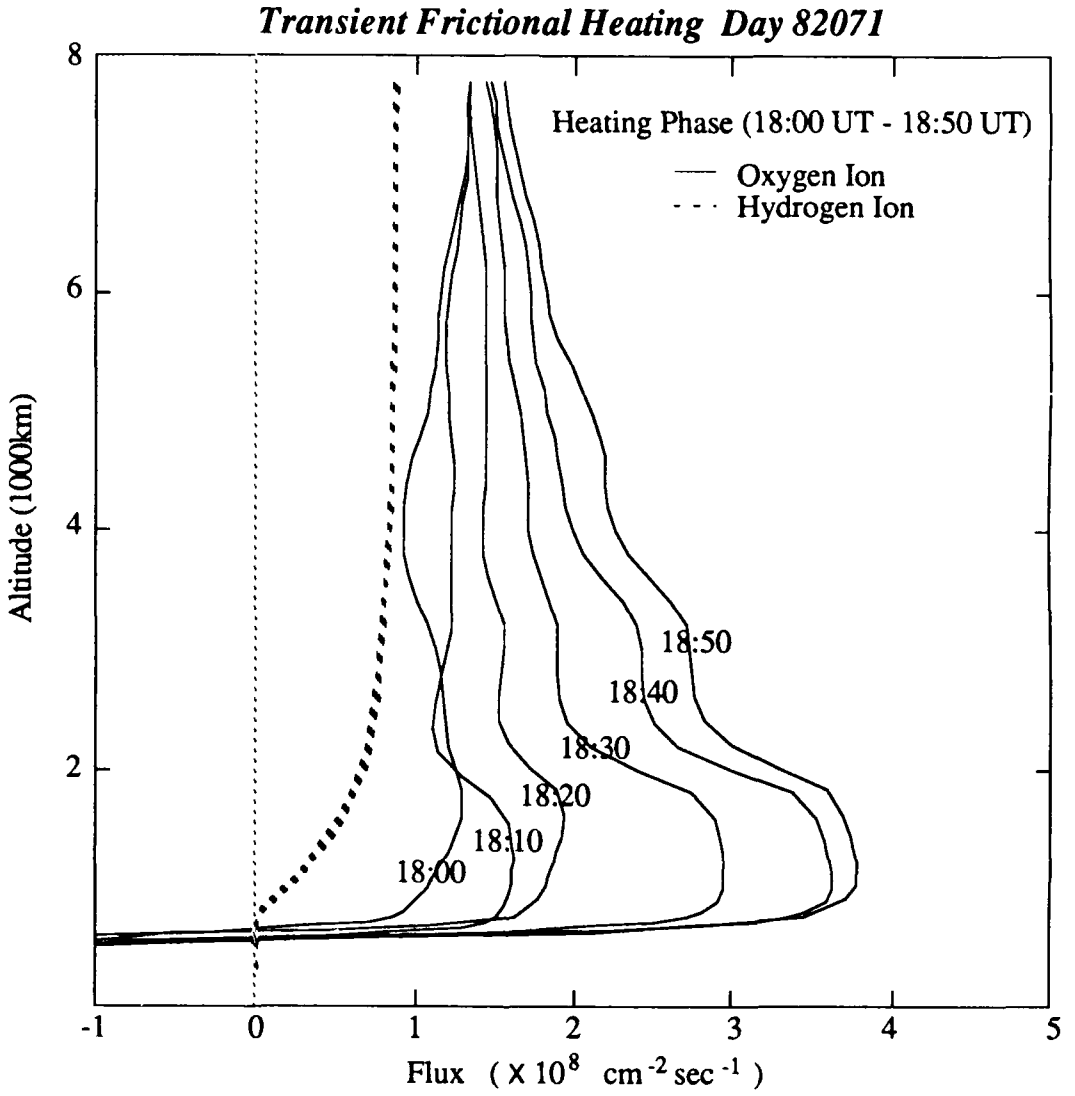

Figure 4.6 Time sequence illustrating the evolution of a heavy ion (O^+) flux transient due to convection into a region of enhanced frictional heating. H^+ fluxes remain essentially unperturbed since the minor ion receives very little of the distributed heating on a per particle basis. Heating and flux transients both maximize near 19 UT at the lowest altitudes while propagating upward.

the ion gas rapidly expands. Thus, the altitude range over which perturbations can occur will depend not only on the ion heating rate but also on the rate at which the ions cool

Shortly after 19:00 UT, the flux tube moves out of the region of strongest relative drift velocities so frictional heating rates begin to decrease. Figure 4.7 shows the evolving flux profile as ion frictional heating decreases sharply after 19:00 UT. As the flux tube moves away from the region of strongest heating, the major ion responds to a change in thermal forcing. Within time scales of minutes, the low altitude (below 1000 km) O^+ flux perturbation has changed sign and O^+ is now observed to stream downward in the lowest

levels as the plasma cools. At higher altitudes however, the O^+ flux perturbation continues to shift upwards, effectively decoupled from the low altitude changes in heating.

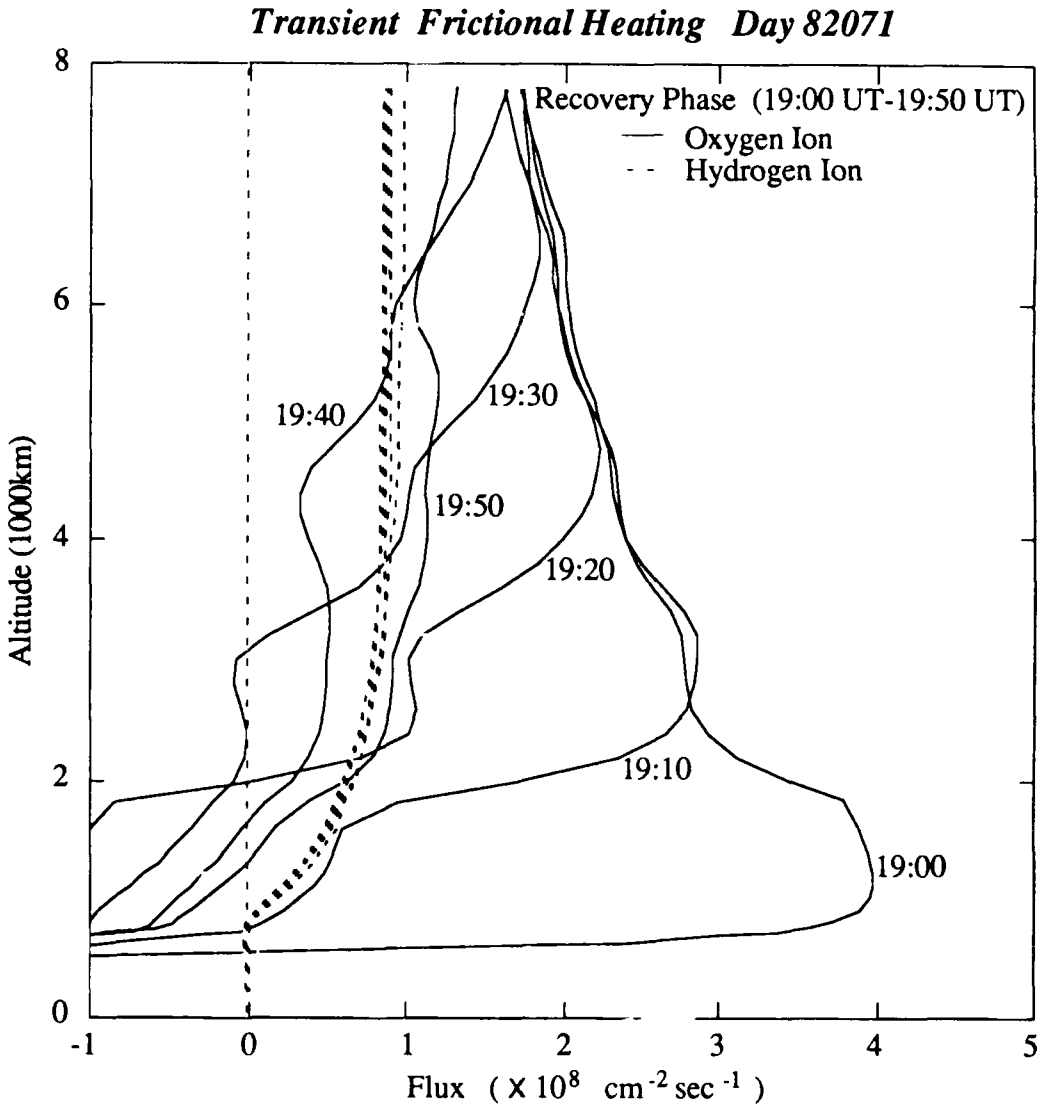

Figure 4.7 Time sequence illustrating the evolution of a heavy ion (O^+) flux transient after maximum low-altitude frictional heating . Rapid cooling to neutrals in the lowest altitudes and adiabatic cooling due to gas expansion causes decay of the flux transient. Differences in recovery flows for the major and minor ion results in a deep layer of counterstreaming beginning just after 19:15 UT and lasting past 19:50 UT.

In fact, modeled O^+ fluxes at 5000 km were enhanced and on the order of 10^8 cm^{-2} sec^{-1} just prior to 19:30 UT even though the period of strongest heating occurred 30 minutes earlier.

Once the heating ceases, the lowest altitudes appear to recover first due to close collisional coupling with the neutral gas component. At higher levels where collisions with

neutrals are less important, adiabatic cooling initially dominates as the plasma rapidly expands upward. As heating rates decrease cooling also proceeds at a slower rate so the transient flux perturbation tends to persist longer at higher altitudes. This behavior suggests that at least two time scales are effective in determining cooling processes. At lower levels, this is set by the ion-neutral collision frequency while at higher altitudes, adiabatic expansion is largely set by transport properties associated with bulk ion flow.

Recovery of the O^+ flux profile for this case appears as a rather slow process since transient fluxes are determined largely by the O^+ number density perturbations. In fact, the first indication of a return to pre-heating conditions does not appear until near 19:50 UT when fluxes start to increase again below 3000 km. At this time, O^+ densities appear to be gradually recovering as a new plasma equilibrium develops in the presence of very weak frictional heating. A downward redistribution of plasma is evident at this time based on the negative (downward) fluxes between 2000 km and 3000 km. Replenishment of O^+ proceeds at a slower rate dictated by photoproduction rates. The recovery process was examined up until 20:00 UT when the calculations stopped. However, a steady state flux profile for this event was not obtained even 60 minutes after maximum heating (20:00 UT) suggesting that recovery continues far "downstream" of the heating source.

Throughout this event, the O^+ flow remained subsonic, however, with an average propagation velocity for the leading edge of the O^+ flux perturbation of approximately 1.9 km/s (equal to the local O^+ acoustic velocity). A much longer recovery period followed, lasting for at least 60 minutes after heating maximum. In the convecting frame of reference, these properties define the distance over which the transient perturbation may be observed (assuming a constant satellite altitude) downstream from the heating source. In this case, a flux transient (increase) at 5000 km appeared minutes after heating began (Figure 4.6 profile labeled 18:00 UT), reached a maximum shortly after 19:20 UT (Figure 4.7), and persisted for about one hour after maximum heating (Figure 4.7, profile labeled 19:50 UT). Transient O^+ upwellings at altitudes near 5000 km within the flux tube considered here might therefore be expected within a few kilometers of the heating source and as far away as 3600 km from the heating event (based on a convection speed of 1 km/sec). This lag in recovery in O^+ fluxes suggests that upward O^+ flows generated by low-altitude ion frictional heating can persist at high altitudes in regions far downstream from the perturbing heat source.

Throughout the heating interval, H^+ upflow velocities and densities exhibit virtually no change from the (preheating) dynamic equilibrium state. As a result, H^+ fluxes remain nearly constant throughout this heating episode during both the heating and recovery phases as shown in Figure 4.6 and 4.7. This behavior occurs because volumetric heating

is shared among the ions according to their relative abundances. H^+ ions comprise only a small percentage of the total ion number density at altitudes where frictional heating is significant. Therefore, as a minor ion species, H^+ receives little in the way of additional energy so that fluxes change don't significantly in response to heating events of this type.

This difference in response between the major and minor ion produces interesting behavior in the topside F-region throughout the variable heating period. For the preheating period and during the interval of increasing heating (from t=0 to t=60 minutes), both O^+ and H^+ flow upward over roughly the same altitude range. As the heating rates start to decrease after 19:00 UT however, O^+ begins to flow downward as it responds to low-altitude cooling. O^+ subsidence following peak heating occurs over a region where H^+ still flows upward resulting in a layer in which both ion populations counterstream. Counterstreaming begins shortly after 19:20 UT according to Figure 4.6. As time progresses, this layer of counterstreaming between O^+ and H^+ grows to a maximum depth of about 2000 km by 19:40 UT.

The presence of counterstreaming ion populations suggests that wave-particle interactions could further enhance O^+ heating. Several theoretical treatments of ion-ion counterstreaming suggest that ion-ion wave modes are excited in plasmas when two or more cold ion beams are streaming relative to one another (Dusenbery and Martin, 1987; Dusenbery et al., 1988; Bergmann and Lotko, 1986). Wave growth may occur and lead to instabilities under certain conditions. A two-stream instability can develop when the relative drift speed exceeds some threshold drift determined by properties of the plasma system. In this case, the streaming velocity of H^+ provides a free energy source for heating the major ion. While parallel (to the magnetic field) propagating waves can preferentially heat O^+ in the parallel degree of freedom, obliquely propagating wave can heat ions in both the parallel and perpendicular direction. Ion heating in both directions has been observed (Ghielmetti et al., 1986) in the vicinity of upflowing ions while DE 1 observations of ion-ion wave heating have been described by Collin et al. (1986) and Kaufmann et al. (1986). Although it is unclear whether the counterstreaming condition predicted here during day 82071 could be unstable, its presence may be indicative of other O^+ energy sources which cannot be fully addressed with the present model treatment but appear as a direct result of different ion responses to low altitude frictional heating.

4.4 Comparison of Model Results to UWI Observations for Day 82071

The coupled TIGCM-polar wind model calculations described above were based on time-dependent conditions coincident with the observed Upwelling Ion event (UWI) illustrated in Figure 4.1. Since time-dependent polar wind model solutions were derived for the 12-20 UT period and extend to the same altitude as the satellite observations, modeled solutions are available for comparison with data preceding, during and after the observed UWI. Used in this manner, model results can be considered at the time of the event and can be used to evaluate the time-dependent plasma state immediately preceding the observed UWI.

In making magnitude comparisons between observed and predicted particle fluxes, careful considerations must be given to the difference in energy of each population. The modeled ion populations have typical energies of a few tenths of an eV compared to the RIMS observations of particles with characteristic energies near 10 eV. In fact, the RIMS measurements constitute an integral measurement since in this event, energy ranges of particles from 0.05 to 50 eV were sampled. Therefore, direct comparisons between modeled and observed flux magnitudes cannot be made. Despite this limitation, there are similarities between transient O^+ upwellings and this UWI event which strongly suggests that ion frictional heating plays an important role.

The most notable similarities between predicted transient fluxes and observed UWI on Day 82071 is the location and time of the modeled event. By examining and recreating the frictional heating history of a convecting flux tube passing near the UWI event, the model results predict large, transient upwellings of O^+ at 5500 km (approximate satellite location) between 18:40 UT and 19:40 UT over a horizontal convection distance of between 70°-78° invariant with peak O^+ fluxes occurring between 19:20 and 19:40 UT. The observed event occurred from about 19:28 to 19:35 UT along the descending node of DE 1 between 78°-68° invariant with peak fluxes at 19:35 UT. Thus, the modeled location and times of transient O^+ flux cover the period and region over which O^+ UWI were observed.

Extending the model computations to earlier periods for the same day, only one other heating event, occurring between 15:40 UT and 17:00 UT, was found. Heating rates during this interval produced similar transients in modeled O^+ fluxes in flux tubes passing through the same area. Unfortunately, DE-1 was not in the same location as in the 19:33 UT event so no in situ observations were available.

In evaluating the model results, the generation of transient O^+ upwelling occurred due to a combination of factors. First, a modest increase between 18:00 and 19:00 UT occurred in cross cap electric potential (Figure 4.1) associated with strong Bz southward IMF conditions. Relative ion-neutral drift velocities increased as the ion convection velocities increased. In the rest frame of the convecting flux tube, low-altitude ion frictional heating increased dramatically (through the V_i-V_n squared term in equation 4.1) as the ions were driven at higher speeds through the slower moving neutrals. At the same time, the convecting flux tube was approaching the dayside convection reversal region. Elevated frictional heating rates are a quasi-permanent feature here since large directional shears persist as ions change direction over a short distance from sunward to antisunward drifts while the neutrals continue in a more or less sunward direction. In the plasma reference frame, this spatial gradient in heating rate translated into an additional temporal increase to ion heating as the flux tube drifted into this region. The combined effects of an increase in convection velocity and the movement into a region of strong ion-neutral velocity shear produced similar increases in heating rates. Both effects were additive in this case resulting in a moderately strong, transient heating event. Based on this analysis, it appears that the combination of a spatially-confined heating region and a convection electric field intensification at the time of heat source transit provided a unique set of conditions which resulted in the generation of transient O^+ fluxes beginning as early as 18:30 UT at F-region altitudes. A subsequent shift in the flux transient upwards provided additional O^+ particles to higher altitudes where further energization to escape velocity could occur.

Despite the important role played by ion frictional heating in this case, it is clear from a comparison between modeled and observed plasma properties that some additional form of energization must also be present. The modeled field-aligned velocities for H+ and O^+ were 10 km/sec and 0.58 km/sec respectively while derived flow velocities are about a factor of two higher (Moore et al., 1986) Additionally, transverse O^+ ion temperatures, based on a drifting Maxwellian fit to the RIMS data, increase to near 8 eV during the event while modeled (isotropic) ion temperatures do not exceed 4000 K. The presence of hundreds of ions at 5000 km, heated to temperatures of almost 10^5 K, requires more energy than can be provided directly by the modeled frictional heating source. It appears likely that in situ energization is most effective to meet these energy requirements since model results here indicate that expansion and adiabatic cooling of the heated ion gas reduces the effectiveness of temperature enhancements due to low altitude frictional heating. Some additional source(s) of bulk heating of the topside plasma, such as those discussed in the introduction, are clearly required to attain such high temperatures.

4.5 Summary

In the present chapter, the time-dependent plasma response to low-altitude ion frictional heating was examined using a coupled model approach. The NCAR TIGCM was used to delineate the time-dependent interaction between the thermosphere and ionosphere. Frictional heating, a natural consequence of this interaction, was calculated along the path of a convecting flux tube and was used as a time-dependent boundary condition for a polar wind calculation. The low altitude ion heating generated transient perturbations to the density and vertical velocity fields within the flux tube column resulting in a 4-fold increase in the upward fluxes of O^+ below 1500 km while fluxes of the lighter H^+ ion remained nearly constant at all altitudes considered The plasma response to heating enhancements was typically on the order of minutes to tens on minutes with a somewhat longer recovery time so that transient effects were displaced downstream of the heating location (or later in UT) due to propagation of the transient up the flux tube. With this method, the presence of preferential ion heating and transient O^+ upwelling has been demonstrated for a time and location in which a higher altitude UWI event was observed.

In simulating topside F-region conditions during a period of observed high-altitude ion upwelling, additional insight has been obtained into the dynamic response to ion heating within the convecting flux tube. In particular, strong enhancements to ion frictional heating rates were identified moments before the observed UWI event. This in itself is not a surprising result since the modeled flux tube was chosen based on its location near the time of the UWI and the frictional heating event was in part, related to a UT effect. The significance of these results rests in the fact that they identify a mechanism for initiating large transient upflows of thermal O^+ and that the process was active just prior and during the observed UWI. Modeled transient fluxes of O^+ were found to double momentarily at the altitude of the observed UWI suggesting that low-altitude frictional heating may play an active role in this event. However, in comparing the observed thermal and flow properties of the plasma to model results, it is apparent that frictional heating alone cannot provide sufficient energy to account for the exceptionally high (10^5 K) ion temperatures and large outflow velocities (5 km/sec for O^+). Although it is likely that the heating rates derived from the the TIGCM under-represent actual heating for this period, additional sources of free energy are clearly needed to provide bulk heating to the plasma in order to attain the observed conditions. Model results indicated a deep layer of ion-ion counterstreaming during this event which could provide one free energy source through wave-particle interactions. Additionally, Moore et al. (1986) discuss the proximity of field-aligned currents to the observed UWI which could also act to provide additional energy. Although

not considered for this case, the effect of field-aligned, current-generated transients in O^+ flows has been demonstrated by Gombosi and Nagy (1989).

Based on the results presented here, it appears that ion frictional heating plays an important role in relation to higher altitude UWI events but that additional energy sources are needed to match characteristic energies of the outflowing ions. The evolution of UWI requires transport of a large number of heavy ions to higher altitudes to conserve flux. At the same time, additional energization is necessary to transform these thermal ions into the heated, suprathermal populations seen by DE 1. This work has demonstrated the effectiveness of frictional heating in transporting heavy ions upwards although precise comparison of numbers is difficult due to the energy differences in observed and modeled populations. In this sense, frictional heating acts as a necessary but not sufficient condition in relation to UWI events. Further case studies such as the one presented here are clearly called for to establish unambiguously whether ion frictional heating events precede every high-altitude observation of upwelling ion events.

CHAPTER 5

OBSERVATIONS OF TRANSIENT OUTFLOWS AND FRICTIONAL HEATING

5.1 Background

Over the last decade, a growing body of observational evidence indicates the frequent occurrence of terrestrial ion outflows at high altitudes (>5000 km) above the auroral and polar latitudes. The importance of these flows is underlined by the significant and highly variable population of terrestrial O^+ found in the near-earth environment (c.f. Chappell, 1988) which was previously thought to contain plasma of solar origin. These observations have generated considerable interest in identifying the underlying ionospheric source(s) and energization mechanisms which support such outflows. A detailed, qu titative assessment of source processes and energization mechanisms has been a difficult task to accomplish since point observations by satellites are not fully representative for the altitude interval over which these flows develop. Additionally, a complete understanding of energization mechanisms and efficiencies could only be possible with a complete vertical description of the plasma phase space distribution function for the outflowing population. Nevertheless, some insight and basic understanding can be gained by examining and relating various ionospheric signatures which occur in different altitude regimes. This more simplified approach, adopted here, will focus on examining and relating the low-altitude ionospheric signatures to outflowing ion populations observed at higher altitudes. In the present chapter, one such signature, that of ion frictional (Joule) heating, is shown to closely coincide with many of the high altitude locations and frequency of ion outflows. Additionally, variations in frictional heating magnitudes are found to match the seasonal and geomagnetic trends in outflowing ion behavior. Taken together, these similarities in occurrence frequency distributions, composition and short

and long term variability suggest that the underlying ionosphere-thermosphere environment plays a central role in defining the character of high altitude terrestrial ion outflows.

Statistical and observational studies of high altitude ion upflows have identified a number of spatial distributions and occurrence frequencies which can be used for a common-trait comparison at lower, F-region altitudes. The statistical approach of Yau et al. (1984, 1985) has yielded a number of important features and relationships. These include: (1) H^+ and O^+ upward flowing ions (UFI) which appear in auroral-oval-like patterns with occurrence frequency peaks that shift equatorwards during disturbed periods and have broader latitudinal extent on the nightside than the dayside; (2) A UFI population over the polar cap dominated by lower energy (than the "auroral" counterpart) O^+ ions; (3) Occurrence frequency and intensity distributions of O^+ UFI which exhibit a marked magnetic dependence whereas the corresponding H^+ UFI distributions display little variation with magnetic activity. These findings highlight the characteristic behavior of the high altitude UFI and indicate that the entire auroral zone contributes to the observed ion outflow. Subsequent studies by Moore et al. (1985); Waite et al. (1985), and Lockwood et al. (1985a, 1985b) identified several important features of the polar UFI populations: (1) They exhibited unique signs of transverse and parallel heating (typically 2 eV and 10 eV respectively); (2) They existed as field-aligned flows embedded in a cooler (<1 eV) polar wind outflow; (3) By considering their field-aligned and horizontal convection velocities, Waite et al. (1984) found that these populations could be mapped back to a common dayside polar cusp/cleft location. Lockwood et al. (1985a) identified a number of terrestrial ions (H^+, He^+, O^{++}, N_2^+, NO^+) in these flows but found that O^+ flows dominated. In fact, they found that O^+ flows could be observed at all Kp during the summer months but only at high Kp during the winter. Additionally, he noted the source latitude moved equatorward with increasing Kp and was highly correlated with the location of field-aligned currents. These findings were consistent with case studies of upwelling ion events reported by Moore et al. (1986) and Waite et al. (1986), in which upwelling ions near the dayside cleft were found to occur in association with field-aligned currents and horizontal convection channels or jets. Moore et al. (1986) found that the correspondence between O^+ heating, its characteristic random energy (about 10 eV) and the flow energy of the convection jet was highly suggestive of a collisional or Joule heating mechanism.

At lower altitudes (<1000 km), observations by satellites and ground-based radar have also identified large upward flows of O^+ associated with field-aligned currents and gradients in the horizontal ion drifts. Heelis et al. (1984) studied two cases of large flux ($>10^{10}$ cm^{-2} sec^{-1}) observed at altitudes near 900 km, and found that both were associated with intense upward field-aligned currents and with parallel and perpendicular acceleration.

Loranc (1989) studied the morphology of field-aligned thermal (<1 eV) ion flows for speeds between 50 m/sec and 3000 m/sec. He investigated the spatial distribution, magnetic activity dependence and occurrence frequency of UFI and found a magnetic activity dependence similar to that reported by Yau et al. (1984) at higher altitudes. More importantly, in the four case studies performed, each low altitude upflowing ion event was associated with enhanced ion temperatures, low energy electron precipitation and field-aligned currents. Large upflows of predominantly O^+ have been detected by radar as well (Winser et al., 1987; Wahlund and Opgenoorth, 1989). EISCAT radar observations by Winser et al. (1989) indicate that large upward ion fluxes preferentially occur near the polar cap/auroral zone boundary in the midnight-dawn MLT sector. They found good agreement, both spatially and temporally, between the upflowing ions and Joule heating (but not particle precipitation) which was associated with strong horizontal electric fields. Such large, low altitude fluxes associated with frictional heating indicate extensive filling of the topside ionosphere or enhanced thermal ion escape, so that similarities in both low altitude heating patterns and high altitude UFI should be present.

With this background in mind, the focus of this chapter is to examine the intensity and high latitude morphology of frictional heating for various geophysical conditions and to compare these features with both thermal ion upwellings, observed by DE 2 and with the higher altitude observations of UFI reported by Yau et al (1984). This study will consider answers to the following questions:

1. Can heating-induced changes in the ionosphere-thermosphere gas modify the source characteristics of upward flowing ions?

2. To what extent do patterns in frictional heating match intermediate and high altitude upflowing ions?

3. Does the response of frictional heating patterns to varying geophysical conditions match that of UFI?

4. Can the observed magnitudes of frictional heating account for the characteristic energy of upwelling ions reported at higher altitudes or are additional energy sources required?

As described in the introduction (Chapter 1), frictional heating plays a major role in the high-latitude momentum and energy budgets. Since this form of heating relies on collisional interaction between ions and neutral species for production and dissipation, both the ionosphere and thermosphere are directly affected. To quantify the energy input as well as its effects on the vertical momentum of the ions, a comprehensive set of measurements of both ion and neutral gas parameters is required.

Several direct and indirect methods are available for determining frictional heating rates in the high-latitude ionosphere, each having unique advantages and disadvantages. Killeen et al. (1984) pointed out the necessity for high spatial and temporal resolution for ion and neutral wind measurements based on time scale considerations of (1) the near-instantaneous response of ions to imposed variations of the electric field and (2) the somewhat slower response of the neutral gas to forcing by the convecting ions. The similarities in velocity for both species will ultimately determine the morphology of ion frictional heating so an overriding requirement exists for simultaneous measurements of total wind vectors. Satellite measurements, such as those made by the Dynamics Explorer 2 satellite, are well suited for this study since high resolution wind, density, temperature and mass measurements are made for both the ions and the neutral gas components. However, satellite observations are somewhat limited (as are other, ground-based techniques) in examining the evolving changes within convecting plasma volume subjected to variations in heating rates over relatively short time scales. Techniques relying on incoherent scatter radar have the advantage of measuring broad-scale heating rates and upward ion flux variations in a highly temporal manner even though certain assumptions and approximations must be made a priori. Both observational methods are used in this chapter to answer the questions posed above since each technique provides useful and complementary insight into the important role of frictional heating.

5.2 Theoretical Background: The Ion Energy Equation

The general form of the ion energy equation describing the production and exchange of energy between ions and other constituents in the F-region ionosphere is (Banks and Kockarts, 1973; Schunk, 1977; St. Maurice and Hanson, 1982; Killeen et al., 1984):

$$\frac{D}{Dt}\left(\frac{3}{2}P_i\right)+\frac{3}{2}P_i\left(\nabla\cdot\mathbf{V}_i\right)+\nabla\cdot\mathbf{q}_i+\mathbf{P}_i:\nabla\mathbf{V}_i=$$

$$\sum_n \frac{n_i m_i \nu_{in}}{m_i+m_n}\left\{3k\left(T_n-T_i\right)\Psi_{in}+m_n\left(\mathbf{V}_i-\mathbf{V}_n\right)^2\Phi_{in}\right\} \qquad (5.1)$$

$$+\,n_i\upsilon_{ie}3K\left(T_e-T_i\right)+n_i\upsilon_{ie}m_e\left(\mathbf{V}_i-\mathbf{V}_e\right)^2$$

where the convective derivative is defined as $\frac{D}{Dt}=\frac{\partial}{\partial t}+\mathbf{V}_i\cdot\nabla$; P_i is the ion scalar pressure; $\mathbf{V}_i$, $\mathbf{V}_n$, and $\mathbf{V}_e$ are the ion, neutral, and electron drift velocities; $\mathbf{q}_i$ is the heat flow vector; $\mathbf{P}_i$ is the ion stress tensor; ν_{in} and ν_{ie} are the ion-neutral and ion electron momentum

transfer collision frequencies respectively; m_i and m_n are the ion and neutral mass respectively; k is the Boltzman constant; n_i is the ion number density; Ψ_{in} and Φ_{in} represent the velocity-dependent collisional cross sections between ion and neutral species. This generalized form of the ion energy equation can be simplified considerably for application to the regions of interest in this study.

In the high-latitude F-region, the ion energy equation can be approximated by a number of simplifying assumptions to obtain an expression which relates energy input, in the form of ion frictional heating, and dissipation through collisional exchange with the neutral gas. These assumptions have been discussed in greater detail by Schunk, 1977; St. Maurice and Hanson, 1982; Killeen et al., 1984 and are summarized here for completeness. The effects of the time derivative can be neglected for events which occur on a time scale longer than $1/\nu_{in}$ which is approximately several seconds based on F-region densities). The advective term, $\mathbf{V}_i \cdot \nabla P_i$ is normally dropped by assuming a horizontally-stratified collision-dominated ionosphere. The heat conduction term, $\nabla \cdot \mathbf{q}_i$ has been examined in detail by Schunk and Soijka (1982) for a wide variety of modeled geophysical conditions and was found not to alter seriously the ion energy balance up to altitudes near 500 km. The viscous heating term can be neglected for spatial scale lengths longer than $(\mathbf{V}_i - \mathbf{V}_n)/\nu_{in}$ which is on the order of a few kilometers in the F-region (Schunk, 1975). The divergence of $\mathbf{V}_i$ term can be neglected since $\mathbf{E}\times\mathbf{B}$ motion is essentially incompressible and the $(\mathbf{V}_i - \mathbf{V}_e)^2$ term is usually dropped since the ion and electron gases are closely coupled by Coulomb forces. In the high latitude F-region, O^+ and atomic oxygen are the major species so ion and neutral collisions are dominated by resonant interactions. For this reason, the collision cross sections, Ψ_{in} and Φ_{in}, are assumed to be independent of velocity (hard-sphere interactions) and are both set to 1. With this assumption, described in detail by St. Maurice and Hanson (1982), a relative drift of at least 1.5 km/sec must occur before significant (>100 K) temperature differences appear. Using the above assumptions and limitations, the ion energy equation simplifies to:

$$\frac{3}{2} n_i k \nu_{in} (T_i - T_n) \cong \frac{n_i}{2} m_n \nu_{in} (\mathbf{V}_i - \mathbf{V}_n)^2 + 3\, n_i\, k\, \nu_{ie} (T_e - T_i) \qquad (5.2)$$

In this form, the ion energy equation expresses an approximate heat balance involving three terms. The term on the left-hand side (term 1) represents the rate of energy transfer between ions and neutrals by collisional heat exchange. This process represents a heat loss for the ions as long as $T_i > T_n$ (which is normally the case), and a thermal heat gain for the neutral gas. The rate of ion cooling is thus proportional to the collision frequency as well as to the temperature difference between ions and neutrals. This has

important consequences since a balance between cooling and heating rates will dictate the local ion temperature. Because ion-neutral collision frequencies are on the order of a few seconds in the F-region and the relative drift speeds rarely exceed 2 km/sec, heat transfer to the neutrals occurs over a relatively short distance of a few kilometers. This distance is shorter than the scale length restriction imposed by the energy equation assumptions described above so we generally assume that heat loss occurs within the same volume space occupied by the ions.

The first term on the right (term 2) represents frictional heating which occurs whenever relative motion exists between the ion and neutral gases. This situation develops under the action of an electric field which can either be externally imposed such as the convection electric field associated with the solar wind-magnetosphere interaction, or internally developed such as that which occurs when thermospheric winds drag ions across magnetic lines of force. In either case charged particles drift relative to one another and relative to the neutral particles. Collisions occur, primarily between ions and neutrals which limit the drift velocities and, in the process, convert a portion of bulk flow energy into random thermal energy with both the O^+ and neutral atomic oxygen receiving equal shares due to their mass equivalence. The last term (term 3) on the right hand side of equation 5.2 represents heat exchange with the electron gas. This term normally acts as a relatively small (less than 10% of the total energy balance (Schunk and Sojka, 1982)) heat source in the high-latitude F-region since downward electron heat conduction from the magnetosphere usually maintains $T_e > T_i$. However, when frictional heating is exceptionally strong, T_i may exceed T_e and for these cases, the last term of the energy equation represents a heat loss for the ions. Before proceeding further, it is useful to relate terms in equation 5.2 to expressions which are sometimes used interchangeably in the literature. The first term on the right hand side represents a frictional heating rate (ergs cm^{-3} sec^{-1}) although the term "frictional heating" is often used. Colliding neutrals and ions are both frictionally heated however, the ions continue to loose this energy to the neutral gas via heat exchange (the T_i-T_n term). The sum of the direct heating experienced by the neutrals and the component transferred from the ions to the neutrals via heat exchange is "Joule heating". The energy directly received by the ions (also a heating rate) is properly referred to as "ion frictional heating". Used in the correct sense, frictional heating is a rate process of volume heating to all (ion and neutral) gas constituents while Joule heating and ion frictional heating refer to the volume heating rates for the neutral and ion gas components respectively. Since the major ion and neutral specie in the high latitude F-region have similar mass, it is useful to approximate ion frictional heating by taking one half the Joule heating rate. This treatment implicitly assumes that complete energy

exchange takes place between ions and neutrals so that all the ion energy is lost locally to the neutrals. This assumption is generally valid for conditions in this study where bulk ion speeds of <2.0 km/sec are considered. However, the assumption of local cooling to the neutrals becomes invalid when exceptionally large DC electric fields produce relative drift velocities between ions and neutrals which exceed the neutral thermal velocity. For these cases the effects of ion heat transport must be considered and ion frictional heating may be different from the value of one half the local Joule heating. In the next section, the simplified ion energy equation is solved using in situ satellite measurements to derive ion frictional heating. This spatially and temporally varying energy input is related to changes in the thermosphere-ionosphere environment to demonstrate the strong influence that frictional heating exerts on ion upwelling.

5.3 DE 2 Observations of Ion Frictional Heating: Case Study

Simultaneous measurements from a number of instruments carried onboard the Dynamics Explorer 2 satellite can be used with the simplified ion energy equation to calculate the magnitude, location and effects of frictional heating in the high latitude ionosphere. The full ion vector winds needed for such calculations are obtained by combining the along-track and cross-track ion wind components from the RPA and IDM instruments respectively (described in Chapter 2). Neutral wind vectors are obtained by merging the meridional wind measurements obtained from the FPI with the zonal component obtained from WATS. The LANG instrument provides electron temperatures and densities while neutral temperatures and composition were determined by the WATS and NACS respectively. These data are measured along the satellite track and are available at the University of Michigan on a local database with 8-second resolution so that ion frictional heating rates and the accompanying changes in the thermosphere-ionosphere environment can be evaluated along the satellite track.

In Figure 5.1, a summary of observed and derived plasma and neutral gas parameters are plotted as a function of universal and local time for a single DE-2 pass over the Southern (summer) Hemisphere. On this date (82327), the satellite orbit was directed along the 18:30-06:30 LST plane with the satellite passing just sunward of the geomagnetic pole (located on the dawn side of the polar plot with a "s"). Geomagnetic activity was high and steady with a Kp value of 7. Plots of the full wind vectors, temperatures, composition and ion heating clearly indicate the intensity of the geomagnetic disturbance. The ion pattern reflects a two-cell convection pattern commonly observed in the polar ionosphere with antisunward flow across the geomagnetic pole, sharp convection reversal shears at lower geomagnetic latitudes and return, sunward flows at still lower geomagnetic

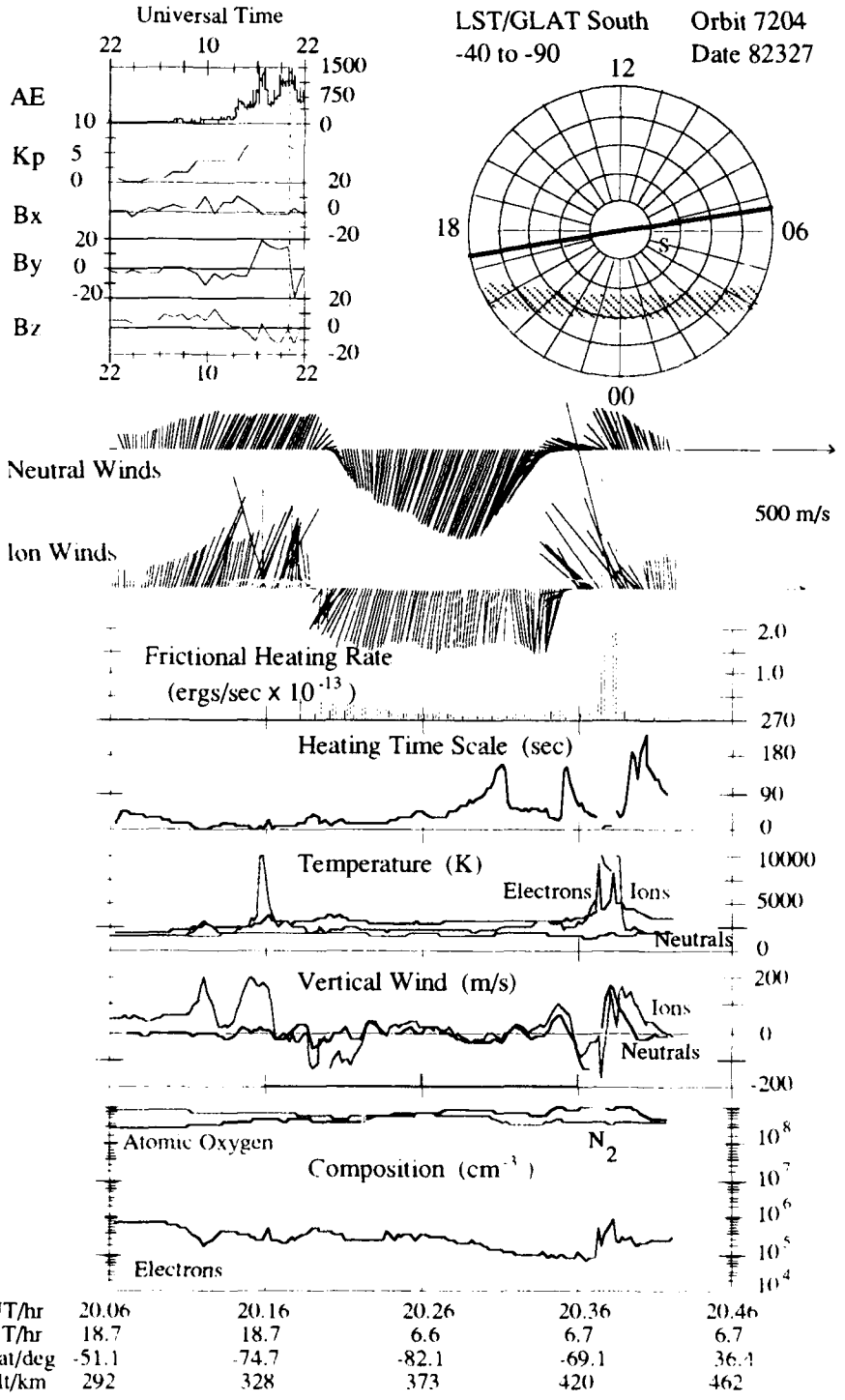

Figure 5.1 Summary plot of observed and derived ionosphere-thermosphere conditions plotted along the DE-2 satellite track for orbit 7204. Enhanced frictional heating occurs near the dayside convection reversal regions due to large relative drift velocities between the ion and neutral gas.

latitudes along the dusk and dawn meridians. Since geomagnetic activity remained relatively high and unchanged for the preceding 6 hours, the ion wind pattern is well-ordered with large ion velocities. Momentum transfer through collisions with neutral particles have caused the neutral winds to acquire a similar directional pattern and high velocities. Despite similarities in a directional sense, the ion velocities remain much higher in response to the imposed electric fields and large relative velocities persist. This relative velocity or speed shear is clearly evident and strongest in the dusk and dawn sunward convection channels and corresponds to maxima in ion frictional heating displayed in Figure 5.1. In this plot, the ion heating rate is calculated according to equation 5.1 but has been normalized in density by expressing the heating rate on a per particle basis. This treatment allows for comparison between observations made at different altitudes, and hence ion densities, along the satellite orbit. In addition to the strong correspondence between regions of large relative drifts and enhanced heating, the heating rates can be seen to vary rapidly along the satellite track with the region of strongest heating confined to localized regions of tens to hundreds of kilometers. The large degree of variability in heating rates results from the quadratic nature of the frictional heating term and the limited spatial extent over which large velocity shears are generally found and will be discussed in more detail shortly. Passes such as this one which span the dayside convection region typically show persistent areas of high ion heating which are strongest at or very close to the the location where sunward streaming ions undergo a strong rotational change in direction or "convection reversal" as they start to flow antisunward over the polar cap. In discussing ion convection reversals, a distinction can made between rotational reversals and shear reversals. In the former, the ion velocity vector changes zonal sense through a meridional flow. Shear reversals occur abruptly however and are normally associated with an equipotential contour at or near the polar-cap boundary. The regions where each type of convection reversal occurs are illustrated in Figure 5.2. Under steady-state conditions the flux tube trajectories coincide with equipotential contours so that each contour in this figure represents the convection drift path of a flux tube. Rotational reversals are commonly found near the dayside convection throat and near the midnight reconnection point and are generally broader in extent as Figure 5.2 indicates.. A boundary extending back from the dayside convection reversal and along the dawn and dusk sectors marks the change in ion drifts from sunward to antisunward flows and represents the location where shear reversals are commonly found. This is another area where elevated ion heating due to the strong directional and velocity shears can be found, especially when the shear reversal boundary

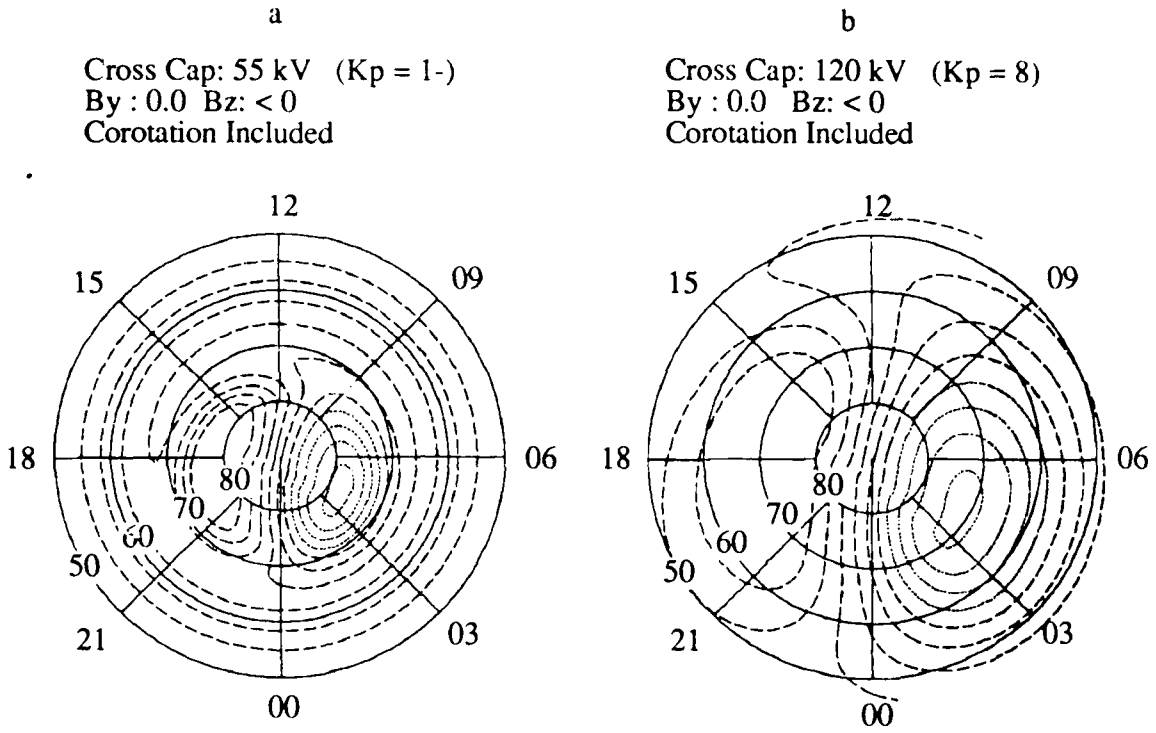

Figure 5.2 Equipotential patterns for low and moderate Kp conditions showing the relative location of the convection reversal boundary, convection throat and dawn and dusk convection channels. These features move in response to changing geophysical conditions shifting the location of strong ion-neutral wind shear and accompanying frictional heating features (courtesy R. Heelis, private communication, 1990).

moves in response to electric field variations. For the dayside reversal region, the ion drifts respond quickly to the changing electric field vector while the slower moving neutrals continue to flow sunward due to the large inertia of the neutral gas, thus creating quasi-permanent regions near the dayside convection throat where frictional heating is enhanced. The heating in this case arises primarily due to a rotational (directional) reversal in the ion drifts and leads to substantial modification of the interacting gases. Depending on the heating magnitude, the resulting transient features in the plasma can be transported along the convecting flux tube's path as it moves across the pole.

The thermosphere-ionosphere response to the strong heating "event' depicted in Figure 5.1 can be seen in the temperatures, vertical velocities and composition variations. The ion temperature profile shows two well defined spikes which closely follow the frictional heating rate profile. Large increases in T_i result when the frictional heating rate exceeds the cooling rate to the neutrals. In this case, the "excess" heating is sufficient to elevate the ion temperature above that of the electrons and, over confined regions, acts as a source of heat for the electron population (the $3Kv_{ie}(T_e - T_i)$ term). Transient electron

heating is apparent in this example near the dawnside convection channel where locally elevated electron densities are observed due to the increased electron scale height. Large changes in the neutral temperatures are not apparent however, even though the neutral gas is heated at approximately the same rate as the ions. This diminished response of T_n occurs because of the very large heat capacity of the more numerous neutrals. Plots of the ion and neutral vertical wind fields show positive (upward) velocity enhancements, especially during the the dawnside heating event. For the ions, the presence of strong ion frictional heating provides a direct mechanism for inducing thermal ion upwellings since the heated plasma and neutral gas expands upwards in response to scale height adjustments. The upward ion velocities observed here are therefore the sum of a bulk, mass-averaged velocity (primarily the neutral component), and a diffusive velocity enhanced by the ion heating. The bulk velocity is generally larger than the major ion diffusive flow, however the sharp increase in upward bulk motion following ion heating can significantly alter the fluxes of upward moving ions by increasing diffusion rates. Compositional changes are somewhat more subtle to detect but are equally important in modifying fluxes of thermal ions. Atomic oxygen and molecular nitrogen, corrected to a constant 300 km altitude level based on a local scale height calculation and plotted along the satellite track indicate a transition from atomic to molecular dominance. This change occurs due to the integrated effects of Joule heating to the neutral gas which occurs in the extended altitude interval below these measurements. Composition changes associated with heating have been studied in some detail by Hays et al. (1973); Prolss (1980); and Killeen et al. (1983). Local depletions in the ion (electron) densities were found to occur through the following reaction sequence:

$$O^+ + N_2 \rightarrow NO^+ + N \qquad (1)$$

$$NO^+ + e \rightarrow N + O \qquad (2)$$

The enhanced ion temperatures and increased N_2 densities act together to increase the rate of ion-atom interchange in reaction 1 resulting in greater production of molecular ions which then rapidly recombine with electrons and dissociate. High ion temperatures are particularly important for this reaction scheme since the rate coefficient for the first reaction varies as $\sim T_i^2$. As Killeen et al. (1984) pointed out, depletions in the ion densities can prolong the duration of frictional heating since they reduce the ion-neutral collision frequency and therefore the rate at which momentum is transferred to the neutral gas. As a result, rotational and velocity shears may persist for longer periods, leading to paths of enhanced frictional heating which extend along the path of the convecting flux tube. A

general decrease in ion densities along the satellite orbit by one order of magnitude can be seen in Figure 5.1. While this trend suggests an overall reduction in thermal ion fluxes through reduced ion densities, spatially confined regions of enhanced ion densities may also appear superimposed on the overall trend of decreasing density. Two density enhancements are present near 20.16 UT and 20.35 UT and coincide with regions of intense ion frictional heating and elevated electron temperature. These features suggest another process at play during large heating events which competes with the reaction scheme previously described and acts to locally increase ion densities. The process occurs whenever ion frictional heating events cause the ions to become heated well above the thermal electron population. The increasing importance of collisional electron heating results in a significant electron temperature increase. The resulting scale height adjustment to the electron population results in an increase locally in the electron density and major ion species (O^+). This mechanism should be most effective at higher altitudes where molecular recombination reactions are less frequent and electron mobility greater. The behavior in Figure 5.1 is consistent with an altitude-dependent process since for approximately similar ion temperatures but different altitudes, the density enhancement is strongest in the dawnside convection region. These density enhancement features appear limited in horizontal extent to 10's of km but, when coupled with coinciding large vertical ion velocities, can result in a local, 100-fold increase in upwelling ion flux within the heated flux tube. The altitude extent of such flux enhancements will depend in large part on collisional and thermal processes in the intervening layer and will be examined in more detail in a Chapter on modeling transient fluxes. Analysis of this orbit thus indicates that strong transients in ion densities and vertical velocities follow directly from ion frictional heating events that are caused by characteristic changes in the thermosphere-ionosphere environment. For this orbit, regions of strong frictional heating are associated with quasi-permanent rotational reversals found on either side of the dayside convection throat and steady but large relative velocity differences associated with a high ion velocity pattern. In contrast to this case where strong heating is present during quasi-steady convection, it is also possible to find enhanced regions of ion frictional heating that arise from temporal variations in the ion convection.

Figure 5.3 summarizes observations and derived quantities measured along another pass (orbit 7214) over the high latitude region where significant ion frictional heating was observed in response to a change in the ion convection pattern. In this case, the neutral wind flow pattern appears disorganized and somewhat irregular across the entire polar cap.

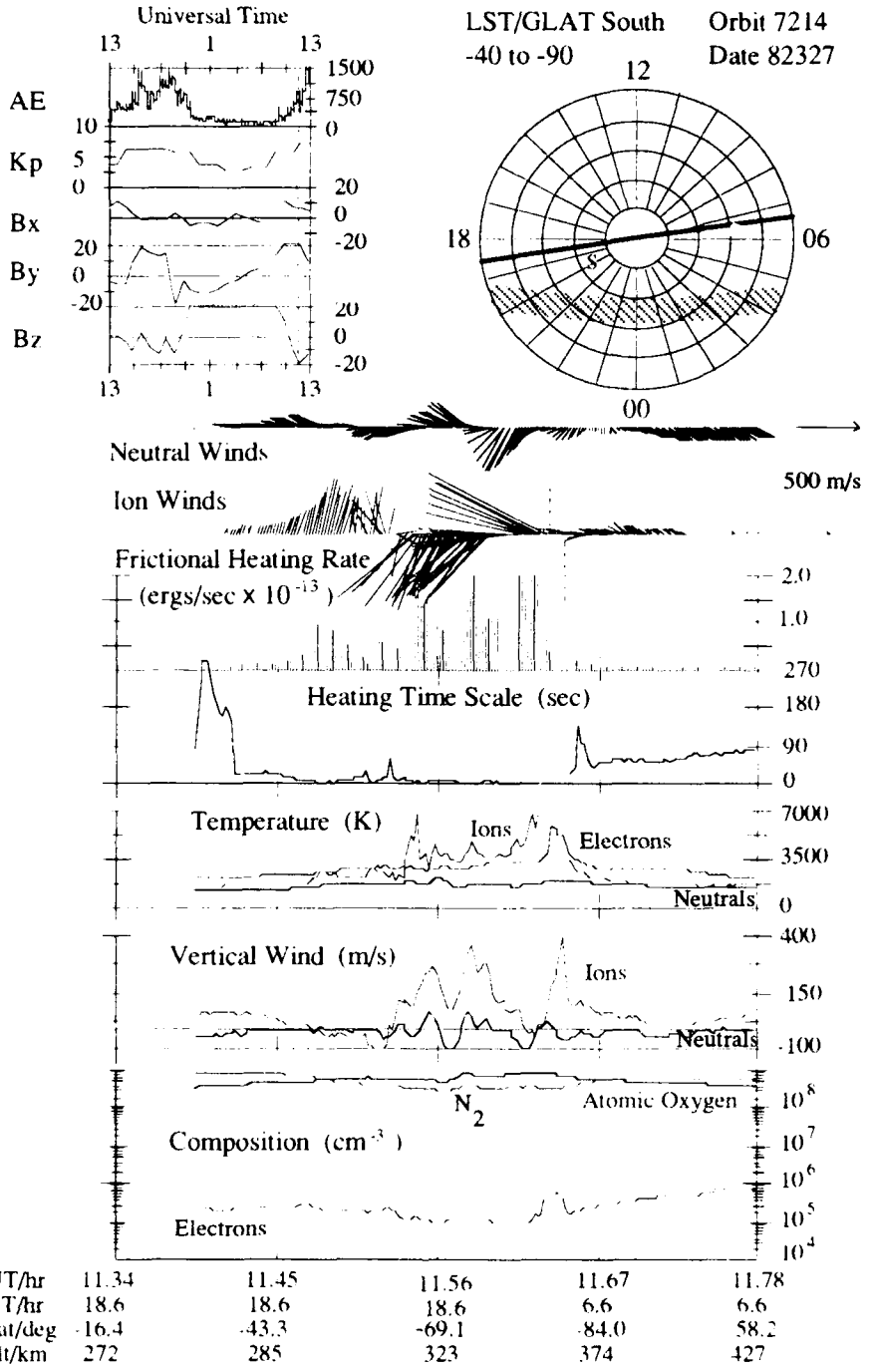

Figure 5.3 Summary of observed and derived ionosphere-thermosphere conditions plotted along the DE-2 satellite track for orbit 7214. A broad region of frictional heating extends across the dayside convection throat due to strong ion convection and a disorganized neutral wind pattern. Intense frictional heating affects the ion temperature, velocity, and density.

Since the neutral flow retains the character of ion flow patterns imposed earlier, these features were probably established by prior ion forcing during a period when the IMF was strongly northward (see magnetic summary plot in Figure 5.2) and therefore reflect a multi-cell convection pattern which is thought to prevail during Bz north conditions. Approximately one hour prior to this orbit, the IMF turned strongly southward while Kp increased from 3_0 at 9 UT to 6_0 by 12 UT. These changes would favor a reconfiguration in ion convection to a more organized two-cell pattern. Ion winds measured along the satellite orbit reflect this two-cell convection structure with high antisunward flow present across the geomagnetic polar cap and with sunward streaming flow in the dawn and dusk convection channels. The neutral winds respond more sluggishly to this change in the ion winds so that an extended area along the satellite track, corresponding to the width of the convection throat, has considerable directional shear present. Ion frictional heating rates for the region are significantly enhanced (from about 11.45 UT to 11.66 UT), with a number of impulsive heating spikes present for locations where ion/neutral velocity differences are greatest. Ion temperatures remain elevated above the electron temperature for the entire period of enhanced ion heating, with peak ion temperatures and upward vertical flows coinciding with heating rate maxima. The most intense heating occurs in the dawn convection channel where strong collisional heating from the ion to the electron population increased the electron temperature by 80% and causing a 50% increase in the local electron density. The association between ion heating events, local density enhancements and strong upwelling ion velocities is clearly evident in this orbit and suggests that directional shears, as well as relative speed differences, are important in determining the location and magnitude of ion frictional heating.

In the past two examples, frictional heating morphology was examined near the dayside convection reversal. For both cases, elevated heating rates were present in both the morning and afternoon convectional reversal regions due to strong directional shears associated with a rotational reversal as large relative speed shears. Shears are also present at other magnetic local times, but may not show MLT symmetries due to differences between neutral wind forcing in the dawn and dusk hemispheres. Orbit 7114, shown in Figure 5.4 illustrates this point since it passes along a different magnetic local time plane corresponding to 16:30 to 04:30 MLT (19:15 to 7:15 LST plane as depicted in the figure). A weak southward IMF before and during this orbit coupled with a decrease in Kp from 3_0 to 2_0 for the 00-03 UT period resulted in a relatively weak and shrinking ion convection pattern. The retreat of the dawn convection channel to higher latitudes resulted in the superposition of sunward flowing ions on a antisunward flow of neutrals. The neutral winds are responding primarily to the solar EUV driven pressure gradient and earlier ion

forcing and are unable to respond as quickly to the changing ion convection pattern . This results in a restricted region in the dawn convection cell where strong directional shear and enhanced ion heating are present. A similar signature of shear and heating is absent in the dusk convection area because the neutral winds there more closely follow the ion flow. This behavior can be found in many of the DE-2 passes and is thought to arise from the response of the neutral winds to different forcing for dusk and dawn sunward convection. channels. In the dawn convection channel, neutral parcels which gain momentum from ions in the dawn convection channel tend to be displaced to the right of their initial direction (equatorward) due to the increasing influence of Coriolis force. This leads to a continual exchange of low-momentum neutral parcels as they are entrained into the ion convection region, accelerated by collisions with convecting ions and then deflected equatorwards out of the regions of strongest convection. This process helps to maintain large relative drifts between the ions and neutrals at the expense of ion momentum. On the dusk side however, deflection by the coriolis force helps to maintain the neutral parcels in the dusk convection channel so they have more time to gain momentum from the ions. As a result, greater neutral wind velocities and characteristically less ion neutral wind shear are present in this sector. This location-specific behavior of the neutrals to ion forcing appears in the pass shown in figure 5.4. With stronger ion-neutral coupling in the dusk cell, directional and speed shears are reduced more rapidly as the ion convection pattern shrinks so that heating in this cell is less persistent. Heating in the dusk region therefore, should not be as high as heating in the dawn side following the poleward shift in the ion convection pattern. Such behavior in the morphology of ion heating has been predicted by Lockwood and Fuller-Rowell (1987) and observed by the EISCAT radar (Lockwood et al., 1987) and is a consequence of the inability of the neutral wind pattern to respond to temporal variations in the cross-cap potential as quickly as the ion wind pattern.

Several characteristic features in ion heating morphology, magnitude and thermosphere/ionosphere response are apparent from the three orbits discussed above. Frictional heating rates were found to be highest at or near the dayside ion convection reversal region where persistent directional shear between ion and neutral winds occurs. Although not discussed, enhanced ion heating should also be high in the nighttime convectional reversal areas for the same reason. Heating in the dawn and dusk convection channels is also apparent with typically higher heating rates present in the dawnside convection channel. Additionally, transient changes in the ion convection patterns due to varying cross-cap potential are found to produce elevated heating rates due to transient increases in ion-neutral drift velocities.

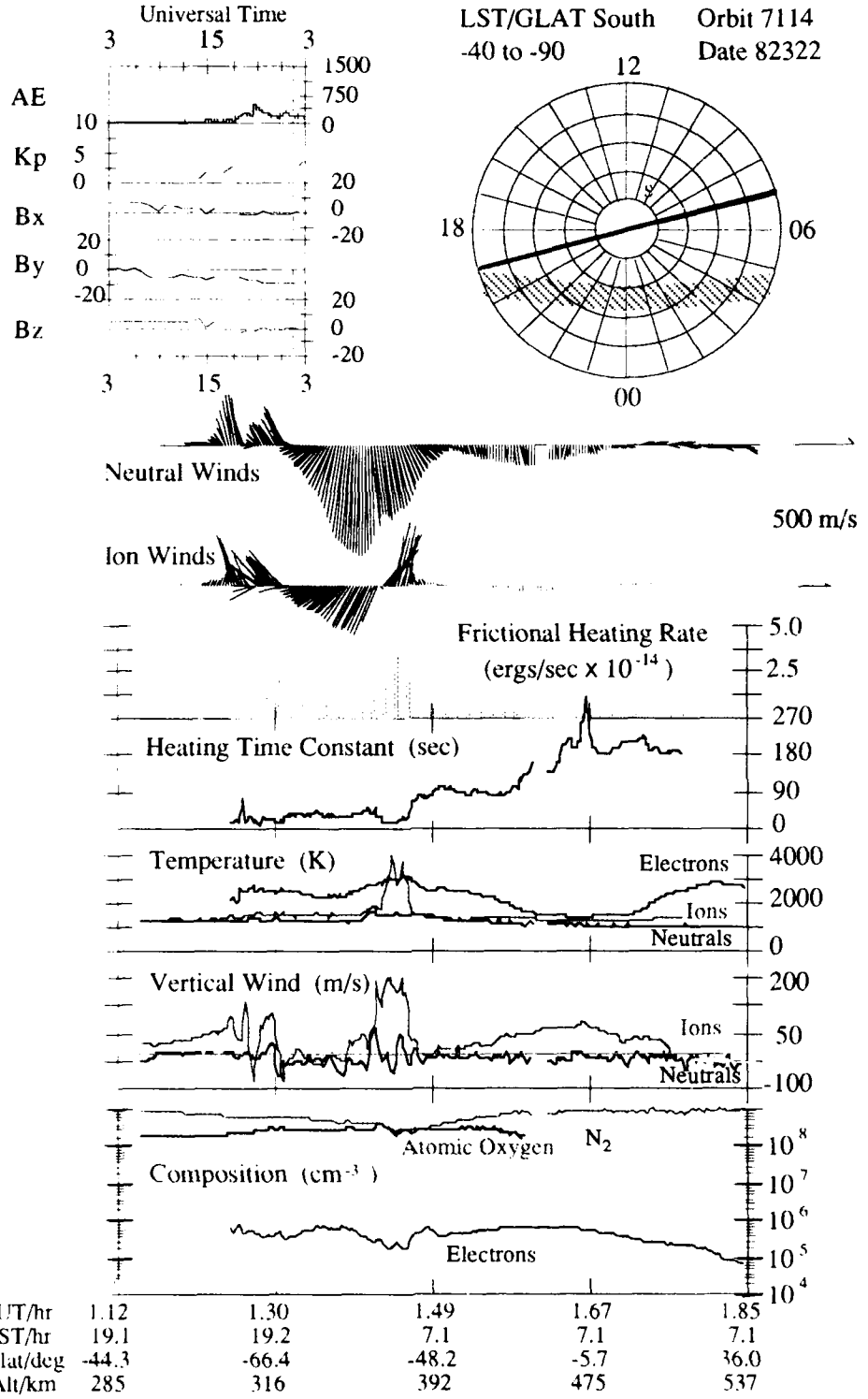

Figure 5.4 Summary plot of observed and derived ionosphere-thermosphere conditions plotted along the DE-2 satellite track for orbit 7114. The inability of the neutral wind to quickly respond to temporal variations in the cross cap potential results in strong frictional heating as the convection pattern shifts poleward.

The magnitude of the heating tends to vary considerably since it is related in a complex manner to (1) the intensity of ion-neutral wind shear (a function of direction and/or speed differences), (2) the local ion and neutral density (both a function of T_i and T_n) and (3) the response time of the neutrals in gaining or loosing ion momentum. Finally, several transient responses in the plasma are apparent. Order of magnitude increases in the ion velocities were associated with ion heating events and, for intense ion heating, the electron gas temperature increased resulting in local density enhancements. These responses, taken together, can result in large, transient fluxes of upflowing thermal ions in support of the more energetic ion outflows observed by the RIMS on DE 1. In the next section, the location, intensity and magnitude of the plasma heating response is examined on a global scale and related to these higher-altitude outflows.

5.4 Global Morphology of Ion Frictional Heating From DE 2

With the fully instrumented observations made over several years by the DE-2 satellite, it is possible to calculate the magnitudes, spatial morphology and transient behavior of frictional heating the high latitudes. Plots of these parameters can be constructed as a function of invariant latitude and magnetic local time and compared to high-altitude outflow observations to identify which types of low-altitude signatures correlate best with UFIs.

The full set of instrumentation available on DE-2 was used to derive averages of ion heating rates, ion-neutral relative wind differences and elevated ion temperatures. These quantities were computed using 8-second observations along the satellite track whenever LANG, WATS, FPI, RPA, IDM and NACS data were available during 1981-1983. Averages were then calculated for bins corresponding to one hour of magnetic local time and 5 degrees of invariant latitude. The latitudinal width chosen for this study represents a compromise between an ability to resolve gross features such as the auroral oval and convection channels and a bin size containing a large enough sample of points to provide a representative average. The averaged data were further separated into bins of low ($0.0 < Kp < 2.7$) and moderate ($2.3 < Kp < 5.3$) geomagnetic conditions for both summer and winter. Observations from both the southern and northern hemisphere were used for the appropriate season based on a selection criteria of solstice ± 50 days. Figures 5.5 and 5.6 illustrate the number of orbits for both winter and summer and the number of heating rates computed for each Kp bin and season. Heating rate calculations are the most limited quantity examined in this study since measurements from nine different sensors were required simultaneously. The geomagnetic and seasonal separation of averaged heating rates, shears and ion temperatures provides additional information on frictional heating

behavior for comparison with higher altitude ion outflow observations. Figure 5.7 shows averages of ion frictional heating rates, ion-neutral wind shear and enhanced ion temperatures for low Kp, summertime (S. Hemisphere) conditions. For this case, both the averaged volumetric and per particle heating rates are depicted to illustrate the difference between these terms. The volumetric heating rate is given by:

$$\frac{n_i}{2} m_n \nu_{in} \left(\mathbf{V}_i - \mathbf{V}_n\right)^2 \qquad (5.4)$$

while the per particle heating rate is obtained by dividing by the local ion density. The volumetric heating rate is somewhat deceptive in its use here for two reasons. As mentioned earlier, routine precession of the satellite perigee across the polar regions introduces a strong altitude bias in the ion (electron) density measurements along the path of changing perigee. Secondly, horizontal gradients in electron density (across the terminator or within the aurora for instance) will change the volume heating even if the shear term remains constant. Spatial plots of average volume heating rates may therefore appear low near dawn due to the generally lower ion densities found in this area. This leads one to conclude falsely that the ion gas is relatively cooler. In fact, ion temperatures in this region can be locally enhanced since the frictional heat input is distributed among fewer ions.

To avoid these difficulties, per particle heating rates are more appropriate for discussions that relate heating rates to ion gas behavior. The shear term is simply $(\mathbf{V}_i\text{-}\mathbf{V}_n)^2$ while averages of enhanced ion temperatures are derived from $T_i\text{-}T_n$ to reduce the effects of diurnal EUV variations. This is less than a perfect indicator of ion frictional heating since several factors combine to influence this quantity. For example, enhanced ion heating from thermal electrons, ion frictional heating and heating or cooling of the neutrals relative to the ions all effect this term. Heating by thermal electrons accounts for generally less than 10% of the ion energy in the high latitude F-region (below 500 km) as discussed earlier. Neutral heating/cooling relative to the ion gas is more problematic and should maximize near, and just after, the evening terminator when neutral cooling rates are high or in regions of strong particle precipitation where neutrals are strongly heated. As a first approximation however, $T_i\text{-}T_n$ can provide some indication of ion response frictional heating, especially when heating rates are high. In comparing the patterns of each plot in Figure 5.7, a clear pattern of enhanced ion heating and elevated ion temperatures can be found which corresponds to the approximate location of the auroral oval. The region is roughly annular in shape, with the strongest heating and ion temperature enhancements confined to invariant latitudes poleward of about 70 degrees.

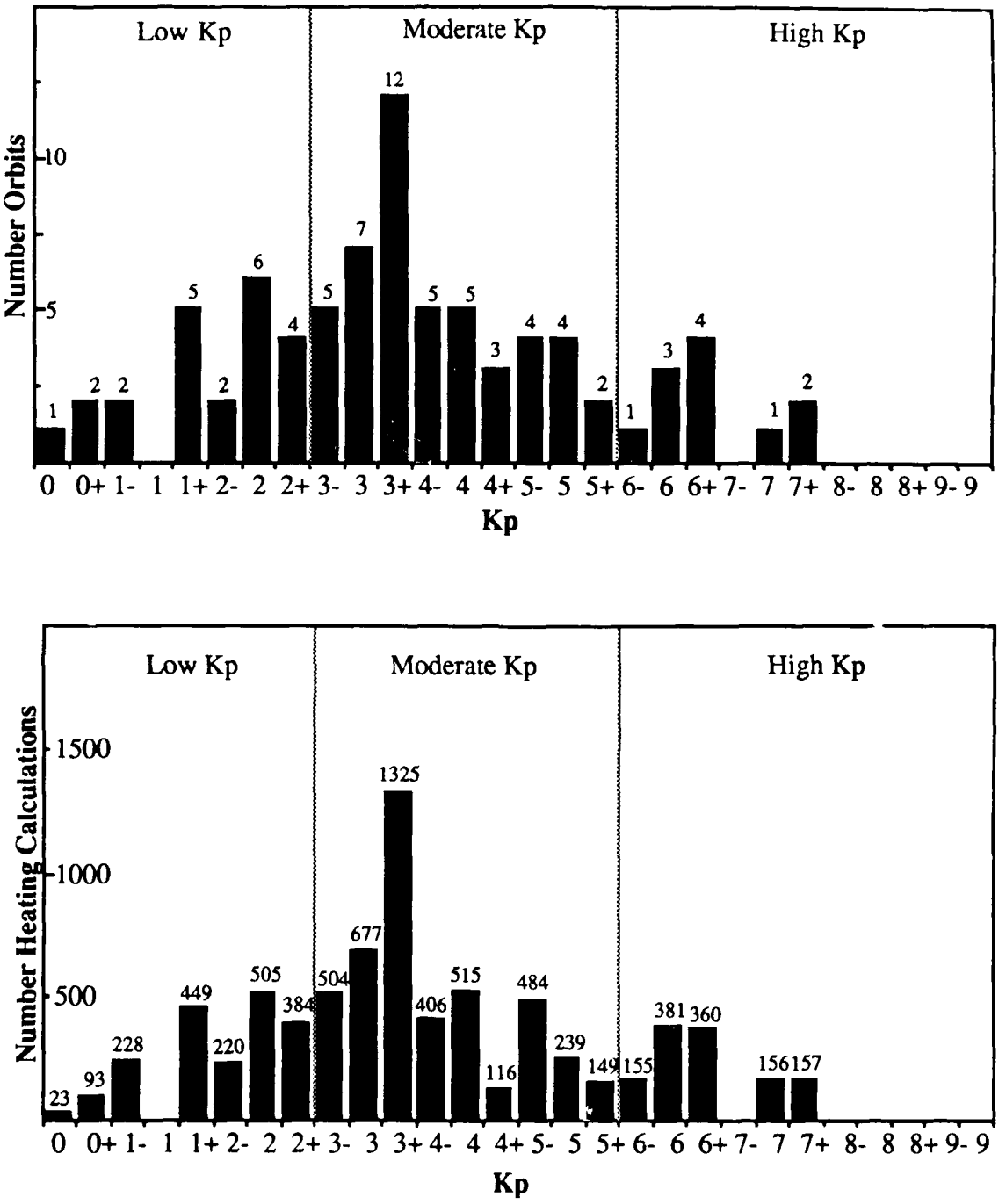

Figure 5.5 Histogram showing the number of orbits (a) and the number of heating calculations (b) as a function of Kp which were used in the summer frictional heating morphology plots. The bin criteria for low, moderate and high levels of geomagnetic activity are also illustrated.

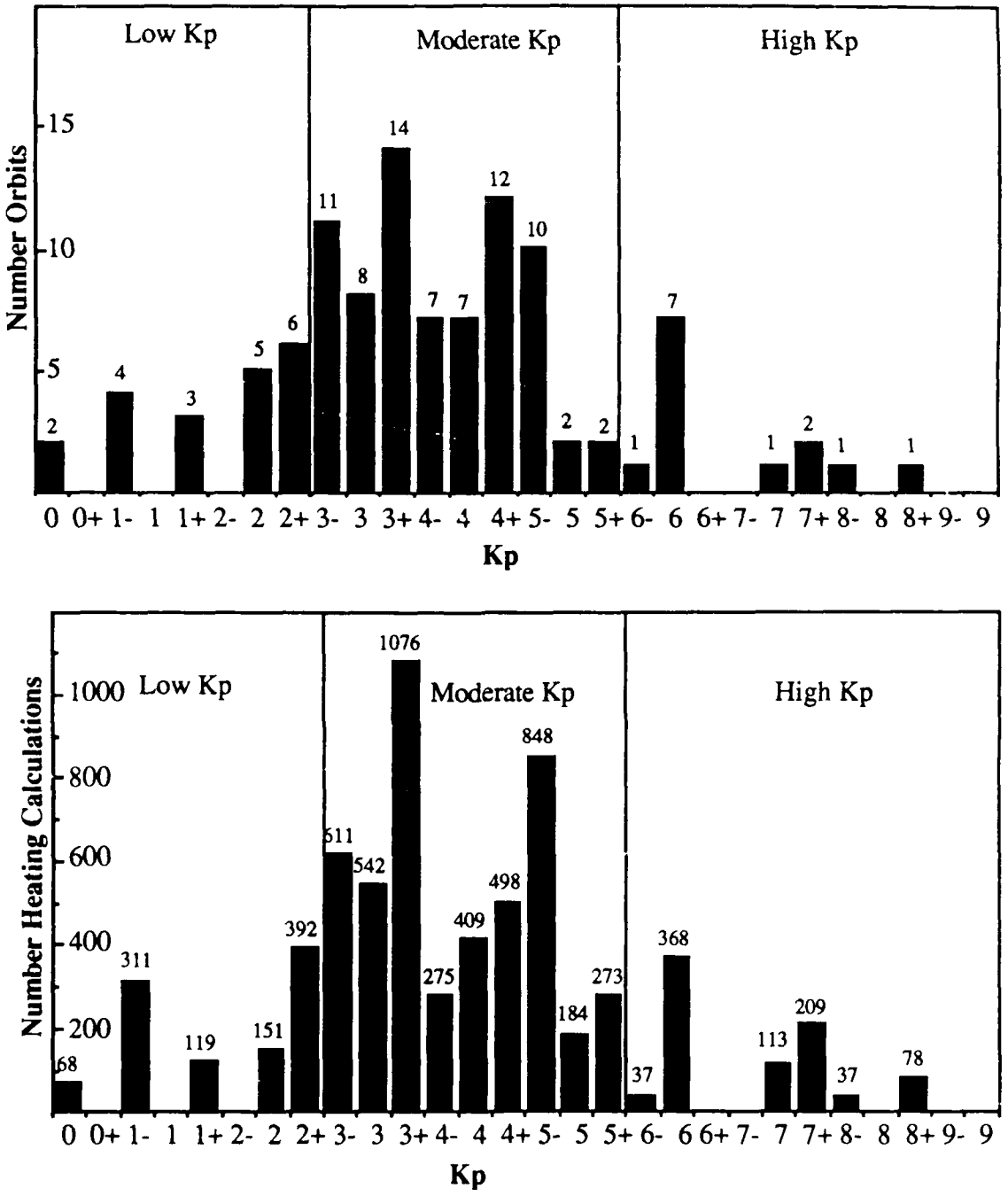

Figure 5.6 Histogram showing the number of orbits (a) and the number of heating calculations (b) as a function of Kp which were used in the winter frictional heating morphology plots. The bin criteria for low, moderate and high levels of geomagnetic activity are also illustrated.

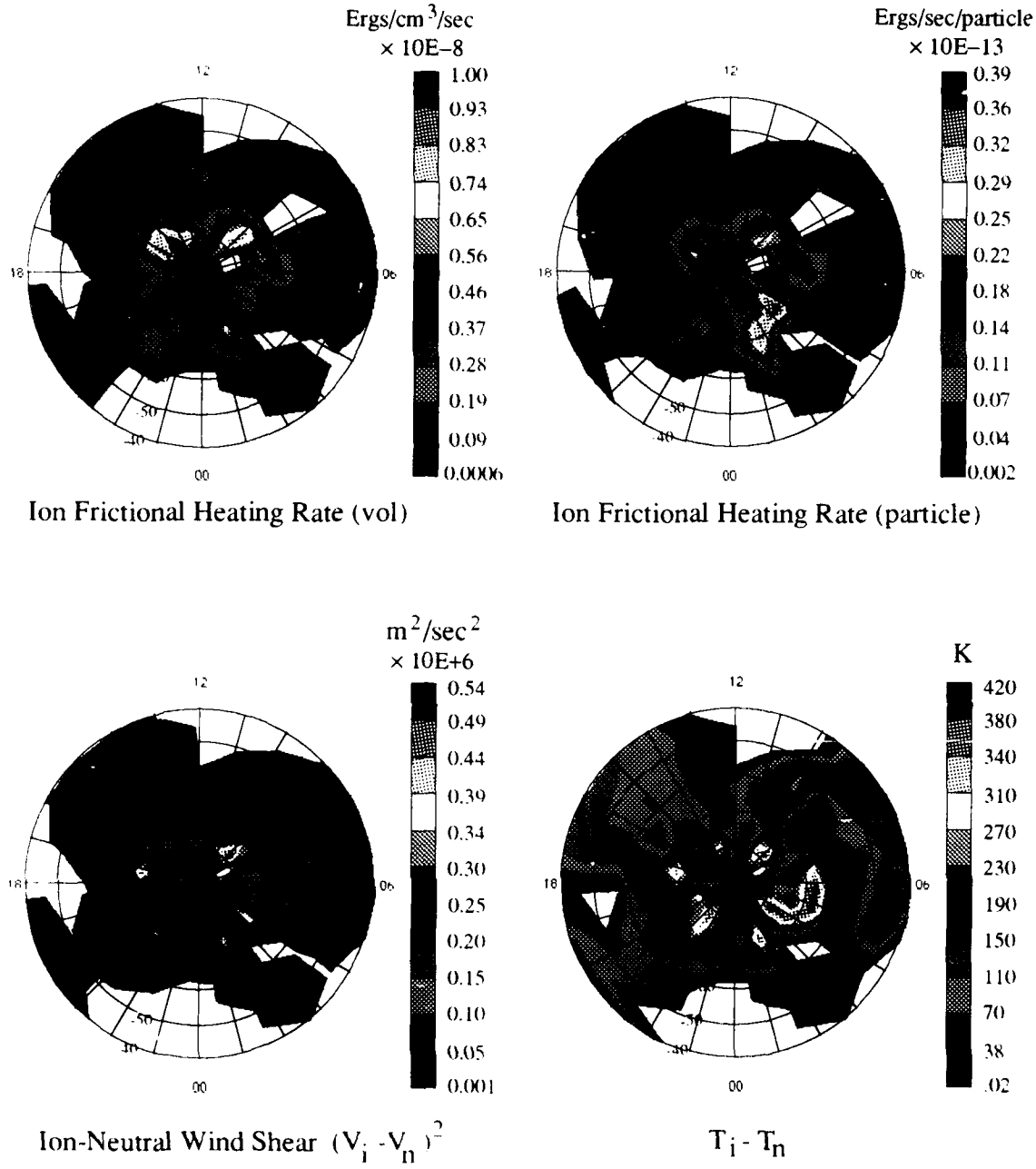

Figure 5.7 Polar plot of average volumetric and per particle ion frictional heating, ion-neutral wind shear and ion temperature enhancement for low Kp summertime conditions. Averages are for 5 degrees invariant latitude and one hour MLT. Strongest ion heating occurs near the convection throat and along the dawn convection channel where shear is high.

The locations of strongest heating also coincide with areas of highest shear and appear where the ions undergo rapid rotational reversals such as near the dayside convection throat and the midnight reversal region. An asymmetry in the frictional heating rates about the noon-midnight magnetic meridian is also apparent with enhanced heating occurring in the dawn convection channel. As noted earlier, this feature arises due to the continual replenishment of low-momentum neutral gas into the region of sunward convecting ions thereby enhancing the relative ion-neutral wind shear. For the dawn convection channel speed shear, and not directional shear, appears to most influence the heating rates. In contrast to the generally good agreement between frictional heating and wind shear patterns, the volume heating rate plot has a less-defined heating pattern due to the effects of the altitude-dependent density values. Enhancements in the ion temperatures are clearly evident in Figure 5.4 and closely match the frictional heating and shear patterns for the globally-averaged data sets. Elevated ion temperatures near the convection throat are evident and appear as persistent features above the weaker diurnal EUV increases in T_n. For this case, strongest enhancements in T_i are located in the dawnside and are related to low ion densities, which reduce the plasma's heat capacity, and to diurnal cooling by the neutrals which also acts to increase the ion-neutral temperature difference. From the present results, it is apparent that the global distribution of frictional heating at high latitudes is determined largely by the location of the auroral oval and the pattern of the convection electric field. For the moderate Kp case ($2.3 < Kp < 5.7$) the correspondence between regions of high frictional heating, strong shear, and elevated ion temperatures is even more striking. The spatial morphology of frictional heating and enhanced ion temperatures is closely tied to the ion convection pattern and therefore, should expand and shift equatorwards with increasing Kp. This behavior is present in Figure 5.8. where averages of ion frictional heating, ion-neutral wind shear and ion temperature enhancement are plotted for moderate levels of geomagnetic disturbance ($2.7 < Kp < 5.7$). The format is similar to Figure 5.7 with the exception that volumetric Joule heating rates are also plotted to show that similarities in the Joule heating and frictional heating patterns which indicate that the thermospheric gas shares in the frictional heating process. The neutral per particle heating rates shown here are on the order of 100 times lower than for the ions due to the much higher neutral particle densities. This explains why the neutral temperatures do not respond as dramatically as that of the ions. Comparing the patterns of ion heating, shear and temperature enhancements for the moderate Kp case, several important features begin to emerge. First, dayside maxima in heating rates are still found at the same approximate latitudes on either side of the convection throat but post-midnight heating in the dawn convection channel has shifted equatorwards.

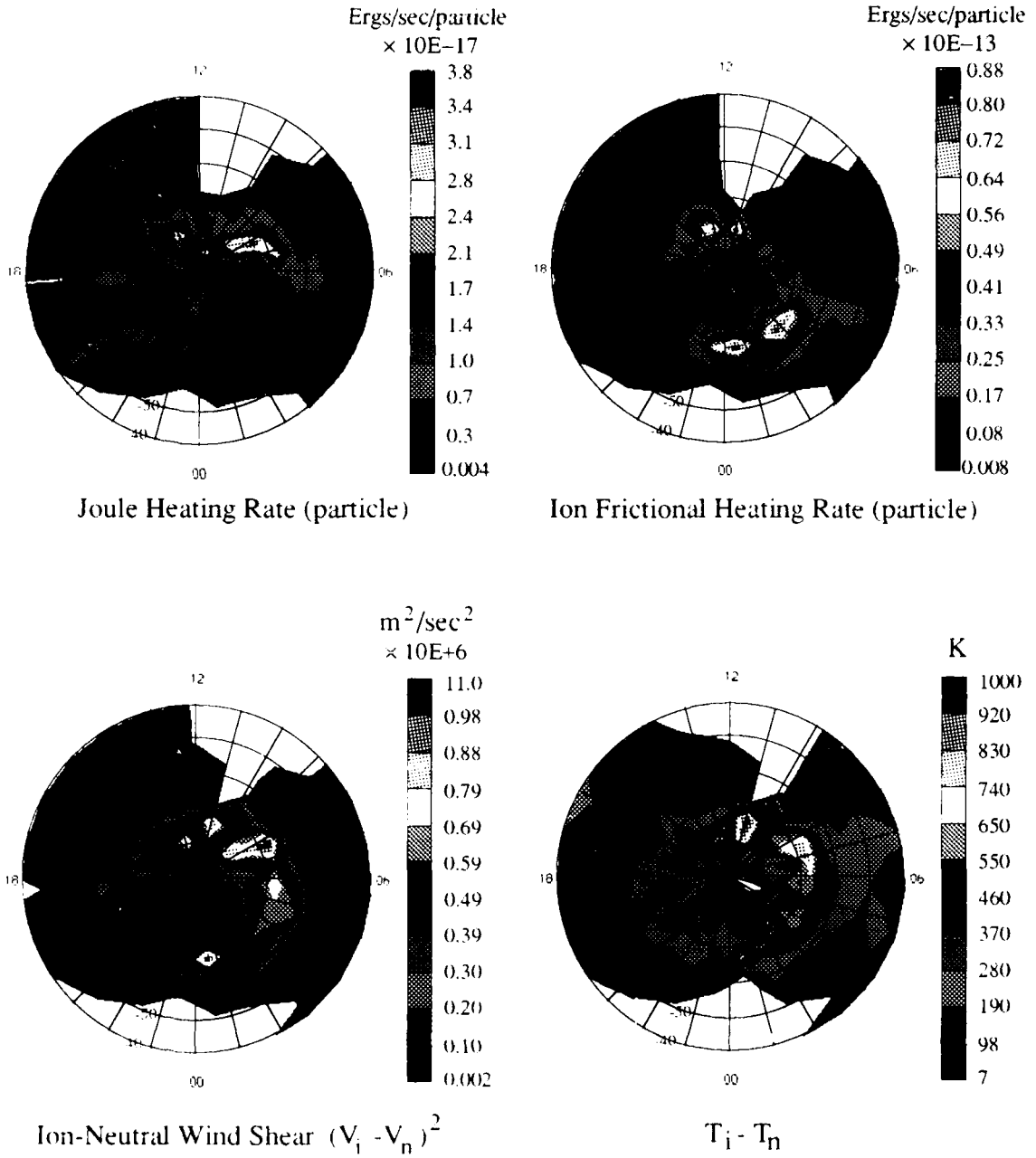

Figure 5.8 Polar plot of average Joule heating, ion frictional heating, ion-neutral wind shear and ion temperature enhancement for moderate Kp summertime conditions. Heating is stronger than for low Kp and the areas of strongest heating have expanded and shifted equatorwards with the expanding ion convection pattern.

Although some spreading in latitude and MLT is inevitable with the large bin size used for these plots, the shift appears real when compared to the ion convection patterns for moderate Kp and has been reported in similar treatments of globally averaged data from the AE-C satellite (Foster et al., 1983). Second, the spatial coverage of strongest heating and shear has expanded both in latitude and magnetic local time. In this case, the shear term most closely matches the ion temperature enhancement pattern suggesting the presence of a region of perturbed plasma within flux tubes convecting sunward along the dawn convection channel. This behavior suggests that a larger, more elongated source region of thermal upwelling fluxes exists for higher levels of Kp since the spatial extent of shear and heating patterns were smaller for the low Kp case. Finally, the magnitudes of shear, heating rates and temperature enhancement are greater for the moderate Kp case and show an appreciable difference from one bin to the next. This implies that, in the rest frame of the flux tube, a greater degree of heating variability may occur along the path of the convecting flux tube. As pointed out in the single orbit study, rapid changes in heating rates were associated with the strongest perturbations in upwelling fluxes. Based on the increased magnitudes and the extended spatial extent of ion frictional heating for the higher Kp case, it appears likely that source regions and the magnitudes of thermal upwellings should be greater for higher levels of geomagnetic activity.

An attempt was made to examine the same patterns and behavior for Kp > 5.7. Binning with this higher Kp criteria however, reduced the number of available orbits. Many of these orbits were sequential resulting in extended coverage of the same storm period. This further reduced the spatial coverage by limiting the measurements along a restricted MLT plane so that only portions of the overall pattern could be identified. Averages of each quantity were further affected by the number of data types required for the calculation. Heating averages were affected the most since the full complement of 9 instrument data sets were needed for each calculation. Despite the limited availability of data, some similarities in pattern and behavior are discernable. Intense frictional heating in the dusk convection channel corresponds with strong shear regions and elevated ion temperatures. These features have shifted equatorward with increased Kp and are larger in magnitude than averages for the previous cases. Lack of data and undersampling of the post midnight-dawn sector prevents analysis of the usually more intense dawn convection heating. The intense shears present on the dawn side however, suggest that a roughly annular heating pattern is probably present. These features indicate that even higher levels of transient heating and upwelling should be present during disturbed geomagnetic conditions.

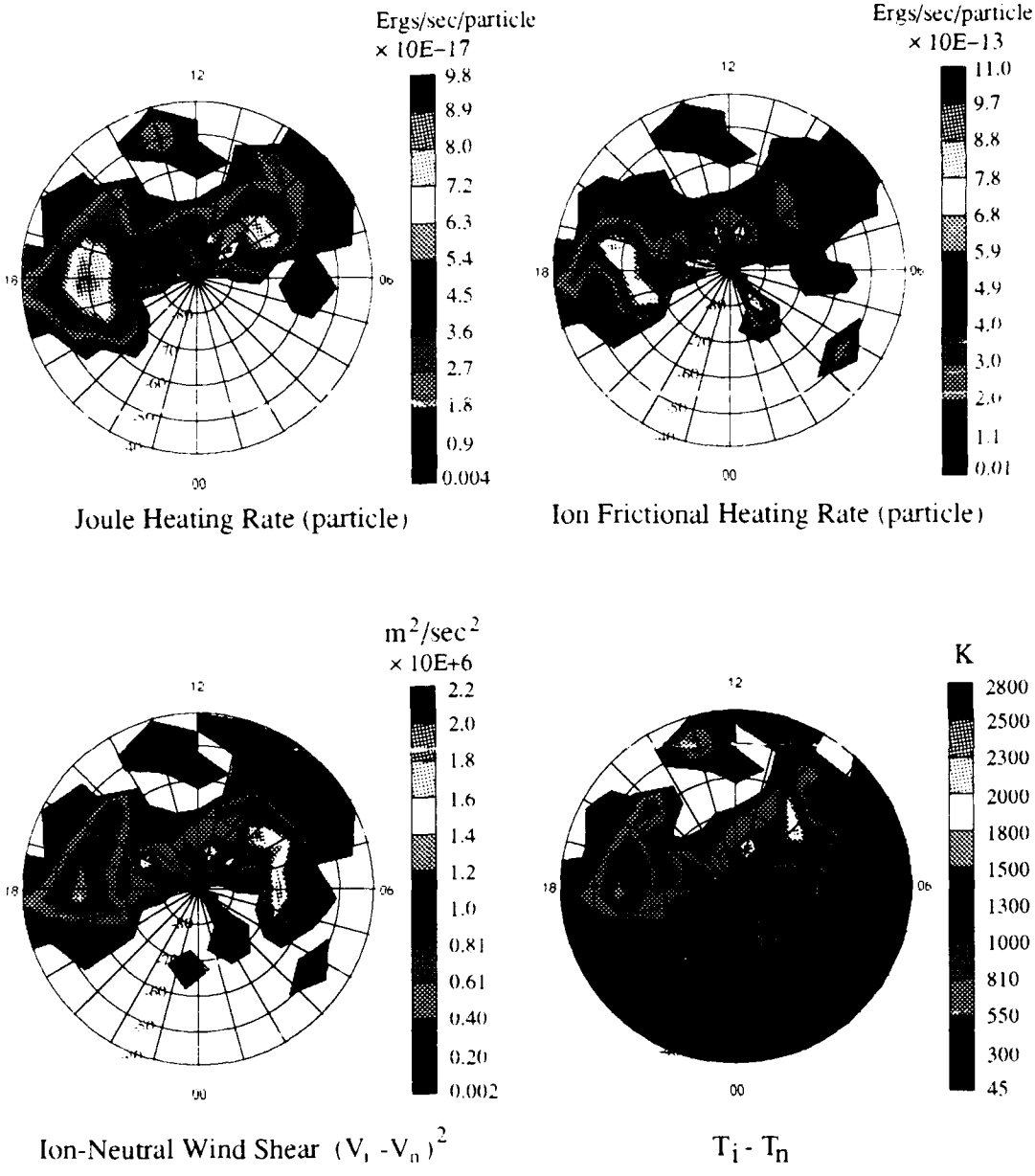

Figure 5.9 Polar plot of Joule heating, ion frictional heating, ion-neutral wind shear and ion temperature enhancement for high Kp summertime conditions. Limited data availability for Kp >5+ results in less MLT/latitude coverage however, further intensification of frictional heating and equatorward expansion of the heating locations is evident.

Similar patterns of ion frictional heating, ion-neutral wind shear, temperature enhancements and vertical flows were found for the wintertime cases. Additionally, similar behavior with increasing Kp was observed in the winter averages. While pattern comparisons provide a unique perspective on the global extent of frictional heating, this technique is limited when comparing features for different Kp or seasonal periods. Quantifying the patterns described above provides a more useful technique for ordering and examining the varying plasma responses to ion frictional heating.

Since the features and behavior of the plasma parameters in question are well ordered in geomagnetic latitude, it is possible to construct zonal (latitudinal) averages of these quantities to gain a better understanding of their Kp and seasonal dependence. This treatment implicitly assumes adequate MLT coverage so that the features present in localized MLT sectors will be represented. This assumption is generally good for the low and moderate Kp cases where a great many measurements are available, but is less valid for the high Kp case. The same data used in the global morphology plots are used to construct latitudinal averages based on the average value for each MLT bins within a 5 degree latitude circle. High latitude coverage is generally good so the averages are represented by many MLT bins. Averages at low latitudes (<55° invariant) were sometimes under-represented since only few bins were available. This does not substantially affect the validity of this technique since the features of interest area normally found above 55°, except during large geomagnetic disturbances. For the largest Kp case, heating and, to a lesser degree, shear calculations are limited to a few storm periods so that full MLT coverage is not possible. Additionally, the extremely high ion temperatures (20,000 K) recorded in several high Kp cases are probably non-Maxwellian. This condition would invalidate their use in the calculation of momentum transfer collision frequencies and results in an overestimation of the heating rates for high Kp conditions by up to one order of magnitude. For this reason, the high Kp case should be treated as a limited representation; actual values may be higher or lower than shown here.

Figure 5.10 is a summary plot showing averaged zonal quantities for the summer case. For frictional heating rates, there is a clear increase in heating magnitude for the higher Kp conditions and an equatorward shift in the location of maximum heating The prominent bifurcation in high Kp heating and peak near 60° is probably not real but results from undersampling in the 65°-85° latitude region and overestimated collision frequencies due to high ion temperatures near 60°. Comparison with the shear profile for the high Kp case supports this conclusion since corresponding features are not present and suggests a smoother and less pronounced peak near 60° should be expected. In fact, the shear term

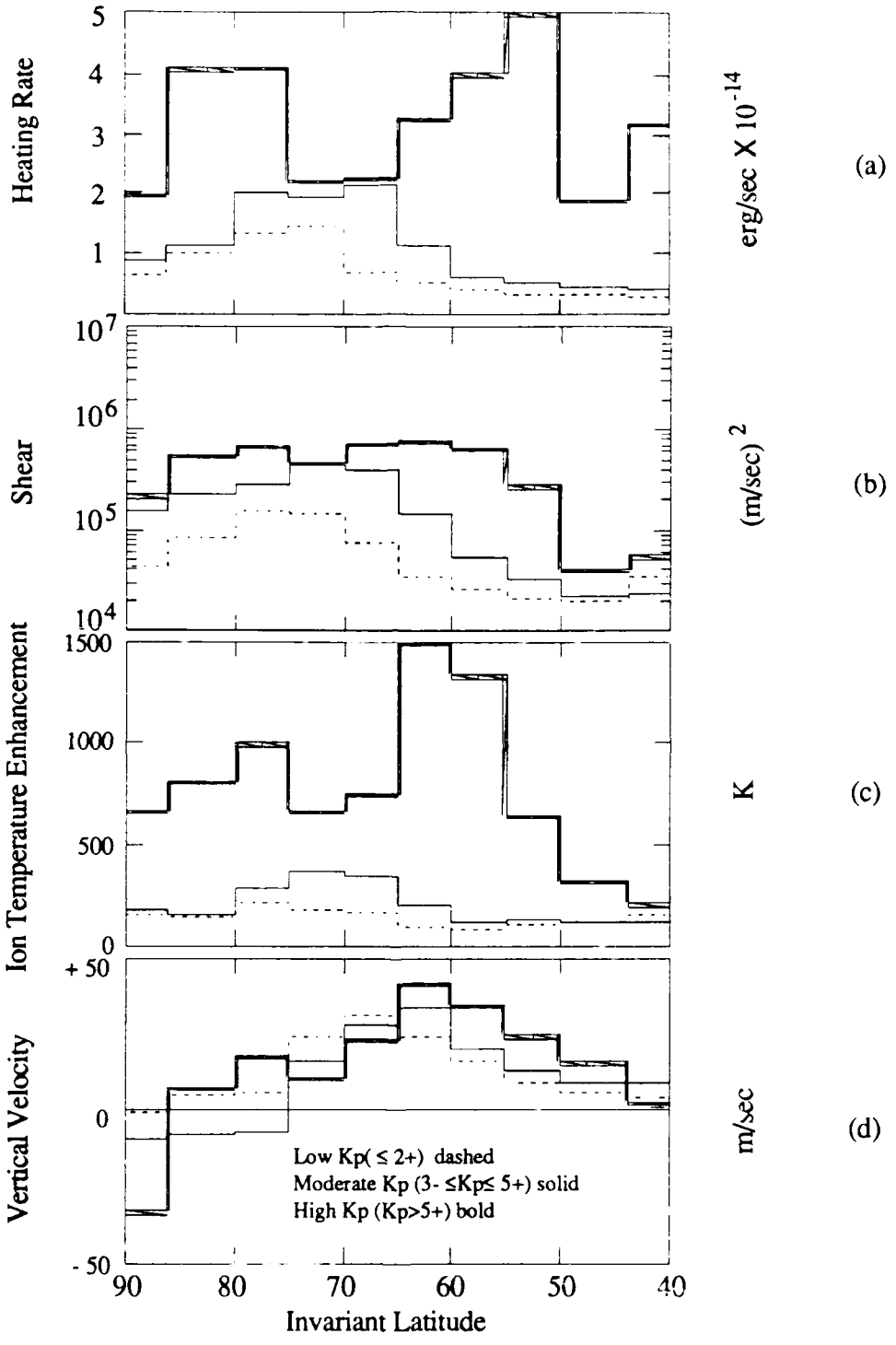

Figure 5.10 Zonally-averaged summertime F-region plasma characteristics for low, moderate and high Kp. Increases in magnitude and an equatorward shift in frictional heating maxima occur with increasing Kp. Shear, ion temperature enhancements and bulk vertical ion flows show similar behavior .

proves to be a very useful indicator of ion heating for this case since the MLT coverage was much greater for the shear averages (16 hours versus 10 hours of magnetic local time). The shear term is considerably larger for moderate Kp than for low Kp, with increases of 30%-50% present above 60° invariant. Associated heating rates are larger, resulting in greater ion temperature enhancements for the corresponding latitudes. The trend towards increasing magnitude and an equatorward shift of maxima in ion heating, ion-neutral wind shear, ion temperature enhancement with increasing Kp is also reflected in zonal averages of vertical ion winds. These profiles of vertical flows must be treated with some caution since the general pattern of upward dayside flows and nighttime subsidence are summed together when zonally-averaged. Nevertheless, the position of strongest upwelling closely follows heating maxima for both low and moderate Kp. Strong downward flows are apparent near the geomagnetic poles with the regions of dowflow expanding during increasing Kp. Large downward flows near the geomagnetic pole and into the midnight sector have been examined by Loranc (1989) and are associated with cooling of the plasma in flux tubes convecting away from a localized heat source. Presumably, the heat source is the dayside convection reversal region where shears and frictional heating are present. Subsequent anti-sunward convection of the flux tube accompanied by cooling and related scale height adjustments results in a net downward flow at highest geomagnetic latitudes. Taken together, these averages suggest that frictional heating, as well as ion upwelling, maximize at auroral latitudes and tend to move equatorward and intensify with increasing levels of geomagnetic activity. In contrast to this prominent summertime behavior, the frictional heating and heating response for the winter high-latitude region is less well-defined.

Figure 5.11 represents zonal wintertime averages for the same intervals of Kp. The major difference for the winter F-region is the lack of a strong EUV flux which tends to dominate summertime ionization and thermal processes. This leads to differences in the mass, momentum and energy budgets for the winter case that are readily seen in the zonal averages of plasma parameters. For instance, winter frictional heating for the low Kp case is significantly higher than the corresponding summertime rate. Higher levels of winter shear are also present suggesting a greater degree of momentum decoupling between ion and neutrals and therefore, more ion heating per particle for the wintertime, low Kp case. The same trend between summer and winter is present for moderate Kp but to a smaller degree. This behavior appears to be partially offset at higher levels of geomagnetic activity by greater heating that increases thermospheric densities and ion-neutral collisions, resulting in less variation between seasonal shear averages. Unlike volumetric heating rates which have been reported as a factor of two lower during winter (Foster et al., 1983),

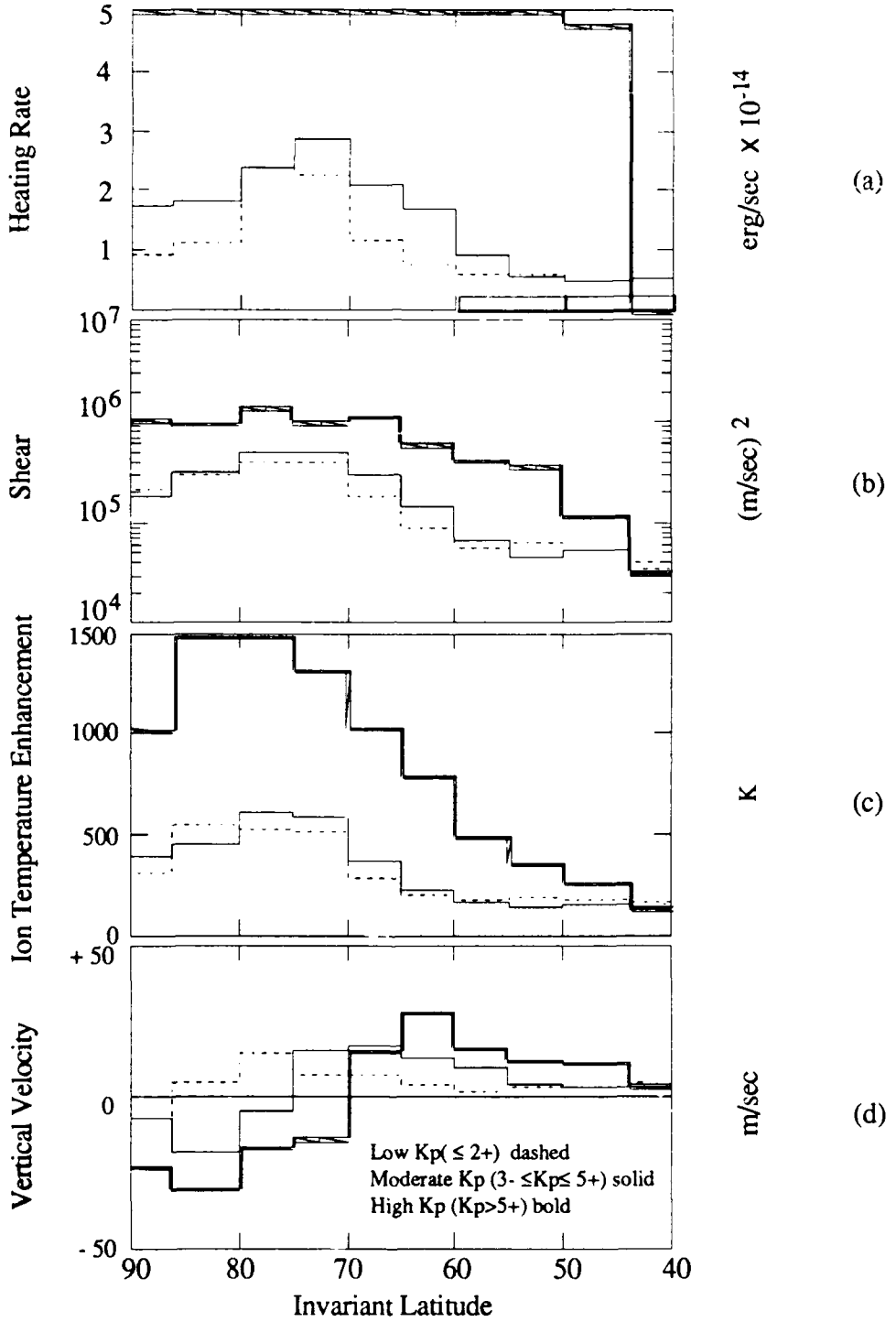

Figure 5.11 Zonally-averaged wintertime F-region plasma characteristics for low, moderate and high Kp. Winter heating rates and shears remain strong due to a decrease in ion density. Summertime trends for increasing magnitude and equatorwards shift of maxima with increasing Kp are present also.

frictional heating averages shown here are unbiased by seasonal density variations since they are normalized to ambient ion densities to obtain per particle rates. This treatment reflects the true amount of heating available to each plasma constituent. Winter ion temperature enhancements reflect the behavior in winter shear averages for increasing Kp and are significantly larger, by a factor of approximately two, than those during summer for both low and high Kp. This behavior is related to seasonal changes in both the ion and neutral temperatures and can be explained using equation 5.2. The ion temperature for the high latitude F-region can be obtained by equating the collisional coupling terms in equation 5.2 to obtain:

$$T_i = T_n\left(\frac{\upsilon_{in}}{\upsilon_{in}+2\upsilon_{ie}}\right)+T_e\left(\frac{\upsilon_{ie}}{\upsilon_{in}+2\upsilon_{ie}}\right)+\frac{\upsilon_{in}m_n}{3k\left(\upsilon_{in}+2\upsilon_{ie}\right)}\left(V_i-V_n\right)^2 \qquad (5.5)$$

Since ion-electron energy coupling is small at high latitudes, this equation simplifies to:

$$T_i = T_n+\frac{m_n}{3k}\left(V_i-V_n\right)^2 \qquad (5.6)$$

The equilibrium ion temperature is related to the neutral gas temperature and to a shear term related to ion frictional heating. The larger ion temperature enhancement during winter results from decreases in neutral temperatures due to reduced EUV fluxes and the higher wintertime shear mentioned earlier. In effect, the slightly higher shear during winter and a much lower heat capacity resulting from low ion densities helps to heat the ions even in the absence of EUV input. Vertical wind averages also show characteristic increases in strength and the equatorward shift in maximum location with increasing Kp, suggesting that the strength and location of frictional heating can significantly enhance the upward transport of plasma. Further analysis of these wind profiles beyond the obvious increase in magnitude and equatorward shift for higher Kp are limited due to the varying degrees of MLT coverage between seasons (hemispheres) and the zonal averaging treatment. The former influences the magnitude of the zonal averaged flows while the latter treatment lumps together the day-night patterns in upwelling and subsidence found across the high-latitude polar region.

Before concluding this section on DE-2 satellite observations of ion frictional heating and the accompanying ion upwelling it is appropriate to consider whether the energy supplied by friction is sufficient to permit the major ion, O^+, to escape. From the introductory chapter, about 9.99 eV or equivalently, about 1.6×10^{-11} ergs per particle are required for an oxygen ion initially at 300 km to overcome gravity. To supply this amount

of energy given a moderate heating rate of 5×10^{-14} erg/sec, one would have to "cook" the O^+ for just over 300 seconds without losing any energy to the neutral gas through collisions. In the frame of the convecting flux tube moving at about 1 km/sec, this places a minimum scale length on the heat source of 320 km. Slower convection velocities would not reduce this scale length since heating rates would decrease as V_i^2. Extended regions of uniform frictional heating are clearly not present in the satellite observations. Furthermore, if consideration is given to the vertical transport occurring within the flux tube which moves ions upwards and out of the maximum heating area, the spatial extent requirement would be even larger. Based on this argument, frictional heating does not appear to be the sole mechanism for ion outflows. Instead, it appears to be an important process for supplying large fluxes of thermal (but somewhat warmed) ions to higher altitudes where additional mechanisms can further energize them to escape velocities. This relationship can be seen by considering the similarities between ion frictional heating and patterns of higher altitude UFIs.

5.5 Comparison of Vertical Ion Flow Morphology to Ion Frictional Heating Derived From DE 2 Measurements

Previous studies of upflowing ions have identified the spatial morphology of both the low altitude bulk ion flows and the higher altitude ion outflow events. In this section the pattern of frictional heating and its behavior with geomagnetic and seasonal influences is related to the results of two studies to highlight the relationship between frictional heating and ion outflows.

Loranc (1989) examined the spatial behavior of low-altitude vertical drifts in more detail using a larger number of IDM measurements than those shown earlier. The larger data set permitted a comparison of occurrence probabilities of both day and night drifts for various levels of Kp in order to quantify the importance and location of vertical drift morphology. Some of his results are shown in Figure 5.12 for dayside drifts during moderate Kp (defined in his study as $3.0 < Kp < 5.7$). The velocity data in Figure 5.12 illustrate three effects. First, the maximum probabilities for all three velocity intervals (50-100, 100-250, 250-3000 km/sec) increase with higher Kp. Second, there is a marked shift of these outflows to lower invariant latitudes for higher Kp. Finally, the latitudinal extent of upward drift increases with increasing Kp. The latter two effects are prominent in both the spatial morphology plots (Figures 5.7 and 5.8) and the zonal averages of ion frictional heating shown here while the reported velocity increase with Kp is consistent with the increases in frictional heating rate. For the nightside region, Loranc analyzed data from the

20-24 MLT sector and found that low velocity downward drifts were observed more frequently that low-velocity upward flows across the polar cap. Downward flows at higher

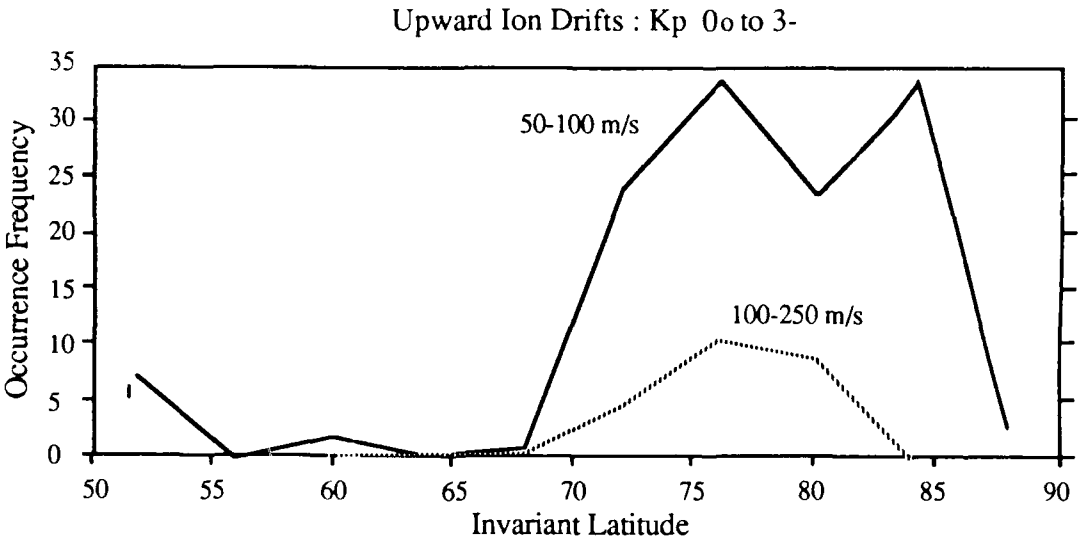

(a)

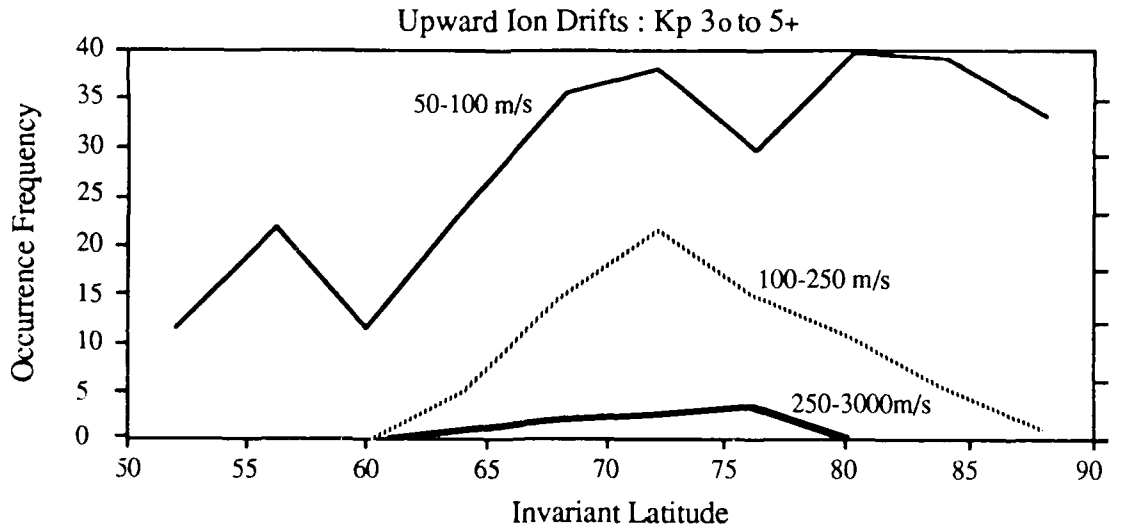

(b)

Figure 5.12 Occurrence frequency distributions for low altitude (200-400 km), daytime (8-12 MLT) ion drifts measured by the DE-2 IDM for low and moderate Kp. The probability of observing high winds increases with Kp and shifts equatorward similar to the behavior of strong frictional heating in Figures 5.7 and 5.8.

velocities were also present, and sometimes dominant over the polar cap. Comparing day and nightside profiles, Loranc found that regions of highest occurrence for strong upward flows were centered at higher invariant latitudes for the dayside. This day-night asymmetry

in invariant latitude can also be found in the frictional heating pattern in Figure 5.7 and 5.8 and is consistent with the latitudinal offset along the noon-midnight meridian of the auroral oval reported by a number of investigators (Holtzworth and Meng, 1975; Gussenhoven et al., 1983). From these observations of strong dayside and auroral upwelling with more frequent downward flows over the polar cap, a general three-dimensional picture begins to develop in which plasma is heated by friction, expands upward and then cools through collisions with the neutrals, resulting in downward flows. In the context of a convecting flux tube, the expansion appears to take place at or very near regions of strong ion-neutral wind shears such as the dawn convection channel or dayside convection reversal zones. This observation is based on the similarities in location of strong shear, heating and upwelling patterns. Likewise, horizontal transport out of the heating region through convection permits the plasma to cool and displaces the associated downward flows to regions downstream of the heat source. The response at higher altitudes is less clear since upflowing particles at this altitude are usually more energetic. However, their frequency of occurrence is strongest in the same regions in which frictional heating maximizes.

As mentioned earlier, Yau et al. (1984, 1985) have examined the occurrence frequency distribution of upflowing ionospheric ions in the auroral and polar regions between 8000 and 23,000 km using the Energetic Ion Composition Spectrometer (EICS) onboard DE-1. Their study identified both H^+ and O^+ UFI occurrence frequency (frequency of observing flux $>10^5$ cm^{-2} sec^{-1} sr^{-1}) behavior for different levels of Kp. Figure 5.13 is a polar plot of O^+ UFI occurrence frequency integrated over all altitudes above 8000 km and grouped as a function of MLT (6 hour bin size) and invariant latitude (4 degree bins). Figure 5.13b is a histogram plot of the same data only averaged over all MLT. These data cover the energy range of 0.01 to 1.0 keV/e and are qualitatively similar to the same plots of H^+. Particles with pitch angles of 100 to 180 (field aligned upward) degrees are plotted in (a), while trapped, conical and beam distributions are displayed in the histogram. Areas of highest probability are coincident with the auroral oval as one might expect. However, within the oval region, a striking correspondence exists between the MLTs of highest occurrence and regions of strongest frictional heating in Figures 5.7 and 5.8. Furthermore, the location of strong UFI occurrence frequency (>0.6) expands and shifts equatorward with increasing Kp just as frictional heating did. Finally, there is a clear asymmetry in the location of strong occurrence probability of UFIs which is also matched in the frictional heating magnitudes. The location, behavior and dawn-dusk asymmetries in UFI occurrence probabilities closely coincides with similar features in the ion frictional heating patterns suggesting that low altitude perpendicular heating is closely linked to the

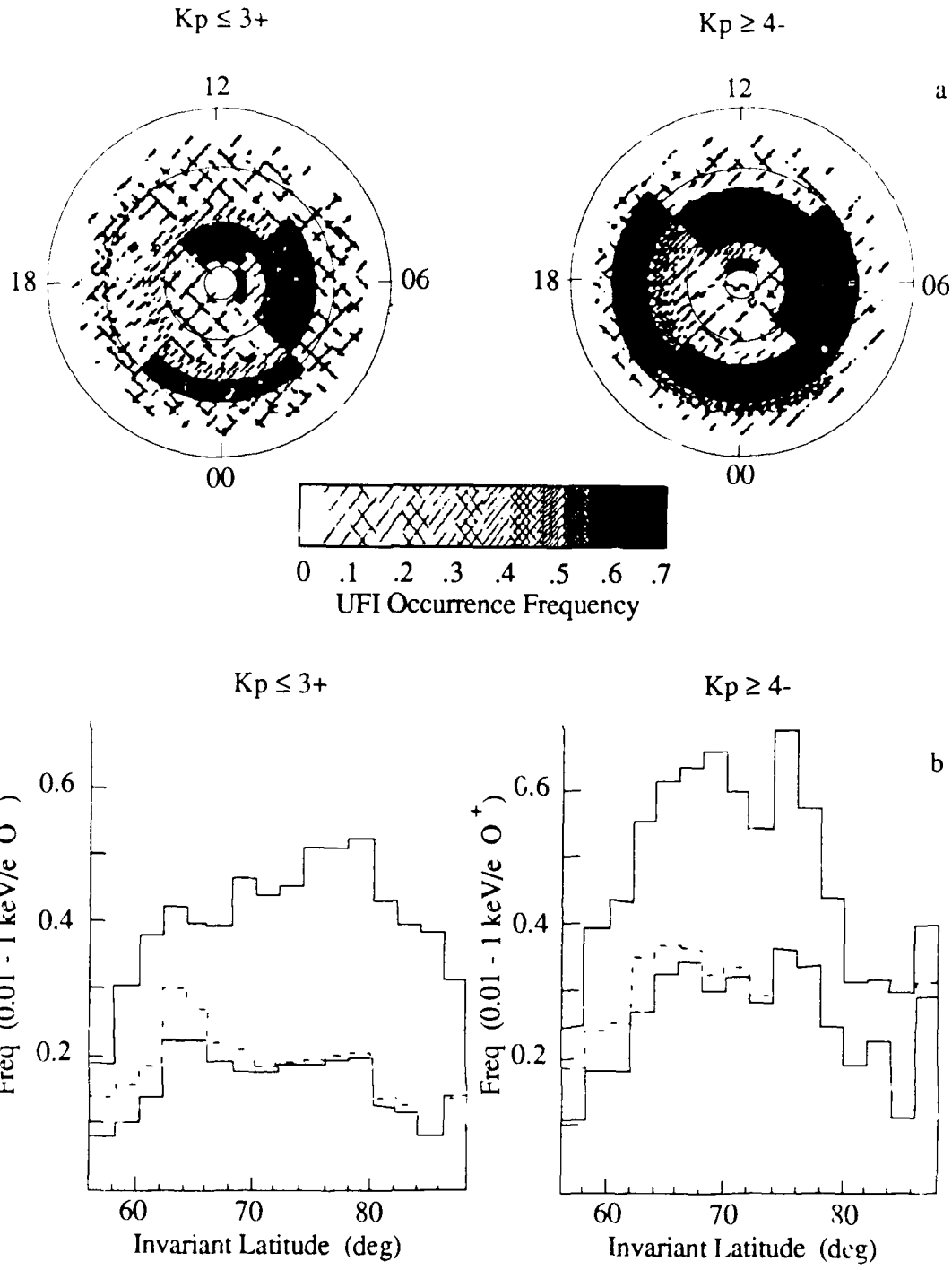

Figure 5.13 Invariant latitude-MLT distribution of occurrence frequency of upward flowing (pitch angle 100°-180°) O^+ for low and high Kp (a). For low KP, the dawn auroral oval segment has high occurrence frequencies. Regions of highest occurrence expand and move equatorward with increasing Kp. In (b), the invariant latitude distributuons show similar behavior. Area above hatching = 160°-180° events; area below hatching = 100°-160° events; hatched area = 80°-100° events. All data are for the energy range 0.01 - 1 keV/e.

observed, high-altitude outflows seen here. Yau et al (1985) also reported a strong magnetic activity dependence on the outflow magnitudes of O^+ fluxes but not H^+ fluxes. This behavior can serve as a further test of UFI dependence on ion frictional heating and will be addressed by modelling in a subsequent chapter. In summary, the similarities in frictional heating patterns and those of UFIs suggest that low-altitude frictional heating is a likely mechanism for moving thermal ions to higher altitudes where some may be further energized and escape.

5.6 Radar Observations of Ion Transport and Frictional Heating: A Case Study

Ground-based observations provide a unique and complimentary perspective on the relationship between ion heating and thermal ion upwelling seen in the satellite data. In particular, high-latitude radar systems have the advantage of sweeping through various ionospheric regions relatively slowly thus providing a greater opportunity to examine spatial and temporal variations that is not possible with a satellite system. The incoherent scatter radar technique described in Chapter 2 is particularly useful in relating heating and dynamical transport processes since direct measurements of plasma densities, temperatures and line-of-sight velocities can be combined with derived heating rates to examine density and velocity perturbations which constitute localized flux variations. Additionally, it is sometimes possible to relate past heating with high-altitude flux perturbations since the latter translate upwards at characteristic velocities. At the same time however, temporal and spatial averaging of the measured parameters is unavoidable, particularly at high altitudes where the plasma volume illuminated by the radar beam can be quite large. Despite this limitation, geophysically useful results can be obtained at the expense of small scale or rapidly fluctuating features by carefully choosing the measurement mode and data processing techniques.

Transmitting Frequency	1290 MHz (23cm)
Geographic Location	66.59° N 50.95° W
Invariant Latitude	64.69°
F-Region (350km) Inv Latitude	74.42° N
F-Region (350km) Declination	321.25°

Table 5.1 Site and operating parameters for the Sondrestrom incoherent scatter radar facility

The incoherent scatter radar facility located at Sondrestrom, Greenland and operated by SRI international, is ideally located for examining high latitude heating and dynamic topside processes since the site is located near 64.7° invariant latitude. Additional site and operating parameters are listed in Table 5.1. Based on the radar's ability to take measurements along the dawn auroral and dayside convection reversal region, a three day campaign was conducted to examine heating and ion upwelling within these regions.

The particular operating mode for this experiment was dictated by a need to examine the highest altitudes for thermal ion fluxes and the lower F-region to determine ion heating rates. A three position sequential scan was devised to include these requirements. One scan mode would look along the magnetic zenith and measure the overall Doppler shift of the returned spectra (or equivalently, the rate of change of phase in the autocorrelation function) to provide line-of-sight (LOS) ion drifts. Two additional scan modes would provide information needed for the heating rate. As discussed in the radar theory section of Chapter 2, the volumetric Joule heating rate can be expressed as

$$Q = \mathbf{J} \bullet \mathbf{E} = \sigma_p E'^2 = \sigma_p (\mathbf{E} + \mathbf{U} \times \mathbf{B})^2 \qquad (5.7)$$

where **U** is the neutral wind velocity and **E'** represents the electric field as seen in reference frame of the neutral wind. Equation 5.7 represents the Joule heating rate but by assuming the local heat exchange occurs between ion and neutral particles, one can scale this rate by 1/2 to obtain the local ion heating rate. Solutions to equation 5.7 require knowledge of the Pedersen conductivity and the imposed electric field. The conductivity is directly available from density measurements and modeled mobility coefficients. The electric field vector is constructed based on two scans looking in independent directions to obtain the north-south and east-west horizontal plasma drifts. Combined with a suitable (modeled) magnetic field vector, the zonal and meridional electric field components are obtained from the relationship:

$$\mathbf{E} = -\mathbf{V} \times \mathbf{B} \qquad (5.8)$$

where **V** represents the horizontal ion drift. This treatment implicitly assumes that spatial and temporal uniformity exists over the region sampled during the scan integration and thus, results in some loss of detail. To counteract this tendency, a combination of high elevation scans and short integration periods are normally used to minimize the errors introduced. With the derived electric field and conductivity terms, the heating rate for each altitude range can be calculated. Values are usually summed over several of the lowest gates (the actual number of gates used depends on the signal-to-noise (SNR) for each gate)

to obtain a height-integrated Joule heating rate (ergs cm^{-2} sec^{-1}). This quantity can be expressed as:

$$\overline{Q} = \overline{J} \bullet \overline{E} = \Sigma_P E'^2 = \Sigma_P (\mathbf{E} + \mathbf{U} \times \mathbf{B})^2 \qquad (5.9)$$

where Σ_P represents the height integrated Pederson conductivity. The value of the neutral wind is unknown so **U** is set to zero. This introduces a bias to the electric field term which is usually small, on the order of a few mV/m (de la Beaujardiere et al., 1984). Finally, a long pulse mode of 320 μs was adopted for maximum altitude coverage. This choice limits range resolution, but provides a stronger return signal from the highest gates so that measurements over 1000 km could be attempted. A three-position scan sequence was selected for this study so that both line of sight drifts and heating rates could be evaluated. Antenna node 1 provides the line-of-sight (LOS) ion velocity measurements nearly along the magnetic zenith by evaluating the shifted frequency spectrum of the returned radar signal from eight spectral range gates set at 197, 346, 496, 646, 796, 947, 1097 and 1247 km. F-region LOS velocities measured in the magnetic zenith at Sondrestrom are essentially the same as the field-aligned velocities. This relationship is shown schematically in Figure 5.14a. The angle between the radar beam and the local dip angle of the magnetic field will vary as a function of altitude due to the oblique pointing direction of the radar. This angle can be obtained from the difference between the antenna elevation angle and the local dip angle at each gate. For this study, the angle varies from about -0.2 degrees at 197 Km to about 0.6 degrees at 1247 km based on the IGRF(1985) magnetic field model. The difference between LOS and field aligned velocities maximizes in the highest gate and is given by the cosine of the angle. At 1247 km, this difference is less than 1%. The relationship between true vertical winds and field-aligned flows is also shown in Figure 5.14b. Due to the high geomagnetic location of the Sondrestrom radar facility, measurements of field-aligned flow are essentially the same as vertical. This relationship is given by:

$$V_Z = V_{||} \sin(I) \qquad (5.10)$$

where V_Z is the true vertical wind, $V_{||}$ the measured field-aligned velocity (LOS velocity) and I, the local dip angle. This difference also maximizes with altitude and amounts to less than 3% for the highest gate since the dip angle is very large (79.6°). A 5-minute integration period was used in this node to boost the SNR since low electron densities and extended range would limit signal strength in the uppermost gates. Antenna nodes 2 and 3 were off-zenith scans used to measure the electric field vector required in the heating

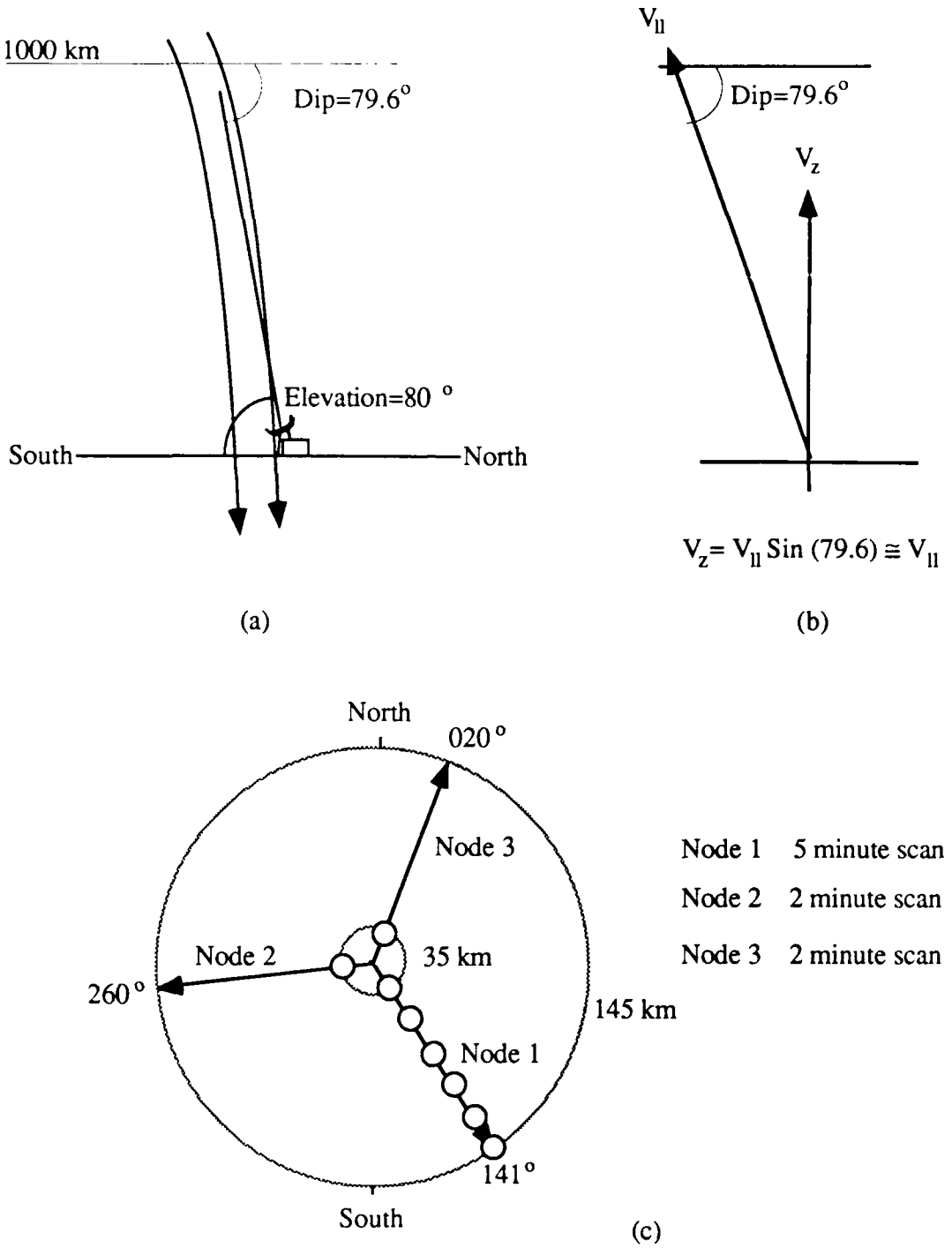

Figure 5.14 The relationship between line-of sight and field-aligned velocities is illustrated in (a). Field-aligned flows and true vertical flows are essentially the same as illustrated in (b) due to the very small angles when observing along the magnetic zenith. The scan sequence and areal coverage of heating and vertical velocity measurements is depicted in (c).

calculations. Based on the high electron densities and reduced range of these measurements, 2 minute scans were sufficient. Figure 5.14c summarizes the operating modes used in this study.

Observations presented here were collected during 3-5 November, 1989 between approximately 7-16 UT. This period corresponds to 5-14 MLT and represents the interval during which the radar moves through the morning convection channel and dayside convection reversal boundary. Since elevated heating rates are often found in both these regions based on DE-2 observations, collecting radar measurements throughout this MLT interval should permit a quantitative comparison of the dynamic plasma response to frictional heating.

Data collected during the three day period spanned a wide range of geophysical conditions. Day 307 was particularly disturbed with measured electric field strengths averaging 80 mV/m. Height-integrated Joule heating rates were also large with values between 10-15 ergs cm^{-2} sec^{-1} occurring throughout the 9 hour interval. Conditions were only moderately active on day 308, with electric field strengths and heating rates reduced by about 60% from the previous day. In contrast, day 309 was exceptionally quiet. Electric field strengths during the interval were less than 10 mV/m suggesting very low ion convection velocities. Corresponding heating rates were less than a few ergs cm^{-2} sec^{-1}. The F10.7 solar radio flux was very high for the three day period with values of 236, 226 and 219 SFUs for day 307, 308, and 309 respectively.

Vertical profiles of density and velocity were averaged and examined separately before combining them to correlate variations in vertical flux with the heating rate. The data were smoothed by averaging over a number of time intervals. Although data were collected to 1200 km, preliminary analysis revealed that velocity values above 800 km were subject to large error and frequently varied in sign and magnitude by hundreds of meters/sec from measurement to measurement. These data were considered unreliable and culled from the data set introducing an upper altitude limit of 950 km for the study. This reduced data set, consisting of 5-minute averages of densities, line of sight velocities and heating rates between 200 km and 950 km, were correlated for various time lags.

Figures 5.15 through 5.17 qualitatively illustrate the variations present in the averaged velocity, density and heating rates which occurred during each of the study days. The data presented here are 30-minute averages with velocity and density fields plotted as a function of altitude and universal time to highlight the range of variability present. The topmost surface plots represent the average LOS velocities and are clearly more variable than the density fields for each case. In general, subsidence (downward flow) was present in most of the two lowest gates as ions moved away from the peak production region.

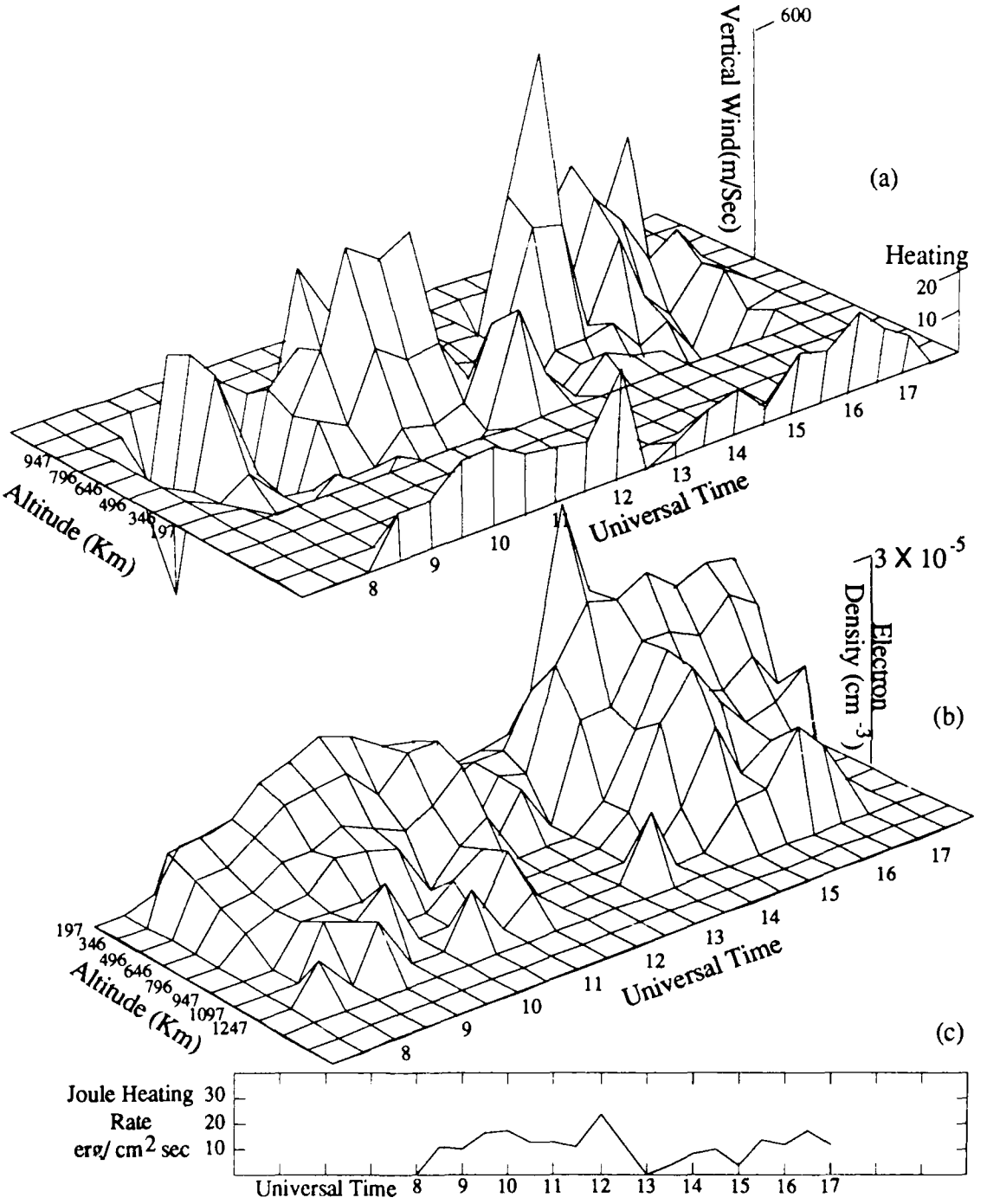

Figure 5.15 Summary plot of the ion vertical velocity (a), electron density (b) and height-integrated Joule heating rates (c) for day 89307. Density and velocity data are shown as surface plots to highlight altitude dependence and variations with heating rates. Density plot is reversed in altitude so that topside features can be seen. Data are for 30 minute averages.

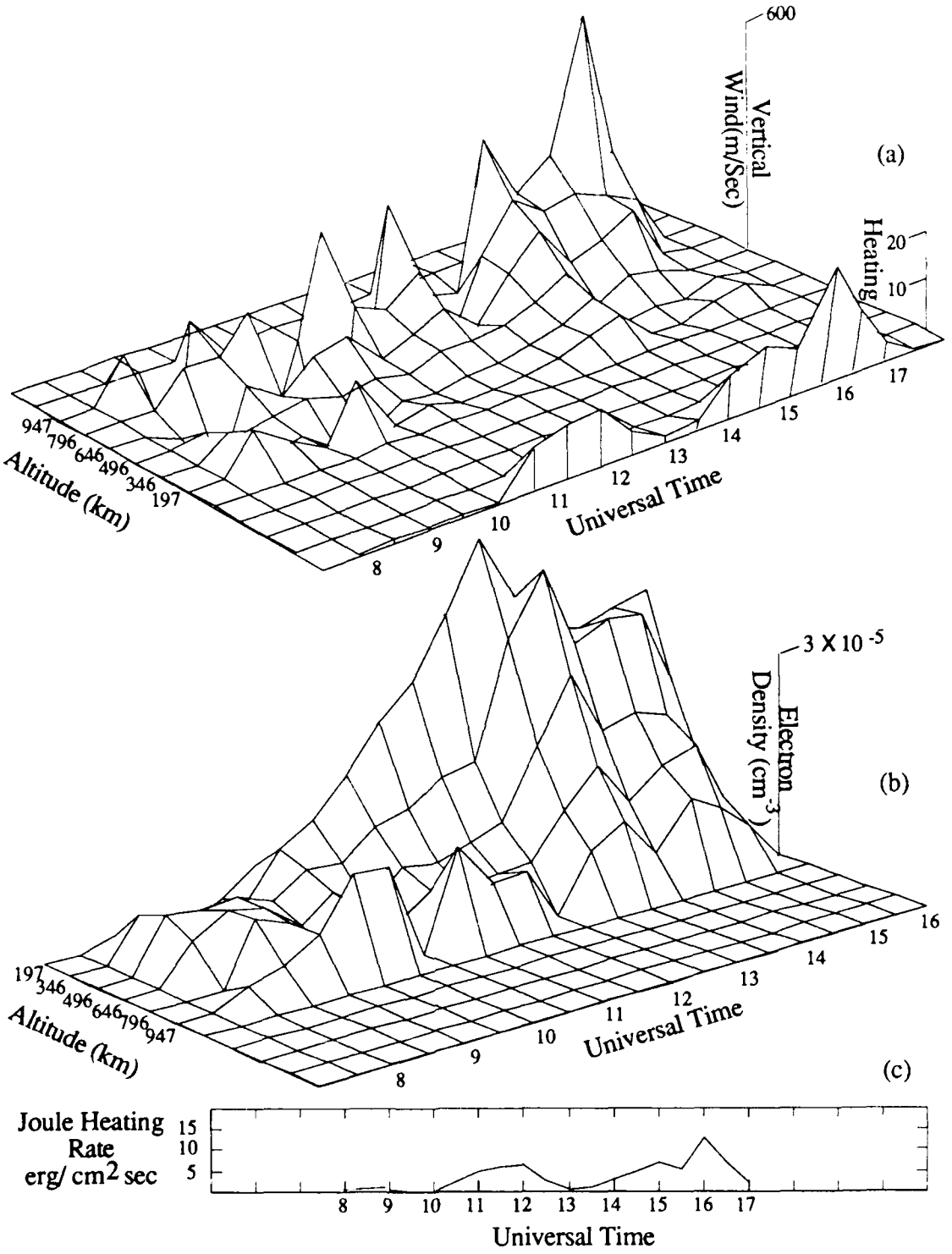

Figure 5.16 Summary plot of the ion vertical velocity (a), electron density (b) and height-integrated Joule heating rates (c) for day 89308. Format is the same as Figure 5.15. Heating rates are lower that the previous day and the velocity field shows less structure however, correspondence between heating enhancements and velocity increases are not clear.

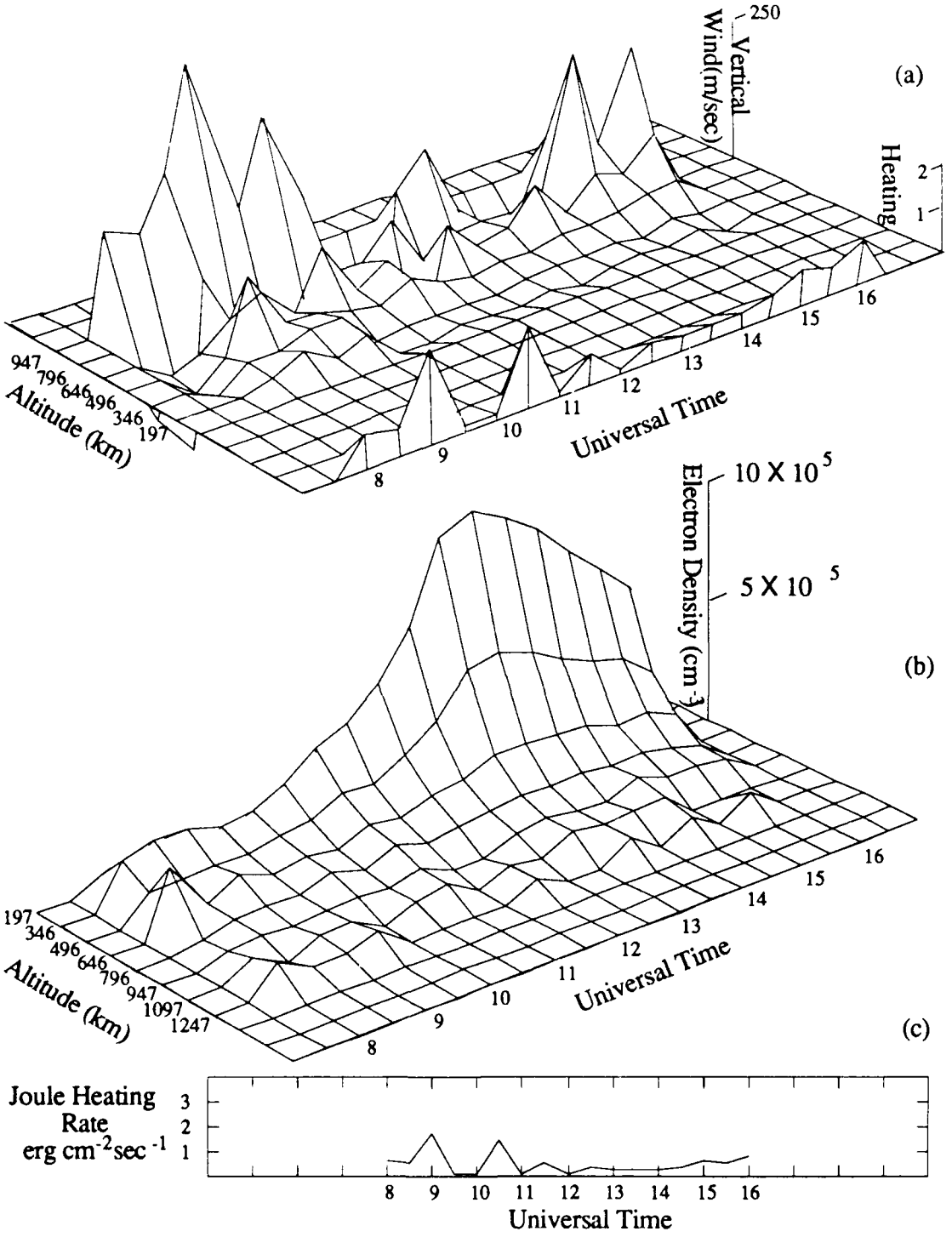

Figure 5.17 Summary plot of the ion vertical velocity (a), electron density (b) and height-integrated Joule heating rates (c) for day 89309. Format is the same as Figure 5.15. Heating rates are very low with the velocity profile and density fields showing less perturbed features.

At times, this flow sense was reversed and low-altitude upward flows could be related to a heating rate increase (Joule heating is plotted along the edge of the surface plot for comparison). However, there are a number of instances when no heating increases were observed where low-altitude upward flows were present. The general trend is for upward flow magnitudes to increase with height, although large downward flows were present especially during day 307 when auroral conditions were most disturbed. Upward flows of 300-500 km/sec were present between 800-950 km on day 307 in contrast to flows of 200-300 km/sec in the same altitude range during day 309. Heating rates for day 309 was also lower by approximately one order of magnitude. In comparing Joule heating enhancements to the vertical flow profiles, there are a number of instances where close correspondence between the two are present. For instance, on day 309, a double peaked heating rate profile between 15 and 16 UT corresponds to enhanced ion flows at the same times. Likewise, large departures in upward ion flows on day 308 between 14 and 15 UT are matched with large heating rates at the same times. Unfortunately, there are a number of cases where heating is enhanced, without strong upflows, or periods with enhanced upflows, but relatively weak heating. The persistence of a great deal of structure in these velocity fields for three days in which heating changes significantly would indicate that other processes besides frictional heating are influencing the vertical winds. Topside density profiles for the three day period show similar behavior in that the density field for day 307 is considerably more structured than for the quiet day (309). For the latter case, the undisturbed diurnal pattern is the dominant feature, with a narrow, well-defined F-region peak and a smoothly increasing density ledge as the radar moves into the local noon sector. Considerably more structure is present in the density fields of the disturbed days. However, in comparing the velocity fields the relative percent variations are far lower for day 309.

Correlations between Joule heating and ion density, vertical velocity and upwelling fluxes were computed for different averages and varying lags between quantities. Diurnal increases in density were removed by subtracting quiet day curve values for each time interval based on the International Reference Ionosphere model (IRI) so that true density variations were considered irrespective of the length of the average. In general, correlations with heating rates were poor on day 307 due to the highly perturbed velocity and density fields. Correlations for day 309 were poor also. Although this day was quiet and the velocity and density fields were less-structured, heating rates were exceptionally low and unchanging. Therefore, transients in heating rates and therefore plasma responses appear to be lacking. Day 308 represented a compromise between these extremes, with sufficient heating variability and better definition in the velocity fields. Figure 5.18

illustrates some of the correlations for each altitude for day 308. Highest correlations were obtained for zero lag correlations suggesting that the observed changes were coincident within the limits of our minimum time resolution of 10 minutes for this day. Density correlations near -0.5 at each altitude were low but statistically significant at the 90 % level. Positive lags, in which the heating rate was retarded in time relative to the averaged density resulted in slight improvements in correlation which were seen at higher altitudes as lags and averages increased from 10 minutes to one hours suggesting that the heating-induced density perturbation was moving up the flux tube. This behavior is difficult to fully test however, since upstream heating rates are assumed to be equal to those measured in the local volume element. The DE-2 data suggests that the assumption of spatial uniformity in heating is not necessarily valid beyond distances of few 10's of km. In contrast to the density behavior, vertical flow correlations were weaker and showed no consistent pattern in altitude at any lag for short term averages as shown in Figure 5.18b. When the velocities were averaged over longer periods (beyond 60 minutes) a significant positive correlation appears, but only below 500 km. When fluxes were computed and correlated with heating rates, the results were similar to the velocity correlations showing only weak correlations with marginal significance (Figure 5.18c). It appears that the weak correlations between velocity and heating tend to dominate the flux correlations. The results of longer-term averaging support this conclusion since significant positive correlations appear when fluxes are averaged over 60 minutes (figure 5.16d), just as they did for velocity averages alone. The correlations between heating and vertical fluxes therefore appear somewhat limited in this study due to the high variability in the measured LOS velocities. Based on these results, several influences were identified which might weaken or otherwise influence these correlations.

In examining the data collection and analysis procedures used in this study, several factors could contribute to weaken the correlation with fluxes. Initially, other forms of heat input such as precipitating particles or field-aligned currents were suspected. These additional heat sources are almost certainly present in the auroral regions examined however their effects should be spatially confined while the correlations showed no improvements when averaged over limited MLT sectors of 2-4 hours. For the same reason, neutral wind induced flows were ruled out since this effect would be confined to a localized region near the local magnetic noon meridian. A component of $\mathbf{E}\times\mathbf{B}$ drift in the vertical could enhance upward flows without heating however such an effect cannot explain the strong velocity gradients apparent in Figures 5.15 through 5.17 and limited to the noon and midnight sectors. On the other hand, the assumption of spatial homogeneity in collecting the measurements effects the data over all MLT and can weaken the flux-heating

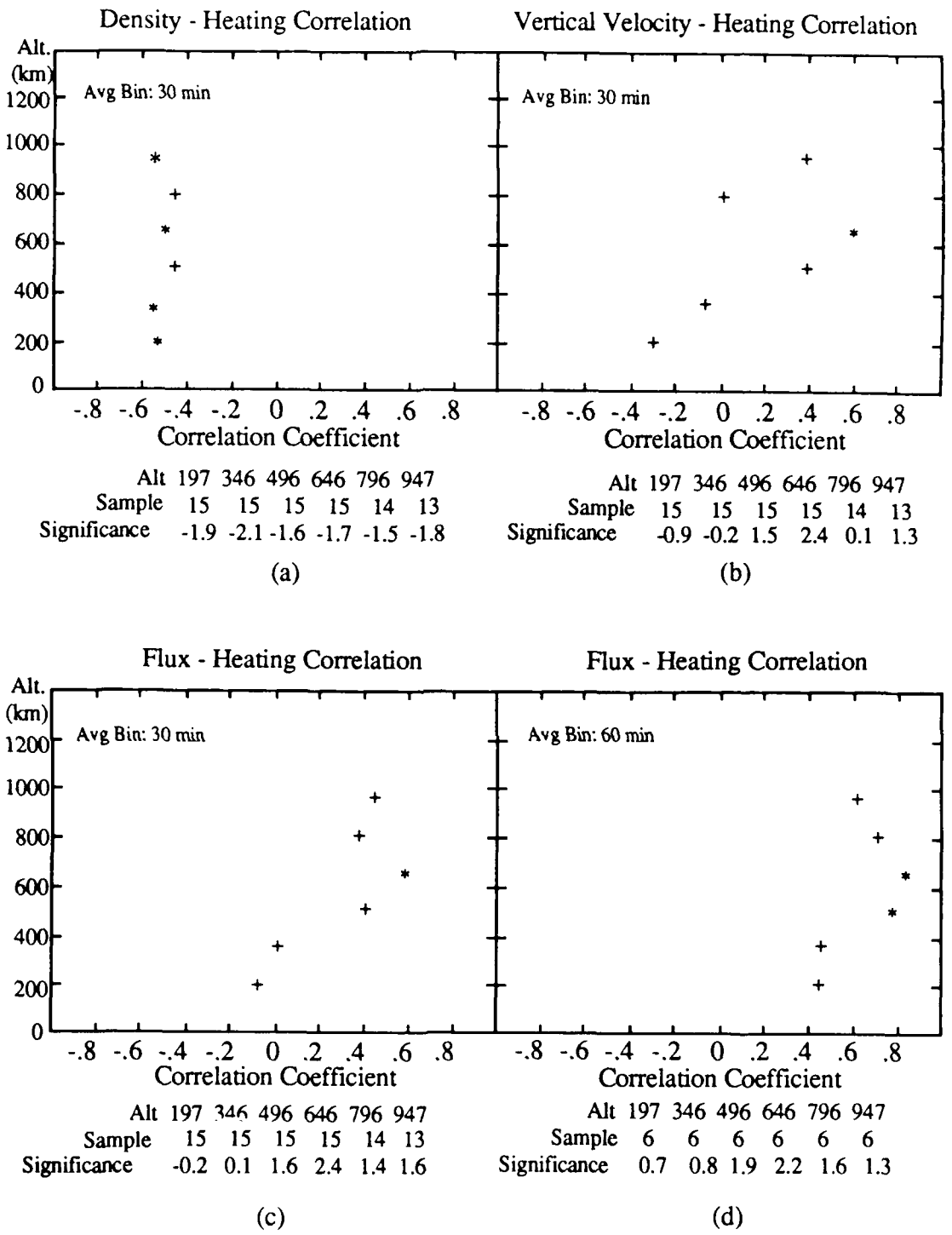

Figure 5.18 Correlations between heating rates and density variations (a), vertical velocities (b) and fluxes (c and d) as a function of altitude for day 89308. All data represent 30 minute averages except for (d) in which 60 minute averages were used. Asterisks represent significance at the 90% level.

correlations in two manners. First, the extended altitude range of nearly 1000 km introduces a horizontal separation in altitude gates of about 145 km based on the LOS scan elevation of 80 degrees (Figure 5.14c). This results in vertical velocity measurements which no longer represent a limited volume space. Instead, the velocities and densities at each altitude gate are more representative of different flux tube volumes, each with its own heating history. Second, the two scans used to make electric field component measurements are made at geographically separate locations from each other and from the zenith observations. The effect is also shown in Figure 5.14c. Assuming the bulk of the height-integrated heating comes from the lowest altitude gate near 200 km, the electric field measurements are made over an effective distance of 70 km. The assumed spatial uniformity may result in an overestimate or underestimate depending on the location of convection channels and convection reversal boundaries. Since the two error sources are independent and cumulative they can be considered together. Taking the larger of the radial distances to be 145 km (based on the horizontal displacement of the upper gate), the effective area over which separate measurements are combined is 70 km × 145 km or about 10,150 km^2. This represents an area several times larger than any suggested by the scale sizes of heating enhancements seen in the satellite data. The strong density correlations in Figure 5.18 probably occur because heating-induced density variations are longer lived and spread across a greater area. Therefore, these variations correspond better to the spatially averaged heating rate. The same effect would reduce velocity-heating correlations since the heating calculation averages out important, transient features while the LOS velocities are highly variable and can only be smoothed by long temporal averages. One final effect which could explain the high degree of variability in the velocity fields involves assumptions in processing the data. LOS drift velocities are computed from the Sondrestrom data by examining the complex autocorrelation function. A uniform plasma drift, in which all ion species drift together, results in phase shift of the ACF which is proportional to the lag (see Chapter 2). This relationship can be expressed as (Vickery, 1980):

$$p(\tau) = p_o(\tau)\exp\left(j\mathbf{k} \bullet \mathbf{V}_d t\right) \tag{5.11}$$

where $p(\tau)$ and $p_o(\tau)$ represent the shifted and unshifted ACF spectrum, τ the ACF lag and $\mathbf{k} \bullet \mathbf{V}_d$ is the drift component along the radar wave vector. The ratio of the real to imaginary part of the ACF spectrum represents the phase and it is the rate of change of the phase (i.e., the slope) which must be fitted to obtain the drift velocity.

$$\phi = \left(\frac{p_i}{p_r}\right) = \tan\left(\mathbf{k} \bullet \mathbf{V}_d t\right) \qquad (5.12)$$

The argument of the tangent is usually small for ionospheric velocities, so the ratio is nearly linear in lag time and the slope is proportional to the drift velocity. When several species are present with different drift velocities, the returned spectrum is no longer symmetric so the ratio will not be linear with lag. Fitting for the nonlinear slope is subject to greater error resulting in LOS drift velocities which may not be representative of either ion species. Differential ion velocities and even ion species counterstreaming frequently occur at auroral latitudes due to unequal heating. The differential velocities can be larger at greater altitudes where collisional coupling is weaker and may explain some of the roughness in the velocity measurements, especially in the highest gates. Together, the assumptions of spatial uniformity and equal ion flow velocities appear to influence the bulk velocity measurements thus reducing the correlation between heating and upwelling ion fluxes. To test this conclusion further, a one dimensional, time-dependent hydrodynamic model (the Polar Wind model described in Chapter 2) was used with variable frictional heating rates applied.

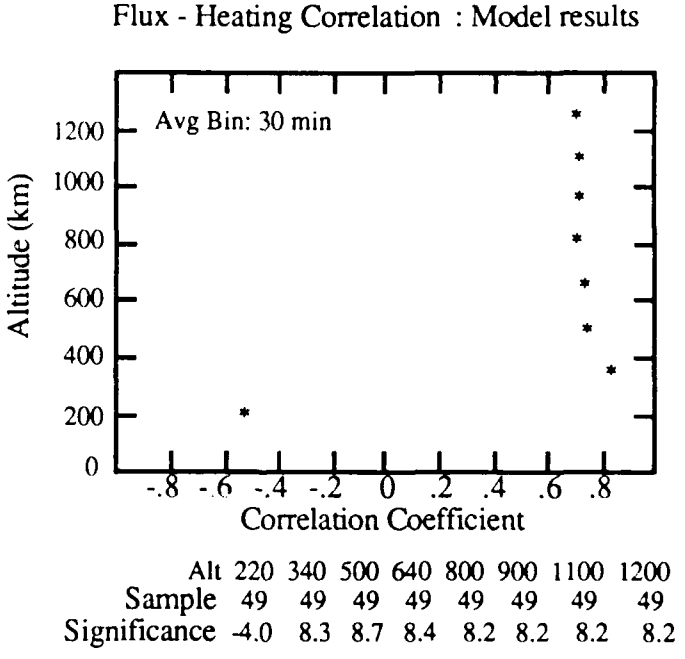

Figure 5.19 Correlations between heating rates and modeled fluxes for the case where only frictional heating was driving the changes in density and velocity fields. Results here suggest the observed behavior of density and velocity variations in the radar data is the result of a number of influences besides ion frictional heating.

The heating rates were derived from wind, density and temperature fields from the NCAR-TIGCM model run using a code which calculates the motion of a flux tube passing along the dawn convection channel. These variable heating rates were supplied to the set of hydrodynamic calculations as a time-dependent lower boundary condition to obtain solutions of diffusive vertical ion flows, number densities and fluxes. Correlations between heating and diffusive fluxes were made at the same approximate altitudes as the radar data and are presented in Figure 5.19.

Since the time-dependent model solutions in this case depend only on the varying heating heat rates applied, a much stronger relationship between heating and ion upwellings is present in the correlations. Additionally, the velocities here are unaffected by the bulk, mass-averaged velocities so prominent in the radar and satellite observations. In this case the model provides a 'best case' condition, since the correlations represent the true (unmodified by bulk drift) diffusive response of the plasma to heating transients. Lack of even higher correlations for this case suggest some degree of inertia to the plasma once it is set in motion by heating or cooling processes. This feature was first reported by Whitteker, and is examined more fully in the Chapter on modeling transient upwelling behavior.

5.7 Summary

In the present chapter, ion frictional heating and its effects on the low-altitude plasma environment were examined and related to high altitude upward flowing ions. Frictional heating is a natural consequence ionosphere/thermosphere interaction resulting in the conversion of bulk flow energy into thermal energy (heat). Frictional heating rates tend to be highly variable in time and space with both the ion convection pattern and the inertial character of the neutral winds determining where ion-neutral velocity differences will occur. Quasi-permanent regions of enhanced frictional heating are found on either side of the dayside convection throat as a result of rotational reversals in the ion flow and predominantly sunward neutral winds. Additional areas of enhanced heating are found in the convection channels with the dawn side exhibiting the higher heating than the dusk side. Heating in these areas tends to be more confined spatially (latitudinally) but with the same magnitudes as the dayside heating. Heating magnitudes were found to increase with larger Kp as the relative ion-neutral wind difference increased. At the same time, the area(s) of strongest heating tended to expand and shift equatorwards. The energy supplied to O^+ ions in the F-region was sufficient to generate large transient upwellings of thermal ions with hundred-fold increases in flux possible however, heating rates do not appear capable of providing the total energy required to permit the heated O^+ to escape based on a

simple treatment of the energy gained during convection through a region of strong frictional heating. In fact, two competing effects are present in the flux tube when frictional heating occurs. First, the heating can temporarily increase the scale height of the major ion resulting in increased ion densities. At the same time, neutral heating increases the concentration of neutral molecular species leading to increased ion loss through ion-atom interchange and dissociative recombination. The dominant process varies depending on altitude with recombination favored below the F-region peak and transport processes important above. These factors appear to control the density response to frictional heating within the flux tube. The low-altitude vertical velocity field also responds to heating and cooling processes resulting in locations of preferred upward and downward flow which are defined by the location and horizontal extent of the heating region in addition to convective transport. Finally, the magnitudes and locations of ion frictional heating were examined for low and moderate levels of geomagnetic activity and were found to exhibit the same behavior as the UFI occurrence frequency measured by EICS on DE-1.

In answer to the original questions posed at the beginning of this chapter, a number of heating induced changes in the plasma and neutral gas have been identified which can modify the source characteristics of upward flowing ions. Density, temperature and scale heights of the heated ion gas is substantially modified resulting in bulk upward motions. Loss rates are also increased as the composition of the neutral gas changes in favor of molecular species. Clear patterns of more intense heating are found for higher levels of Kp and an equatorward shift in heating locations are also observed. These behaviors are also found in the higher altitude UFIs with regions of strongest heating matching highest UFI occurrence frequency. While frictional heating appears to be an important factor in supporting large fluxes of heavy UFI, it does not appear to act alone based on the energy required for escape by O^+. Instead, it appears that large fluxes of O^+ are driven upward in the flux tube by frictional heating. Some of the population has sufficient energy to escape but most, if not subjected to additional energization, will cool and flow downward at some location.downstream of the heat source. For this reason, the entire process of heating, upward transport cooling and convection away from the heating region should be best considered in a time-dependent, three-dimensional framework. Accurate modelling of any given event thus becomes a formidable task since a great number of variable factors must be adequately specified.

CHAPTER 6

CONCLUSIONS AND REMARKS

Observations of terrestrial ions in almost all areas of the magnetosphere have generated considerable interest into the potential source regions, source strengths and transport processes responsible for distributing these ions throughout the near-Earth environment. The high-latitude regions have received a great deal of investigative emphasis in this respect because thermal and heated terrestrial ion populations are often observed flowing along open or auroral field lines. The superposition of a cold, thermal population, traditionally known as the "polar wind" and heavy ion upwellings, consisting chiefly of O^+, indicates that the topside ionosphere is one major source and, at the same time, suggests that topside processes and thermosphere-ionosphere interactions are considerably more complex than originally considered.

The research described in this thesis focused on evaluating the processes and influences responsible for modulating these terrestrial ion flows. In particular, emphasis was placed on identifying how thermosphere-ionosphere coupling affects the source strength, composition and location of both the light ion and heavy ion component of thermal ion upwelling. This aspect of research has particular relevance to the broader issue of terrestrial ion outflows in that it quantifies the magnitude of ion upflows and identifies the processes responsible for their variable nature. Knowledge of the source strength and character is vital to our understanding of the influence and importance of the terrestrial plasma within the magnetosphere.

The investigative contributions described in the preceding Chapters have examined thermal ion transport from both the theoretical and experimental perspective. Towards this end, the following research objectives were central to this contribution :

(1) To quantify the magnitudes and compositional variability of steady-state polar wind flows under various solar and geophysical conditions.

(2) To identify the role of low-altitude ion frictional heating in transient heavy ion (O^+) upwellings.

(3) To relate the location, magnitudes and characteristics of low altitude transient upwelling to high-altitude observations of field-aligned ion outflows.

The use of both theoretical modeling and observations from in situ, as well as ground-based, instruments provided complimentary perspectives of the processes which influence ion upwelling intensity and transient behavior. With this insight, each of the stated objectives were fulfilled.

The central theoretical focus involved the use of a time-dependent hydrodynamic model developed by Gombosi et al. (1985). However, several modifications to the model were required to permit accurate specification of thermospheric and ionospheric processes which define the magnitudes of the ion upwelling. First, a routine to calculate height-dependent neutral oxygen photoionization frequency was developed to replace the fixed lower boundary value since significant attenuation of EUV radiation can occur above 200 km for high solar zenith angle situations. This routine scales the solar EUV spectrum ($\lambda <$ 911Å) based on the F10.7 solar radio flux and uses an MSIS-86 neutral atmosphere in conjunction with a Chapman function to determine attenuation characteristics above any given location. Additionally, for large optical depths ($1 < \tau < 9$) the importance of photoelectron impact ionization can approach that of direct EUV. Enhancements to the primary ionization due to photoelectrons were added using the analytical formulation developed by Richards and Torr (1988). With these revisions, photoionization frequencies can be determined self-consistently since the same static neutral atmosphere, which acts through collisions to impede ion transport, is also used to determine the source strength for production of the major ion, O^+. To model wintertime cases, analytic expressions which describe ionization rates based on an altitude-dependent energy flux were adapted and included in the model to account for ionization due to electron precipitation. This modification permitted the full range of impact ionization types to be considered, including polar rain, cusp and auroral electron precipitation. These modifications extend the utility of the original model to any local time, season, or solar condition. When compared to solar and seasonal distributions from satellite measurements (Chapter 3), steady-state density profiles of the major and minor ion species were found to be in close agreement, indicating that the modeled production, loss and transport processes are properly accounted for.

Under the assumption of steady-state, the model was used to derive solutions for O^+ and H^+ upwellings for a number of solar-geophysical conditions for a location at 80°

invariant latitude at 12 MLT (17 UT). Over long time scales like the 11-year solar cycle, H^+ fluxes were found to be invariant with flux-limited magnitudes (at 4000 km) of about 4×10^7 cm^{-2} sec^{-1}; however, O^+ flows increased by one order of magnitude from a solar minimum low of 8×10^6 cm^{-2} sec^{-1} to 9×10^7 cm^{-2} sec^{-1} at solar maximum. These results are the first to suggest that a low speed ambipolar flow of O^+ exists which exceeds the H^+ fluxes during solar maximum. The O^+ flows persist above the region of maximum H^+ charge exchange with field-aligned velocities of a few cm/sec, but with very large number densities so that fluxes in excess of charge-exchange requirements can occur. Different solar cycle behaviors in H^+ and O^+ fluxes were found to arise from structural changes in the thermospheric composition and scale heights during the increased EUV fluxes at solar maximum. Greater O^+ fluxes occur due to increased O^+ number densities which resulted from higher photoproduction rates, reduced molecular loss and local increases in neutral oxygen number densities. Opposing changes in the H^+ density and field-aligned flow velocity for the two solar cycle extremes produced near constant fluxes. The distinctive flux behaviors for both H^+ and O^+ produced a marked shift towards O^+-enriched upwellings at solar maximum and match the behavior of observed ion outflows of both energetic O^+ and H^+. Similar solar cycle behavior has also been found in both the keV O^+ and H^+ plasma sheet densities measured near geosynchronous altitudes (6.6 Re).

A unique aspect of the steady-state model solutions was the low-speed ambipolar flow by the major ion, O^+. Most models treat O^+ as a stationary background gas. This work has shown that O^+ executes an upward-directed ambipolar flow at very low speeds (few cm/s), but is capable of supporting very high fluxes due to the large O^+ number densities found throughout the high-latitude topside ionosphere. To test the sensitivity of modeled density distributions to O^+ flow velocity, parametric variations in the low-speed flow were made and the resulting steady-state density profile for O^+ compared to satellite measurements. As the flow speed was reduced towards the diffusive limit of $\mathbf{u}=0$, loss by transport diminished so that densities increased everywhere. The resulting density profile for the major ion in summertime was clearly in excess of observed distributions and provides evidence that O^+ has a net upward flux which acts to reduce the topside scale height for this non-stationary ion.

Seasonal behaviors were also considered in order to evaluate the role of ionization sources. For summer, the dominant and strong influence of solar EUV provides smoothly varying fluxes of H^+ and O^+ across all latitudes and local times of the polar regions. For winter, only a small portion of the ionosphere receives solar illumination so the importance of impact ionization sources due to transient and spatially confined electron precipitation takes on a dominant role. Winter fluxes are found to be highly variable in magnitude and

composition based on the ionization history of individual flux tubes. Winter H^+ fluxes vary slightly less than the O^+ flux with the latter changing by a factor of 10 for the representative extremes considered in this study.

Finally, local time variations in O^+ and H^+ fluxes were considered by comparing steady-state flux solutions at various local solar times (LST). Along a constant geomagnetic latitude, variations in LST most strongly influenced the flux magnitudes through changes in the solar zenith angle, which modify the O^+ photoproduction rates. Variations in both O^+ and H^+ were smaller than in the seasonal and solar cycle cases and for all local times examined for summer solstice, O^+ fluxes remained higher than H^+ flows.

Taken together, these results indicate that O^+ production is a major influence in modulating the character and intensity of steady-state polar ion upwellings for both O^+ and, to some extent, H^+. Variations in the modeled O^+ fluxes are most effectively influenced by changes in O^+ number densities, which are related, in turn, to solar activity levels, solar zenith angles or in winter, impact ionization sources. In both summer and winter, the results of this work indicate that a quasi-permanent region of enriched O^+ upwelling is present near local noon due to these factors. This result offers some evidence that an optimum set of thermal ion flow conditions persist in the underlying thermosphere/ionosphere in the same general region where unusually large ion outflows are observed. In contrast, H^+ fluxes are less variable due to the flux-limited constraint imposed by frictional coupling with the major ion, O^+. H^+ fluxes exhibit almost no solar cycle variations, but change considerably in winter based on the availability of O^+ which dictates H^+ density distributions through charge exchange and, in turn, is dependent on ionization source(s) and strength.

The theoretical treatment of transient heavy ion outflows demonstrated the role played by frictional heating in the lower ionosphere. Ion heating rates were derived from changes in the relative drift velocity of ion and neutral winds brought about by temporal variations in the convection electric field. A Lagrangian representation was adopted to prescribe time dependent ion heating, derived from the TIGCM, in the moving frame of a convecting flux tube. Coupling the TIGCM solutions to the polar wind model represents the first time these two models have been employed in this manner to provide a time-dependent specification of thermosphere-ionosphere coupling. This method extends the one-dimensional characterization of polar ion upwellings used in the polar wind model so that horizontal, in addition to vertical, influences can be considered when modeling transient flows.

In examining the time-dependent plasma response to low-altitude ion frictional heating, preferential heating of the major ion (O^+) occur due to greater collisional

interaction with the thermospheric gas than that experienced by H^+. The O^+ heating led to scale height changes that produced large (a factor of 3-4 increase) flux transients, which shift upwards in the flux tube column on time scales of tens of minutes. Local perturbations in the number density and field-aligned flow velocity of O^+ were noted in response to scale height changes caused by the ion heating. The modeled minor ion, H^+ received much less heating, so H^+ flows were not affected. These results demonstrated a preferential mechanism which initiates O^+ transient upwellings based not on mass per se, but on relative abundance of species with the dominant (major) ion effected most. Additionally, the model results predict that a period of ion-ion counterstreaming immediately follows the maximum heating period in which O^+ flows downward against the upflowing H^+ as the plasma cools. The coupled model approach was used for a case study simulation on a day on which an UFI event was detected by the DE-1 RIMS. The model simulations predicted a thermal O^+ flux transient at the same altitude and approximate location as observed by RIMS based only on transient ion heating specified by the TIGCM for that day. Comparing the modeled plasma conditions with multi-instrument measurements from DE-1, it is clear that transverse frictional heating cannot provide sufficient energy to match observations. Nevertheless, the initiation of such transient heavy ion fluxes by frictional heating is clearly demonstrated on this day. Further examination of this case, and others, points to a quasi-permanent frictional heating enhancement which prevails near the dayside convection reversal boundary so that convecting flux tubes experience periods of elevated heating and transient upwellings as they convect first sunward then antisunward across the polar cap. This mechanism, in addition to a universal time variation in convection electric field, was also found to be important in influencing the ion heating rates during the simulation described above. In evaluating the role of frictional heating, the collisional process of frictional heat generation was found to be self-limiting for two reasons. First, very large convective velocities help maintain large relative ion-neutral velocities and produce high heating rates, but at the same time, reduce the duration of heating experienced by the flux tube as it convects across the localized heating source. This behavior suggests that localized regions with persistent directional shears may be more effective at initiating O^+ upwellings than regions experiencing speed shears since slower transit times do not affect the directional shear. Second, once heated, the ions move upwards out of the strongest heating, thus limiting the amount of transverse energization that might occur. Together, these factors limit the amount of energy that can be converted from bulk to thermal forms so that additional energy sources appear necessary in the evolution of thermal ion upwellings into energetic outflows. In summary, this aspect of the study has helped identify the role of frictional

heating in initiating transient upwelling of ions and further underscores the unique conditions which persist in the dayside cusp/cleft region that act to locally increase transient O^+ flows above their steady-state magnitudes.

In the experimental portions of this work, the morphology of frictional heating was examined more closely and related to higher altitude upflowing ion events (ions having escape energies) and upwelling ion events (UWI). In particular, multi-instrumented observations by DE-2 were used to derive frictional heating rates along the satellite track. The derived rates are somewhat larger than the model-derived rates due to the course spatial resolution of the model and exhibit considerably more spatial structure than the model can describe. Typical heating enhancements were found to occur on horizontal scales of 10's to 100's of kilometers in latitude. Increases by an order of magnitude were commonly seen in heating rates due to large ion-neutral relative drift vectors. Two distinct types of frictional heating regions were identified. One type is found in the dawn (and to a lesser degree, the dusk) convection channel where speed shears persist due to entrainment of low momentum neutral particles into an area of high ion velocities. A second region occurs near the cusp/cleft area, where semi-permanent directional shears persist due to the strong spatial gradients in the ion velocity vector. Derived ion frictional heating rates were compared to the ion internal energy (3/2 kT) to quantify a heating response time scale. Typically, the ions are found to experience an energy gain equal to their internal energy every 2-5 minutes (discounting cooling). Within the regions of strong heating however, this time decreases to a few seconds suggesting that the plasma response to heating will occur almost simultaneously with the heating increase. Despite the very large rates of frictional heating sometimes seen, the bulk ion temperature remains below a few eV (<30,000 K) suggesting that most of the ions have insufficient energy to overcome gravity and escape. Very large, 100-fold enhancements in upwelling plasma are sometimes seen in these heating regions but cannot be fully attributed to frictional heating alone since the strongest heating generally falls at or within the auroral regions where particle precipitation and field-aligned currents may also contribute energy to the bulk flows. Likewise, large, downward directed fluxes are observed and appear to be related to post-heating relaxation as the plasma cools to background temperatures.

An extensive set of ionospheric plasma measurements, taken during multiple orbits across the polar latitudes were combined to obtain patterns of average global heating for low, moderate, and high levels of geomagnetic activity. Heating magnitudes were found to increase significantly with larger Kp as the relative ion-neutral velocity difference increased. At the same time, the areas of strongest heating tended to expand and shift equatorwards. Asymmetric heating patterns along the local noon-midnight magnetic

meridian were evident with the dawn side receiving greater heating. Both the magnitude and locations of ion frictional heating were examined for low and moderate levels of activity and were found to exhibit the same behavior as the UFI occurrence frequencies measured by the energetic ion mass spectrometer (EICS) on DE-1.

Simultaneous observations along the same field line using incoherent scatter radar also suggest that frictional heating in the lower F-region plays a role in evolving plasma upwellings but the radar data were inconclusive since large transient upwellings were also found at times where frictional heating was not varying significantly. The large spatial integrations necessary to compute frictional heating, taken over relatively long periods reduced the ability of the radar to resolve the time-dependent electric fields associated with transient heating enhancements. This would act to reduce correlations between heating rate increases and ion upwellings. For this study, positive correlations between heating and upwelling fluxes were strongest but only for long-term averages of 60 minutes. Correlations ran from 0.42 to 0.85, depending on altitude, while a model simulation showed consistently higher correlation (0.75 to 0.83) at all altitudes using 15-minute or 30-minute averages. Despite these limitations, several conclusions were made concerning the radar observations. First, it is difficult to make high-altitude radar measurements in conjunction with observations of low-altitude heating since the long integration periods needed to boost signal strength tend to limit the temporal resolution of the low-altitude measurements. This tends to destroy the coherence between the ion heating signal and plasma response since both processes are evaluated over different time intervals. Second, given the wide variance in observed field-aligned flows, it appears that ion motion can be strongly influenced by other, unmeasured processes such as precipitation or neutral winds. Heating due to energy deposition by precipitating particles was not characterized in this study but would certainly affect topside ion motions. Finally, for one day in which heating and auroral activity was at an extreme low, a steady transition from up and down ion flows to predominantly upward motion was detected as the local time of observation moved from pre-dawn to local noon suggesting that EUV heating helps to organize a diurnal pattern with upward flows in the daytime and subsidence in the night. This same general pattern has been observed in the DE-2 vertical ion drifts by Loranc (1989).

In summary, this research identified a number of ionospheric processes which are influential in modulating the composition and intensity of polar wind flows. Additionally this work identified a quasi-permanent region of enhanced ion upwelling near the dayside cusp/cleft where both modeled ion fluxes were at a maximum, independent of any "topside demand" other than the nominal pressure gradient which exists along open flux tubes. Finally, average patterns of low-altitude frictional heating appear to match well with the

occurrence frequency for upward flowing ions suggesting that this form of heating is an important influence in the dynamics of the topside ionosphere and in initiating transient upflows of heavy ions.

REFERENCES

REFERENCES

Ashour-Abdalla, M., and H. Okuda, Turbulent heating of heavy ions on auroral field lines, J. Geophys. Res., 89, 2235, 1984.

Axford, W. I., The polar wind and the terrestrial helium budget, J. Geophys. Res., 73, 6855, 1968.

Axford, W. I., and C. O. Hines, A unifying theory of high-latitude geophysical phenomena and geophysical storms. Can. J. Phys., 39, 1433-1464, 1961.

Baker, D. N., E. W. Hones, Jr., D. T. Young, and J. Birn, The possible role of ionospheric oxygen in the initiation and development of plasma sheet instabilities, Geophys. Res. Lett., 9, 1337, 1982.

Balsiger, H., P. Ederhardt, J. Geiss, and D. T. Young, Magnetic storm injection of 0.9- and 16-keV/e solar and terrestrail ions into the high-altitude magnetosphere, J. Geophys. Res., 85, 1645, 1980.

Banks, P. M., Plasma transport in the topside polar ionosphere, in The Polar Ionosphere and Magnetospheric Processes, edited by G. Scovli, Gordon & Breach Publishing Co., New York, 1969.

Banks, P. M., Observations of Joule and particle heating in the auroral zone, J. Atmos. Terr. Phys., 39, 179-193, 1977.

Banks, P. M., and T. E. Holzer, The polar wind, J. Geophys. Res., 73, 6846, 1968.

Banks, P.M., and T.E. Holzer , Features of Plasma Transport in the Upper Atmosphere, J. Geophys. Res., 74, 6304-6316, 1969.

Banks, P.M., and T. E. Holzer, High-latitude plasma transport: The polar wind, J. Geophys. Res., 74, 6317-6332, 1969.

Banks, P. M., and G. Kockarts, Aeronomy, Academic, New York, 1973.

Barakat, A. R., and R. W. Schunk, Transport equations for multi-component anisotropic space plasmas: A review, Plasma Phys., 24, 389, 1982.

Barakat, A. R., and R. W. Schunk, O^+ ions in the polar wind, J. Geophys. Res., 88, 7887, 1983.

Barakat, A. R. and R. W. Schunk, Effect of hot electrons in the polar wind, J. Geophys. Res., 89, 9771, 1984.

Barakat, A. R., R. W. Schunk, T. E. Moore, and J. H. Waite, Jr., Ion escape fluxes from the terrestrial high-latitude ionosphere, J. Geophys. Res., 92, 12255-12266, 1987.

Bauer, S. J., The structure of the topside ionosphere, in Electron Density Profiles in Ionosphere and Exosphere, edited by Jon Frihaagen, p. 387, North-Holland Publishing Company, Amsterdam, 1966.

Bergmann, R., Electrostatic ion (hydrogen) cyclotron and ion current and upward ion beams, J. Geophys. Res., 89, 953, 1984.

Bergmann, R., and W. Lotko, Transition t › unstable ion flow in parallel electric fields, J. Geophys. Res., 91, 7033-7045, 1986.

de la Beaujardière, O., V. B. Wickwar, C. A. Leger, M. A. McCready, and M. J. Baron, The software system for the Chatanika incoherent-scatter radar, SRI Projects 4964 and 4995 Tech. Rep., 2nd ed., SRI International, Menlo Park, CA, 127 pp., 1984.

Bowles, K. L., Observations of vertical incidence scatter from the ionosphere at 41 Mc/sec, Phys. Rev. Lett., 1, 454-455, 1958.

Bowles, K. L., Incoherent scattering by free electrons as a technique for studying the ionosphere and exosphere: Some observations and theoretical considerations, J. Research NBS, 65D, 1-13, 1961.

Brinton, H. C., J. M. Grebowsky, and H. G. Mayr, Altitude variation of ion composition in the mid-latitude trough region: Evidence for upward plasma flow, J. Geophys. Res., 76, 3738, 1971.

Brice, N., Bulk motion of the magnetosphere, J. Geophys. Res., 72, 5193-5211, 1967.

Burgers, J. M., Flow equations for composite gases. Acedemic Press, New York, 1969.

Cannata, R. W. and T. I. Gombosi, Modeling the solar cycle dependence of quiet-time ion upwelling at high geomagnetic latitudes, J. Geophys Res. Lett., 1141, 1989.

Cannata, R.W., T. L. Killeen, T. I. Gombosi, A. G. Burns, and R. G. Roble, Modelling of time-dependent ion outflows at high geomagnetic latitudes, Adv. Space Res., 8, 889-892, 1988.

Carignan, G. R., B. P. Block, J. C. Maurer, A. E. Hedin, C. A Reber, and N. W. Spencer, The neutral mass spectrometer on Dynamics Explorer, Space Science Inst., 5, 429-441,1981.

Chandler, M. O. and J. H. Waite, Jr., Observations of ion outflows at high geomagnetic latitudes, J. Geophys. Res., in press, 1990.

Chappell, C. R., The terrestrial plasma source: A new perspective in solar terrestrial processes from Dynamics Explorer, Rev. Geophys., 26, 229, 1988.

Chappell, C. R., S. A. Fields, C. R. Baugher, J. H. Hoffman, W. B. Hanson, W. W. Wright, and H. D. Hammack, The retarding ion mass spectrometer on Dynamics Explorer-A, Space Sci. Instrum., 5, 477, 1981.

Chappell, C. R., T. E. Moore, and J. H. Waite, Jr., The ionosphere as a fully adequate source of plasma for the Earth's magnetosphere, J. Geophys., Res., 92, 5896, 1987.

Chappell, C. R. , R. C. Olsen, J. L. Green, J. F. E. Johnson, and J. H. Waite, Jr., The discovery of nitrogen ions in the earth's magnetosphere, Geophys. Res. Lett., 9, 937, 1982.

Collin, H. L. , R. D. Sharp and E. G. Shelley, The magnitude and composition of the outflow of energetic ions from the ionosphere, J. Geophys. Res., 89, 2185, 1984.

Collin, H. L., E. G. Shelley, A. G. Ghielmetti, and R. D. Sharp, Observations of transverse and parallel acceleration of terrestrial ions at high latitudes, in Ion Acceleration in the Magnetosphere and Ionosphere, Geophys. Monogr. vol.38, edited by T. Chang et al., AGU, Washington, D. C., 1986a.

Collin, H. L., E. G. Shelley, and R. Bergmann, The heating of upflowing ion beams by an H^+ / O^+ two-stream instability (abstract), Eos Trans. AGU, 67, 1164, 1986b.

Craven J. D., A. Y. Kamide, L. A. Frank, S. I. Akasofu, and M. Suguira, Distribution of aurora and ionospheric currents observed simultaneously on a global scale. Magnetospheric Currents, Geophysical Monograph, vol. 28, 137-146, 1984.

Craven, P. D., R. C. Olsen, C. R. Chappell, and L. Kakani, Observations of molecular ions in the earth's magnetosphere, J. Geophys. Res., 90, 7599, 1985.

Creekmore S. P., J. M. Straus, R. M. Harris, B. K. Ching, and Y. T. Chiu, A global model of thermospheric dynamics-I. wind and density fields derived from a phenomenological temperature, J. Atmos. Terr. Phys., 37, 491-515, 1975.

Curtis, S. A., W. R. Hoegy, L. H. Brace and J. D. Winningham, Cusp altitudinal electron temperature gradient: Dyanmics Explorer-2 implictions for heating mechanisms, J. Geophys. Res., 90, 4415, 1985.

Demars, H. G., and R. W. Schunk, Transport equations for multi-species plasmas based on individual bi-Maxwellian distributions, J. Phys. D., 12, 1051, 1979.

Dessler, A. J., and F. C. Michel, Plasma in the geomagnetic tail, J. Geophys. Res., 71, 1421, 1966.

Dickinson, R. E. and E. C. Ridley, A Numerical model for the dynamics and composition of the Venusian thermosphere, J. Atmos. Sci., 32, 1219-1231, 1975.

Dickinson, R. E., E. C. Ridley, and R. G. Roble, A three-dimensional, time-dependent general circulation model of the thermosphere, J. Geophys. Res., 86, 1499-1512, 1981.

Dickinson, R. E., E. C. Ridley and R. G. Roble, Thermospheric general circulation with coupled dynamics and composition, J. Atmos. Sci., 41, 205-219, 1984.

Dougherty, J. P. and D. T. Farley, Jr., A theory of incoherent scattering of radio waves by a plasma, Proc. Roy. Soc. London, A, 259, 79-99, 1960.

Dougherty, J. P. and D. T. Farley, Jr., A theory of incoherent scattering of radio waves by a plasma 3. Scattering in a partly ionized gas, J. Geophys. Res., 68, 19, 5473-5486, 1963.

Dusenbery, P. B., and R. F. Martin, Jr., Generation of broadband turbulence by accelerated auroral ions, 1. Parallel propagation, J. Geophys. Res., 92, 3261, 1987.

Dusenbery, P. B., R. F. Martin, Jr., and R. M. Winglee, Ion-Ion waves in the auroral region: Wave excitation and ion heating, J. Geophys. Res., 93, 5655-5664, 1988.

Evans, J. V., Theory and practice of ionosphere study by Thomson scatter radar, Proc. IEEE, 57, 4, 496-530, 1969.

Evans, J. V., Some post-war developments in ground-based radiowave sounding of the ionosphere, J. Atmos. Terr. Phys., 36, 2183-2234, 1974.

Farley, D. T., J. P. Dougherty, and D. W. Barron, A theory of incoherent scattering of radio waves by a plasma 2. Scattering in a magnetic field, Proc. Roy. Soc. London, A, 263, 238-258, 1961.

Fejer J. A., Scattering of radio waves by an ionized gas in thermal equilibrium in the presence of a uniform magnetic field, Canad. J. Phys., 39, 716-740, 1961.

Frank, L. A., J. D. Craven, J. L. Busch, and J. D. Winningham, Polar views of the earth's aurora with Dynamics Explorer. Geophys. Res. Lett., 9, 1001-1004, 1982.

Fuller-Rowell, T. J., and D. S. Evans, Height integrated Pedersen and Hall conductivity patterns inferrred from the TIROS-NOAA satellite data. J. Geophys. Res.,92, 7606-7618, 1987.

Fuller-Rowell, T. J. and D. Rees, A three-dimensional time-dependent global model of the thermosphere, J. Atmos. Sci, 37, 2545-2567, 1980.

Ganguli, S. B., H. G. Mitchell, Jr., and P. J. Palmadesso, Behavior of ionized plasma in the high latitude topside ionosphere: The polar wind, Planet. Space Sci., 35, 703, 1987.

Ganguli, S. B., and P. J. Palmadesso, Classical and anomalous transport processes in the auroral return current region, in Modeling Magnetospheric Plasma, Geophys. Monogr. Ser., vol. 44, edited by T. E. Moore and J. H. Waite, pp. 171-176, AGU, Washington, D.C., 1988.

Ghielmetti, A. G., E. G. Shelley, H. L. Collin, and R. D. Sharp, Ion specific differences in energetic field aligned upflowing ions at 1 RE, in Ion Acceleration in the Magnetosphere and Ionosphere, Geophys. Monogr. Ser., vol.38, edited by T. Chang et al., AGU, Washington, D. C., 1986.

Ghielmetti, A. G., R. G. Johnson, R. D. Sharp, and E. G. Shelley, The latitudinal, diurnal, and altitudinal distributions of upward flowing energetic ions of ionospheric orgin, Geophys. Res. Lett., 5, 59, 1978.

Godunov, S. K., Raznostnyi metod chislennogo raschcta razryunykh reshenii gidrodinamiki (A difference scheme for numerical solutions of gas dynamical equations with discontinuities), Matematicheskii Sbornik, 47 (89), 271-306, 1959.

Gombosi, T. I., T. E. Cravens, A. F. Nagy, and J. H. Waite, Jr., Time-dependent numerical simulation of hot ion outflow from the polar ionosphere, in Ion Acceleration in Magnetosphere, Geophys. Monogr. Ser., vol. 38, edited by T. Chang, pp. 366-371, AGU, Washington, D.C., 1986.

Gombosi, T. I., T. E. Cravens and A. F. Nagy, A time-dependent theoretical model of the polar wind: preliminary results, Geophys. Res. Lett., 12, 167, 1985.

Gombosi, T. I., and T. L. Killeen, Effects of thermospheric motions on the polar wind: A time dependent numerical study, J. Geophys. Res., 92, 4725, 1987.

Gombosi, T.I., and A. F. Nagy, Time-dependent polar wind modeling, Adv. Space Res., 8, 859-868, 1988.

Gombosi, T.I., and A. F. Nagy, Time-dependent modeling of field-aligned current-generated ion transients in the polar wind, J. Geophys. Res., 94, 359-369, 1989.

Gombosi, T. I., and R. W. Schunk, A comparative study of plasma expansion events in the polar wind, Planet. Space Sci., 36, 753, 1988.

Gordon, W. E., Incoherent scattering of radio waves by free electrons with applications to space exploration by radar, Proc. IRE, 46, 1824-1829, 1958.

Gorney, D. J., A. Clarke, D. Rowley, J. Fennell, J. Ludmann, and P. Mizera, The distribution of ion beams and conics below 8000 km, J. Geophys. Res., 86, 83, 1981.

Grad, H., On the kinetic theory of rarefied gases, Comm. Pure Appl. Math., 2, 331, 1949.

Grad, H., Principles of the kinetic theory of gases, Handbuch der Physik XII, 205-294, 1958.

Grebowsky, J. M., and W. R. Hoegy, Solar maximum - minimum extremes in the summer noontime polar cap F-region ion composition- The measurements, J. Geophys. Res., in press, 1990.

Green, J. L. and J. H. Waite Jr., On the orgin of polar ion streams, Geophys. Res. Lett. 12, 149, 1985

Gurnett, D. A., and L. A. Frank, A region of intense plasma wave turbulence on auroral field lines, J. Geophys. Res., 82, 1031, 1977.

Gussenhoven, M. S., D. A. Hardy, and N. Heinemann, Systematics of the Equatorward diffuse auroral boundary, J. Geophys. Res., 88, 5692, 1983.

Gussenhoven, M. S., D. A. Hardy, R. L. Carovillano, Average electron precipitation in the polar cusps, in The Polar Cusp, NATO ASI Series, 145, edited by J. Holet and A. Egeland, pp. 85-97, Reidel, Dordrecht, 1985.

Hagfors, T. and R. A. Brockelman, A theory of collision dominated electron density fluctuations in a plasma with applications to incoherent scattering, Phys. Fluids, 14, 6, 1143-1151, 1971.

Hanson, W. B., R. A. Heelis, R. A. Power, C. R. Lippincott, D. R. Zuccaro, B. J. Holt, L. H. Harmon, and S. Sanatani, The retarding potential analyser for Dynamics Explorer-B, Space Sci. Instrum., 5, 503-510, 1981.

Hanson, W. B., and T. N. L. Patterson, Diurnal variation of the hydrogen concentration in the exosphere, Planetary Space Sci., 11, 1035, 1963.

Hanson, W. B., D. R. Zuccaro, C. R. Lippincott, and S. Santani, The retarding potential analyzer on Atmosphere Explorer, Radio Sci., 8, 333-339, 1973.

Hanson, W. B., R. A. Heelis, R. A. Power, C. A. Lippincott, D. R. Zuccaro, B. J. Holt, L.H. Harmon, and S. Sanatani, The retarding potential analyser for Dynamics Explorer- B, Space Science Inst., 5, 503-510, 1981.

Hargreaves, J. K., The Upper Atmosphere and Solar-Terrestrial Relations, Van Nostrand Reinhold, New York, 1979.

Hardy, D. A., M. S. Gussenhoven, and E. Holeman, A statistical model of auroral electron precipitation. J. Geophys. Res., 90, 4229-4248, 1985.

Harris, I. and H. G. Mayr, Diurnal variations in the thermosphere 1. Theoretical formulation, J. Geophys. Res., 80, 3925-3933, 1975.

Harris, I. and W. Priester, On the diurnal variations of the upper thermosphere, J. Atmos. Sci., 22, 3, 1965.

Hays, P. B., R. A. Jones, and M. H. Rees, Auroral heating and the composition of the neutral atmosphere, Planet. Space. Sci., 21, 559-570, 1973.

Hedin, A. E., A revised thermospheric model based on mass spectrometer and incoherent scatter data: MSIS-83, J. Geophys. Res., 88, 10170-10188, 1983.

Hedin, A. E., MSIS-86 thermospheric model, J. Geophys. Res., 92, 4649-4662, 1987.

Heelis, R. A., W. B. Hanson, C. R. Lippoincott, D. R. Zuccaro, L. H. Harmon, B. J. Holt, J. E. Doherty, and R. A. Power, The ion drift meter for Dynamics Explorer-B, Space Science Inst., 5, 511-521, 1981.

Heelis, R. A., J. K. Lowell, and R. W. Spiro, A model of the high-latitude ionospheric convection pattern, J. Geophys. Res., 87, 6339-6345, 1982.

Heelis, R. A., J. D. Winningham, M. Sugiura, and N. C. Maynard, Particle acceleration parallel and perpendicular to the magnetic field observed by DE-2, J. Geophys., Res., 89, 3893, 1984.

Hinteregger, H. E., Representations of solar EUV fluxes for aeronomical applications, Adv. Space Res., 86, 801-813, 1981.

Hinteregger, H. E., K. Fukui, and B. R. Gilson, Observational, reference and model data on solar EUV, from measurements on AE-E, Geophys. Res. Lett., 8, 1147, 1981.

Hoffman, J. A., Mass spectrometer measurement of ionospheric compsition, in Proceedings of the International Conference on Mass Spectroscopy, edited by K. Ogata and T. Hayakawa, p1068, University of Tokyo Press, Tokyo, Japan, 1970.

Hoffman, R. A., Dynamics Explorer program, EOS, 61, 689-692, 1980.

Hoffman, J. H., W. H. Dodson, C. R. Lippincott, and H. D. Hammack, Initial ion composition results from the ISIS 2 satellite, J. Geophys. Res., 79, 4246, 1974.

Hoffman, J. H. and W. H. Dodson, Light ion concentrations and fluxes in the polar regions Banks during geomagnetically quiet times,.J. Geophys. Res., 85, 626, 1980.

Hoffman, R. A., G. D. Hogan, R. C. Maehl, Dynamics explorer spacecraft and ground operations systems, Space Sci. Instrum., 5, 349-367, 1981.

Holtzworth, R. H., and C.-I. Meng, Mathematical representation of the auroral oval, Geophys. Res. Lett., 2, 377, 1975.

Holzer, T. E., J. A. Fedder, and P. M. Banks, A comparison of kinetic and hydrodynamic models of an expanding ion-exosphere, J. Geophys.Res., 76, 2453-2468, 1971.

Horwitz, J. L., Parabolic heavy ion flow in the polar magnetosphere, J. Geophys., Res., 92, 175, 1987.

Horwitz, J. L., Features of ion trajectories in the polar magnetosphere, Geophys. Res. Lett., 11, 1111, 1984.

Horwitz, J. L., The ionosphere as a source for magnetospheric ions, Rev. Geophys. Space Phys., 20, 929, 1982.

Horwitz, J. L., The kinetic approach in magnetospheric plasma transport modeling, in Modeling Magnetospheric Plasma, Geophys. Monogr. Ser., vol. 44, edited by T. E. Moore and J. H. WaiteJr., pp. 11-20, AGU, Washington, D. C., 1988.

Horwitz, J. L. and M. Lockwood, The cleft ion fountain: A two-dimensional kinetic model, J. Geophys. Res., 90, 9749, 1985.

Kaufmann, R. L., and G. R., Ludlow, Interaction of H^+ and O^+ beams: Observations at 2 and 3 RE, in Ion Acceleration in the Magnetosphere and Ionosphere, Geophys. Monogr. Ser., vol.38, edited by T. Chang et al., AGU Washington, D. C., 1986.

Kaufmann, R. L., G. R. Ludlow, H. L. Collin, W. K. Peterson, and J. L. Burch, Interaction of Upgoing auroral H^+ and O^+ beams, J. Geophys. Res., 91, 10,080, Killeen, T. L., P. B. Hays, G. R. Carignan, R. A. Heelis, W. B. Hanson, N. W. Spencer and L. H. Brace, Ion-neutral coupling in the high latitude F-region: Evaluation of ion heating terms from Dynamics Explorer 2, J. Geophys. Res., 89, 7495-7508, 1984.

Killeen, T. L., P. B. Hays, G. R. Carigan, R. A. Heelis, W. B. Hanson, N. W. Spencer, and L. H. Brace, Ion-neutral coupling in the high-latitude F-region: evaluation of ion heating terms from Dynamics Explorer 2, J. Geophys. Res., 89, 7495-7508, 1984.

Killeen, T. L. and R. G. Roble, An analysis of the high-latitude thermospheric wind pattern calculated by a Thermospheric General Circulation Model. 2. Neutral parcel transport, J. Geophys. Res., 91, 11291-11307, 1986.

Killeen, T. L. and R. G. Roble, Thermosphere Dynamics driven by magnetospheric sources: contributions from the first five years of the Dynamics Explorer program, Rev. Geophys. Space Phys., 26, 329-367, 1988.

Kirby, K., E. R. Constantinides, S. Babeu, M. Oppenheimer, and G. A. Victor. Photoionization and photoabsorption cross - sections of thermospheric secies: He, O, N_2 and O_2, At. Data Nucl. Data Tables, 23(1), 1979.

Kelley, M. C., The Earth's Ionosphere, Academic Press, San Diego, 1989.

Lemaire, J., O^+, H^+, and He^+ ion distributions in a new polar wind model, J. Atmos. Terr. Phys., 34, 1647-1658, 1972.

Lemaire, J. and M. Scherer, Model of the polar ion-exosphere, Planet. Space Sci., 18, 103-120, 1970.

Lemaire, J. and M. Scherer, Simple model for an ion-exosphere in an open magnetic field, Phys. Fluids, 14, 1683-1694, 1971.

Lemaire, J. and M. Scherer, Ion-exosphere with asymmetric velocity distribution, Phys. Fluids, 15, 760-766, 1972.

Lemaire, J. and M. Scherer, Kinetic models of the solar and solar winds, Rev. Geophys. Space Phys., 11, 427-468, 1973.

Lennartsson, W., and E. G. Shelley, Survey of 0.1- to 16-keV/e plasma sheet ion composition, J. Geophys. Res., 91, 3061, 1986.

Lockwood, M., Thermospheric control of the auroral source of O^+ ions for the magnetosphere, J. Geophys. Res., 89, 301, 1984.

Lockwood, M., B. J. I. Bromage, R. B. Horne, J.-P. St.-Maurice, D. M. Willis, and S. W. H. Cowley, Non-Maxwellian ion velocity distributions observed using EISCAT, Geophys. Res. Lett., 14, 111-114, 1987.

Lockwood, M., M. O. Chandler, J. L. Horwitz, J. H. Waite, Jr., T. E. Moore and C. R. Chappell, The cleft ion fountain, J. Geophys. Res., 10, 9736, 1985a.

Lockwood, M., and T. J. Fuller-Rowell, The modelled occurence of non-thermal plasma in the ionospheric F region and the possible consequences for ion outflows into the magnetosphere, Geophys. Res. Lett., 14, 371-374, 1987.

Lockwood, M., J. H. Waite, T. E. Moore, J. F. E. Johnson, and R. C. Chappell, A new source of suprathermal O^+ ions near the dayside polar cap boundary, J. Geophys. Res., 90, 4099, 1985b.

Loranc, M. A., A study of the ionospheric signature of ion supply from the ionosphere to the magnetosphere, Ph. D. Thesis, University of Texas at Dallas, 1988.

Ludin, R., and E. M. Dudinin, Solar wind energy transfer regions inside the dayside magnetopause-III. Accelerated heavy ions as tracers for MHD-processes in the dayside boundary layers, Planet. Space Sci., 33, 891, 1985.

Lundin, R., B. Hultqvist, E. Dubinin, A. Zackarov, and N. Pissarenko, Observations of outflowing ion beams on auroral field lines at altitudes of many Earth radii, Planet. Space Sci., 30, 715, 1982.

Maeda, H., Neutral winds and ion drifts in the polar ionosphere caused by convection electric fields-1, J. Atmos. and Terr. Phys., 38, 197-205, 1976.

Maeda, H., Neutral winds and ion drifts in the polar ionosphere caused by convection electric fields-2, J. Atmos. and Terr. Phys., 39, 849-858, 1977.

Mange, P., The distribution of minor ions in electrostatic equilibrium in the high atmosphere, J. Geophys. Res., 65, 3833-3834, 1960.

Marubashi, K., Escape of the polar-ionospheric plasma into the magnetospheric tail, Rep. Ionos. Space Res. Japan, 24, 322-346, 1970.

Mayr, H. G. and I. Harris, Some characteristics of electric field momentum coupling with the neutral atmosphere, J. Geophys. Res., 83, 3327-3336, 1978.

Mikkelsen, I. S., T. S. Jorgensen, M. C. Kelley, M. F. Larsen, and E. Pereira, Neutral winds and electric fields in the dusk auroral oval 2. Theory and model, J. Geophys. Res., 86, 1525-1536, 1981.

Mitchell, H. G., Jr., and P. J. Palmadesso. A dynamic model for the auroral field line plasma in the presence of field-aligned current, J. Geophys. Res., 88, 2131, 1983.

Moore, T. E., Modulation of terrestrial ion escape flux composition (by low-altitude acceleration and charge exchange chemistry), J. Geophys. Res., 85, 2011, 1980.

Moore, T. E., Superthermal ionospheric outflows, Rev. Geophys. Space Phys., 22, 264, 1984.

Moore, T. E., C. R. Chappell, M. Lockwood and J. H. Waite, Jr., Superthermal ion signatures of auroral acceleration processes, J. Geophys. Res., 90, 1611, 1985.

Moore, T. E., M. Lockwood, M. O. Chandler, J. H. Waite, Jr., C. R. Chappell, A. Persoon and M. Sugiura, Upwelling O^+ ion source characteristics, J. Geophys. Res., 91, 7019, 1986.

Nagai, T., J. H. Waite , Jr., J. L. Green, C. R. Chappell, R. C. Olsen, and R. H. Comfort, First measurements of supersonic polar wind in the polar magnetosphere, Geophys. Res. Lett., 11, 1984.

Nishida, A., Formation of a plasmapause, or magnetospheric plasma knee by combined action of magnetospheric convection and plasma escape from the tail, J. Geophys. Res., 71, 5669, 1966.

NOAA, Prelim. Report and Forcast of Solar Geophysical Data, SESC PRF 457, U.S. Dept. of Commerce, Boulder, CO, 7, 1984.

Olsen, R. C., The hidden ion population of the magnetosphere, J. Geophys. Res., 87, 3481-3488, 1982.

Oppenheimer, M., A. Dalgarno, and H. C. Brinton, Ion chemistry of N_2^+ and the solar ultraviolet flux in the thermosphere, J. Geophys. Res., 81, 3762, 1976.

Ottley, J. A. and R. W. Schunk, Density and temperature structure of helium ions in the topside polar ionosphere for subsonic outflows, J. Geophys. Res., 85, 4177-4190, 1980.

Palmadesso, P. J., S. B. Ganguli, and H. G. Mitchell, Multi-moment fluid simulations of transport processes in the auroral zones, in Modeling Magnetospheric Plasma, Geophys. Monogr. Ser., vol. 44, edited by T. M. Moore and J. H. Waite, pp. 133-143, AGU, Washington, D. C., 1988.

Peterson, W. K., E. G. Shelley, G. Haerendel, and E. Paschmann, Energetic ion composition in the subsolar magnetopause and boundary layer, J. Geophys. Res., 87, 2139-2145, 1982.

Prolss, G. W., Magnetic storm associated perturbations of the upper atmosphere: recent results obtained by satellite-borne gas analyzers, Rev. Geophys., 183-202, 1980.

Raitt, W. J., and R. W. Schunk, Composition and characteristics of the polar wind, in Energetic ion composition in the earth's magneto sphere, edited by R. G. Johnson, Terra Scientific, 99-141, Tokyo, 1983.

Raitt, W. J., R. W. Schunk, and P. M. Banks, A comparison of the temperature and density structure in high and low speed thermal proton flows, Planet Space Sci., 23, 1103-1117, 1975.

Raitt, W. J., R. W. Schunk, and P. M. Banks, The influence of convection electric fields on thermal proton outflow from the ionosphere, Planet. Space Sci., 25, 291-301, 1977.

Raitt, W. J., R. W. Schunk, and P. M. Banks, Helium ion outflow from the terrestrial ionosphere, Planet. Space Sci., 26, 255-268, 1978a.

Raitt, W. J., R. W. Schunk, and P. M. Banks, Quantitative calculations of helium ion escape fluxes from the polar ionospheres, J. Geophys. Res., 83, 5617-5624, 1978b.

Reiff, P. H., Models of auroral zone conductances. Magnetospheric Currents, Geophysical Monograph 28, 180-191, 1984.

Reiff, P. H., and J. G. Luhman, Solar wind controls of the polar cap voltage, Proceedings of Solar Wind Magnetosphere Coupling, editors Y. Kamide and J. A. Slaven, D. Riedel Publishing Co., Boston, p. 453, 1986.

Richards, P. G., and D. G. Torr, Ratios of photoelectron to EUV Ionization Rates for Aeronomic Studies. J. Geophys. Res., 93, 4060, 1988.

Richmond, A. D., M. Blanc, B. A. Emery, R. H. Wand, B. G. Fejer, R. F. Woodman, S. Ganguly, P. Amayenc, R. A. Benke, C. Calderon, and J. V. Evans, An empirical model of quiet-day ionospheric electric fields at middle and low latitudes, J. Geophys. Res., 85, 4658-4664, 1980.

Rishbeth, H. and W. B. Hanson, A comment on plasma 'pile-up' in the F-region, J. Atmos. Terr. Phys., 37, 1055-1064, 1975.

Roble, R. G. and E. C. Ridley, An auroral model for the NCAR thermospheric general circulation model, Annales Geophysicae, 5A, 369-382, 1987.

Roble, R. G., E. C. Ridley, and R. E. Dickinson, On the global mean structure of the thermosphere, J. Geophys. Res., 92, 8745-8758, 1987.

Roble, R. G., E. C. Ridley, A. D. Richmond and R. E. Dickinson, A coupled thermosphere/ionosphere general circulation model, Geophys. Res. Lett., 15, 1325-1328, 1988.

Roth, I., and M. K. Hudson, Lower hybrid heating of ionospheric ions due to ion ring distributions in the cusp, J. Geophys. Res., 90, 4191, 1985.

Samson, J. A. R., and P. N. Pareek, Absolute photoionization cross sections of atomic oxygen, Phy. Rev. A, 31, 1470. 1985.

Schunk, R. W., Transport equations for aeronomy, Planet. Space Sci., 23, 437-485, 1975.

Schunk, R. W., Mathematical structure of transport equations for multispecies flows, Rev. Geophys. Space Phys., 15, 429-445, 1977.

Schunk, R. W., The terrestrial ionosphere, in Solar-Terrestrial Physics, R. L. Carovillano, and J. M. Forbes, eds., p. 609-676, 1983.

Schunk, R. W., An updated theory of the polar wind, Adv. Space Res., 6, 79, 1986.

Schunk, R. W., The polar wind, in Modeling Magnetospheric Plasma, Geophys. Monogr. Ser., vol. 44, edited by T. M. Moore and J. H. Waite, Jr., pp. 219-228, AGU, Washington, D. C., 1988.

Schunk, R. W., P. M. Banks, and W. J. Raitt, Effects of electric fields and other processes upon the nighttime high latitude F layer, J. Geophys. Res., 81, 3271, 1976.

Schunk, R. W.and A. F. Nagy, Electron temperature in the F region of the ionosphere: theory and observations, Rev. Geophys. Space Phys., 16, 355-399, 1978.

Schunk, R. W.and A. F. Nagy, Ionospheres of the terrestrial planets, Rev. Geophys. Space Phys., 18, 813-852, 1980.

Schunk, R. W., W. J. Raitt, and A. F. Nagy, Effect of diffusion-thermal processes on the high-latitude topside ionosphere, Planet. Space Sci., 26, 189, 1978.

Schunk, R.W., and Watkins, D. S., Proton temperature anisotropy in the polar wind, J. Geophys. Res., 87, 171-180, 1982.

Schunk, R.W., W. J .Raitt, , and P. M. Banks, Effect of electric fields on the daytime high-latitude E and F regions, J. Geophys. Res., 80, 3121-3130, 1975.

Schunk, R. W., and J. J. Sojka, Ionospheric hot spot at high latitudes, Geophys. Res. Lett., 9, 1045, 1982.

Schunk, R. W. and J. J. Sojka, Ion temperature variations in the daytime high-latitude F-region, J. Geophys. Res., 87, 5169-5183, 1982.

Schunk, R. W. and J. J. Sojka, A three-dimensional time-dependent model of the polar wind, J. Geophys. Res., 94, 8973, 1989.

Schunk, R. W. and J. C. G. Walker, Thermal diffusion in the topside ionosphere for mixtures which include mutiply-charged ions, Planet. Space Sci., 17, 853-868, 1969.

Schunk, R. W. and J. C. G. Walker, Thermal diffusion in the F_2-region of the ionosphere, Planet. Space Sci., 18, 535-557, 1970.

Schunk, R.W., and J. C. G. Walker, Transport properties of the ionospheric electron gas, Planet. Space Sci., 18, 1535-1550, 1970.

Schunk, R. W. and D. S. Watkins, Comparison of solutions to the thirteen-moment and standard transport equations for low speed thermal proton flows, Planet. Space Sci., 27, 433-444, 1979.

Schunk, R. W. and D. S. Watkins, Electron temperature anisotropy in the polar wind, J. Geophys. Res., 86, 91-102, 1981.

Sharp, R. D., R. G. Johnson, and E. G. Shelley, Observation of an ionospheric acceleration mechanism producing energetic (keV) ions primarily normal to the geomagnetic field direction, J. Geophys. Res., 82, 3324, 1977.

Shelley, E. G., R. G. Johnson, and R. D. Sharp, Satellite observations of energetic heavy ions during a geomagnetic storm, L. Geophys. Res., 77, 6104, 1972.

Shelley, E. G., W. K. Peterson, A. G. Ghielmetti and J. Geiss, The polar ionosphere as a source of energetic magnetospheric plasma, Geophys. Res. Lett., 9, 941, 1982.

Singh, N. and R. W. Schunk, Temporal behavior of density perturbations in the polar wind, J. Geophys. Res., 90, 6487, 1985.

Singh, N., and R. W. Schunk, Ion acceleration in expanding ionospheric plasmas, in Ion Acceleration in the Magnetosphere and Ionosphere, Geophys. Monogr. Ser., vol. 38, p. 362, AGU, Washington, D. C., 1986.

Sojka, J. J., and R. W. Schunk, A theoretical study of the global F region for June solstice, solar maximum, and low magnetic activity, J. Geophys. Res., 90, 5285, 1985.

Sojka, J. J., and R. W. Schunk, A theoretical study of the production and decay of localized electron density enhancements in the polar ionosphere, J. Geophys. Res., 91, 3245-3253, 1986.

St. Maurice, J.-P. and W. B. Hanson, Ion frictional heating at high latitudes and its possible use for an in situ determination of neutral thermospheric winds and temperatures, J. Geophys. Res., 87, 7580-7602, 1982.

St. Maurice, J.-P. and W. B. Hanson, A statistical study of F region ion temperatures at high latitudes based on Atmosphere Explorer C data, J. Geophys. Res., 89, 987-996, 1984.

Straus, J. M., S. P. Creekmore, R. M. Harris, B. K. Ching, and Y. T. Chiu, A global model of thermospheric dynamics-II. wind, density, and temperature fields generated by EUV heating, J. Atmos.Terr. Phys., 37, 1245-1253, 1975a.

Straus, J. M., S. P. Creekmore, R. M. Harris, and B. K. Ching, Effects of heating at high latitudes on global thermospheric dynamics, J. Atmos.Terr. Phys., 37, 1545-1554, 1975b.

Straus, J. M. and M. Schultz, Magnetospheric convection and upper atmospheric dynamics, J. Geophys. Res., 81, 5822-5832, 1976.

Thayer, J.P., Neutral wind vorticies in the high-latitude thermosphere, Ph. D. Thesis, University of Michigan, 1990.

Thomson, J. J., Conduction of electricity through gases, p 321, Cambridge University Press, London, 1906.

Torr, D. G., and M. R. Torr, Chemistry of the thermosphere and ionosphere, J. Atmos. Terr. Phys., 41, 797, 1979.

Torr, M. R., and D. G. Torr, Ionization frequencies for solar cycle 21: Revised, J. Geophys. Res., 90, 6675-6678, 1985.

Torr, M. R., D. G. Torr, and R. A. Ong, Ionization frequencies for major thermospheric constituents as a function of solar cycle 21, Geophys. Res. Lett., 6, 771-774, 1979.

Vasyliunas, V. M., Interaction between the magnetospheric boundary layers and the ionosphere, in Proceedings of Magnetospheric Boundary Layers Conference, Eur. Space Agency Spec. Publ., ESA SP-148, edited by B. Battrick, pp. 387-393, Noordwijk, The Netherlands, 1979.

Vickrey, J. F., Incoherent Scatter Theory - An intuitive approach, lecture notes presented at the Chatanika Radar School, 1980.

Vickrey, J. F., W. E. Swartz, and D. T. Farley, Incoherent scatter measurement of ion counterstreaming, Geophys. Res. Lett., 3, 217-220, 1976.

Walker, J. C. G., Space science without rockets: measurements of ionospheric properties at the Arecibo Observatory, EOS, 59, 4, 180-189, 1978.

Walker, J. C. G., Radar measurement of the upper atmosphere, Science, 206, 180-189, 1979.

Wickwar, V. B., C. Lathuillere, W. Kofman, and G. Lejeune, Elevated electron temperatures in the auroral E layer measured with the Chatanika Radar, J. Geophys. Res., 86, A6, 4721-4730, 1981.

Wahland, J.-E., and H. J. Openoorth, Observations of thin auroral ionization layers by EISCAT in connection with pulsating aurora, J. Geophys. Res., 94, 17223-17233, 1989.

Waite, J. H., Jr., T. E. Moore, M. O. Chandler, M. Lockwood, and A. Persoon, and M. Suguira, Ion energization in upwelling ion events, in Ion Acceleration in the Magnetosphere and Ionosphere, edited by T. Chang, p. 61, AGU, Washington, D. C., 1986.

Waite, J. H., T. Nagai, J. F. E. Johnson, R. C. Chappell, J. L. Burch, T. L. Killeen, P. B. Hays, G. R. Carignan, W. K. Peterson, and E. G. Shelley, Escape of suprathermal O^+ ions in the polar cap, J. Geophys. Res.,90, 1619, 1985.

Whalen, J. A., A quantitative description of the spatial distribution and dynamics of the energy flux in the continuous aurora. J. Geophys. Res., 88, 7155-7169, 1983.

Winningham, D., and W. Heikkila, Polar cap auroral electron fluxes observed with ISIS-1, J. Geophys. Res.,79, 949, 1974

Winser, K., G. O. L. Jones, and P. J. S. Williams, Variations in field-aligned plasma velocity with altitude and latitude in the auroral zone: EISCAT observations and the physical interpretation, Physica Scripta, 1987.

Winser, K., M. Lockwood, and G. O. L. Jones, On thermal plasma observations using EISCAT: Aspect angle dependence, Geophys. Res. Lett., 14, 957, 1987.

Winser, K., M. Lockwood, G. O. L. Jones, and K. Suvanto, Observations of nonthermal plasmas at different aspect angles, J. Geophys. Res., 94, 1439-1449, 1989.

Yau, A. W., P. H. Beckwith, W. K. Peterson and E. G. Shelley, Long term (solar cycle) and seasonal variations of upflowing ionospheric ion events at DE 1 altitudes, J. Geophys. Res., 90, 6395, 1985.

Yau, A. W., E. G. Shelley, W. K. Peterson, and L. Lenchyshyn, Energetic auroral and polar ion outflow at DE 1 altitudes: Magnitude, composition, magnetic activity dependence, and long-term variations, J. Geophys. Res., 90, 8417-8432, 1985.

Yau, A. W., B. A. Whalen, W. K. Peterson and E. G. Shelley, Distribution of upflowing ionospheric ions in the high-altitude polar cap and auroral ionosphere, J. Geophys. Res., 89, 5507, 1984.

Yeh, H. C., and J. C. Foster, Storm time heavy ion outflow at mid-latitude, 95, 7881-7892, 1990.

Young, D. T., Experimental aspects of ion acceleration in the Earth's magnetosphere, in Ion Acceleration in the Magnetosphere and Ionosphere, Geophys. Monogr. Ser., vol. 38, edited by T. Chang, p. 17, AGU, Washington, D.C., 1986.

Young, D. T., H. Balsiger and J. Geiss, Correlations of Magnetospheric ion composition with geomagnetic and solar activity, J. Geophys. Res., 87, 9077, 1982.

Zinin, L. V., Yu, I. Galperin, K. S. Latyshev, and S. A. Grigoriev, Nonstationary field-aligned fluxes of thermal ions O^+ and H^+ outside the plasmapause: refinement to the polar wind theory, in: Results of the ARCAD-3 Project and the recent Programmes in Magnetospheric and Ionospheric Physics, Cepadues, Toulouse, pp. 391, 1985.